

Hydrogen Induced Cracking and Sulfide Stress Cracking  
Evaluation of Low Alloy Casing Pipes

by

Saoussen Ouhiba

A thesis submitted in partial fulfillment of the requirements for the degree of

Master of Science

in

Materials Engineering

Department of Chemical and Materials Engineering  
University of Alberta

© Saoussen Ouhiba, 2017

## Abstract

Casing pipes used in sour service are prone to two forms of failure: hydrogen induced cracking (HIC) and sulfide stress cracking (SSC). The objective of this thesis is to investigate the resistance of L80 ERW and Seamless steel pipe, with five different chemical compositions, to both HIC and SSC. Analysis included electron microprobe analysis (EMPA) of macro-segregation at the centerline of the ERW pipes and Scanning Electron Microscopy (SEM) and Optical Microscopy (OM) characterization of the inclusions (i.e., size, composition, morphology and number) present in each steel. These inclusions characteristics were correlated with the HIC and SSC cracking parameters.

The susceptibility of L80 steel to HIC was evaluated using HIC testing based on NACE TM0284. Three parameters including crack length ratio (CLR), crack thickness ratio (CTR) and crack sensitivity ratio (CSR) were measured to determine the HIC resistance of the different tested materials. HIC cracks were observed at the center of the HIC samples. Investigation of the fracture surfaces of opened HIC cracks using SEM and EDX revealed that manganese sulfide (MnS) inclusions are the main initiation sites of HIC cracks.

The susceptibility of L80 steel to SSC was also determined using slow strain rate tests (SSRT) based on ASTM G129. Two parameters that are reduction in area ratio (RAR) and plastic strain to failure ratio (PSFR) were calculated to assess the resistance of the tested steels to SSC. Fractography was carried out to identify the mode of fracture and the origin of the SSC cracks. SSC cracks were found to initiate from corrosion pits formed at the SSRT sample surface and then propagate in a brittle transgranular manner.

A qualitative and quantitative characterization of the inclusions present in L80 steel was performed. This study confirmed that MnS inclusions are the main initiation sites of HIC cracks.

Al enriched inclusions were also found to play a role in the initiation and propagation of HIC cracks. However, their role is less significant than the role of MnS inclusions. For the SSRT tests, due to the SSRT sample orientation relative to the applied stress, clusters of Al enriched inclusions were found to be the main initiation sites of SSC cracks.

EMPA X ray mapping and line scanning of the major chemical elements (Mn, Cr, Si and P) across the HIC cracks were conducted to detect and quantify the macro-segregation behavior of these elements. EMPA X-ray maps showed that there is an enrichment of the zone around the HIC cracks in the above mentioned alloying elements, especially in phosphorus. The EMPA X-ray maps results were confirmed by EMPA line scans results that showed that the concentration of P around the HIC crack is at least 6 times higher than the nominal concentration of P. However, no clear correlation was found between CLR and the segregation ratios of the different analyzed elements determined by EMPA, which suggests that there are other factors that play a role in propagation of HIC cracks.

## **Acknowledgements**

I would like to acknowledge and thank my supervisors Dr. Hani Henein and Dr. Jingli Luo for their guidance and support. I would like to thank Dr. Barry Wiskel for his invaluable counsel during this study.

I would like to thank Roxanne Stankieveh and Dr. Laurie Collins of EVRAZ NA Inc., Regina for providing L80 casing pipes, for their helpful suggestions and for enabling me to use their facilities to conduct hydrogen induced cracking (HIC) testing. Special thanks to Curtis Finch of EVRAZ NA Inc., Regina for his assistance and help with HIC tests. Thanks to Andrew Locock and Pusong Wang for helping me with electron microprobe analysis (EMPA).

I would like to extend my thanks to EVRAZ NA Inc., Enbridge, Trans-Canada Pipeline, UT Quality and Alliance Pipelines for their financial sponsorship of this work along with the Natural Sciences and Engineering Research Council (NSERC) of Canada.

# Table of Contents

Abstract.....	ii
Acknowledgements.....	iv
Table of Contents.....	v
List of Tables.....	x
List of Figures.....	xi
List of Abbreviations.....	xviii
Chapter 1 Introduction.....	1
1.1. Source of hydrogen in steel.....	2
1.2. Hydrogen induced cracking.....	3
1.3. Sulfide stress cracking.....	4
1.4. Importance of HIC and SSC.....	5
1.5. Objective and structure of the thesis.....	6
Chapter 2 Literature review.....	7
2.1. Casing steel for sour service.....	7
2.1.1. Sour service.....	7
2.1.2. Casing tubes.....	8
2.1.3. API standard grades for sour service.....	8
2.1.4. NACE MR 0175 material recommendation for sour service.....	9
2.2. L80 steel.....	11
2.2.1. Chemistry.....	11
2.2.2. Heat-treatment and mechanical properties.....	12
2.3. Hydrogen embrittlement mechanisms.....	13
2.3.1. Hydrogen-enhanced localized plasticity.....	14
2.3.2. Hydrogen-induced decohesion.....	15

2.3.3. Hydride formation and cleavage.....	15
2.3.4. Synergistic/competitive action of hydride formation, HELP and HID .....	16
2.4. Factors affecting SSC and HIC resistance in low-alloy steels .....	17
2.4.1. Effect of alloying elements and impurities.....	17
2.4.2. Effect of microstructure.....	23
2.4.3. Effect of inclusions .....	25
2.4.4. Effect of grain size and crystallographic texture .....	29
2.4.5. Effect of centerline segregation.....	31
2.5. Fracture mechanisms.....	35
2.5.1. Ductile fracture .....	35
2.5.2. Transgranular cleavage.....	37
2.5.3. Intergranular fracture.....	39
2.6. Summary .....	40
Chapter 3 Materials and experimental methods.....	41
3.1. Steels studied.....	41
3.2. Sample preparation.....	42
3.3. Micro-hardness measurements.....	43
3.4. Characterization of inclusions.....	43
3.5. Hydrogen induced cracking tests .....	45
3.5.1. Introduction .....	45
3.5.2. Testing apparatus.....	45
3.5.3. Test environment .....	46
3.5.4. Sample preparation .....	46
3.5.5. Test procedure .....	47
3.5.6. Evaluation of samples.....	48

3.6. Study of centerline macro-segregation using electron microprobe analyzer (EMPA) .....	50
3.6.1. Introduction of EMPA .....	50
3.6.2. Study of centerline macro-segregation using EMPA .....	50
3.7. Slow strain rate tests.....	51
3.7.1. Introduction of SSRT.....	52
3.7.2. Test setup.....	52
3.7.3. Sample preparation .....	53
3.7.4. Test procedure .....	54
3.7.5. Analysis and reporting of test results .....	56
Chapter 4 Results .....	58
4.1. Microstructures.....	58
4.2. Vickers micro-hardness.....	62
4.3. Hydrogen induced cracking test results .....	63
4.3.1. HIC parameters.....	63
4.3.2. Morphologies of HIC cracks .....	67
4.3.3. HIC initiation sites.....	68
4.4. Slow strain rate test results.....	71
4.4.1. Stress-crosshead displacement curve.....	72
4.4.2. Reduction in area ratio (RAR).....	73
4.4.3. Plastic strain to failure ratio (PSFR).....	74
4.6. Fractography.....	75
4.6.1. Ductile fracture in air.....	75
4.6.2. Brittle fracture in an H <sub>2</sub> S saturated environment.....	77
4.7. Characterization of inclusions.....	81
4.7.1. Qualitative analysis (Inclusions morphology, chemistry and distribution).....	81

4.7.2. Size and fraction analysis of manganese sulfides (MnS) .....	85
4.7.3. Size and fraction analysis of globular and cubic inclusions in L80 steel .....	86
4.8. Study of centerline macro-segregation in L80 steel .....	88
4.8.1. EMPA X-ray mapping .....	89
4.8.2. EMPA Line scans .....	95
4.9. Summary .....	102
Chapter 5 Discussion .....	104
5.1. Precipitation of Manganese sulfide (MnS) inclusions in L80 steel .....	104
5.1.1. Effect of Mn and S contents on MnS number and length .....	104
5.1.2. Thermodynamic calculations .....	105
5.2. Role of inclusions in HIC .....	107
5.2.1. Role of MnS inclusions .....	107
5.2.2. Role of Al enriched and TiN inclusions .....	110
5.2.3. Susceptibility of different inclusions to HIC .....	111
5.3. Role of inclusions in SSC .....	112
5.3.1. Effect of toughness anisotropy on SSC propagation .....	112
5.3.2. Role of MnS inclusions .....	113
5.3.3. Role of Al enriched and TiN inclusions .....	114
5.4. Centerline macro-segregation .....	118
5.4.1. Centerline macro-segregation behavior of Mn, Cr, Si and P .....	119
5.4.2. Effect of centerline macro-segregation on HIC propagation .....	120
5.5. Summary .....	123
Chapter 6 Conclusions and Recommendations .....	124
6.1. Conclusions .....	124
6.2. Recommendations .....	125



References.....	127
Appendix A ImageJ processing procedure .....	138
Appendix B Safety precautions in handling H <sub>2</sub> S.....	140
Appendix C Vickers micro-hardness results.....	143
Appendix C.1 .....	143
Appendix C.2 .....	144
Appendix C.3 .....	145
Appendix C.4 .....	146
Appendix D HIC parameters (CLR, CTR, CSR) results .....	147
Appendix D.1 .....	147
Appendix D.2 .....	148
Appendix D.3 .....	149
Appendix E Morphologies of HIC cracks .....	150
Appendix F SSRT results of samples tested in air and H <sub>2</sub> S solution.....	151
Appendix G Representative fractographs of SSRT samples .....	155
Appendix H Dispersion of inclusions .....	158
Appendix I EMPA results.....	164
Appendix I.1 .....	164
Appendix I.2.....	170
Appendix I.3 .....	176

## List of Tables

Table 2.1: Process of manufacture, tensile and hardness requirements for casing grades according to API 5CT-specification [18]. .....	9
Table 2.2: MR 0175 recommendation of casing grades with respect to temperature [14]. .....	11
Table 2.3: Chemical requirements for L80 steel-type 1 according to API 5CT-specification and to ERCB-Directive 10 [13,18]. .....	12
Table 3.1: Chemical composition (wt%) of the tested L80 casing steels. ....	42
Table 3.2: Used conditions during EMPA X-ray mapping and line-scanning. ....	51
Table 4.1: Morphology and chemistry of the main inclusions found in all L80 steels studied. ...	83
Table 5.1: Mean coefficients of linear expansion of steel matrix and different inclusions [127]. .....	108
Table 5.2: Equilibrium partition coefficients of solute elements in $\delta$ -ferrite and in austenite [137]. .....	120
Table B.1: Health effects from short-term exposure to hydrogen sulfide. ....	140

## List of Figures

Figure 1.1: Schematic of HIC, SSC and SOHIC [4].....	1
Figure 1.2: Global description of HE interaction aspects. ....	2
Figure 1.3: Schematic of hydrogen entry during HIC [6].....	3
Figure 1.4: Step-wise cracking [9].....	4
Figure 1.5: SEM micrograph showing blisters on the surface of the sample [10].....	4
Figure 1.6: Sulfide stress cracking in a low alloy steel [9].....	5
Figure 1.7: National Energy Board-regulated pipeline rupture causes. ....	5
Figure 2.1: Regions of environmental severity with respect to the SSC of carbon and low alloy steels [15].....	8
Figure 2.2: Schematic representation of MR 0175-2009/ISO 15156 materials recommendation at room temperature [20]. ....	10
Figure 2.3: Microstructure of water-quenched L80 steel showing lath martensite [23].....	13
Figure 2.4: Schematic of the effect of banded structure and M/A islands on SSC resistance [47]. .....	19
Figure 2.5: Two sulfo-oxide inclusions: a) 1-CaO-Al <sub>2</sub> O <sub>3</sub> 2-(Ca,Mn)S, b) 1-Al <sub>2</sub> O <sub>3</sub> 2-MnS [67].	21
Figure 2.6: 1-Al <sub>2</sub> O <sub>3</sub> -MgO, 2-CaS [67].....	21
Figure 2.7: Total inclusions fraction % vs. Reduction in area ratio (RAR) for Mn-Cr-Mo steels [19].....	25
Figure 2.8: Relationship between sulfur content and stress level for fracture in 200 hours [91].	26
Figure 2.9: HIC crack nucleation from TiN inclusion [92]. ....	27
Figure 2.10: SEM micrographs of a fracture surface after constant load test with continuous hydrogen charging [93].....	28
Figure 2.11: Grain size number dependence of hydrogen content in the matrix.....	30
Figure 2.12: Schematic representation of the one strand, curved continuous casting process [107].....	32
Figure 2.13: Schematic illustration of the dendrites growth [109]. ....	33
Figure 2.14: Influence of the solidification shrinkage and bulging on the solute distribution across the centerline after 6 rolls [113].....	34
Figure 2.15: HIC along segregated band at the mid-wall position [114].....	35

Figure 2.16: SEM fractograph which shows a ductile fracture in a low carbon steel. A spherical inclusion at the center of a microvoid.....	36
Figure 2.17: Formation of the cup and cone fracture surface in uniaxial tension [116].....	37
Figure 2.18: SEM micrograph showing a cleavage fracture in a mild steel [117]. .....	38
Figure 2.19: Formation of river patterns, as a result of a cleavage crack crossing a twist boundary between grains [116].....	38
Figure 2.20: Schematic representation of the cleavage fracture micromechanisms: a) intact material, b) microcrack initiation from an intragranular particle, c) microcrack propagation across the particle and through the grain, d) crossing of the grain boundary [116]. .....	39
Figure 3.1: Location in the pipe where specimen for microscopic observation was taken (left), Mounted and polished sample (right). .....	43
Figure 3.2: The cutting location of samples for inclusion characterization.....	44
Figure 3.3: Illustration of cleanliness examination using optical microscopy.....	44
Figure 3.4: A schematic representation of a typical HIC test assembly. ....	45
Figure 3.5: Location in the pipe where the HIC samples were taken. ....	47
Figure 3.6: A photo of an actual machined HIC sample.....	47
Figure 3.7: Sections to be examined after exposure to HIC environment. ....	48
Figure 3.8: Crack dimensions to be used in calculating CSR, CLR and CTR. ....	49
Figure 3.9: Experimental setup of the SSRT test.....	53
Figure 3.10: a,c) Location in the pipe where the SSRT sample was machined, b) photo of a machined and untested SSRT sample. ....	54
Figure 3.11: Dimensions of the specimen used for SSRT tests [19]. ....	54
Figure 4.1: SEM image of MnCr steel.....	59
Figure 4.2: SEM image of High Mo steel.....	59
Figure 4.3: SEM image of High Mn steel.....	60
Figure 4.4: SEM image of TiB steel. ....	60
Figure 4.5: SEM image of SMLS steel.....	61
Figure 4.6: SEM image of TiB steel showing prior austenite grain boundaries. ....	62
Figure 4.7: Vickers micro-hardness profile across the centerline band in High Mo steel.....	63
Figure 4.8: Average values of CLR for HIC samples.....	64
Figure 4.9: Average values of CTR for HIC samples.....	65

Figure 4.10: Average values of CSR for HIC samples.....	66
Figure 4.11: An optical micrograph showing an example of a HIC crack in MnCr steel. ....	67
Figure 4.12: An optical micrograph of a TiB sample presenting a HIC crack at mid-thickness..	68
Figure 4.13: (a) SEM image of a TiN inclusion inside a HIC crack in TiB steel, (b) EDS X-ray spectrum of the TiN inclusion.....	69
Figure 4.14: SEM image of an opened HIC crack in High Mo steel showing elongated flat MnS inclusions (blue rectangle). ....	70
Figure 4.15: SEM image of an opened HIC crack in TiB steel showing elongated flat MnS inclusions (blue rectangle). ....	71
Figure 4.16: Stress-crosshead displacement curves for High Mo steel in air and in NACE A solution saturated with H <sub>2</sub> S.....	73
Figure 4.17: Reduction in Area Ratio (%) for different tested types of L80 steel.....	74
Figure 4.18: Plastic Strain to Failure Ratio (%) for different tested types of L80 steel. ....	75
Figure 4.19: SEM image of the fracture surfaces of MnCr steel showing a typical cup and cone fracture after failure in air. ....	76
Figure 4.20: A high-magnification SEM image of a ductile fracture surface showing dimples. .	76
Figure 4.21: (a) A macroscopic SEM image of the fracture surface of SMLS sample after SSRT in an H <sub>2</sub> S saturated environment, (b) % RAR as a function of % area of the brittle fracture surface (the trend is shown by a dashed line connecting between the data points). ....	78
Figure 4.22: A magnified SEM image of the initiation site for SSC in Figure 4.21 (a). ....	79
Figure 4.23: A magnified SEM image of the initiation site for SSC in TiB steel. ....	80
Figure 4.24: Fracture mode in SMLS steel. ....	81
Figure 4.25: An optical micrograph taken at mid-thickness of High Mo steel and showing elongated and globular inclusions.....	82
Figure 4.26: Optical micrograph taken at mid thickness of the pipe in High Mo steel. ....	84
Figure 4.27: Size distribution of MnS inclusions in the different types of L80 steel. ....	85
Figure 4.28: Total length of MnS inclusions for the different types of L80 steel. ....	86
Figure 4.29: Size distribution of all inclusions except MnS in all studied L80 steels.....	87
Figure 4.30: Total number of all inclusions present in all studied L80 steels except MnS inclusions. ....	88

Figure 4.31: EMPA X-ray map generated for Mn across the pipe wall thickness in an as received sample taken at 90° from the weld in High Mo steel (the dashed rectangle indicates the centerline macro-segregation band).....	90
Figure 4.32: (a) EMPA SE image showing High Mo sample after HIC test, (b) Mn EMPA X-ray map of the surface shown in (a).....	91
Figure 4.33: (a) Optical micrograph of High Mo sample lightly etched with Nital 2%, (b) Mn EMPA X-ray map of the region shown in (a).....	92
Figure 4.34: S EMPA X-ray map of the same area shown in Figure 4.33 (b).....	93
Figure 4.35: Cr EMPA X-ray map of the same area shown in Figure 4.33 (b).....	94
Figure 4.36: P EMPA X-ray map of the same area shown in Figure 4.33 (b).....	95
Figure 4.37: Location of the line scan on the Mn EMPA X-ray map of a High Mo as received sample. ....	96
Figure 4.38: Mn concentration profile along the line scan shown in Figure 4.37. ....	97
Figure 4.39: P concentration profile along the line scan shown in Figure 4.37. ....	98
Figure 4.40: Location of the line scans on the optical micrograph of High Mo sample. ....	99
Figure 4.41: Mn concentration profile along the line scans 1 and 2 shown in Figure 4.40.....	100
Figure 4.42: Variation of segregation ratios of Mn, Cr and Si along the line scans 1 and 2 shown on Figure 4.40. ....	101
Figure 4.43: Variation of the segregation ratio of P along the line scans 1 and 2 shown on Figure 4.40.....	102
Figure 5.1: Effect of [Mn][S] on number and total length of MnS inclusions (the trends are shown by the dashed lines connecting the data points). ....	105
Figure 5.2: Prediction of MnS inclusions precipitation using the Scheil-Gulliver model (Thermo-Calc).....	106
Figure 5.3: Effect of number of MnS inclusions on HIC resistance.....	109
Figure 5.4: Effect of maximum length of MnS on HIC resistance. ....	110
Figure 5.5: Effect of Al enriched and TiN inclusions on HIC resistance. ....	111
Figure 5.6: Schema of orientation of different types of inclusions during SSRT performed in the longitudinal direction for a sample taken from an ERW pipe. ....	113
Figure 5.7: Effect of MnS inclusions on RAR.....	114
Figure 5.8: Effect of Al enriched and TiN inclusions on RAR. ....	115

Figure 5.9: Number of MnS inclusions versus number of other inclusions in different L80 steels. .....	116
Figure 5.10: Comparison between dimensions of MnS inclusions and dimensions of other inclusions (mainly Al enriched oxides) in the plane perpendicular to the applied stress. ....	118
Figure 5.11: EMPA measured segregation ratios (SR) of Mn, Si, Cr and P across the HIC cracks in 4 HIC tested L80 samples. ....	119
Figure 5.12: Relationship between the segregation ratio of Mn determined by EMPA across the HIC crack and the crack length ratios measured on each section. ....	122
Figure 5.13: Relationship between the segregation ratio of P determined by EMPA across the HIC crack and the crack length ratios measured on each section. ....	122
Figure C.1: Vickers Micro-hardness profile across the centerline band in TiB steel. ....	143
Figure C.2: Vickers micro-hardness profile across the centerline band in High Mn steel. ....	144
Figure C.3: Vickers micro-hardness profile across the centerline band in MnCr steel. ....	145
Figure C.4: Vickers micro-hardness profile from the inner surface to the center of the pipe in SMLS steel. ....	146
Figure D.1: CLR (%) values measured at different locations in the pipe for the HIC tested L80 steels. ....	147
Figure D.2: CTR (%) values measured at different locations in the pipe for the HIC tested L80 steels. ....	148
Figure D.3: CSR (%) values measured at different locations in the pipe for the HIC tested L80 steels. ....	149
Figure E.1: Optical micrograph of a HIC crack observed in a section cut at 90° from High Mo steel. ....	150
Figure E.2: Optical micrograph of a HIC crack observed in a section cut at 180° from High Mn steel. ....	150
Figure E.3: Optical micrograph of a HIC crack observed in a section cut at 180° from TiB steel. .....	150
Figure F.1: Stress versus crosshead curves for MnCr steel. ....	151
Figure F.2: Stress versus crosshead displacement curves for SMLS steel. ....	152
Figure F.3: Stress versus crosshead displacement curves for High Mn steel. ....	153
Figure F.4: Stress versus crosshead displacement curves for TiB steel. ....	154

Figure G.1: SEM images of the fracture surface of MnCr steel in air (left) and in H <sub>2</sub> S (right).	155
Figure G.2: SEM images of the fracture surface of High Mo steel in air (left) and in H <sub>2</sub> S (right).	155
Figure G.3: SEM images of the fracture surface of SMLS steel in air (left) and in H <sub>2</sub> S (right).	156
Figure G.4: SEM images of the fracture surface of High Mn steel in air (left) and in H <sub>2</sub> S (right).	156
Figure G.5: SEM images of the fracture surface of TiB steel in air (left) and in H <sub>2</sub> S (right).....	157
Figure H.1: Two optical micrographs taken in High Mo pipe at 90° from the weld and at the center of the pipe and adjacent to each other showing different distributions of inclusions, (a) shows a lower number of inclusions, (b) shows a higher number of inclusions. ....	158
Figure H.2: Optical micrograph taken at (a) centerline and (b) close to the pipe wall in High Mo steel. ....	159
Figure H.3: Optical micrograph taken at (a) centerline and (b) close to the pipe wall in TiB steel. ....	160
Figure H.4: Optical micrograph taken at (a) centerline and (b) close to the pipe wall in MnCr steel. ....	161
Figure H.5: Optical micrograph taken at (a) centerline and (b) close to the pipe wall in High Mn steel. ....	162
Figure H.6: Optical micrograph taken at (a) centerline and (b) close to the pipe wall in SMLS steel. ....	163
Figure I.1: Mn EMPA X-ray map across the total thickness of MnCr 180° Section 3. ....	164
Figure I.2: Mn EMPA X-ray map of a small area around a HIC crack in MnCr 180° Section 3. ....	165
Figure I.3: Mn concentration profile along the line scans 1 and 2 shown in Figure I.2. ....	166
Figure I.4: Cr concentration profile along line scans 1 and 2 shown in Figure I.2.....	167
Figure I.5: Si concentration profile along line scans 1 and 2 shown in Figure I.2. ....	168
Figure I.6: P concentration profile along line scans 1 and 2 shown in Figure I.2. ....	169
Figure I.7: Mn EMPA X-ray map across the total thickness of High Mn 180° Section 2. ....	170
Figure I.8: Mn EMPA X-ray map of the area indicated by a square in Figure I.7. ....	171
Figure I.9: Mn concentration profile along the line scans 1 and 2 shown in Figure I.8. ....	172
Figure I.10: Cr concentration profile along line scans 1 and 2 shown in Figure I.8.....	173



Figure I.11: Si concentration profile along line scans 1 and 2 shown in Figure I.8. ....	174
Figure I.12: P concentration profile along line scans 1 and 2 shown in Figure I.8. ....	175
Figure I.13: Mn EMPA X-ray map across the total thickness of TiB 90° Section 2.....	176
Figure I.14: Mn EMPA X-ray map of the area indicated by a square in Figure I.13. ....	177
Figure I.15: Mn concentration profile along the line scans 1 and 2 shown in Figure I.14. ....	178
Figure I.16: Cr concentration profile along the line scans 1 and 2 shown in Figure I.14.....	179
Figure I.17: Si concentration profile along the line scans 1 and 2 shown in Figure I.14. ....	180
Figure I.18: P concentration profile along the line scans 1 and 2 shown in Figure I.14. ....	181

## List of Abbreviations

API	American Petroleum Society
ASTM	American Society for Testing and Materials
CLR	Crack Length Ratio
CSR	Crack Sensitivity Ratio
CTR	Crack Thickness Ratio
EDX	Energy Dispersive X ray spectroscopy
EMPA	Electron Microprobe Analyzer
ERCB	Energy Resources Conservation Board
ERW	Electric Resistance Weld
HE	Hydrogen Embrittlement
HIC	Hydrogen Induced Cracking
MnS	Manganese Sulfide
NACE	National Association of Corrosion Engineers
OM	Optical Microscope
PSFR	Plastic Strain to Failure Ratio
RAR	Reduction in Area Ratio
SEM	Scanning Electron Microscope
SMLS	Seamless
SR	Segregation Ratio
SSC	Sulfide Stress Cracking
SSRT	Slow Strain Rate Test
TiN	Titanium Nitride
WDS	Wavelength Dispersive X ray Spectroscopy

## Chapter 1 Introduction

With conventional oil and gas reserves dwindling, the oil and gas industry is shifting to environments rich in hydrogen sulfide [1]. Under these conditions, environmentally assisted cracking (EAC) has been recognized as a dominant contributing factor to failures and leaks in downhole pipes [2,3]. Three main environmental cracking phenomena, which are schematically represented in Figure 1.1, can take place:

1. Stress-oriented hydrogen-induced cracking (SOHIC)
2. Hydrogen-induced cracking (HIC): also known as stepwise cracking (SWC)
3. Sulfide stress cracking (SSC) [2,4]

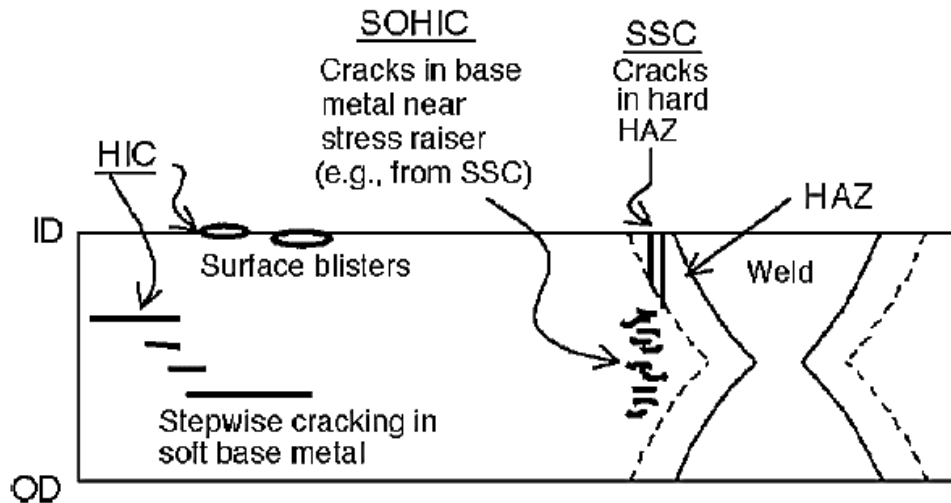


Figure 1.1: Schematic of HIC, SSC and SOHIC [4].

Three conditions need to be simultaneously satisfied to induce any of these types of hydrogen damage: a hydrogen source, an applied or a residual stress and a susceptible material. Figure 1.2 illustrates this concept where hydrogen embrittlement (HE) occurs at the interaction of these above mentioned factors. HE includes HIC and SSC. In the absence of any of these conditions, HE does not take place [5].

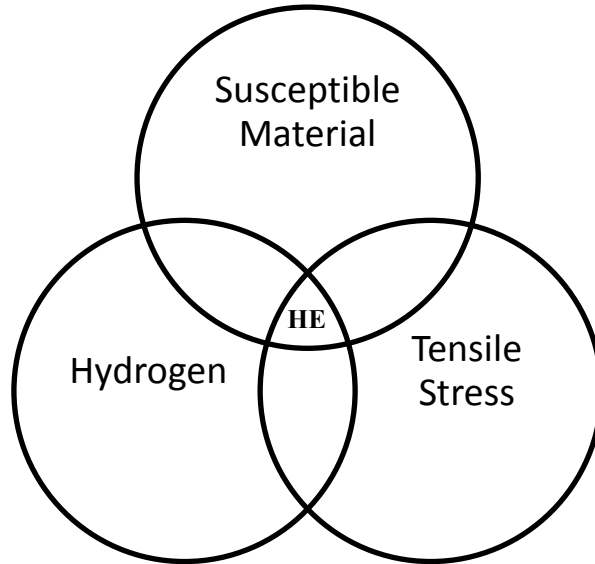
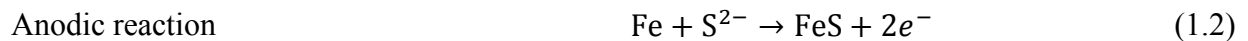


Figure 1.2: Global description of HE interaction aspects.

### 1.1. Source of hydrogen in steel

One source of atomic hydrogen (H) in the steel is the reaction between iron (Fe) and hydrogen sulfide (H<sub>2</sub>S). H<sub>2</sub>S dissolves in water according to reaction (1.1), which is followed by reactions (1.2), (1.3) and (1.4) [6,7].



In practice, iron sulfide corrosion products can take other molecular forms such as FeS<sub>2</sub>, Fe<sub>7</sub>S<sub>8</sub> or Fe<sub>9</sub>S<sub>8</sub> depending on the pH, H<sub>2</sub>S partial pressure and oxidizing potential of the environment [7].

Normally, the hydrogen atoms produced in the cathodic reaction combine to form molecular hydrogen on the surface of the steel. However, the presence of sulfide ions inhibits the recombination reaction of atomic hydrogen, promoting the diffusion of atomic hydrogen into the steel [6]. Hence, hydrogen atoms that enter the metallic lattice are trapped at metallurgical defects such as inclusion/matrix interfaces, voids, impurities, dislocations or micro-cracks and can cause HE and subsequent failure of the steel [2].

## 1.2. Hydrogen induced cracking

HIC is a form of HE in low-strength steel (typically < 80 ksi (550 MPa)) during exposure to wet hydrogen sulfide environments and it appears in the form of cracks or blisters [4]. HIC occurs when hydrogen atoms diffuse to internal defects such as the interface between inclusions and matrix or cavities in the steel and combine to form hydrogen molecules that are too large to diffuse out. Hence, hydrogen molecules accumulate at the inclusion-matrix interface leading to an increase in the pressure as shown in Figure 1.3. An increase in the pressure leads to an increased tensile stress at the inclusion-matrix interface. When the tensile stress reaches a critical value, a HIC crack initiates. This type of cracking is usually oriented parallel to the rolling plane of the steel and is associated with inclusions and segregation bands in the steel. HIC cracks form in the absence of an externally applied stress and propagate by linking up in a stepwise manner as shown in Figure 1.4. A surface blister forms when cracks near the surface cannot propagate further inside the steel sample. Figure 1.5 gives an example of blisters on the surface of the steel [2,8].

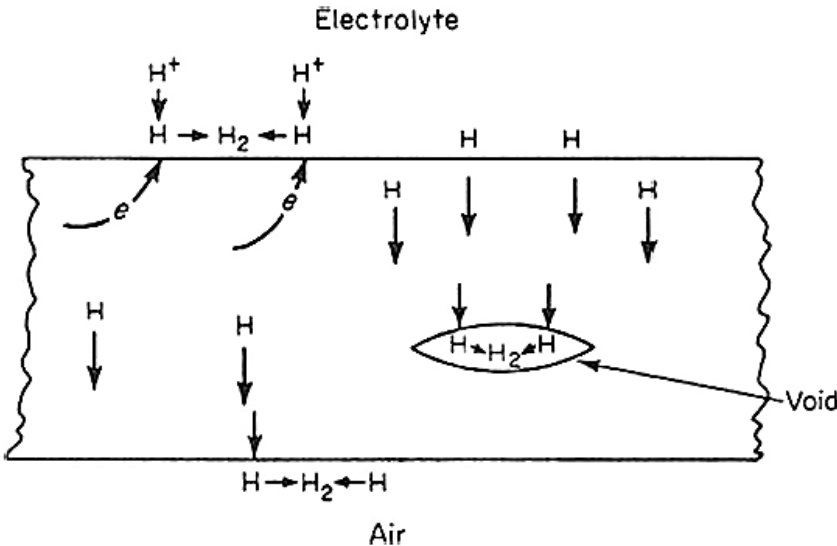


Figure 1.3: Schematic of hydrogen entry during HIC [6].

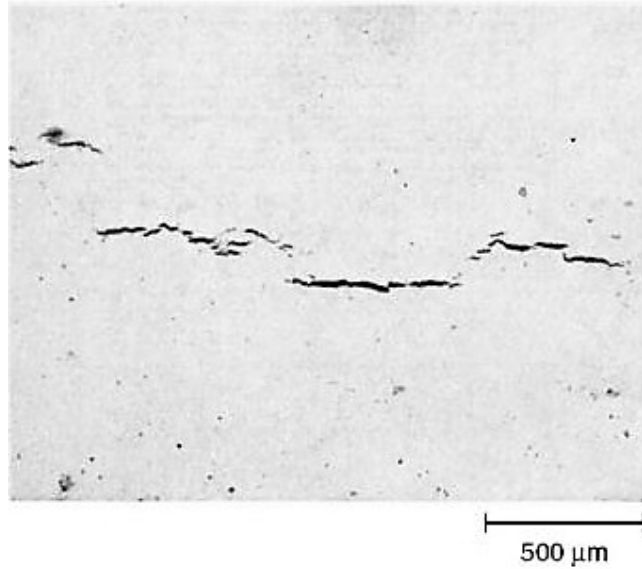


Figure 1.4: Step-wise cracking [9].

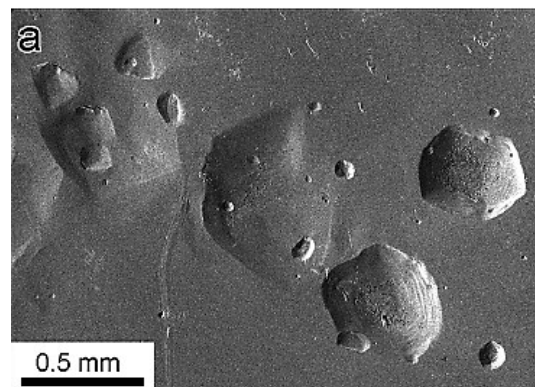


Figure 1.5: SEM micrograph showing blisters on the surface of the sample [10].

### 1.3. Sulfide stress cracking

SSC is another form of HE that occurs in high-strength steel under the combined action of an externally applied stress and an aqueous environment containing  $H_2S$  at room temperature. SSC occurs usually in a brittle manner with a direction perpendicular to the applied stress as shown in Figure 1.6. Steels with hardness of 22 Rockwell C or higher are susceptible to SSC in sour environments [11]. This level of hardness can be found in high-strength steel or in the hard heat-affected zone (HAZ) near a weld. SSC cracks initiating at hard HAZ usually stop when they reach the soft base metal [4].

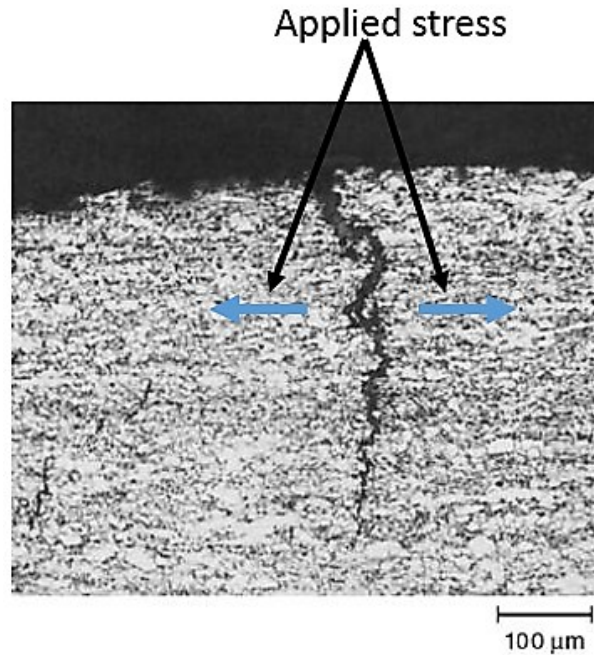


Figure 1.6: Sulfide stress cracking in a low alloy steel [9].

#### 1.4. Importance of HIC and SSC

Figure 1.7 shows the causes for the reported ruptures on National Energy Board (NEB)-regulated pipelines between 1991 and 2009. The primary cause of ruptures on NEB-regulated pipelines was cracking. Cracking includes HIC, SSC, mechanical damage delayed cracking, and corrosion fatigue [12]. Thus, HIC and SSC are among the main causes for pipeline failures, which explains the importance of studying these two forms of HE in this thesis. The category of other causes includes improper operation, fire and yet to be determined causes [12].

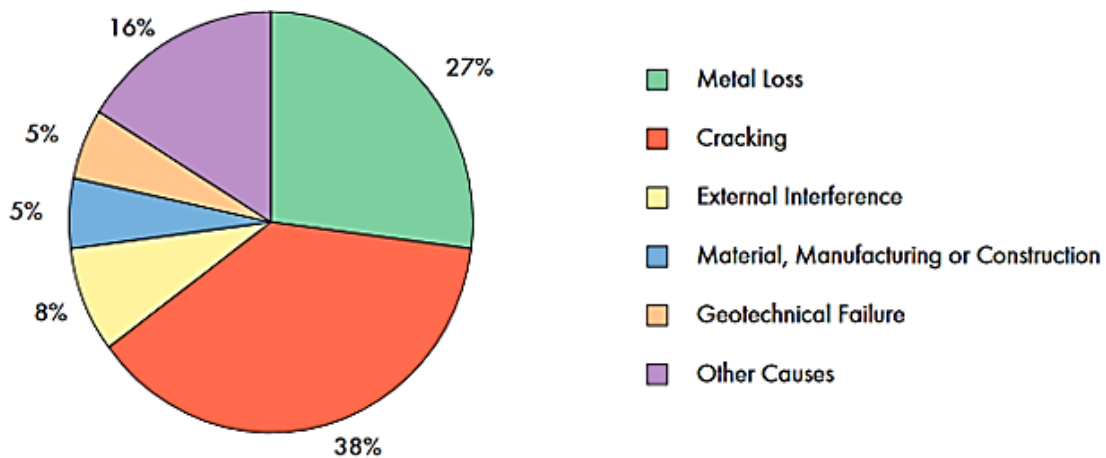


Figure 1.7: National Energy Board-regulated pipeline rupture causes.

## 1.5. Objective and structure of the thesis

The objective of this work is to understand the effect of the main metallurgical factors (i.e., inclusions and centerline segregation) on HIC and SSC in order to improve the resistance of L80 steel to HIC and SSC. The main types of inclusions responsible for initiation of HIC and SSC cracks will be identified, and the role of centerline segregation in the propagation of HIC cracks will be investigated. These metallurgical factors will be evaluated principally using two tests: HIC and slow strain rate tests (SSRT). The HIC tests will be based on NACE TM0284, while, the SSRT will be based on ASTM G129. Thus, the susceptibility of the L80 steels to failure due to exposure to hydrogen (i.e., HE) will be evaluated with and without an applied stress. A qualitative and quantitative characterization of the inclusions present in L80 steel will be conducted to study the effect of the different types of inclusions on these two forms of HE. An electron microprobe analysis (EMPA) technique including X-ray mapping and line scans will be developed to investigate the effect of centerline macro-segregation on HIC susceptibility of L80 steel.

To accomplish these objectives described above, this thesis is divided into 6 chapters. The literature review in Chapter 2 presents an introduction to casing steel for sour service in particular L80 steel, to HE mechanisms, to factors affecting HIC and SSC and to fracture mechanisms in metals. The detailed information of the tested materials (five types of L80 steel) and the experimental procedures are described in Chapter 3. Chapter 4 presents the summarized experimental results obtained from microstructure observations, Vickers micro-hardness testing, HIC tests, SSRT tests, SSRT fracture surface examinations, qualitative and quantitative analysis of inclusions and EMPA technique results. Discussion of the results presented in Chapter 4 is found in Chapter 5, while conclusions along with recommendations are summarized in Chapter 6. Additional results supporting Chapter 4 are shown in the Appendices.



## Chapter 2 Literature review

This literature review includes an introduction to casing steel for sour service especially L80 steel, which is used as the tested material in this work. This is followed by a review of HE mechanisms. A review of the factors affecting HIC and SSC is also presented. Finally, the fracture mechanisms in metals are described in this chapter.

### 2.1. Casing steel for sour service

This section begins with a definition to sour service, which is the environment where L80 steel is used, along with an introduction to casing tubes in general. This introduction to sour service and casing tubes is followed by the American Petroleum Institute (API) grades suitable for sour service. In addition, the recommendations provided by the National Association of Corrosion Engineers (NACE) for selection of casing steel are presented.

#### 2.1.1. Sour service

The directive 010 written by the Energy Resources Conservation Board (ERCB) specifies what a sour service is: a sour service refers to an environment containing a partial pressure of  $H_2S$  greater than 0.3 kPa (0.05 psi) [13].

According to NACE MR0175-Part 2, the severity of a sour environment, with respect to the SSC of a carbon or low-alloy steel, can be assessed using Figure 2.1 where both the pH of the environment and the  $H_2S$  partial pressure are taken into account. The region number represents the severity from the less severe (Region 0) to the most severe (Region 3).

Region 0 is considered as a sweet environment, where no precautions are required for the selection of steels for use under these conditions. The materials required for regions 1, 2 and 3 are documented in NACE MR0175-Part 2, Annex A [14] and will be presented in detail in sections 2.1.3 and 2.1.4.

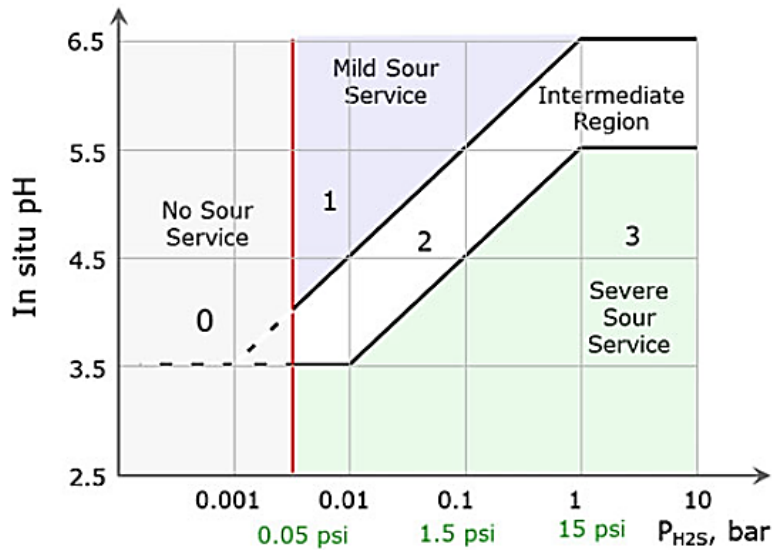


Figure 2.1: Regions of environmental severity with respect to the SSC of carbon and low alloy steels [15].

### 2.1.2. Casing tubes

Casing is the tubing that is inserted into a recently drilled well. Casing tubes are used to support the sides of a well hole by preventing the walls of the well from caving in. Casing tubes protect also the wellstream and the fresh water reservoirs from contamination. As oil demands are increasing, oil fields now being explored require drilling to depths beyond 20,000 ft [16]. At these depths, high formation pressures and hydrogen sulfide gas are often encountered, which require casing tubes to have at the same time a high yield strength and a good resistance to hydrogen embrittlement [16,17].

### 2.1.3. API standard grades for sour service

Various casing steels for sour service have been specified in API 5CT specification such as J55, K55, C90, T95 and L80 [18].

API standardized L80, C90 and T95 casing and tubing products for sour service applications at all temperatures in 1975, 1985 and 1989 respectively [17–19]. All these grades are required to be heat-treated by the quench and temper process because it provides a better resistance to hydrogen embrittlement than as-rolled, normalized or normalized and tempered steels. In addition to the quench and temper process, L80 is required by the API tubular good specification to have a

controlled hardness that does not exceed 23 Rockwell C and a yield strength that is maintained within the range of 552 and 655 MPa (80 and 95 ksi) [17,18].

In 2011, a new casing grade C110 was finally standardized by API for use in sour environments after being tested and standardized by the National Association of Corrosion Engineers (NACE) [18].

The required hardness and yield strength for all the above mentioned grades are summarized in Table 2.1 [18]. The maximum hardness readings reported in Table 2.1 correspond to the maximum hardness readings of single points. The maximum hardness average values reported in Table 2.1 correspond to the maximum hardness average values of three points.

Table 2.1: Process of manufacture, tensile and hardness requirements for casing grades according to API 5CT-specification [18].

Grade	Manufacturing Process	Yield Strength (ksi)		Max hardness reading (HRC)	Max hardness average value (HRC)
		min	max		
J55	Seamless or ERW	55	80	22	22
K55	Seamless or ERW	55	80	22	22
L80-type 1	Seamless or ERW	80	95	23	22
C90-type 1	Seamless	90	105	25.4	25
T95-type 1	Seamless	95	110	26.5	25
C110	Seamless	110	120	30	30

#### 2.1.4. NACE MR 0175 material recommendation for sour service

In addition to the standardized API grades, NACE provides recommendation for the manufacture and selection of oilfield equipment [14,17,20]. Selection is based on three main environmental parameters (Temperature, H<sub>2</sub>S partial pressure and pH) which are presented in Figure 2.2 [14,20].

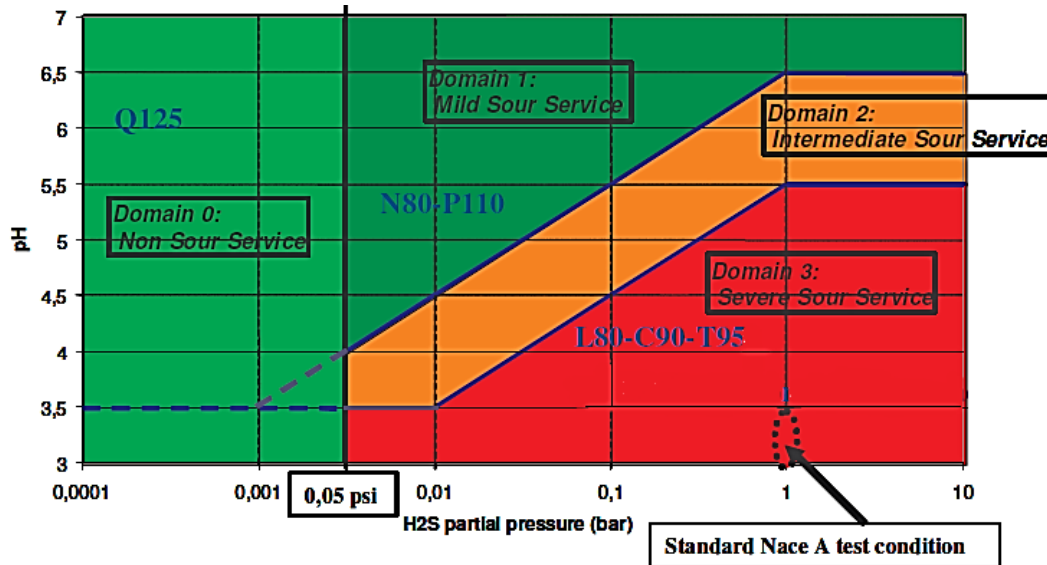


Figure 2.2: Schematic representation of MR 0175-2009/ISO 15156 materials recommendation at room temperature [20].

Table 2.2 tabulates ISO and API grades of casing and tubing depending on the temperature. A higher temperature allows the use of higher grades such as P110 and Q125 in sour service. A quenched and tempered L80 grade with a Cr-Mo chemistry is acceptable at all temperatures [14]. In addition, higher strength grades, namely C100, C105 and C110 have been standardized by NACE. These three grades are required to have a yield strength that can only be 15 ksi higher than the SMYS and a hardness value lower than 30 Rockwell C. They must be also made of Cr-Mo low alloy steels and quenched and tempered to offer a good resistance to hydrogen embrittlement [14,17,20].

Table 2.2: MR 0175 recommendation of casing grades with respect to temperature [14].

For all temperatures	For $\geq 65$ °C (150 °F)	For $\geq 80$ °C (175 °F)	For $\geq 107$ °C (225 °F)
ISO 11960 <sup>a</sup> grades: H40 J55 K55 M65 L80 type 1 C90 type 1 T95 type 1	ISO 11960 <sup>a</sup> grades: N80 type Q C95	ISO 11960 <sup>a</sup> grades: N80 P110	ISO 11960 <sup>a</sup> grade: Q125 <sup>b</sup>
Proprietary grades as described in A.2.2.3.3	Proprietary Q & T grades with 760 MPa (110 ksi) or less maximum yield strength  Casings and tubulars made of Cr-Mo low-alloy steels as described in A.2.2.3.2.	Proprietary Q & T grades with 965 MPa (140 ksi) or less maximum yield strength	
Temperatures given are minimum allowable service temperatures with respect to SSC. Low temperature toughness (impact resistance) is not considered, equipment users shall determine requirements separately.			
<sup>a</sup> For the purposes of this provision, API 5CT is equivalent to ISO 11960:2001.			
<sup>b</sup> Types 1 and 2 based on Q & T, Cr-Mo chemistry to 1 036 MPa (150 ksi) maximum yield strength. C-Mn steels are not acceptable.			

## 2.2. L80 steel

This section provides the main properties of L80 steel (i.e., chemistry, quench and temper heat-treatment and the required mechanical properties).

### 2.2.1. Chemistry

L80 is available in type 1, 9 Cr and 13 Cr. Because L80-9Cr and L80-13Cr are used only in CO<sub>2</sub> environments, this study will focus on L80-type 1, which will be referred to as L80 steel throughout this thesis [21]. The high yield strength of L80 steel is achieved by the addition of small amounts of alloying elements and limiting the amount of harmful elements such as phosphorus and sulfur [21]. Both API-5CT specification and ERCB-Directive 10 have specified the basic chemistry for L80 steel which is summarized by Table 2.3 [13,18]. C, Mn, P and S contents specified by ERCB directive are lower than the amounts specified by API 5CT specification.

Table 2.3: Chemical requirements for L80 steel-type 1 according to API 5CT-specification and to ERCB-Directive 10 [13,18].

<b>Element</b>	<b>API 5CT-specification</b>	<b>ERCB-Directive 10</b>
C	0.43	0.32 (may be raised to 0.35% if S < 0.005% and P < 0.015%)
Mn	1.90	1.40 (may be raised to 1.45% if S < 0.007%, and to 1.50% if S < 0.005%)
Mo	Non-specified	Non-specified
Cr	Non-specified	Non-specified
Ni	0.25	Non-specified
Cu	0.35	Non-specified
P	0.03	0.020 (P may be raised to 0.025% if Cr + Mo > 0.30%, and to 0.025% if S < 0.005%)
S	0.03	0.010 (S < 0.015% if Cr + Mo > 0.60%)
Si	0.45	Non-specified
P+S	Non-specified	0.025 (may be raised to 0.030% if Cr + Mo > 0.30%, and to 0.035% if Cr + Mo > 0.6%)

### 2.2.2. Heat-treatment and mechanical properties

L80 steel undergoes a quench and temper heat treatment after pipe forming. The pipe is austenized to 925°C for few minutes (i.e.,  $\approx 5$  minutes). Proper austenitization requires uniform heating of the pipe in the austenitizing furnace in order to prevent excessive grain growth which can have a detrimental influence on the mechanical properties of the pipe [20,22]. Afterwards, the pipe is water-quenched in order to form martensite, which is supersaturated with dissolved carbon, thus producing a very hard phase [22]. Figure 2.3 shows an example of lath martensite commonly found in low-alloy steels such as L80 steel after quenching.

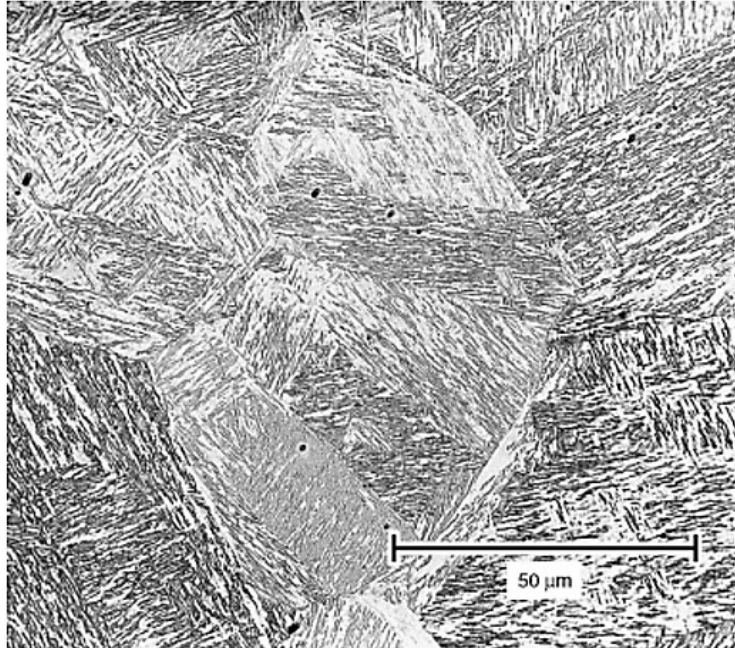


Figure 2.3: Microstructure of water-quenched L80 steel showing lath martensite [23].

Following quenching, tempering between 500 and 700°C is undertaken to improve the toughness of the pipe. A minimum tempering temperature of 566°C has been required by API for grade L80. During tempering, the carbon atoms diffuse and form  $Fe_3C$  and alloy carbides. The resultant microstructure is referred to as tempered martensite.

The properties of the tempered steel are primarily determined by the size, shape, composition and distribution of the carbides that form. These changes in the microstructure usually decrease hardness, tensile strength and yield strength and increase ductility and toughness, which improves the resistance of the steel to SSC and HIC [22].

Traditionally, grade L80 was the highest strength grade used in sour service applications [20]. L80 steel good resistance to SSC and HIC is due to the quench and temper heat treating process as well as its low hardness (maximum 23 Rockwell C) and relatively low yield strength (80 to 95 ksi) [18].

### 2.3. Hydrogen embrittlement mechanisms

Numerous mechanisms of HE have been proposed and argued for in the literature. However, of the many suggestions, three mechanisms appear to be viable: hydrogen-enhanced localized

plasticity (HELP), hydrogen-induced decohesion (HID) and hydride formation and cleavage [24].

### 2.3.1. Hydrogen-enhanced localized plasticity

Beachem [25] was the first to postulate that hydrogen in solid solution enhances dislocation mobility. This concept was reintroduced by Lynch [25] and further studied by Birnbaum [25], who conducted in situ deformation experiments in a controlled environment transmission electron microscope on a wide range of fcc, bcc, and hcp disordered and ordered metallic systems and who observed an increase in the dislocation velocity. This phenomenon is explained below.

The mobility of dislocations is affected by elastic interactions between dislocations and between dislocations and other stress centers such as solute atoms and precipitates. Hydrogen moves to dislocations to reduce their stress fields. Therefore, hydrogen atmospheres are formed around dislocations, which shields the interaction of dislocations with other elastic obstacles such as other dislocations or solute atoms leading to an increase in the dislocation mobility [25].

For example, in the case of the interaction between two edge dislocations, the shielding effect of hydrogen results in a decrease in the magnitude of the shear stress exerted by one dislocation on another. As a consequence, the repulsive force between two parallel dislocations of the same sign or the attractive force between two parallel dislocations of opposite signs is reduced. This reduction in the force between two dislocations leads to a decrease in the barrier in the dislocation motion and hence a movement of dislocations at a lower level of applied stress. Thus, the fracture process is a highly localized plastic failure process around the crack tip rather than an embrittlement [25].

By modelling hydrogen induced ductile fracture of A533B nuclear reactor steel, Dadfarnia et al. found that hydrogen induces a crack that propagates by growth of multiple voids at the vicinity of the crack tip followed by linkage to the crack tip [26]. The fracture toughness in the presence of hydrogen was reduced by 70% and the tearing modulus  $dJ/d\Delta a$ , which is a measure of the strain energy that must be provided to the crack tip to enable it to advance by a unit crack length, was almost diminished to zero. This result shows how hydrogen induced fractures appear brittle macroscopically, while the local mechanism at the microscale is mainly ductile [26].



### 2.3.2. Hydrogen-induced decohesion

This mechanism is one of the oldest proposed mechanisms and is often the most cited mechanism. It is supported primarily by the observations that in non-hydride forming materials, hydrogen embrittlement is not accompanied by a significant local deformation, by theoretical calculations of the effect of hydrogen on the atomic potentials and by a thermodynamic argument [27].

The repulsive forces determining the distance between Fe atoms are due to the overlapping of their d bands. The dissolution of hydrogen in Fe lattice increases the concentration of the electrons of these d bands, which produces an increase in the repulsive forces between Fe atoms, or in other words, a decrease in the cohesive strength of the lattice [28,29].

Being immobile, interstitial atoms such as hydrogen pin the dislocations. The pinning of dislocations by hydrogen is about one order of magnitude smaller compared with that for nitrogen and carbon atoms. If interstitial atoms are sufficiently mobile to follow dislocations in the course of plastic deformation, they affect the plastic flow depending on the local electron structure around the moving dislocations. The density of free electrons is increased in hydrogen atmospheres in the vicinity of dislocations, which decreases the cohesive force between Fe atoms and hence decreases the stress for dislocation movement [30].

The fracture strength of a solid material is a function of the cohesive forces that exist between atoms. The breaking of atomic bonds is expected when the stress concentration at the crack tip exceeds the cohesive force. Sufficiently high hydrogen concentrations that accumulate in regions of triaxial stress weakens the cohesive force between the metal atoms such as described above. The local maximum tensile stress becomes equivalent or greater than the lattice cohesive force and fracture occurs [27].

### 2.3.3. Hydride formation and cleavage

This mechanism is supported by microscopic observations and by thermodynamic calculations. It has been observed in systems where hydrides are either stable or can be stabilized by applying a stress field, e.g. Mg, Ta, Nb, V, U, Ti, Zr and their alloys. In this case, the embrittlement occurs by diffusion of hydrogen to the crack tip under the influence of a stress gradient, nucleation of a hydride phase and brittle cleavage. The crack propagates through the hydride and stops when it

reaches the matrix. Subsequently, a new hydride forms either autocatalytically or because of external loading and then cleavage reinitiates [31,32].

The hydride model is not applicable to iron and nickel alloys since they require extremely high hydrogen pressures in the GPa range to form hydrides [32].

#### 2.3.4. Synergistic/competitive action of hydride formation, HELP and HID

These three viable mechanisms are competitive in the sense that the mechanism that occurs first will determine the failure of the material. For example, in hydride-forming systems, fracture will occur by stress-induced hydride formation and cleavage if the external stress reduces the hydride solvus enough to promote hydride formation. At temperatures above the stress-free solvus temperatures, ductile rupture via HELP takes place instead of hydride formation and cleavage.

Similarly, intergranular embrittlement by HID is allowed when hydrogen segregates to grain boundaries. In the absence of such segregation, the failure is due to HELP. Finally, some materials such as beta Ti alloys can fail by the three mechanisms at the same time under certain conditions [33].

Ahn et al. focused on non-hydride forming systems and investigated the synergy between HELP and HID by performing simulations of subcritical brittle intergranular cracking in IN903 and by using cohesive elements to describe grain-boundary separation. Their calculations suggested a moderate reduction of cohesive energy (about 15%), while a purely brittle intergranular fracture of IN903 with no plasticity would require a reduction of the cohesive strength of the grain boundaries by an amount of the order of 85%. Hence, they concluded that hydrogen induced fractures are always accompanied by HELP, but in varying degrees, depending on the concentration of hydrogen in metal [26].

Recently, simultaneous action of HELP and HID mechanisms were detected. However, the overview of hydrogen embrittlement in steels under various conditions remains unclear and the coexistence of different hydrogen embrittlement mechanisms is still not well documented [34,35].

## 2.4. Factors affecting SSC and HIC resistance in low-alloy steels

The behavior of carbon and low-alloy steels in H<sub>2</sub>S environments depends on different parameters:

- Environmental parameters: H<sub>2</sub>S partial pressure, pH of the water phase, presence of sulfur or other oxidants, and exposure temperature;
- Metallurgical parameters: chemical composition, strength, hardness of the material, heat-treatment condition, microstructure, grain size and cleanliness of the material [14].

Since it is impossible for materials engineers to have a control over the environmental parameters, the next part of the literature review will focus only on the metallurgical parameters that affect SSC and HIC resistance.

### 2.4.1. Effect of alloying elements and impurities

In this section, the role of the main alloying elements Mn, S, Mo, Ti, Al, Ca, P, Si and Cr will be described in detail.

#### 2.4.1.1. Manganese and Sulfur

Mn and S are considered together because Mn tends to combine with S to form MnS inclusions. Mn is one of the abundant elements on earth and it is added to all carbon and alloy steels in amounts of 0.3% or more. Mn plays an important role in increasing the hardenability by lowering the transformation points. Mn is also a powerful de-oxidizer. S is usually an undesirable impurity in the steel rather than an alloying element and tends to form FeS at the grain boundaries in the absence of Mn. FeS are very harmful. FeS can cause hot shortness due to their lower melting point and thus remain liquid at rolling temperatures. Also, FeS are more brittle than MnS and can have an adverse effect on the mechanical properties of the steel. For these reasons, Mn is added to steel and MnS are preferred to FeS [36–38].

Although MnS have a better plasticity than FeS and help to avoid cracks to appear during the rolling process, they can degrade both the fracture toughness and the corrosion resistance of the steel. MnS were identified as the initiation sites of hydrogen induced cracks in many studies [39–42]. The harmful effect of elongated MnS inclusions can be reduced by lowering the S content or by Ca additions.

Another disadvantage of Mn is its tendency to segregate at the centerline of the strip produced by hot rolling continuously cast steel slabs [43]. Therefore, recent attempts have been made to use lower levels of Mn to the range of 0.2-0.5 wt%. At this low level and at a given S content, the formation of MnS from the liquid will take place later in the solidification process and hence the MnS are smaller in size. BlueScope Steel in Australia succeeded in achieving a better toughness in low Mn steels at higher S levels by dramatically reducing the occurrence of centerline segregation banding and the size of MnS inclusions [40,44]. Asahi et al. found also that a decrease in Mn content has a positive effect on the SSC resistance since it increases the SSC threshold stress [45]. However, Hejazi et al. found that decreasing the Mn content from 1.2% to 0.5% in the steels resulted in a decrease in fracture toughness [40].

#### 2.4.1.2. Molybdenum

As the grade number of pipeline increases to meet high strength and toughness, the addition of alloying elements such as Mo is important. Mo promotes the formation of low-temperature transformation structures, which can increase the strength of the steels. Mo is also a strong carbide former and is usually present in alloy steels in amounts less than 1% [37,46]. Liao and Lee studied the microstructural effect associated with Mo additions on SSC. They found that the banded pearlite becomes more dispersed and less continuous as a result of Mo addition, leading to an improvement in the SSC resistance. On the other hand, the number of martensite/austenite islands increases with Mo content as a result of the decrease in transformation temperature of second phases. The effect of banded structure and M/A islands on SSC resistance is summarized in Figure 2.4. Combining these two effects, Liao and Lee concluded that the best SSC resistance is obtained at 0.3% Mo [47].

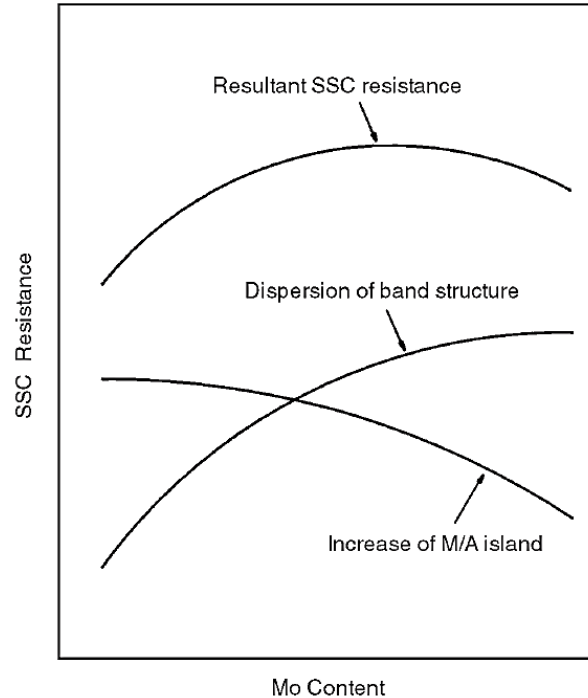


Figure 2.4: Schematic of the effect of banded structure and M/A islands on SSC resistance [47].

Another reason behind the beneficial effect of Mo on the resistance of low alloy steel to hydrogen sulfide damage is the precipitation during tempering of fine carbides that resist coarsening. Craig showed that fine carbides  $Fe_2MoC$  form in AISI 4130 steel modified with 0.75 wt% Mo when tempered above  $600^{\circ}C$ . These fine carbides act as hydrogen traps decreasing the detrimental effect of hydrogen observed in the standard 4130 alloy [48]. Finally, the addition of Mo leads to the formation of fine-grained acicular ferrite at a relatively low carbon content, producing an optimum strength-toughness balance [49,50]. For example, Koh et al. found that a single addition of 0.3 wt% Mo or a combined addition of Cr and Mo can improve the SSC resistance of low alloy steels by modifying the microstructure from ferrite to acicular ferrite [50].

### 2.4.1.3. Titanium

Ti in low alloy steel can provide grain refinement, precipitation strengthening and sulfide shape control[51]. Ti tends to combine with N to form TiN precipitates that can retard both austenite grain growth during continuous casting and grain growth of recrystallized austenite during controlled rolling. To maintain a fine dispersion of small TiN ( $<1\mu m$ ), the Ti content is limited to approximately 0.01 wt%. Otherwise, TiN can form in the liquid and the TiN size can be larger

than  $1\mu\text{m}$  which is harmful to the mechanical and corrosion properties of the steel. Furthermore, Ti is a strong carbide former which can be used for the precipitation strengthening of low alloy steels. The addition of Ti also changes the nature of inclusions from Mn-based inclusions such as MnS to Ti-based ones such as (Mn,Ti)S,  $\text{Ti}_4\text{C}_2\text{S}_2$ , TiO, and  $\text{Ti}_2\text{O}_3$  [51–53].

The effect of Ti(C,N) on the resistance of low alloy steels to HIC has been studied by Hejazi et al. who proved that the precipitated Ti carbonitrides act as beneficial hydrogen traps in hydrogen sulfide environment, leading to a delay in HIC[54]. It was found that the largest number of irreversible traps is associated with the largest volume fraction of fine Ti(C,N) precipitates [55].

#### 2.4.1.4. Aluminum

Al is added to steel as a deoxidizer. Al combines with oxygen to form alumina inclusions (aluminum oxides). Any excess of Al combines also with N to form AlN. Although AlN does not contribute to precipitation hardening, it plays an important role on grain refinement by retarding grain growth in steels, resulting in improved mechanical properties [37,51,56]. Al can be very detrimental to HIC and SSC. In fact, in many studies, it was reported that HIC and SSC cracks primarily nucleated at Al oxides [57–62]. However, several authors showed that the main nucleation sites for HIC are MnS rather than Al oxides [42,63,64]. Recently, there has been a great interest in Al additions, in the range of 1-2wt%, to austenitic Fe-Mn-C steels. Al additions can increase the stacking fault energy of the alloy which reduces stress concentrations at grain boundaries pile-ups, leading to a decrease in the concentration of H transported to stressed grain boundaries by piled-up dislocations [56,65,66].

#### 2.4.1.5. Calcium

Ca is a strong deoxidizer since it forms Ca oxides (CaO). The addition of Ca can change the composition of Al oxides from pure alumina to Ca aluminates ( $\text{CaO-Al}_2\text{O}_3$ ).

Another purpose of Ca addition is sulfide shape control. During solidification, S segregates to grain boundaries forming sulfides. These sulfides grow in length during hot rolling and can degrade the mechanical properties of the material. When Ca is added to the melt, the S is bound to Ca oxides or Ca aluminates and not deposited as sulfide inclusions at grain boundaries during the steel solidification [37,51,67]. Figure 2.5 shows microscopic examinations of oxide-sulfides

with an oxide core and a sulfide surface layer. When the content of Ca increases, its content in the surface ring increases, forming CaS as shown in Figure 2.6 [67].

Therefore, the addition of Ca has a positive effect on HIC resistance by modifying elongated MnS to globular Ca-Mn sulphides, which are very difficult to deform during rolling unlike MnS [68]. The addition of Ca to the steel in an amount ensuring that  $\text{Ca/S} > 0.14$  and  $\text{Ca/S} > 0.7$  decreases considerably the number and the area fraction of long inclusions [67].

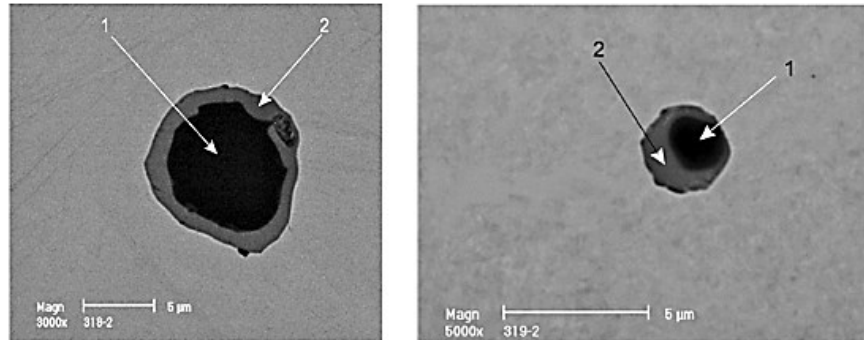


Figure 2.5: Two sulfo-oxide inclusions: a) 1-CaO-Al<sub>2</sub>O<sub>3</sub> 2-(Ca,Mn)S, b) 1-Al<sub>2</sub>O<sub>3</sub> 2-MnS [67].

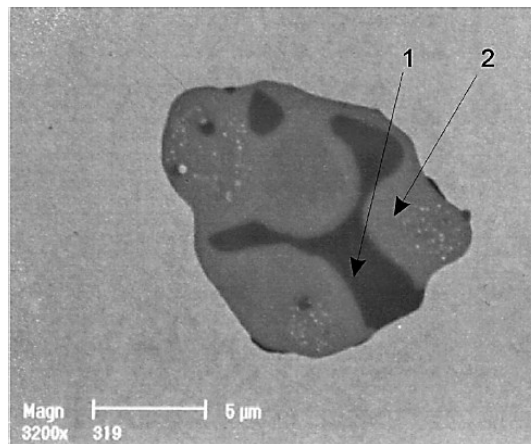


Figure 2.6: 1-Al<sub>2</sub>O<sub>3</sub>-MgO, 2-CaS [67].

#### 2.4.1.6. Phosphorus

P is considered as an impurity in the steel. P increases strength and hardness of the steel, but severely decreases ductility and toughness [37,51].

P tends to segregate to the grain boundaries, causing a reduction in the cohesive strength of grain boundaries. Grain-boundary segregation of P occurs in the range 400-600°C, for example, during slow cooling from a high-temperature or during isothermal treatment in this range of temperatures. This phenomenon is called temper embrittlement (TE).

As a result of TE, the DBTT increases and the fracture appearance in the brittle range (below the DBTT) changes from transgranular cleavage to intergranular decohesion, essentially along prior austenite grain boundaries [69–73]. It is widely known that grain coarsening enhances TE.

It has been shown in several studies that P segregation at prior austenite grain boundaries promotes not only TE, but also, intergranular cracking of high strength low alloy steels in the presence of hydrogen [45,74].

Since the same mode of fracture is associated with HIC or SSC and TE, there is an important question of whether TE can act synergistically with SSC or HIC. Yoshino and McMahon proposed a cooperative relation between TE and HE in a high strength steel [75]. The maximum cohesive force along prior austenite grain boundaries is lowered by the buildup of segregated impurities such as P. The collected hydrogen can lower this cohesive force still more, leading to crack growth along these grain boundaries at lower values of stress intensity [75].

However, Shimazu et al. demonstrated that there is no marked indication of the synergistic action of HE and TE [76]. Hence, this combined effect is not totally understood.

#### 2.4.1.7. Silicon

Si is one of the principal deoxidizers used in steelmaking. As a result of deoxidation, it can form silicate stringers. Si is added also in order to increase solid solution strength and hardness as well as to increase hardenability [51,77].

Several authors found that the threshold stress intensity is independent of Si content in ultra-high strength low alloy steel, but that the crack growth rate was significantly lowered when Si content is above 1.5 wt% [78,79]. First, Si inhibits  $\epsilon$  carbides formation during tempering process at low temperatures. Being hard phases,  $\epsilon$  carbides promote intergranular brittle cracking in the tempered martensitic steel. Secondly, the Si containing steel has higher density of low-angle grain boundaries that reduce the hydrogen diffusivity. Finally, Si promotes grain refinement which makes the crack propagation more difficult [79].

#### 2.4.1.8. Chromium

Cr is another essential element in low alloy steels. Cr is a strong carbide former. Cr carbides provide wear and abrasion resistance and high-temperature strength [37,51].



However, opinions on the effect of Cr on SSC or HIC is not unanimous [79]. Park et al. examined the effect of a Cr addition on the corrosion resistance of low alloy steel by electrochemical measurements. They observed that a protective  $\text{Cr}_2\text{O}_3$  layer formed around the Cr-containing steel, leading to an increase in the corrosion resistance of the steel [80].

However, another study showed later that Cr, in the presence of Cu, tends to segregate at the grain boundaries. Localized corrosion is then enhanced by the galvanic action between the grain that acts as an anode and the grain boundary that acts as a cathode [81].

Besides, grain-boundary enrichment with Cr during austenitizing can lead to an enhanced segregation of P at the grain boundaries due to the chemical affinity between these two elements. Thus, steels containing Cr may be prone to temper embrittlement and hence to hydrogen embrittlement [82]. Koh et al. concluded that the combined addition of Cr and Mo is recommended for SSC resistance of steels, since they promote acicular ferrite formation, where as a single addition of Cr enhances the local corrosion of steels under external loading [50].

Finally, Song et al. showed that Cr carbides can act as H traps decreasing H diffusivity, leading to an enhanced delayed fracture resistance [79].

#### 2.4.2. Effect of microstructure

Microstructure is known to play a significant role in HIC and SSC. Microstructure is one of the variables that can be optimized during the steel manufacturing in order to improve the HIC or SSC resistance. Hence, numerous studies have been conducted to study the effect of the microstructure.

It was shown by Parkins that quenching was detrimental to the SSC resistance of high strength low alloy steels, with cracks following prior-austenite grain boundaries or martensite lath boundaries. Parkins found also that quenching followed by tempering or normalizing could improve the SSC resistance of high strength low alloy steels because tempering the martensite at sufficiently high temperatures produces a relatively dislocation-free matrix with uniform dispersion of spheroidized carbides [83].

A more recent study conducted by Carneiro et al. confirmed the previous finding by proving that a refined and homogeneous quenched and tempered bainite/martensite microstructure had the best performance with respect to both HIC and SSC whereas the ferritic-pearlitic microstructures showed a greater susceptibility to  $\text{H}_2\text{S}$  related failure [84].

Mohtadi-Bonab studied X70 pipeline steel by applying different heat treatments. He found that tempered martensite was highly susceptible to HIC just as ferrite/bainite, martensite/retained austenite and acicular ferrite/bainite microstructures even though the tempering process is known to improve HIC resistance [85].

The development of thermo-mechanical control process (TMCP) technology made the achievement of a fine and uniform acicular ferrite microstructure possible. From there, investigators started to focus on microstructures controlled by TMCP.

Zhao et al. compared an acicular ferrite-dominated microstructure to an ultrafine equiaxed ferrite microstructure and to a ferritic-pearlitic microstructure. Ferritic-pearlitic microstructure was the most susceptible to SSC, which could be explained by the fact that carbides and MnS inclusions usually precipitate along the banded pearlite. Hydrogen easily diffuses to the interfaces between these precipitates and the banded pearlite and reaches the critical concentration. A crack initiates and easily propagates through the susceptible cracking path provided by the segregated pearlite bands. However, the SSC susceptible banded pearlite is completely eliminated in acicular ferrite and ultrafine ferrite leading to more resistant microstructures. The ultrafine ferrite was in a second position. The acicular ferrite-dominated microstructure had the best SSC resistance, which is due to its dispersed precipitates, high-density tangled dislocations and randomly-oriented grain boundaries that act as strong hydrogen traps [86].

Dong et al. concluded by studying the HIC resistance of X70 steel that cracks tend to appear at the grain boundary of polygonal ferrite, but not the grain boundary of acicular ferrite. Hence, acicular ferrite (AF) shows a better HIC resistance than polygonal ferrite (PF) [87].

A strong correlation between the trapping efficiency and microstructure of steel was found by Park et al. In fact, the hydrogen trapping efficiency increased in order by degenerate pearlite, bainite and acicular ferrite. The same researcher found that the main initiation sites of internal cracks were locally agglomerated martensite/austenite constituents for the ferritic-bainitic and acicular ferritic steels. In comparison with bainite, acicular ferrite was more resistant to HIC thanks to its high toughness that impedes the crack propagation [88].

### 2.4.3. Effect of inclusions

In this section, the effect of the amount of inclusions and of the main types of the inclusions (i.e., Manganese sulfides, Titanium nitrides and oxides) present in steel on HIC and SSC will be presented.

#### 2.4.3.1. Amount of inclusions

Huang showed in her thesis by performing SSC tests on L80 steel that, within the same alloying group, SSC susceptibility increases as the total inclusion fraction increases. Figure 2.7 shows the relationship between the total inclusion area fraction and the ratio of reduction in area (RAR). A lower value of RAR means a higher susceptibility to SSC [19].

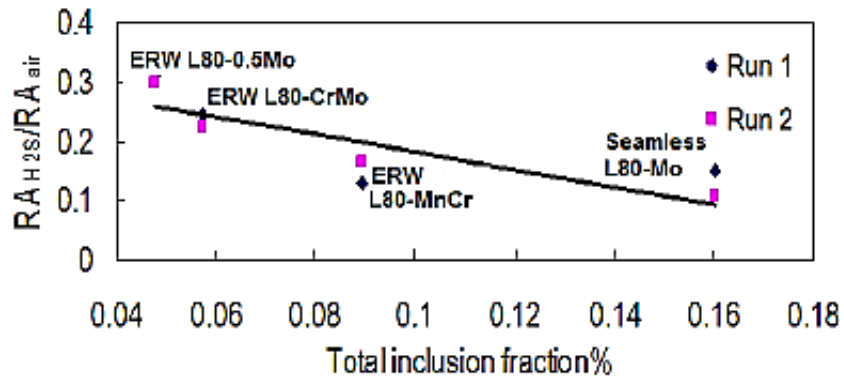


Figure 2.7: Total inclusions fraction % vs. Reduction in area ratio (RAR) for Mn-Cr-Mo steels [19].

#### 2.4.3.2. Manganese sulfides

MnS are soft inclusions that easily deform during rolling, leading to elongated inclusions which are considered to be harmful to impact and fracture toughness of the steel [89].

MnS exhibit also a much higher value of a thermal expansion coefficient than the steel matrix. Therefore, during cooling, the sulfides shrink in volume much more than the steel matrix leading to the formation of voids between the inclusions and the steel. As a result, stress fields increase around them during cooling [90]. These tensile stresses can initiate cracks at the interface between the inclusion and the matrix [89].

Teruhisa Ohki was among the first researchers who investigated the relationship of sulfur content and sulfide shape to SSC characteristics. For studying the effect of sulfur, the standard chemical composition for oil well pipe was taken as a constant with different amounts of sulfur and the structure was fully quenched and tempered. For studying the effect of the shape of sulfide inclusions, rare earth metals (Ce and La) were added to some samples for controlling the shape. Corrosion tests were performed using a four point bend test in an H<sub>2</sub>S-containing environment. The effects of sulfur content and shape controlling on SSC are summarized in Figure 2.8. Figure 2.8 shows that spheroidizing manganese sulfides, together with reducing sulfur content, lower the susceptibility to SSC [91].

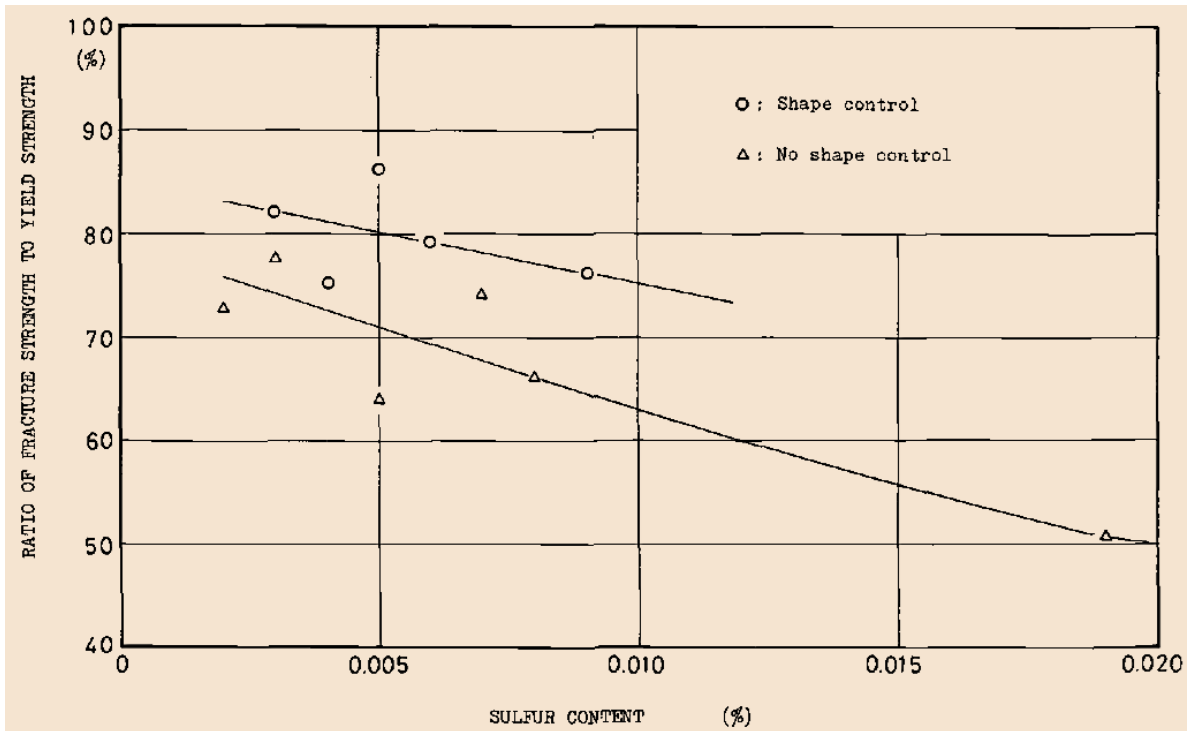


Figure 2.8: Relationship between sulfur content and stress level for fracture in 200 hours [91].

A further investigation on the influence of sulfur content and sulfide distribution on HIC in pressure vessel and pipeline steels was carried out by Domizzi et al. [42]. Metallographic observation of HIC specimens after testing showed that many cracks are associated with MnS inclusions and that they extend along the pearlitic or pearlitic-martensitic bands. HIC susceptibility was empirically correlated to the average length of MnS (LM) and to the total length of MnS per unit area (LA) (Equation (2.1)), or to LM and sulfur content (S) (Equation

(2.2)). The correlations were obtained for steels with a sulfur content between 0.005 and 0.015 wt% and a banding microstructure having microhardness lower than 300 HV.

Equation (2.1) suggests that a good resistance to HIC ( $UAL < 20\%$ ) can be reached in steels having sulfur content as high as 0.015% provided that the average length of MnS (LM) is lower than  $17\ \mu\text{m}$  and that no hard bands are present in the microstructure [42].

$$UAL (\%) = 5.43 \times 10^{-2} \times LM^2 \times LA \quad (2.1)$$

$$UAL (\%) = 38.118 \times LM^2 \times S^{1.5} \quad (2.2)$$

where UAL is the ultrasonic attenuation level.

### 2.4.3.3. Titanium nitrides

Ti-nitrides were also reported as major nucleation sites for cracks. Figure 2.9 shows an example of HIC crack that initiates at the interface between rhombic TiN inclusion and the matrix [92].

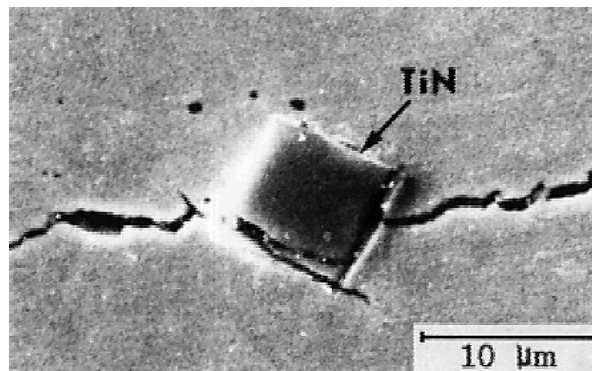


Figure 2.9: HIC crack nucleation from TiN inclusion [92].

Todoshchenko et al. observed a lot of TiC/TiN particles on the fracture surface of high strength carbon steels that were tensile tested at constant load under continuous electrochemical hydrogen charging [93]. A characteristic feature of the fracture surface was fish eyes as shown in Figure 2.10 (a). Figure 2.10 (b) shows that the fish eyes were formed around large TiC/TiN particles between  $5$  and  $20\ \mu\text{m}$  [93].

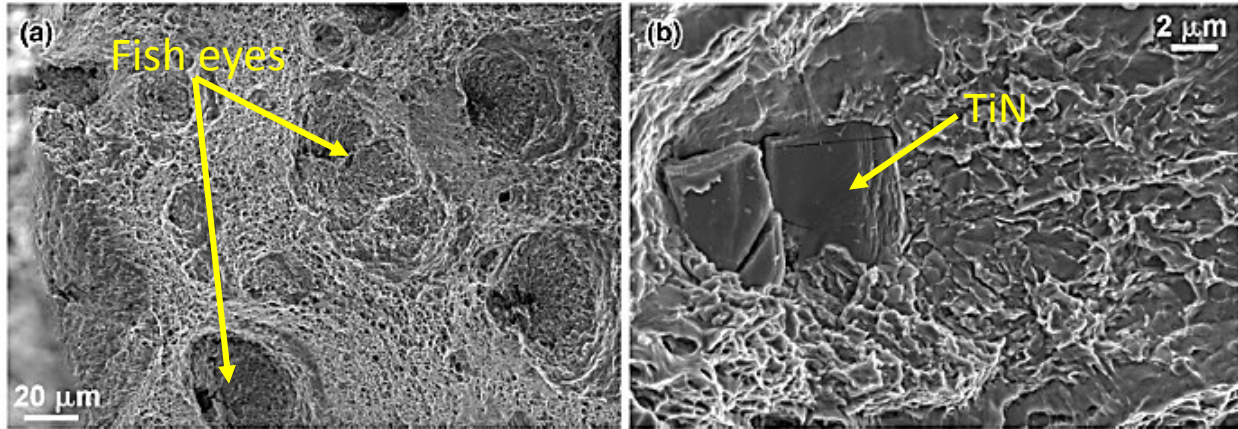


Figure 2.10: SEM micrographs of a fracture surface after constant load test with continuous hydrogen charging [93].

#### 2.4.3.4. Oxides

Oxide inclusions such as alumina and calcium aluminates are stress raisers due to their lower thermal coefficient of expansion compared to that of steel leading to the formation of cavities around the inclusion [89].

Dong et al. found that most of inclusions present in the HIC cracks of an X70 steel are oxides of Ca, Fe, Mn and Al. The possible reason behind these cracks may be the size of the inclusions. Usually the sizes of nitrides of Ti and Nb are very small (less than 1 μm on average) whilst the diameter of oxides and other inclusions is typically 2-3 μm. The maximum diameter of oxides observed in X80 steel was 7 μm. Thus, due to their larger size, inclusions such as Ca-oxides can attract more hydrogen than nitrides [94].

Kim et al. demonstrated that oxide inclusions and clusters with a size over 20 μm in maximum length are the initiation sites in steels which have bainitic ferrite structure. As soon as a HIC crack initiates at an oxide cluster, the crack propagates in a quasi-cleavage manner following hard microstructure such as M/A constituents [58].

The latter was confirmed by Koh et al. who found that the critical inclusion cluster diameter for HIC nucleation was about 20 μm for ferrite/bainite and 150 μm for ferrite/acicular ferrite [95]. Although several types of inclusion were present in X80 and X100 steels, it was found that HIC cracks initiated mainly at Al and Si oxides. There was no crack associated with the elongated MnS inclusion and Ca-Al-O-S inclusion [59,60,87].

Finally, Sojka et al showed that all the SSC cracks nucleated from globular oxides [63].

## 2.4.4. Effect of grain size and crystallographic texture

This section begins with an introduction to the effect of grain size on HIC and SSC resistance, followed by a description of the effect of crystallographic texture on HIC and SSC susceptibility.

### 2.4.4.1. Grain size

Another important parameter for hydrogen damage in a material is the grain size. Within one grain, the individual atoms form a crystalline lattice. The interface between two grains is called grain boundary. The grain boundaries hinder the motion of dislocation resulting in an increase in the strength of the material. Therefore, the mechanical properties of a material are improved by grain refinement, which is expressed by the Hall-Petch equation (2.3).

$$\sigma_y = \sigma_0 + k_y d^{-\frac{1}{2}} \quad (2.3)$$

where  $\sigma_y$  is the yield strength,  $d$  is the average grain diameter,  $\sigma_0$  and  $k_y$  are constants. Hence, small grains are often preferred for their high strength and toughness [96].

A fine grain size not only improves the mechanical properties but also increases the resistance to hydrogen embrittlement.

However, no unified explanation of the positive effect of grain refinement has yet been established. According to Bernstein and Thompson, the origin of this positive effect is probably due to an increasing number of trapping sites as the grain boundary area per unit volume increases [97].

Fuchigami et al. [98] showed that finer prior austenite grain size increases the hydrogen absorption capacity in quenched and tempered medium carbon steel leading to a reduction in SSC susceptibility. A refinement of prior austenite grain size leads to a larger grain boundary area resulting in an increase in the absorbed hydrogen content. Additionally, the hydrogen absorption capacity is increased by plastic straining due to the reduction of the density of vacancies that are created by dislocation dynamics [98].

The same conclusion was drawn by Takasawa et al. who studied the effect of grain size on hydrogen embrittlement of high-strength low-alloy steel in a high pressure hydrogen atmosphere. Figure 2.11 shows that hydrogen content in the matrix increases with decreasing grain size number in both series. The grain size number is inversely proportional to the grain size [99].

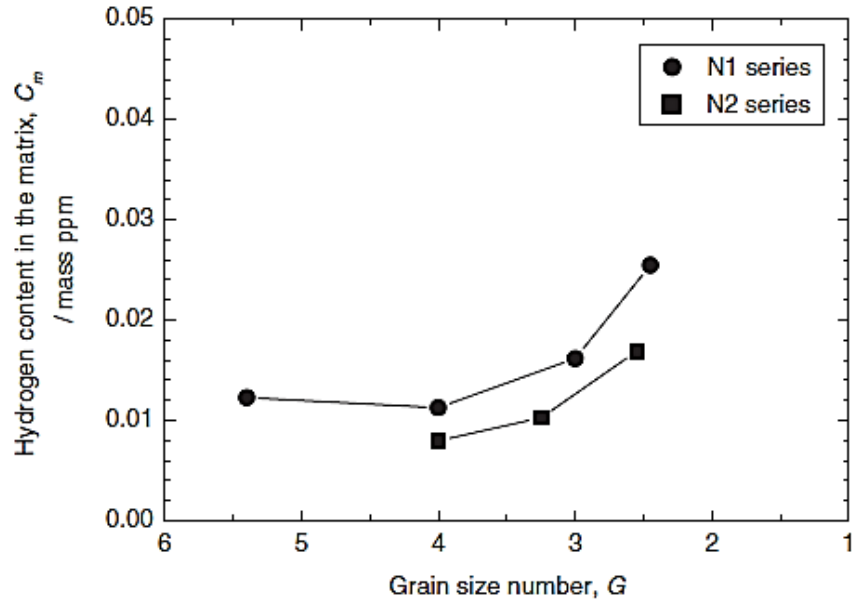


Figure 2.11: Grain size number dependence of hydrogen content in the matrix.

However, Ichimura et al. pointed out the contradictory effects of grain size on hydrogen diffusion. They found that grain boundaries can either increase or decrease the hydrogen diffusion rate [100].

As the grain size decreases, the mobility of hydrogen increases due to the presence of larger grain boundary area per unit volume. But when the grain size decreases remarkably, the nodes and junction points can act as hydrogen traps leading to a reduction in the hydrogen mobility and therefore an increase in HIC susceptibility. Consequently, the diffusion coefficient of hydrogen will be a maximum at an optimum grain size [40]. These opposing effects were reported by some other researchers [85,101].

#### 2.4.4.2. Crystallographic texture

Texture and grain orientation appear to be also potentially important parameters. The term texture means the crystallographic orientation of grains in a polycrystalline material. During the manufacturing process, grains may be oriented in a preferred orientation leading to the presence of a texture.

Venegas et al. investigated the effect of texture on HIC susceptibility in API X46 steel and they showed that warm rolling below recrystallization temperature produces a  $\{111\}$ //ND dominant



texture leading to an increase in the HIC resistance [102].  $\{hkl\}$ //ND represent grain orientations with  $\{hkl\}$  planes parallel to the steel rolling plane.

Ghosh et al. showed that  $\{001\}$ //ND grains provide an easy cleavage path for crack propagation leading to a significant decrease in HIC resistance [103].

However, Masoumi et al. found that HIC cracks propagated not only through  $\{001\}$ //ND oriented grains, but also along the grain oriented with  $\{111\}$ //ND [104].

The same result was confirmed by Mohtadi-bonab who reported that there is no preferred direction for HIC crack propagation [105].

An important thing to note from this literature review is that the effect of grain size and crystallographic texture is not completely understood.

#### 2.4.5. Effect of centerline segregation

This section includes an introduction to continuous casting, an introduction to microsegregation and to centerline macrosegregation and a study of the effect of centerline macrosegregation on HIC susceptibility.

##### 2.4.5.1. Continuous casting of steel

Continuous casting transforms molten metal into solid on a continuous basis. The principle of steel continuous casting is shown in Figure 2.12. In this process, molten steel flows from a ladle, through a tundish into the mold. The tundish not only provides a continuous flow to the mold, but also plays the role of a refining vessel to float out detrimental inclusions into the slag layer. The molds are generally water-cooled copper molds. In contact with the mold, the molten steel is cooled down to form a solid shell. The solid shell must be thick enough to support the liquid pool. Below the mold, the solid shell is further cooled down by spraying water. Afterwards, the strand is reheated and transferred to a rolling mill [106,107].

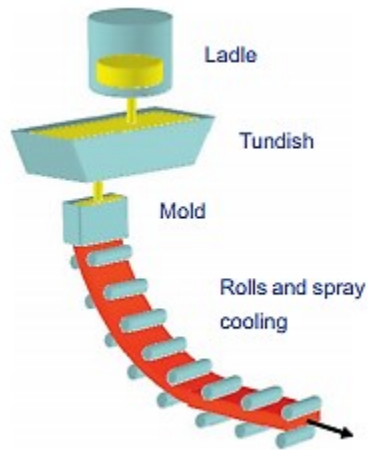


Figure 2.12: Schematic representation of the one strand, curved continuous casting process [107].

The big challenge in continuous casting is to cast steel continuously without defects. Unfortunately, centerline-segregation during the solidification of the liquid steel is an inevitable defect, arising from the higher solubility of alloying elements in the liquid steel than in the solid [107].

### 2.4.5.2. Segregation

Segregation is classified, according to its scale, as micro-segregation or macro-segregation. Positive segregation means that the concentration of the alloying element in a region is higher than its nominal concentration while a negative segregation means that the content is lower than the average concentration [107].

#### 2.4.5.2.1. Microsegregation

During the first stage of solidification of the cast slab, the dendrites start to grow from the external surfaces to the center in a columnar way as shown in Figure 2.13. Since solutes are more soluble in liquid than in solid, solute elements will be rejected from the dendrites to the interdendritic liquid. Freezing of the solute enriched liquid between the dendrites leads to micro-segregation [107].

Micro-segregation is not generally a major quality problem because subsequent homogenization or hot working operations can reduce it [108]. But if the micro-segregation is high during solidification, it may cause hot cracking and inclusions [107].

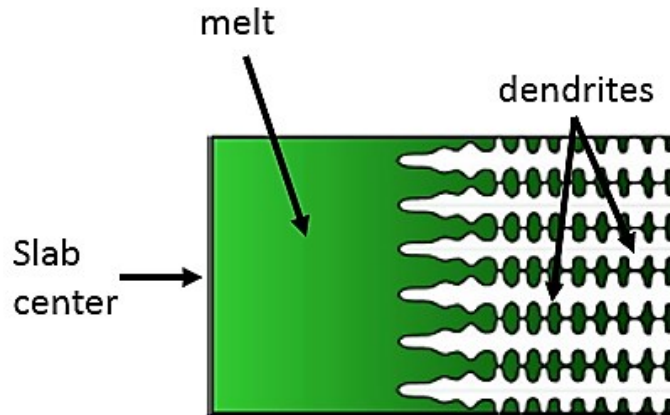


Figure 2.13: Schematic illustration of the dendrites growth [109].

#### 2.4.5.2.2. Centerline macrosegregation

Macrosegregation refers to a non-uniform chemical composition over a macroscopic area in the slab and is considered more harmful than micro-segregation [110].

Centerline macro-segregation arises from the large-scale flow of the molten steel due to solidification shrinkage and bulging during rolling [111–113]. In fact, the micro-segregated liquid between the dendrites moves outward from the dendritic region to the surrounding bulk liquid, leading to a positive segregation in the centerline of the slab. Bulging is considered as the major cause for such outward flow. The micro-segregated liquid can also move inward. The density of the solid steel is higher than that of the liquid phase, causing solidification shrinkage and hence an inward flow of the liquid in order to compensate for the volume difference. The result of the inward flow is a negative segregation at the center part of the slab [107,111–113].

The combined effect of bulging and solidification shrinkage on centerline segregation is summarized in Figure 2.14. Figure 2.14 shows the carbon macro-segregation distribution in the slab through thickness after the molten steel passed through 6 rolls. It is clear that bulging alone leads to a strong positive segregation at the centerline while shrinkage leads to a negative one. With both bulging and shrinkage, a positive centerline segregation followed by a negative one takes place [113].

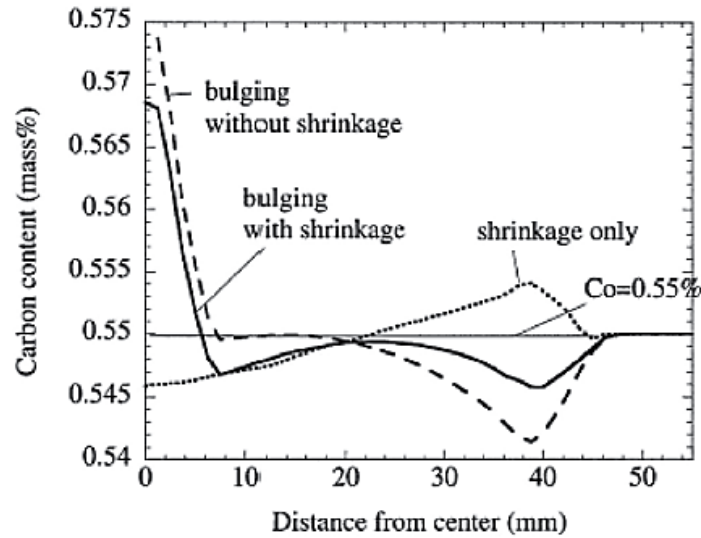


Figure 2.14: Influence of the solidification shrinkage and bulging on the solute distribution across the centerline after 6 rolls [113].

#### 2.4.5.3. Effect of centerline macrosegregation

Brown and Jones observed severe HIC cracking at the mid-wall thickness of several pipeline steels where bands of martensite/bainite were formed as shown in Figure 2.15. By performing microprobe analysis, they detected an increase in Mn and C concentrations of 50% and 40% respectively in the centerline band. They concluded that the combination of high inclusion content with bands of low temperature transformation products at the centerline of a pipe leads to an area of a high susceptibility to HIC [114].

Matsumoto et al. investigated the effect of centerline segregation and homogenization treatment on HIC. They found that the HIC susceptibility of pipeline steels increases with an increase in the hardness of the centerline segregation zone and that the hardness of the segregation zone increases with an increase in the carbon equivalent content or in the P content [115]. Therefore, a reduction of centerline segregation plays an important role in increasing the resistance of low alloy steel to HIC. A long-term homogenization treatment for 10 or 20 hours at 1200 or 1300°C has been shown to be effective in decreasing the concentrations of segregated elements at the centerline. However, from an industrial point of view, a long homogenization treatment is not profitable and decreases productivity [115].

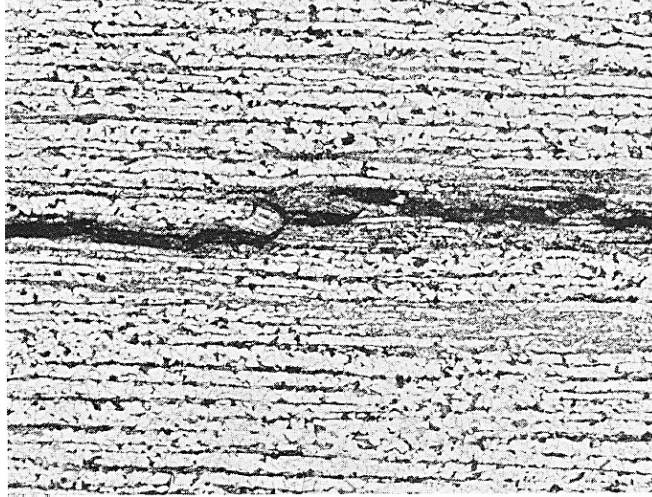


Figure 2.15: HIC along segregated band at the mid-wall position [114].

## 2.5. Fracture mechanisms

Ductile fracture, cleavage and intergranular fracture are the most common fracture mechanisms in metals and alloys. Thus, these fracture mechanisms are described in this section, which is based on reference [116].

### 2.5.1. Ductile fracture

Ductile materials usually fail as the result of nucleation, growth, and coalescence of microscopic voids that initiate at inclusions and second-phase particles. In very pure materials, the tensile specimens neck down to a sharp point leading to almost 100% reduction in area (RA). However, materials that include inclusions and second phase particles fail at much lower strains. A ductile fracture goes through the following stages:

1- Void nucleation: a void forms around a second phase particle or inclusion when sufficient stress is applied to break the interfacial bonds between the particle and the matrix. Numerous models for estimating void nucleation stress have been proposed. Argon et al. model predicts that the nucleation strain decreases as the hydrostatic stress increases, meaning that a triaxial tensile stress field is more likely to cause void nucleation. However, according to this model, void nucleation is independent of the particle size. Another model for void nucleation at submicron particles was proposed by Goods and Brown. This model assumes that dislocations near a particle increase the stress at the interface. As a result, the local stress concentration increases

with decreasing particle size. Thus, voids form much more readily with smaller particles than larger ones. However, experimental observations are different since voids usually nucleate at large particles such as inclusions [116].

2- Void growth and coalescence: once voids form around particles, they grow and eventually coalesce by means of plastic strain and hydrostatic stress. A dimpled fracture surface is characteristic of a ductile fracture as shown in Figure 2.16. A cup and cone fracture surface is also commonly observed in uniaxial tensile tests (Figure 2.17). The neck produces a triaxial stress state at the center of the specimen, leading to void nucleation and growth at the larger particles (Figure 2.17, a). The voids coalesce forming a penny-shaped flaw (Figure 2.17, b). The penny-shaped flaw produces deformation bands at  $45^\circ$  from the tensile axis. This concentration of strain allows voids to nucleate at even small particles (Figure 2.17, c). Total fracture occurs soon after these smaller voids form and results in the cup and cone appearance of the fracture surfaces (Figure 2.17, d). The central region of the fracture surface shows a dimpled appearance whereas the outer region appears relatively smooth due to the presence of smaller and closely spaced dimples [116].

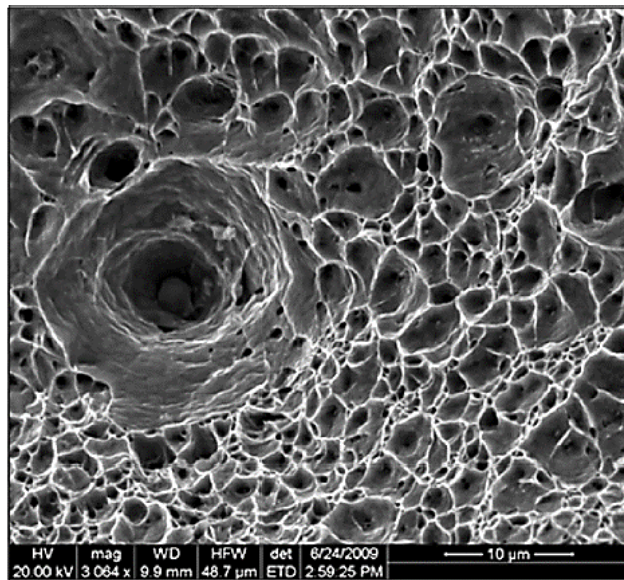


Figure 2.16: SEM fractograph which shows a ductile fracture in a low carbon steel. A spherical inclusion at the center of a microvoid.

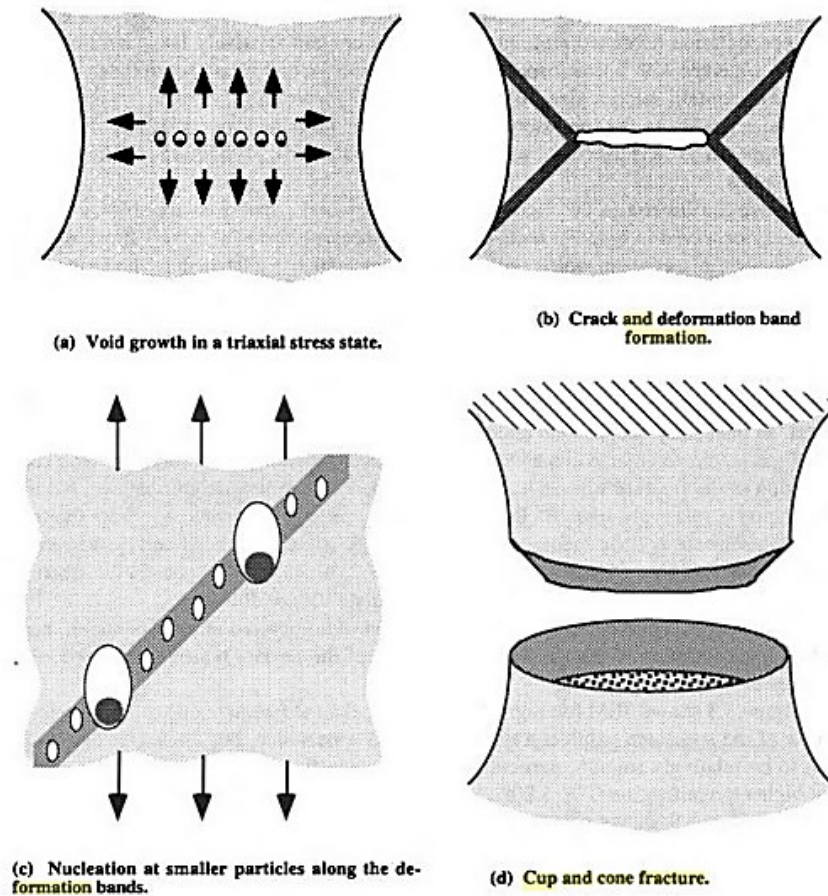


Figure 2.17: Formation of the cup and cone fracture surface in uniaxial tension [116].

## 2.5.2. Transgranular cleavage

Cleavage consists of the rapid propagation of a crack along a particular crystallographic plane. It is a brittle fracture. Cleavage fracture occurs along planes with low atomic density as fewer bonds must be broken. Since the fracture path follows the planes with the lowest atomic density, it changes direction every time it crosses a grain boundary. Hence, the fracture path of a cleavage is transgranular in a polycrystalline material.

Figure 2.18 shows SEM fractograph of cleavage fracture in a mild steel. The multifaceted surface and the river patterns are characteristics of cleavage in a polycrystalline material. Each facet represents a single grain. River patterns often form at the passage of a grain boundary as illustrated in Figure 2.19. To accommodate the twist mismatch between the two cleavage planes, the crack forms on many parallel planes resulting in multiple cracks. At the end, the multiple cracks converge into a single crack [116].

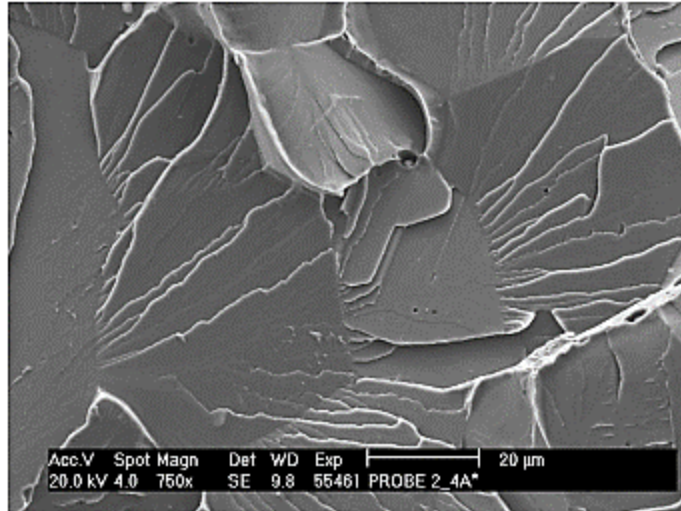


Figure 2.18: SEM micrograph showing a cleavage fracture in a mild steel [117].

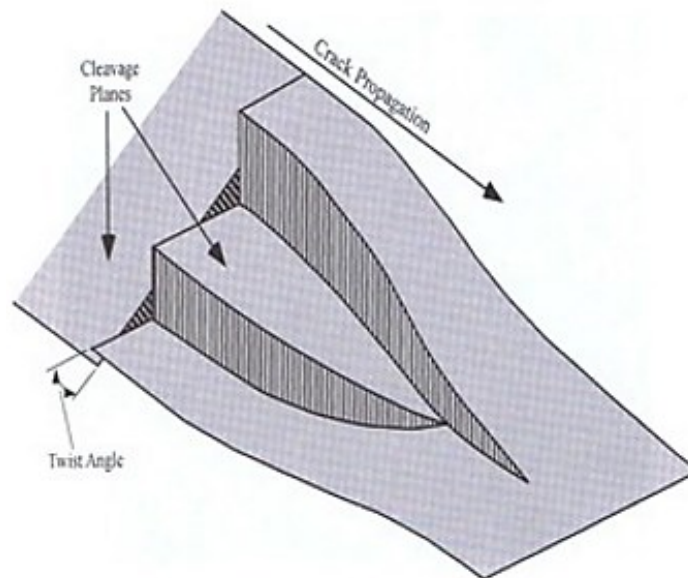


Figure 2.19: Formation of river patterns, as a result of a cleavage crack crossing a twist boundary between grains [116].

Cleavage of ferritic steels follows usually the following steps shown in Figure 2.20:

1. A sharp micro-crack has to nucleate in order to initiate a cleavage fracture. This micro-crack can be created either by dislocation pile-up at a grain boundary carbide or by inclusions and second-phase particles because of the plastic strain in the surrounding matrix.



2. The micro-crack propagates across the particle and then along a (100) cleavage of the neighboring matrix.
3. The crack propagates to the neighboring grains across the grain boundary [116].

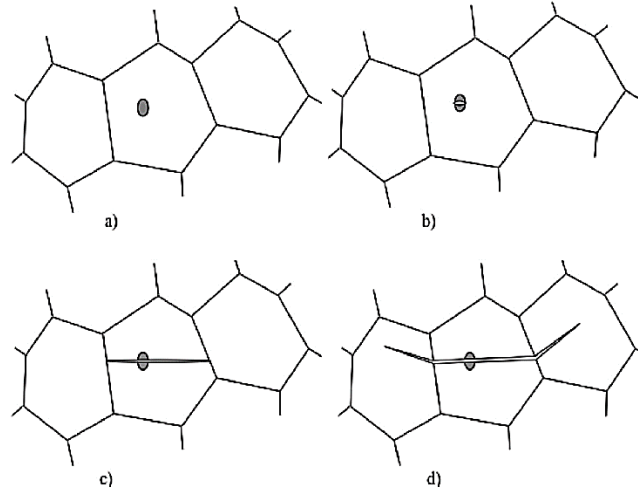


Figure 2.20: Schematic representation of the cleavage fracture micromechanisms: a) intact material, b) microcrack initiation from an intragranular particle, c) microcrack propagation across the particle and through the grain, d) crossing of the grain boundary [116].

### 2.5.3. Intergranular fracture

Intergranular fracture corresponds to another brittle mode of failure. Most metals usually fail either by the coalescence of voids formed at inclusions and second-phase particles or by transgranular cleavage.

However, under special circumstances such as environmentally assisted cracking which is the case in this study, cracks can form and propagate along grain boundaries. Precipitation of brittle phases on the grain boundaries during improper tempering can cause intergranular cracking. For example, tempered martensite embrittlement which is a result of tempering at 350°C and temper embrittlement which happens when an alloy steel is tempered at 550°C can lead both to segregation of phosphorus and sulfur at prior austenite grain boundaries.

The transition between cleavage and intergranular cracking takes place when the ratio  $R_{cl}$  defined in (2.4) is lower than one.

$$R_{cl} = 1.2 - \frac{\gamma_b}{2\gamma_s} \quad (2.4)$$

where  $\gamma_b$  is the surface free energy of the grain boundary and  $\gamma_s$  is the surface free energy of a surface exposed by cleavage [116].

In a previous study conducted by Takasawa et al., it was observed that the fracture morphology changes from quasi-cleavage fracture to intergranular fracture with increasing the grain size of a high strength low alloy steel in an SSC test [99].

## 2.6. Summary

L80 steel is commonly used for casing in sour service due to its improved mechanical properties. Because of its exposure to environments rich in hydrogen sulfide, L80 steel experiences mainly the following forms of hydrogen embrittlement: hydrogen induced cracking (HIC) and sulfide stress cracking (SSC).

The main mechanisms of hydrogen embrittlement, including hydrogen-enhanced localized plasticity, hydrogen-induced decohesion and hydride formation and cleavage, as well as the interaction between these three mechanisms were presented in Chapter 2.

Previous works showed that HIC and SSC depends on metallurgical factors including alloying elements, impurities, microstructure, inclusions, grain size, crystallographic texture and centerline segregation.

In addition, it was found that the fracture of steel in air is mainly ductile while the fracture in a sour environment is mainly brittle (i.e., transgranular cleavage or intergranular or mixed fracture).

However, a simultaneous study of the susceptibility of L80 steel to HIC and to SSC and a quantitative analysis of the effect of centerline segregation on HIC susceptibility were not conducted previously.

Therefore, a number of experimental procedures were developed to assess HIC and SSC susceptibility of L80 steel, which will be presented in detail in Chapter 3.

## Chapter 3 Materials and experimental methods

In this chapter, the chemical compositions of the L80 steels studied in this work are reported. This is followed by sample preparation procedure for microstructure observation and Vickers micro-hardness testing. The method developed to characterize the inclusions is introduced. Then, HIC tests procedure along with the electron microprobe analysis (EMPA) technique developed to study the centerline segregation in HIC tested samples are presented. Finally, SSRT procedure is described.

### 3.1. Steels studied

Five chemical compositions of L80 steel that were provided by Evraz Inc. NA were studied in this work. The specified minimum yield strength (SMYS) was 552 MPa (80 ksi) and the maximum hardness was 23 HRC. To achieve those properties, all the steel pipes were quenched and tempered.

Four of the provided steels were electric resistance weld (ERW) pipes while one of them was seamless (SMLS). ERW pipe is manufactured by cold-forming a sheet of steel into a cylindrical shape. An electric current is then used to heat the edges for the fusion weld. However, SMLS pipe is manufactured by piercing a hot round steel billet. The main advantage of seamless pipe is the elimination of seam-related defects. Nominal compositions of L80 steels are shown in Table 3.1.

MnCr, High Mo, High Mn and SMLS steels were alloyed with Mn-Cr-Mo while TiB steel was alloyed with Ti-B. The main elements are reported in Table 3.1. The nominal concentration of C was similar in all the studied steels. In contrast, the nominal concentrations of Mn, Cr, Mo, Ti and S were different. For example, High Mo had the highest level of Mo (0.49 wt%), High Mn had the highest levels of Mn and Cr and TiB had the highest level of Ti (0.03 wt%).

Table 3.1: Chemical composition (wt%) of the tested L80 casing steels.

Steel Name	C	Mn	Cr	Mo	Ti	S
MnCr	0.25	1.13	0.34	0.12	0	0.0006
High Mo	0.25	0.66	0.22	0.49	0.001	0.0022
High Mn	0.25	1.34	0.46	0.01	0.005	0.0008
TiB	0.25	1	0.14	0.02	0.03	0.0014
SMLS	0.27	1.15	0.37	0.15	0.001	0.0007

### 3.2. Sample preparation

The as-received samples were sectioned as shown in Figure 3.1. They were mounted using epoxy resin so that the surface indicated by an arrow in Figure 3.1 could be examined. The mounted samples were then ground and polished using an autopolisher (Buehler EcoMet 250 Pro) according to the following procedure:

- The samples were ground in sequence with 240, 320, 400, 600, 800 and 1200 grit SiC sand papers with water as a coolant.
- The sample surfaces were then polished using 6 and 3  $\mu\text{m}$  water-based diamond polishing suspensions (MetaDi Supreme Suspensions).
- Final polishing was done with 1  $\mu\text{m}$  water-based diamond polishing suspension (MetaDi Supreme Suspensions).
- The sample surfaces were rinsed with water after each grinding or polishing step.
- Finally, the samples were cleaned with ethyl alcohol and dried in warm air.

For metallography, the sample surfaces were etched with 2% Nital solution (2mL nitric acid + 98mL ethanol) until the color of the polished sample changed (usually 6 seconds). Then, the sample surfaces were rinsed and dried.

An Olympus BX61 optical microscope in a Bright Field mode and a Tescan Vega3 scanning electron microscope (SEM) equipped with energy-dispersive X-ray detector (EDX) were used to observe the microstructure. Vickers micro-hardness measurements were also performed on these samples after removing the etched surfaces by polishing with 1  $\mu\text{m}$  diamond polishing suspension.

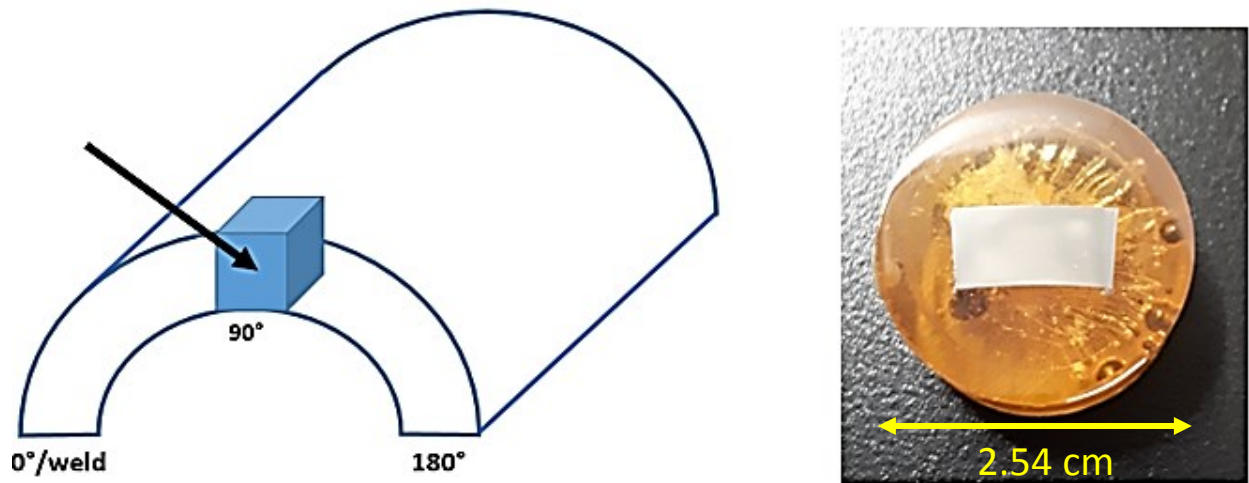


Figure 3.1: Location in the pipe where specimen for microscopic observation was taken (left), Mounted and polished sample (right).

### 3.3. Micro-hardness measurements

Micro-hardness was performed on polished samples (prepared as shown in Section 3.2). A Wilson VH3100 automatic micro-hardness tester was used for the micro-hardness tests. A load of 500 g and a dwell time of 10 seconds were used. For an ERW pipe, three vertical lines of 20 Vickers hardness indents were performed across the mid thickness of the sample. For a SMLS pipe, three vertical lines of 20 Vickers hardness indents were performed from the inner surface to the center of the sample. The distance between two consecutive indents on the same line was 150  $\mu\text{m}$ .

### 3.4. Characterization of inclusions

The sample was cut as shown in Figure 3.2. The arrow indicates the surface of the sample that was polished (as described in Section 3.2). Then, the polished surface of the sample was scanned from bottom to top as shown in Figure 3.3 using Olympus BX61 optical microscope. About a total of 160 optical micrographs at a magnification of 240X were taken from each sample.

98 micrographs of these 160 micrographs that were taken at mid thickness of the sample were later processed using ImageJ (procedure described in Appendix A) to measure number, area

fraction and average size of the inclusions and classify them by aspect ratio into globular and cubic (aspect ratio  $< 2$ ) or elongated inclusions (aspect ratio  $\geq 2$ ).

In addition, SEM equipped with EDX was used to identify the type of the inclusions present in each sample. For this purpose, random inclusions were analyzed using EDX on the surface of the sample.

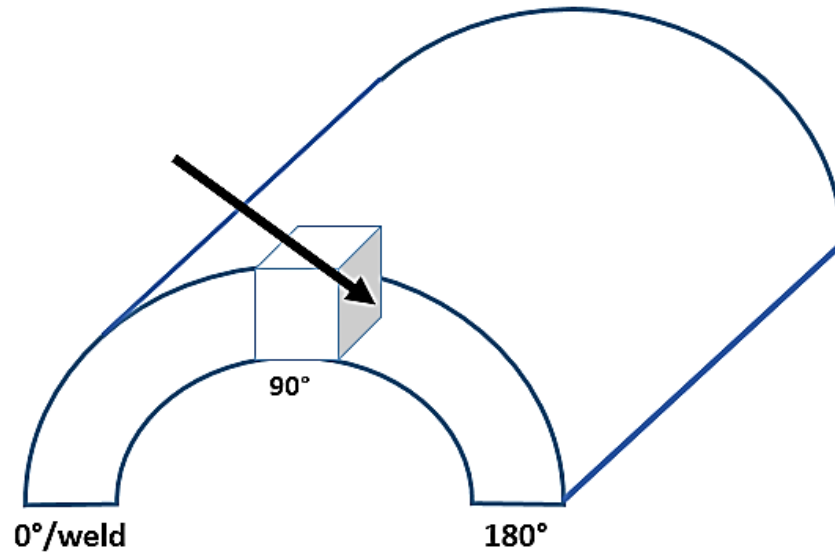


Figure 3.2: The cutting location of samples for inclusion characterization.

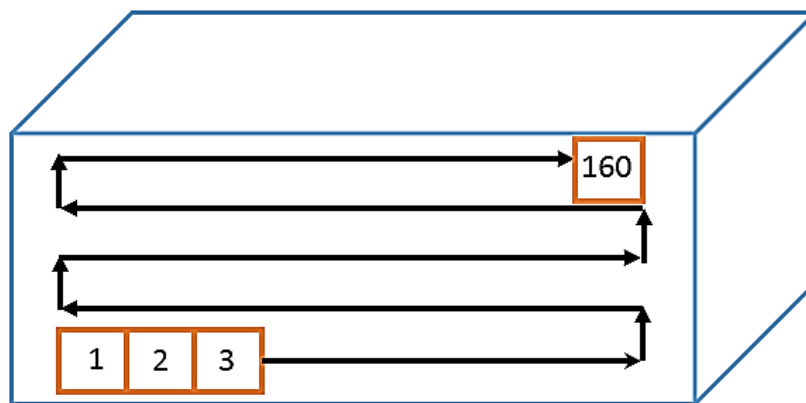


Figure 3.3: Illustration of cleanliness examination using optical microscopy.

### 3.5. Hydrogen induced cracking tests

This section introduces hydrogen induced cracking (HIC) tests by describing the testing apparatus, the test environment, the sample preparation, the test procedure and finally the evaluation of test results.

#### 3.5.1. Introduction

NACE TM0284-2011 standard test method was used to evaluate the HIC susceptibility of the steels. The test method consists of exposing unstressed test specimens to an acidified, hydrogen sulfide saturated aqueous solution at ambient temperature and pressure. The test does not duplicate service conditions. The test is intended to provide reproducible test environment capable of evaluating the susceptibility of a steel sample to HIC in relatively short time. Appendix B presents the safety precautions taken during working with H<sub>2</sub>S.

#### 3.5.2. Testing apparatus

A typical test assembly is shown in Figure 3.4. The glass test vessel should be airtight and large enough to contain the test specimens with provisions for purging and introduction of H<sub>2</sub>S. 10% sodium hydroxide solution was prepared and used as scrubber solution to neutralize the outlet H<sub>2</sub>S gas from the test before venting in the fume hood.

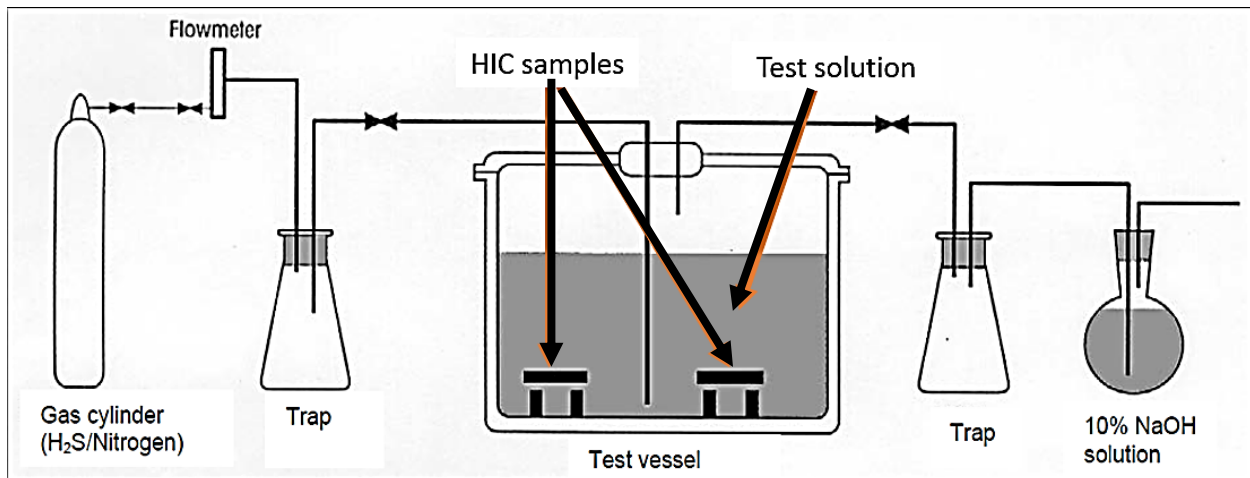


Figure 3.4: A schematic representation of a typical HIC test assembly.

### 3.5.3. Test environment

NACE TM0284 test solution A was used as test environment in this experiment. The test solution consisted of 5 wt% sodium chloride (NaCl) and 0.5 wt% glacial acetic acid (CH<sub>3</sub>COOH) dissolved in distilled water. Nitrogen (Praxair, 100% purity) was introduced near the bottom of the sealed test vessel to remove oxygen from the test solution. After purging, Hydrogen sulfide gas (Praxair, 100% purity) was bubbled through the test solution. After H<sub>2</sub>S saturation, a positive pressure of H<sub>2</sub>S was maintained at a constant flow rate to ensure that the solution remained saturated with H<sub>2</sub>S. The pH of the solution should be between 2.3 and 3.3 immediately after H<sub>2</sub>S saturation. At the end of the test, the pH of the test solution should not exceed 4 and the concentration of H<sub>2</sub>S in the test solution should be at least 2300 ppm (measured by iodometric titration).

### 3.5.4. Sample preparation

Three test samples were taken from each pipe. For an ERW pipe, the samples were taken from the weld, 90° from the weld and 180° from the weld. For a SMLS pipe, the samples were taken 120° apart around the circumference. The longitudinal axis of the test specimens was parallel to the longitudinal axis of the pipe for both ERW and SMLS pipes. The samples were machined from the mid thickness of the pipe. Figure 3.5 shows the orientation of the test specimens and from where in the pipe they were taken. Figure 3.6 is a picture of a machined HIC sample with dimensions. The machining shall result in a bare metal surface with a surface roughness equivalent to at least 320 grit. For machining, the last two passes shall not remove more than 0.05 mm of material.



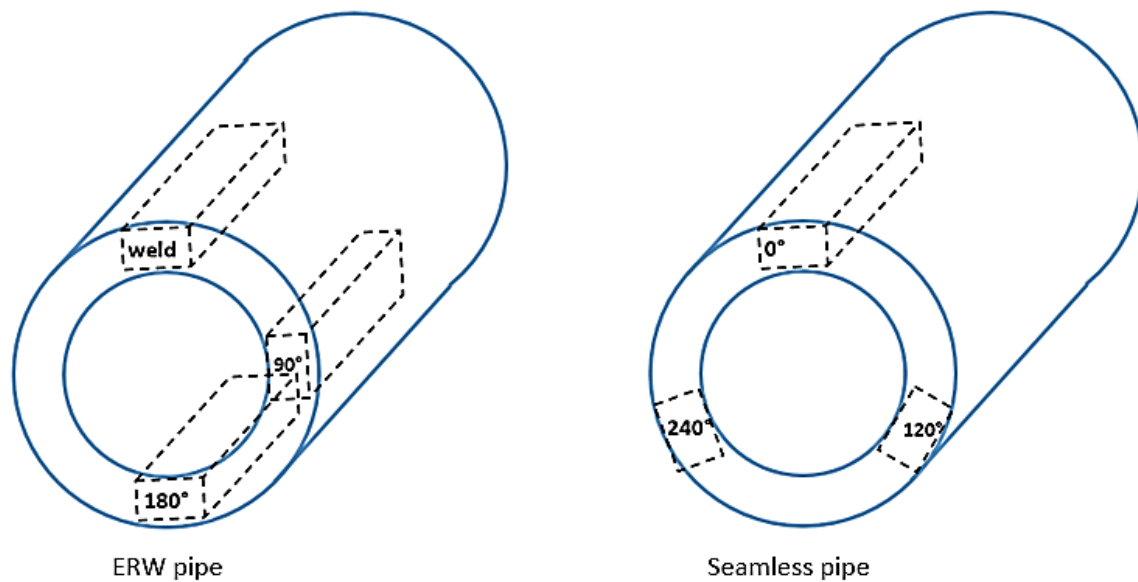


Figure 3.5: Location in the pipe where the HIC samples were taken.

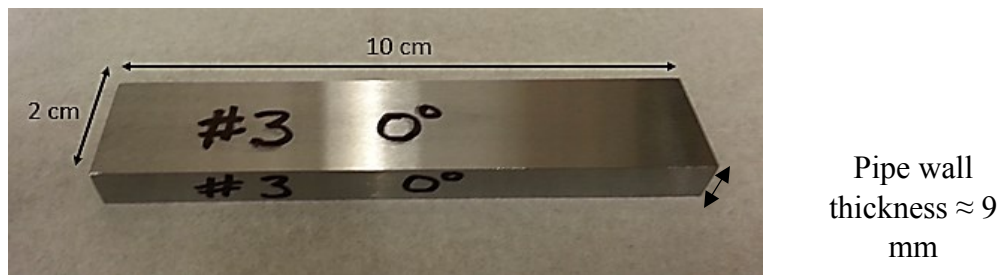


Figure 3.6: A photo of an actual machined HIC sample.

### 3.5.5. Test procedure

- The test specimens were placed all together in the test vessel in a way that their longitudinal axis was horizontal. The test specimens were separated from the test vessel and each other by glass rods.
- The ratio of the test solution volume to the total surface area of test specimens immersed in the test vessel was 8 mL/cm<sup>2</sup>. The test solution volume was 7 L.
- The initial pH of the test solution was measured using a pH meter and it was 2.72.
- The sealed test vessel was purged of air with N<sub>2</sub> for 30 min at a rate of 100 mL/min per liter of test solution.

- After purging, H<sub>2</sub>S gas was introduced in the test vessel at a rate of 200 mL/min per liter of test solution for 1 hour. Thereafter, a positive pressure of H<sub>2</sub>S was maintained at a constant flow rate (20 mL/min) to ensure that the test solution remained saturated with H<sub>2</sub>S.
- Right after H<sub>2</sub>S saturation, the pH of test solution was measured and it was equal to 2.85.
- The test duration was 96 hours and the test time started immediately upon completion of the 1 hour H<sub>2</sub>S introduction period.
- The temperature of the test solution during the test was  $25 \pm 3^{\circ}\text{C}$ .
- At the end of the test, the pH of the test solution was 3.72.
- The concentration of H<sub>2</sub>S in the test solution was measured by iodometric titration and was 3099 ppm at the end of the test.
- After testing, the exposed test specimens were rinsed with water to remove scale and deposits.
- Finally, the test specimens were sectioned for examination as shown in Figure 3.7.

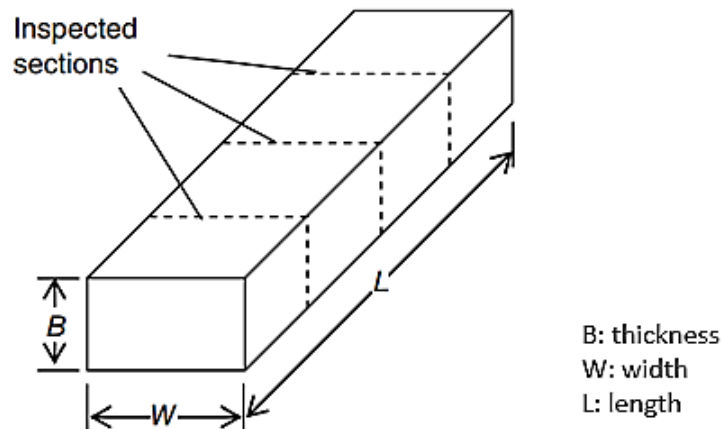


Figure 3.7: Sections to be examined after exposure to HIC environment.

### 3.5.6. Evaluation of samples

Each section was polished metallographically and etched for 3 minutes using 2% Nital to reveal the cracks on the surface. Only a light etch was used as heavy etch may obscure small cracks.

Cracks were measured as illustrated in Figure 3.8. Cracks separated by less than 0.5 mm were considered a single crack according to NACE TM0284 standard. All cracks visible at magnifications up to 100X were included in the calculation. The crack sensitivity ratio (CSR), crack length ratio (CLR) and crack thickness ratio (CTR) were calculated for each section using the following equations (3.1), (3.2) and (3.3).

$$CSR = \frac{\sum a \times b}{w \times t} \times 100\% \quad (3.1)$$

$$CLR = \frac{\sum a}{w} \times 100\% \quad (3.2)$$

$$CTR = \frac{\sum b}{t} \times 100\% \quad (3.3)$$

where a is the crack length, b is the crack thickness, W is the section width and T is the section thickness.

Since each test sample is cut into three sections and three samples were prepared from each pipe, the average of 9 values of CLR, CTR and CSR was calculated at the end of the test.

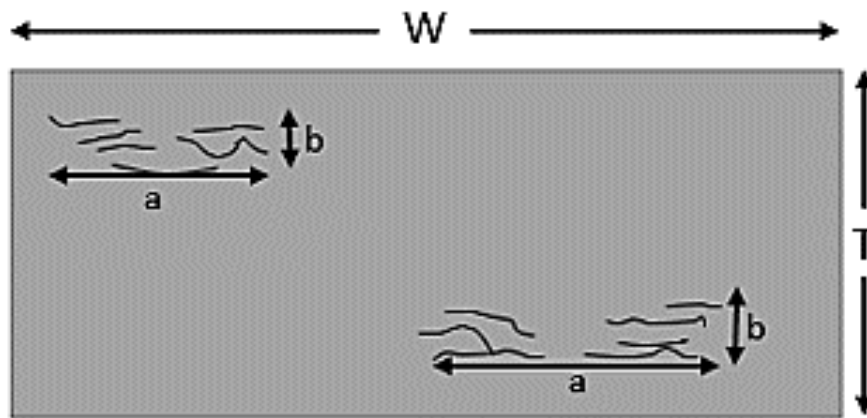


Figure 3.8: Crack dimensions to be used in calculating CSR, CLR and CTR.

### 3.6. Study of centerline macro-segregation using electron microprobe analyzer (EMPA)

This section begins with an introduction of the apparatus EMPA. This is followed by a description of the EMPA technique developed to analyze qualitatively and quantitatively centerline macro-segregation across an as received sample and around the HIC cracks observed on HIC tested samples. This technique includes X-ray mapping across the pipe wall thickness of the samples (i.e., both as received and HIC tested samples) and line scanning of the concentration of the main alloying elements across the centerline segregation band in the as received sample and across the HIC cracks in HIC tested samples.

#### 3.6.1. Introduction of EMPA

The EMPA is a fully qualitative and quantitative method of non-destructive elemental analysis of micron-sized volumes at the surface of materials. Detection limits vary with both sample and analytical conditions, but are typically lower than 500 ppm (0.05 wt%).

This technique consists of bombarding a sample with a focused electron beam and collecting the characteristic X-rays generated from the sample surface. Since characteristic X-rays have a wavelength proportional to the atom from which they are produced, the sample composition can be easily identified. These characteristic X-rays are detected by WDS spectrometers that are based on Bragg's law and that use various mono-crystals. A quantitative analysis for a given element in an unknown sample is accomplished by comparing the number of its generated characteristic X-rays with the number generated by a standard of known composition. By scanning the electron beam over the surface of a sample, X-ray maps showing spatial distribution of an element can be obtained.

#### 3.6.2. Study of centerline macro-segregation using EMPA

A CAMECA SX100 EMPA was used for chemical elemental analysis. The instrument features 5 wavelength dispersive spectrometers and an energy dispersive spectrometer.

The analyzed samples were 5 samples: 1 as received sample cut from High Mo steel pipe at 90° from the weld and 4 HIC tested sections cut respectively from High Mo, TiB, MnCr and High

Mn steels (namely High Mo 90° section 2, TiB 90 ° section 2, MnCr 180 ° section 3 and High Mn 180° section 2).

These 4 HIC tested sections were chosen to be analyzed using EMPA because they presented long HIC cracks at the center. Thus, after evaluation of HIC testing results, these 4 sections were polished with 1 µm diamond polishing suspension to remove the etched surface.

The detected elements were Mn, Cr, P and Si. Elemental X-ray mapping followed by line scans were performed. X-ray mapping reveals the spatial distribution of a given element and therefore detecting the areas where this element segregates. Then, 2 line scans across the HIC cracks were carried out to measure the concentration of these elements around the HIC crack and compare their measured concentrations with their nominal concentrations.

For the High Mo as received sample, the surface of the sample was prepared according to section 3.2. The detected elements were Mn and P. Elemental X-ray mapping of Mn followed by line scans of Mn and P were performed in order to reveal the distribution of this chemical elements across the pipe wall thickness and compare these results to the results obtained from the HIC tested sample.

Table 3.2: Used conditions during EMPA X-ray mapping and line-scanning.

<b>Experimental conditions</b>	<b>X-ray mapping</b>	<b>X-ray line scanning</b>
Current (nA)	200	100
Voltage (kV)	20	10
Beam size (µm)	Fully focused beam (< 1 µm)	Fully focused beam (< 1 µm)
Count time (s)	20 ms / pixel	120 s per element (60 s peak and 30 s background on each side)
Pixel size	10 µm × 10 µm (for a large area) 1 µm × 1 µm (for a small area)	NA

### 3.7. Slow strain rate tests

This section introduces slow strain rate tests (SSRT) by describing the test equipment, the sample preparation, the test procedure and finally the analysis of the test results.

### 3.7.1. Introduction of SSRT

SSRT is an accelerated test to investigate the resistance of the steel to sulfide stress cracking (SSC). The SSRT involves applying a constant strain rate to the specimen while it is exposed to a sour environment. The advantage of this test compared to the proof ring test is that it provides rapid results. The average strain rate should be slow enough to produce failure or cracking of the specimen in a reasonable period of time for evaluation purposes. The strain rate should be in the range from  $10^{-4}$  to  $10^{-7}$  /s according to the ASTM G129 standard. The SSRT is a comparative evaluation and therefore it was conducted in two environments: in air and in NACE TM0177 standard solution A (5wt% NaCl and 0.5wt% CH<sub>3</sub>COOH in distilled water) saturated with H<sub>2</sub>S. The preparation of this solution was similar to the preparation of the test solution in the HIC test. The safety precautions taken during SSRT test are presented in Appendix B.

### 3.7.2. Test setup

Model TTS-25kN low speed material testing machine from Adelaide Testing Machine (ATM) Inc. was used for this test. The test set-up was composed of a load frame, a drive mechanism, a 25kN load cell, a test vessel, two tensile grips, and a computer control system with TC-100 testing software which was included with the TTS-25kN testing machine. The test vessel was made of glass and was capable of being purged with gases before testing and resistant to leakage during the test. Figure 3.9 shows the experimental set-up.

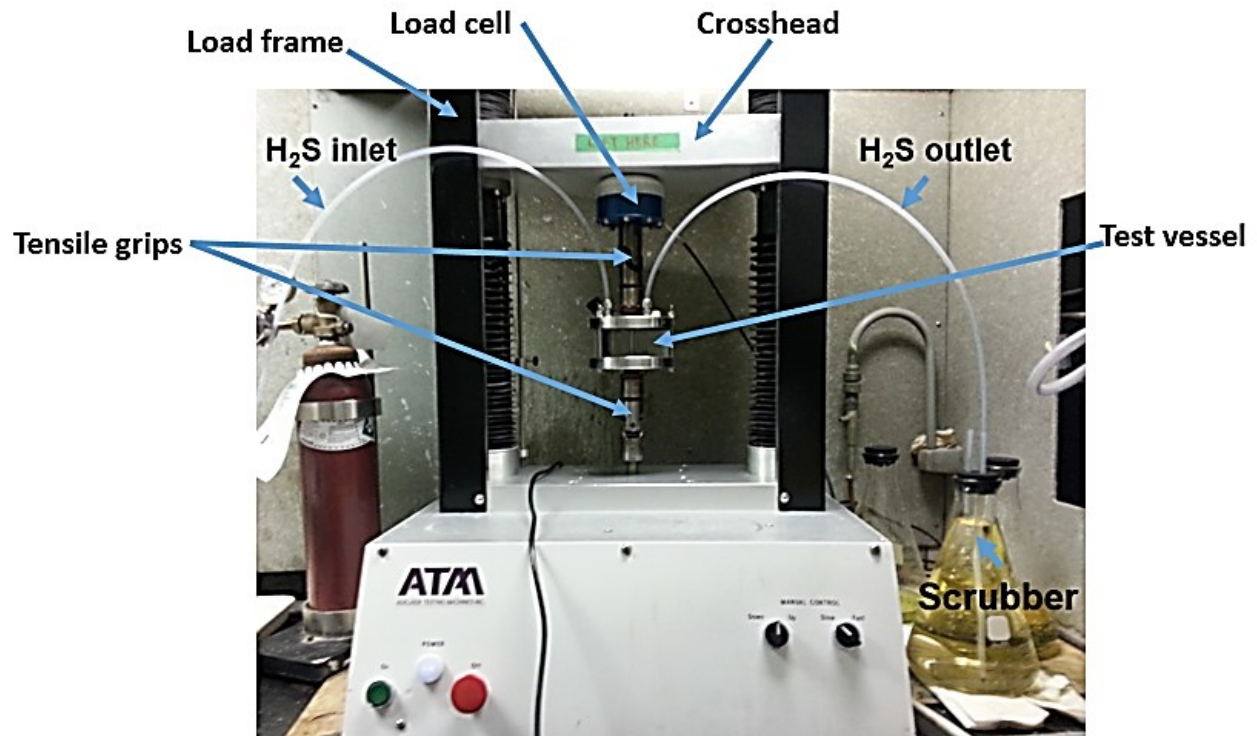


Figure 3.9: Experimental setup of the SSRT test.

### 3.7.3. Sample preparation

Uniaxial tensile test specimens were used for this test. The specimens were prepared from the mid-thickness of the pipe at 90° from the weld for ERW steel and at 0° for SMLS steel as shown in Figure 3.10. The dimensions of an SSRT specimen are shown in Figure 3.11. The samples were machined according to NACE TM0177-2005 standard. The average surface roughness of the gauge section was 0.25  $\mu\text{m}$ . In machining operations, the final two passes should remove no more than a total of 0.05 mm of material.

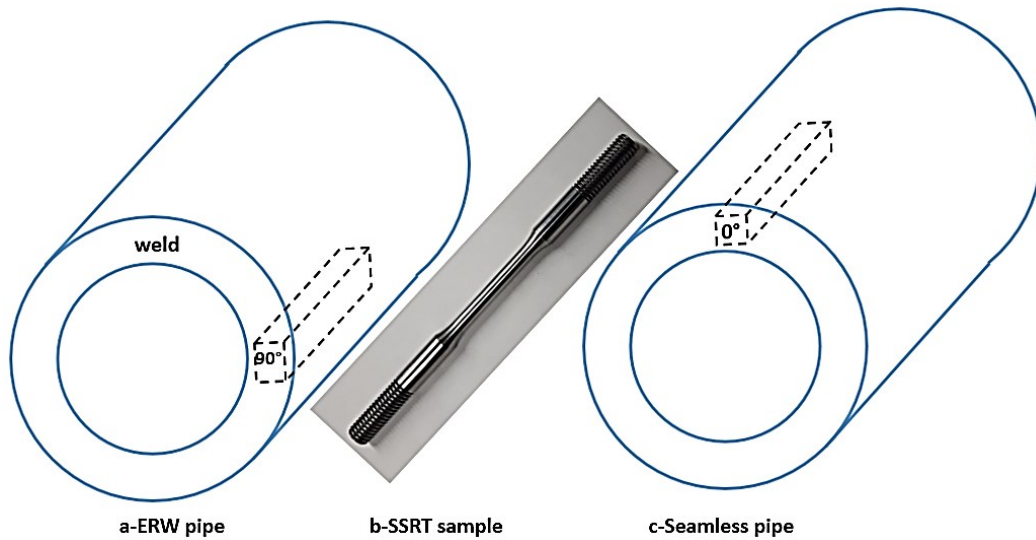


Figure 3.10: a,c) Location in the pipe where the SSRT sample was machined, b) photo of a machined and untested SSRT sample.

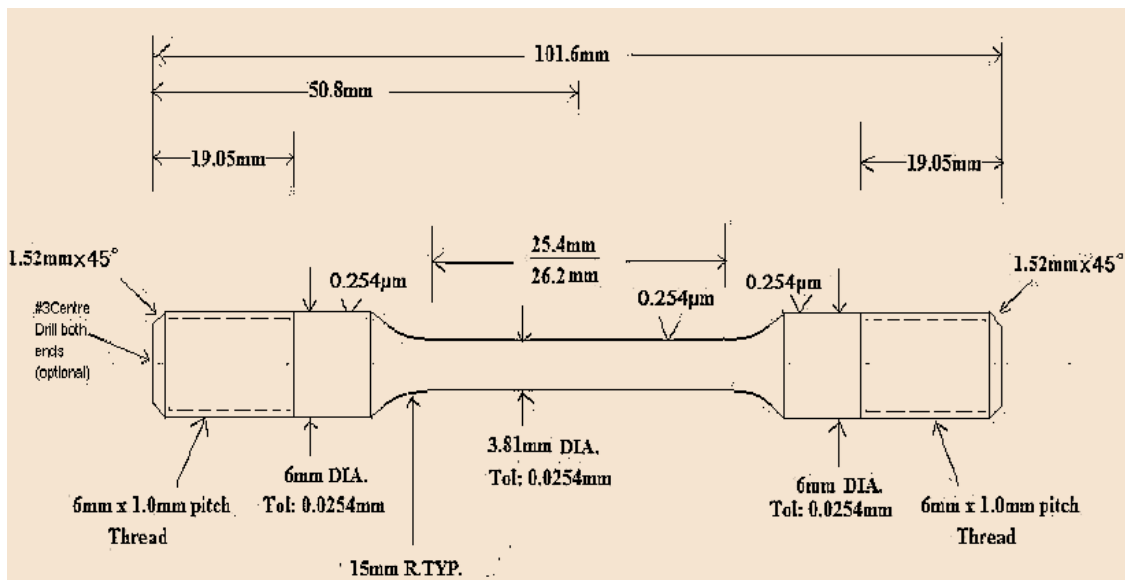


Figure 3.11: Dimensions of the specimen used for SSRT tests [19].

### 3.7.4. Test procedure

- NACE TM0177 test solution A (5wt% NaCl and 0.5wt% CH<sub>3</sub>COOH dissolved in distilled water) and 25% NaOH solution were prepared prior to the test.
- The gauge section diameter of the SSRT specimen was measured using a caliper to the nearest 0.025 mm and the value was recorded.



- The SSRT specimen and the internal surfaces of the test vessel were cleaned and degreased using Ethanol. Care was taken thereafter not to contaminate both of them.
- The test vessel, SSRT specimen and grips were assembled. Stainless steel specimen grips were tightened to the test specimen and then threaded on the bottom of the SSRT machine and the load cell. To maintain accurate loading and to minimize bending load being applied to the load cell, the grips mounted on the SSRT machine had to be accurately aligned.
- The operating parameters (i.e., specimen name, specimen dimensions, test number, data sampling rate, strain rate etc.) were input into the TC-100 software.
- A preload of 25N was applied on the specimen using the preload function in the TC-100 software to avoid the backlash in the grips prior to running the test.
- The test solution A was transferred into the test vessel. The gauge section was immersed completely in the test solution.
- The test solution was purged with pure nitrogen N<sub>2</sub> for 1 hour at a high flow rate (≈100 mL/min) to remove any oxygen in the test vessel before introducing H<sub>2</sub>S. At the same time, a check for leakage from the test vessel was done. A simple procedure for this check was to apply a mild soap solution to the fittings, tubing and seals. Soap bubbles indicated leakage of gas.
- After purging with N<sub>2</sub> and successfully passing the leak check, H<sub>2</sub>S gas was introduced in the test vessel for 1 hour at a high flow rate (≈100 mL/min). After that, a continuous flow of H<sub>2</sub>S at a low flow rate (1 bubble/s) was maintained to keep the saturation of the solution with H<sub>2</sub>S. Any H<sub>2</sub>S gas coming out was released through the scrubber solution. For safety measures, the test was done in a well-ventilated fume hood. The H<sub>2</sub>S and N<sub>2</sub> gas cylinders, the testing machine, the scrubber solution and the tubes were located inside the fume hood. Three H<sub>2</sub>S gas detectors type Altair were used to detect the H<sub>2</sub>S concentration outside the test vessel. One detector was located inside the fume hood in proximity to the H<sub>2</sub>S cylinder. Another detector was located close to the test vessel. And the last detector was nearby the fume hood. In case of a leak, the gas detector was alarmed and the valve at the H<sub>2</sub>S cylinder was closed.
- The test specimen was immersed in the H<sub>2</sub>S environment for 24 hours after the saturation of the test solution before straining to allow time for hydrogen diffusion.

- SSRT was then started by setting a strain rate of  $1.96 \times 10^{-6}$ /s which is equivalent to a crosshead displacement rate of 0.05  $\mu\text{m/s}$  in the TC-100 software.
- Data were recorded continuously (every 3s) throughout the test period with a suitably calibrated x-y recorder that displayed the load or stress on the SSRT specimen versus time, displacement or strain.
- After failure, the data acquisition was stopped. The valve on the H<sub>2</sub>S cylinder was shut down.
- The test vessel was purged with nitrogen for 20 minutes to remove any residual H<sub>2</sub>S.
- At the end, the test vessel was opened and the two sections of the failed SSRT specimen were carefully removed.
- The two sections of SSRT specimen were rinsed with water, cleaned ultrasonically with Ethanol and dried with compressed air.

### 3.7.5. Analysis and reporting of test results

Two basic types of results were obtained from this SSRT:

- Visual examination of the fracture surface under scanning electron microscope (SEM) or optical microscope (OM)
- Measurement of the ductility parameters of the SSRT specimen and comparison with the baseline material properties determined in air

Two ductility parameters were used in evaluating the results of the SSRT: plastic strain to failure and reduction in area.

The reduction in area (RA) was calculated according to (3.4)

$$RA = \frac{D_i^2 - D_f^2}{D_i^2} \times 100 \quad (3.4)$$

where  $D_i$  is the initial gauge section diameter in mm and  $D_f$  is the final gauge section diameter at fracture location in mm (measured on an optical micrograph of the cross section of the fractured surface)

The plastic strain to failure (PSF) was determined from the stress versus strain curve by subtracting the elastic strain at failure from the total strain at failure. The use of plastic strain to failure instead of total strain to failure minimizes variabilities between test results from

differences in test machine compliance, which are most significant in the elastic region of the stress strain curve.

Two SSRT tests were done in the air and the average reduction in area and plastic strain to failure were calculated. Two SSRT tests were also performed in H<sub>2</sub>S saturated test solution.

The comparison of the ductility parameters determined in the H<sub>2</sub>S saturated test environment with those determined in air was performed using the following ratios.

$$\begin{array}{l} \text{Reduction in area ratio} \\ \text{(RAR)} \end{array} \quad \text{RAR(\%)} = \frac{\text{RA in H}_2\text{S}}{\text{Average RA in air}} \times 100 \quad (3.5)$$

$$\begin{array}{l} \text{Plastic strain to failure} \\ \text{ratio (PSFR)} \end{array} \quad \text{PSFR(\%)} = \frac{\text{Plastic strain in H}_2\text{S}}{\text{Average plastic strain in air}} \times 100 \quad (3.6)$$

Ductility ratios near 100% indicate high resistance to SSC while low values generally indicate low resistance to SSC.

## Chapter 4 Results

In this chapter, microstructure, micro-hardness, HIC and SSC resistance, qualitative and quantitative analysis of inclusions and centerline macro-segregation results in 5 types of L80 steels are presented. The HIC standard test, based on the ASTM 0284 standard, was performed and three parameters including CLR, CTR and CSR were measured to study the HIC resistance of the steel specimens. The SSRT, based on the ASTM G129 standard, was also carried out in air and in hydrogen sulfide saturated environment and two parameters that are RAR and PSFR were calculated to assess the resistance of the different steels to SSC. Fractography was used to identify the mode of fracture and the origin of the cracks in HIC and SSC tests. A qualitative and quantitative study of the inclusions was carried out to correlate the HIC and SSRT results to the inclusions content and shape. Finally, the effect of centerline macro-segregation on the propagation of HIC cracks was investigated using EMPA. Line scanning and X ray mapping of the major chemical elements (Mn, Cr, Si and P) were performed in order to detect and quantify the macro-segregation of these elements around the HIC cracks.

### 4.1. Microstructures

Figure 4.1 to Figure 4.5 are SEM images of the different tested L80 steels taken at the same magnification (i.e., 3000X) and from mid thickness of the pipe. The microstructure of these quenched and tempered steels is mainly composed of tempered martensite. The carbides are distributed inside the ferrite and along the grain boundaries.

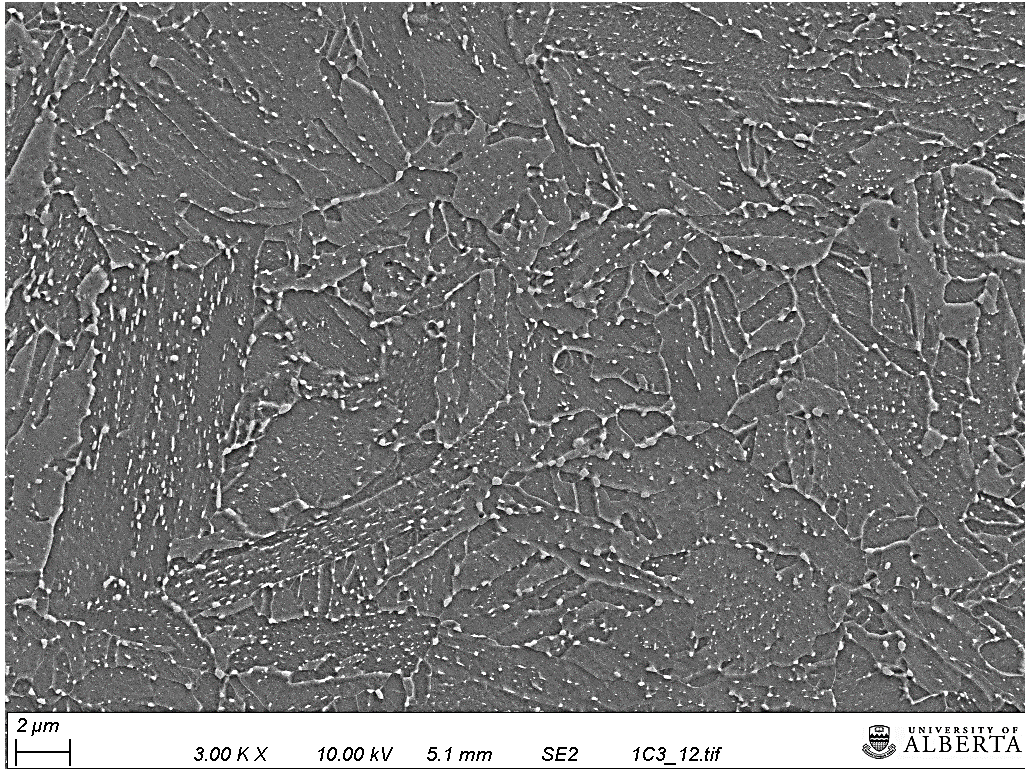


Figure 4.1: SEM image of MnCr steel.

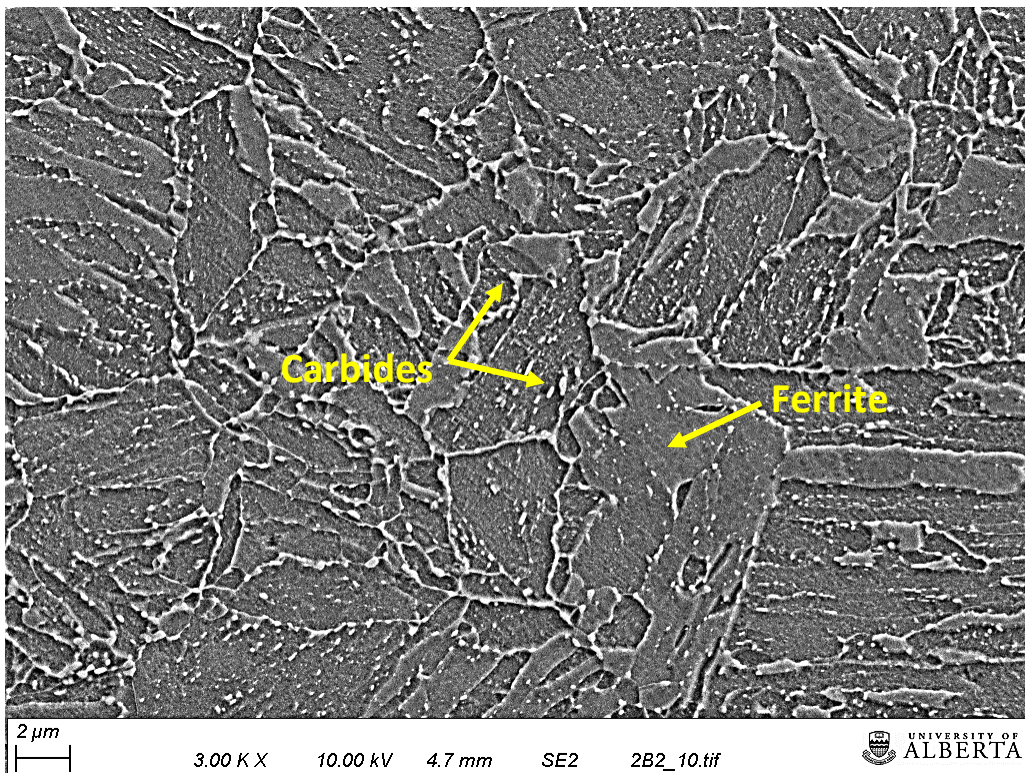


Figure 4.2: SEM image of High Mo steel.

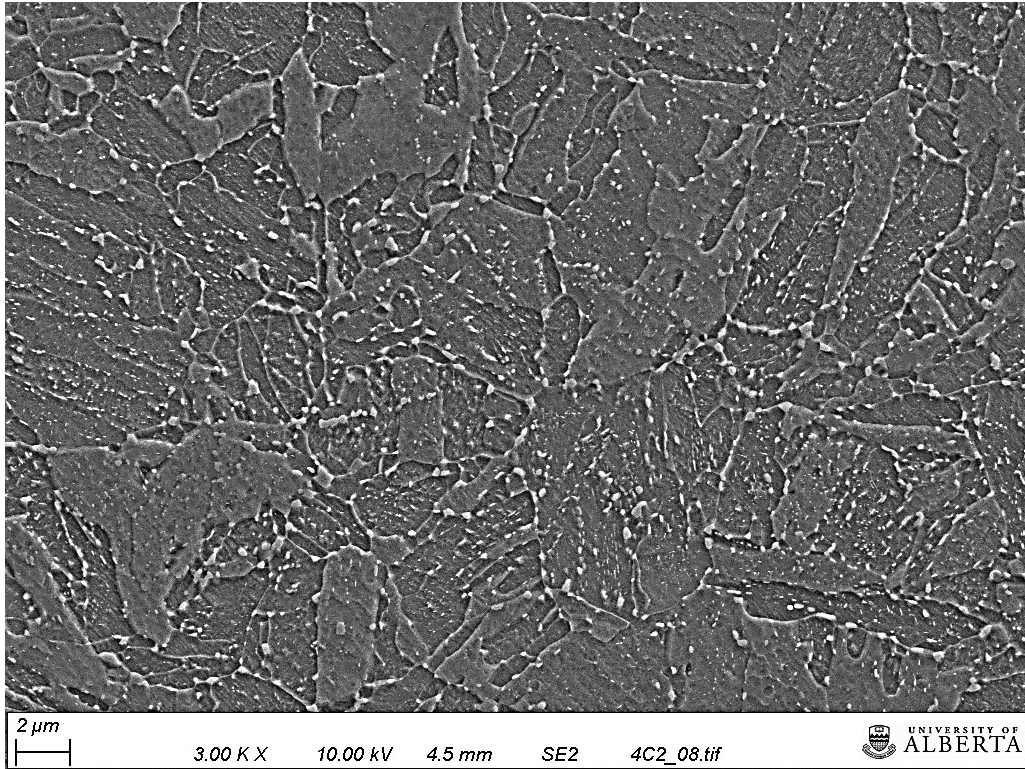


Figure 4.3: SEM image of High Mn steel.

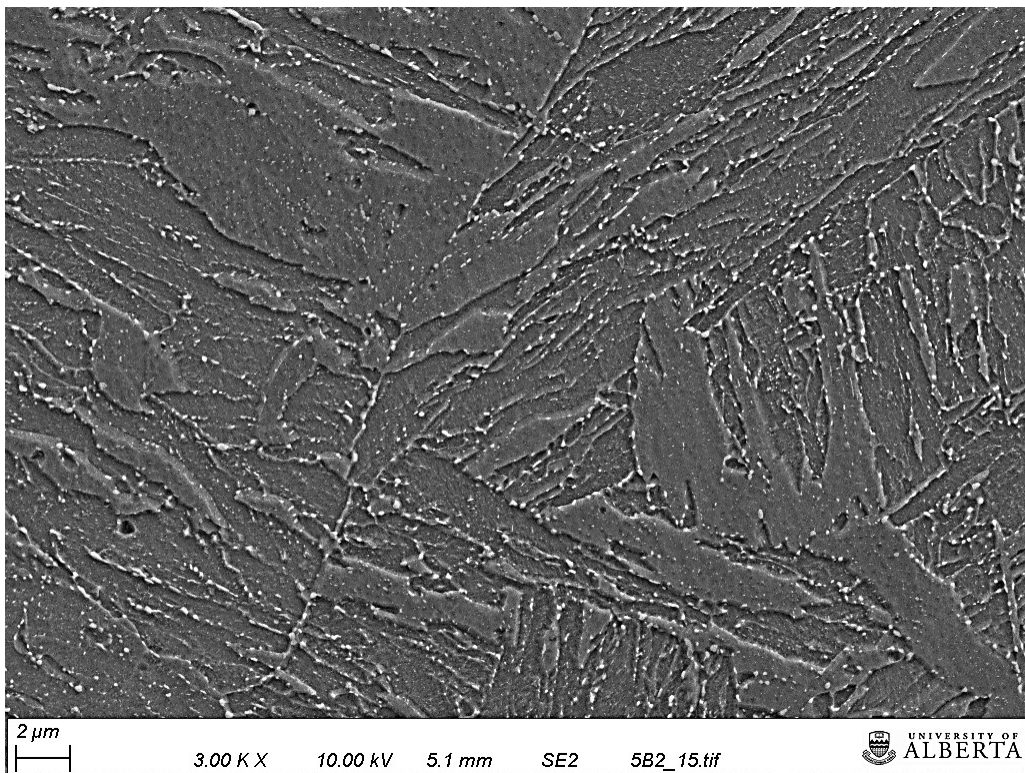


Figure 4.4: SEM image of TiB steel.

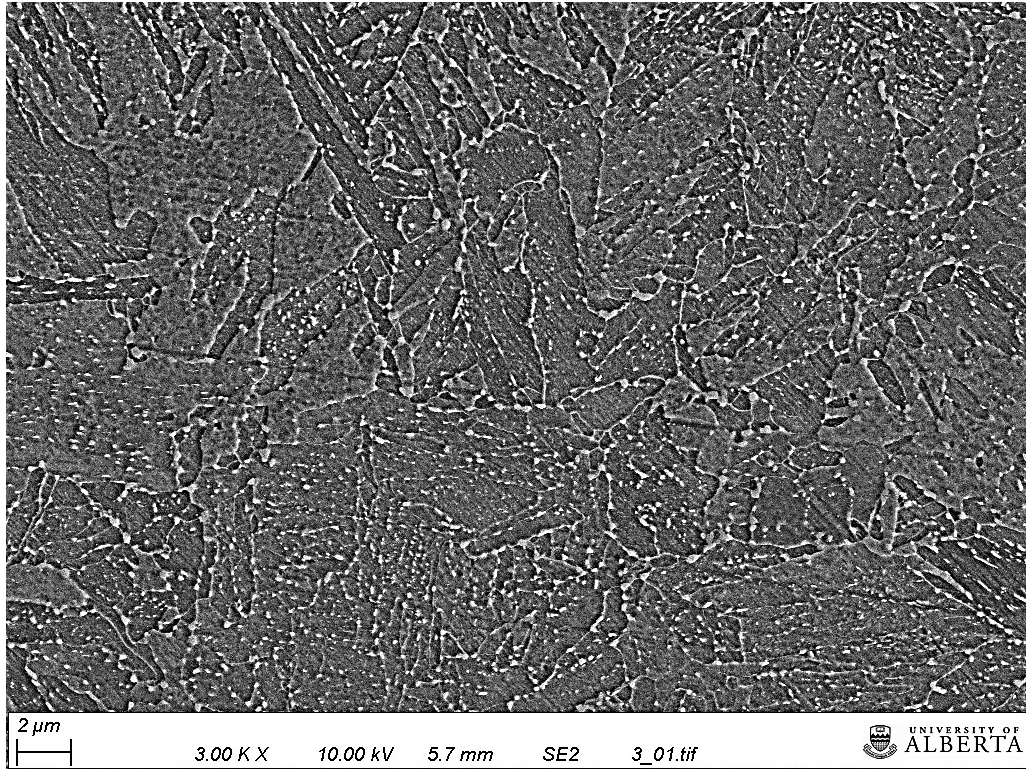


Figure 4.5: SEM image of SMLS steel.

Figure 4.6 is an SEM image of TiB steel taken at a lower magnification (i.e., 1000X). Prior austenite grain boundaries are clearly revealed, which suggests the segregation of impurities such as P and S at the grain boundaries.

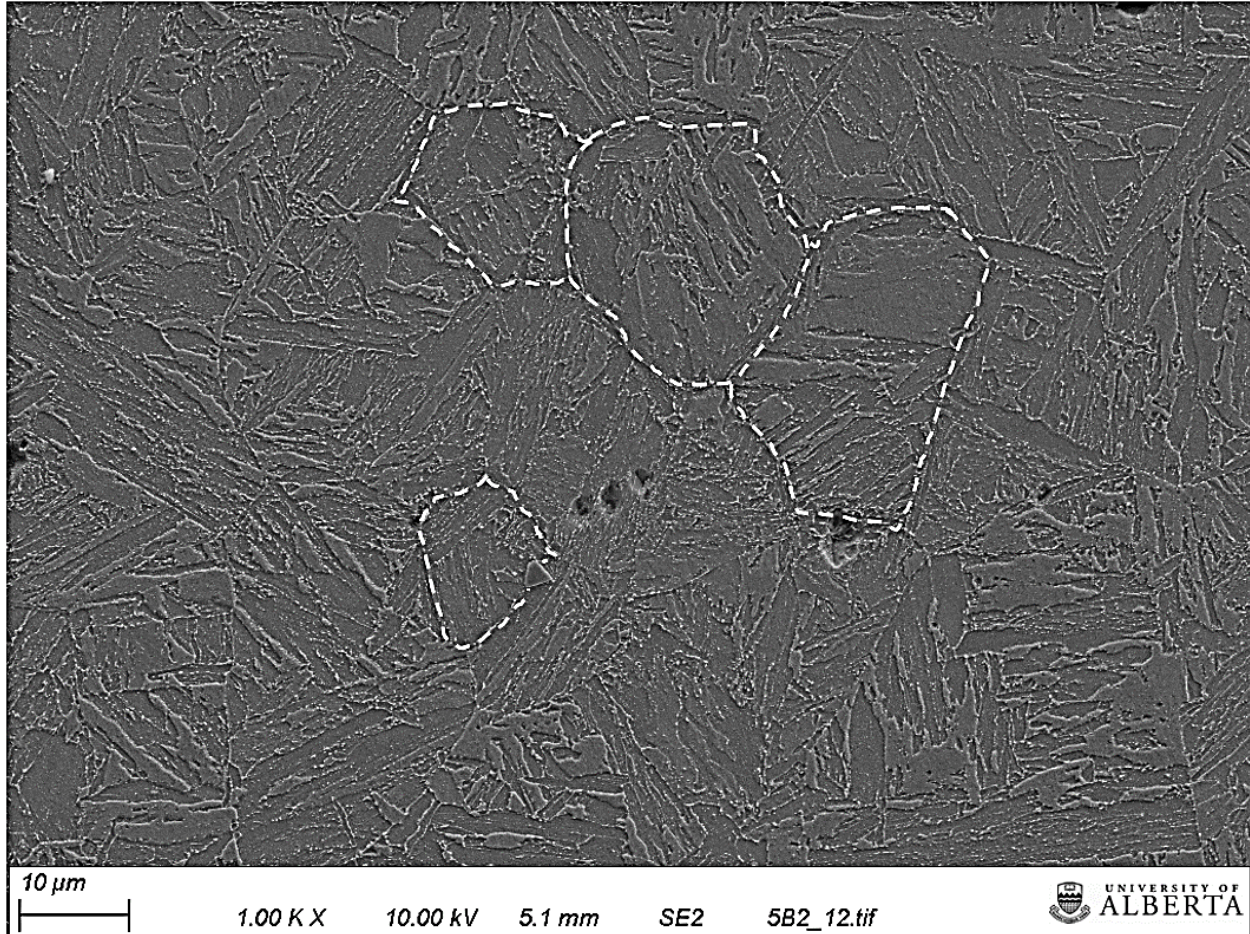


Figure 4.6: SEM image of TiB steel showing prior austenite grain boundaries.

## 4.2. Vickers micro-hardness

Vickers micro-hardness measurements were performed vertically across the centerline band for samples prepared from ERW pipes (i.e., High Mo, TiB, High Mn and MnCr steels). For SMLS steel, Vickers micro-hardness measurements were performed vertically from inner surface of the pipe to the center. Figure 4.7 is an example of Vickers micro-hardness measurements performed on High Mo steel. The Vickers micro-hardness measurements performed on the other L80 steels (i.e., TiB, High Mn, MnCr and SMLS steels) are presented in Appendix C.1, Appendix C.2, Appendix C.3 and Appendix C.4.

The micro-hardness profile does not show an increase in the micro-hardness values at the mid thickness of the pipe, which suggests that this technique is not efficient in revealing the centerline macro-segregation band in pipe samples.



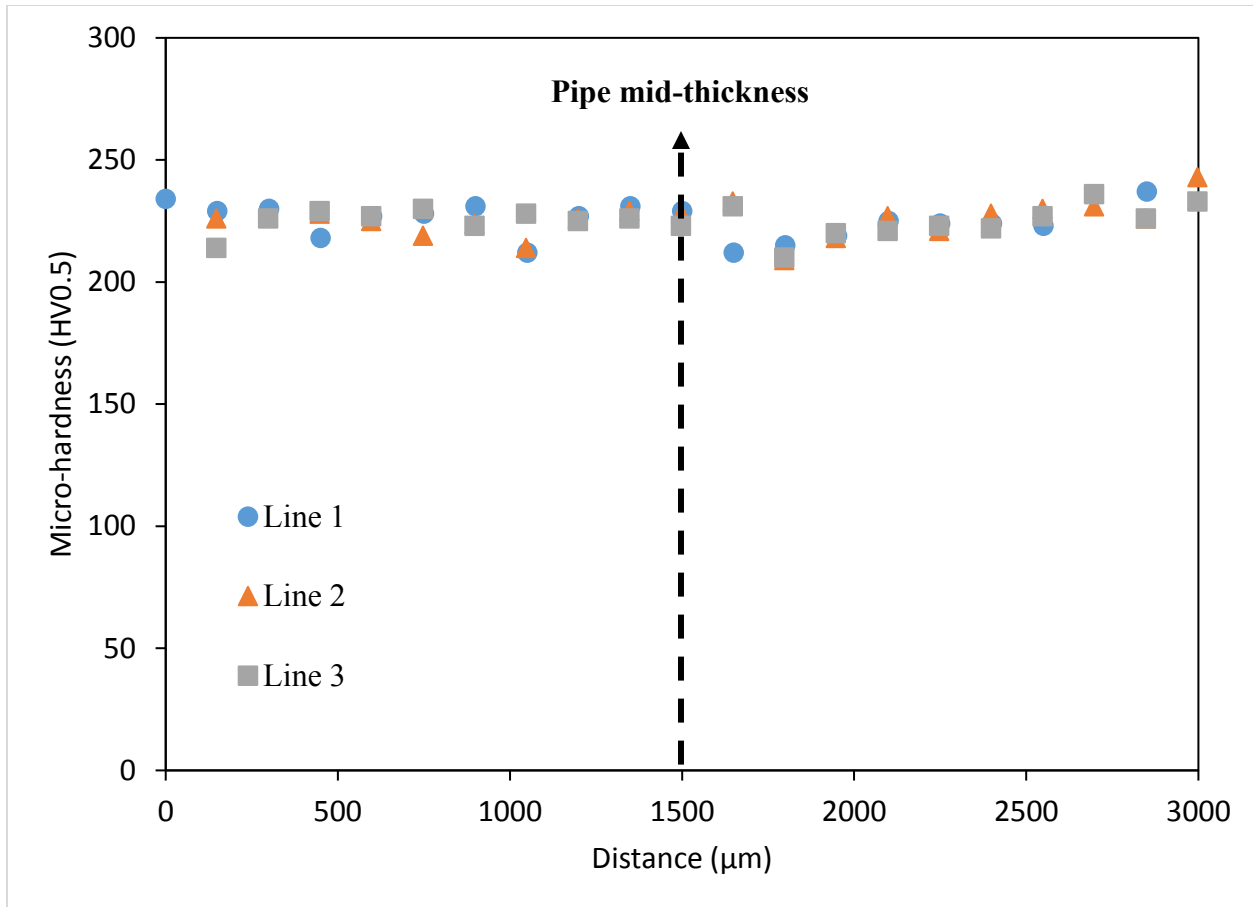


Figure 4.7: Vickers micro-hardness profile across the centerline band in High Mo steel.

### 4.3. Hydrogen induced cracking test results

The results of HIC tests including the calculated values of HIC parameters, the morphology of HIC cracks and the identification of HIC initiation sites are presented in this section.

#### 4.3.1. HIC parameters

The HIC susceptibility is evaluated based on three parameters: crack length ratio (CLR), crack thickness ratio (CTR) and crack sensitivity ratio (CSR). These parameters were defined in Chapter 3.5.6.

Figure 4.8 shows the average values of CLR for all 5 tested steels. In terms of CLR, High Mo and TiB are the most susceptible steels to HIC while SMLS is the most resistant to HIC. The average values of CLR for High Mo and TiB steels are well above the acceptance limit (i.e.,

CLR < 15%) adopted by ISO 15156, which means that these steels are not recommended for sour service.

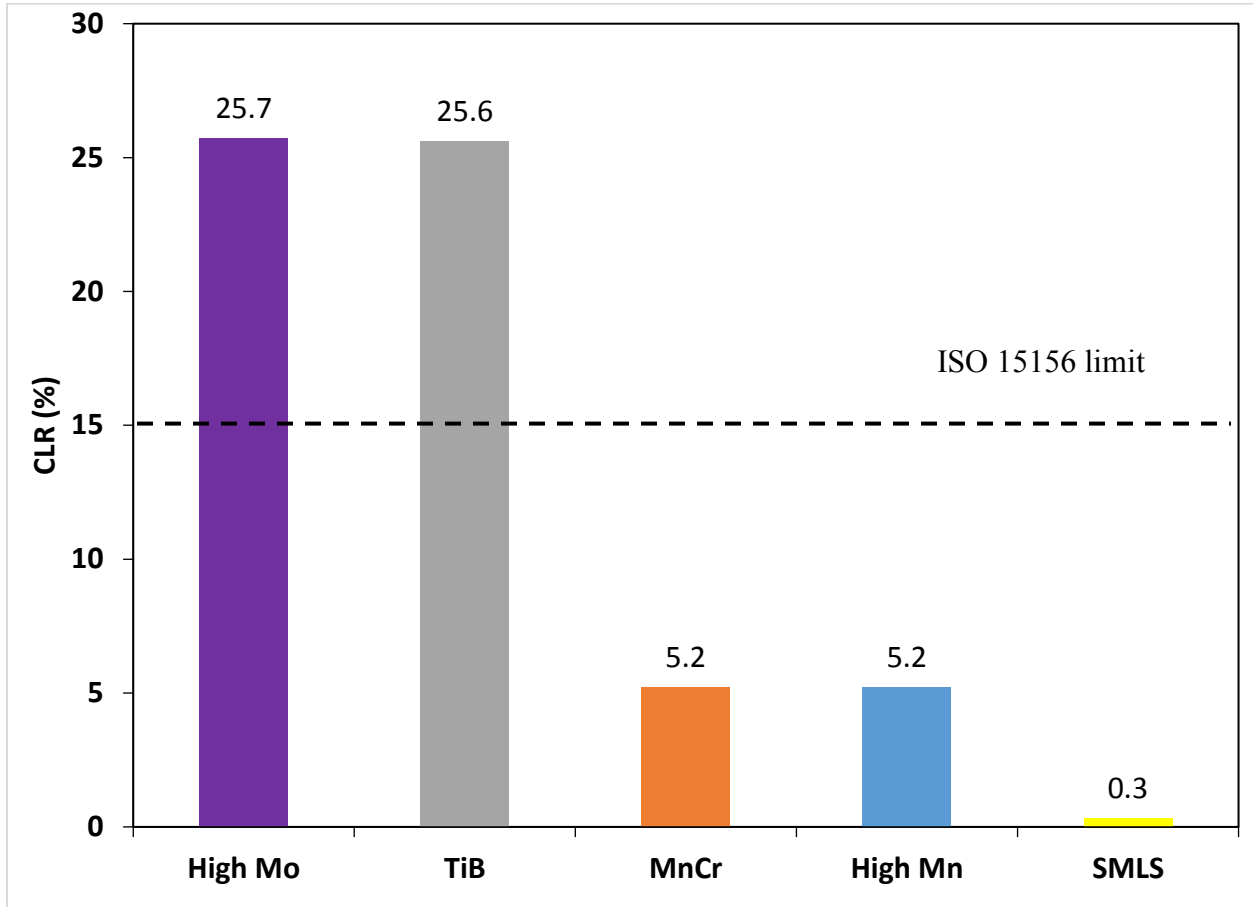


Figure 4.8: Average values of CLR for HIC samples.

Figure 4.9 shows the average values of CTR for the same tested steels. In terms of CTR, High Mo is the most susceptible steel to HIC while SMLS is the most resistant steel to HIC, which is consistent with the results of CLR. The average values of CTR for High Mo and TiB steels are well above the acceptance limit (i.e., CTR < 5%) adopted by ISO 15156, which means that these steels are again not recommended for sour service.

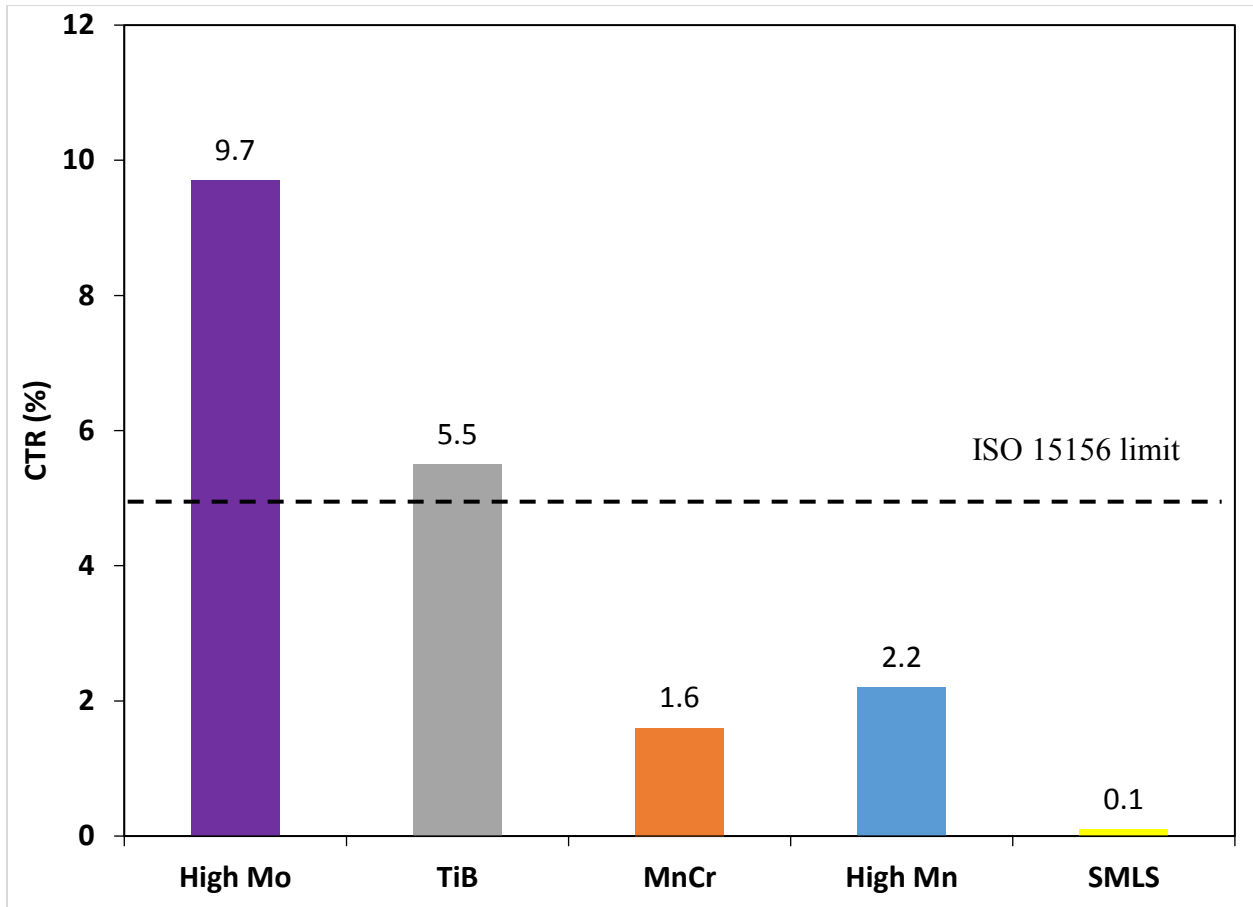


Figure 4.9: Average values of CTR for HIC samples.

Figure 4.10 shows the average values of CSR for the tested steels. In terms of CSR, High Mo is the most susceptible steel to HIC while SMLS is the most resistant steel to HIC, which is consistent with the results of CLR and CTR. The average values of CSR for High Mo steel are well above the acceptance limit (i.e., CSR < 2%) adopted by ISO 15156.

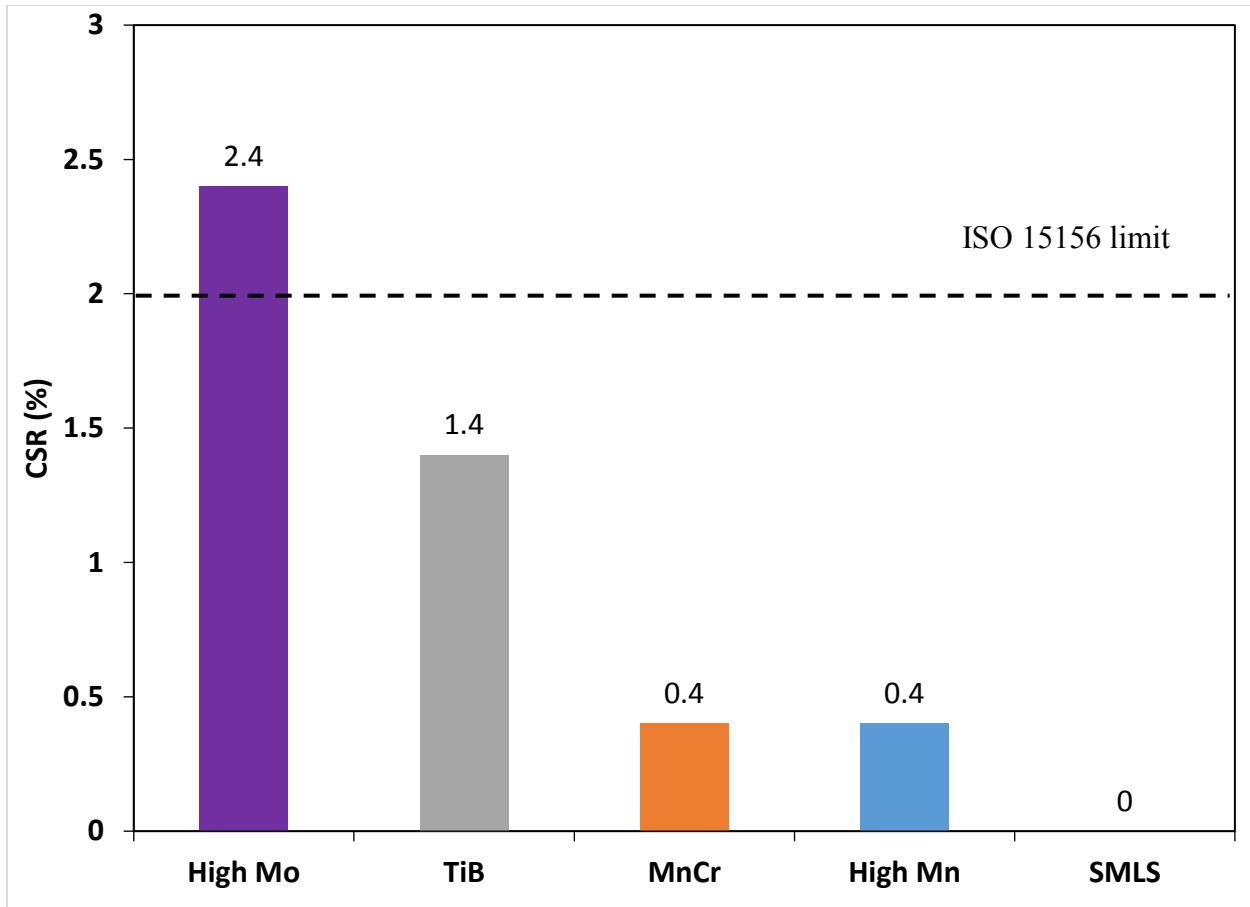


Figure 4.10: Average values of CSR for HIC samples.

In conclusion, High Mo and TiB steels exhibit the highest susceptibility to HIC whereas SMLS exhibits the best resistance to HIC. The difference in the HIC resistance of the different steels will be discussed in Chapter 5.

In addition to the average values of CLR, CTR and CSR presented in this section, the values of CLR, CTR and CSR at different locations (weld, 90°, 180° for ERW pipes and 0°, 120° and 240° for SMLS pipe) are shown respectively in Appendix D.1, Appendix D.2 and Appendix D.3. Values of CLR, CTR and CSR at different locations show significant scatter. This scatter may be due to the inhomogeneous distribution of non-metallic inclusions in the steels as seen in Figure H.1 (Appendix H). As previously discussed in section 2.4.3, the number of non-metallic inclusions are one of the dominant factors affecting HIC. The role of inclusions in HIC will be investigated later in Section 4.3.3 and in Section 5.2.

### 4.3.2. Morphologies of HIC cracks

Figure 4.11 shows an example of HIC cracks in MnCr steel. Examples of HIC cracks in other types of L80 steel are shown in Appendix E.

In all L80 steels, HIC cracks are located at the mid-thickness of the pipe, which suggests the role of centerline macro-segregation band in the initiation and propagation of HIC cracks. The role of centerline macro-segregation on HIC will be investigated in detail in Section 4.8 and discussed in Section 5.4.

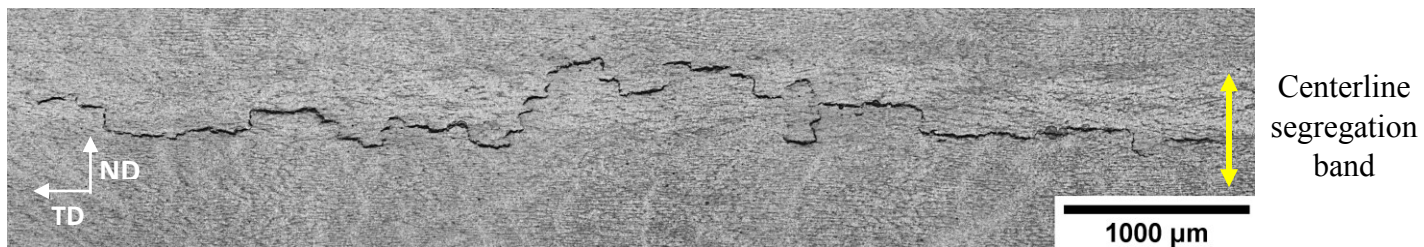


Figure 4.11: An optical micrograph showing an example of a HIC crack in MnCr steel.

The propagation path of HIC cracks in TiB steel was revealed using Marshall's etchant. Figure 4.12 is an optical micrograph of a TiB sample showing a HIC crack at mid-thickness. The HIC tested steel exhibits an intergranular fracture morphology along prior-austenite grain boundaries with a small amount of cracking along the lath-martensite boundaries.

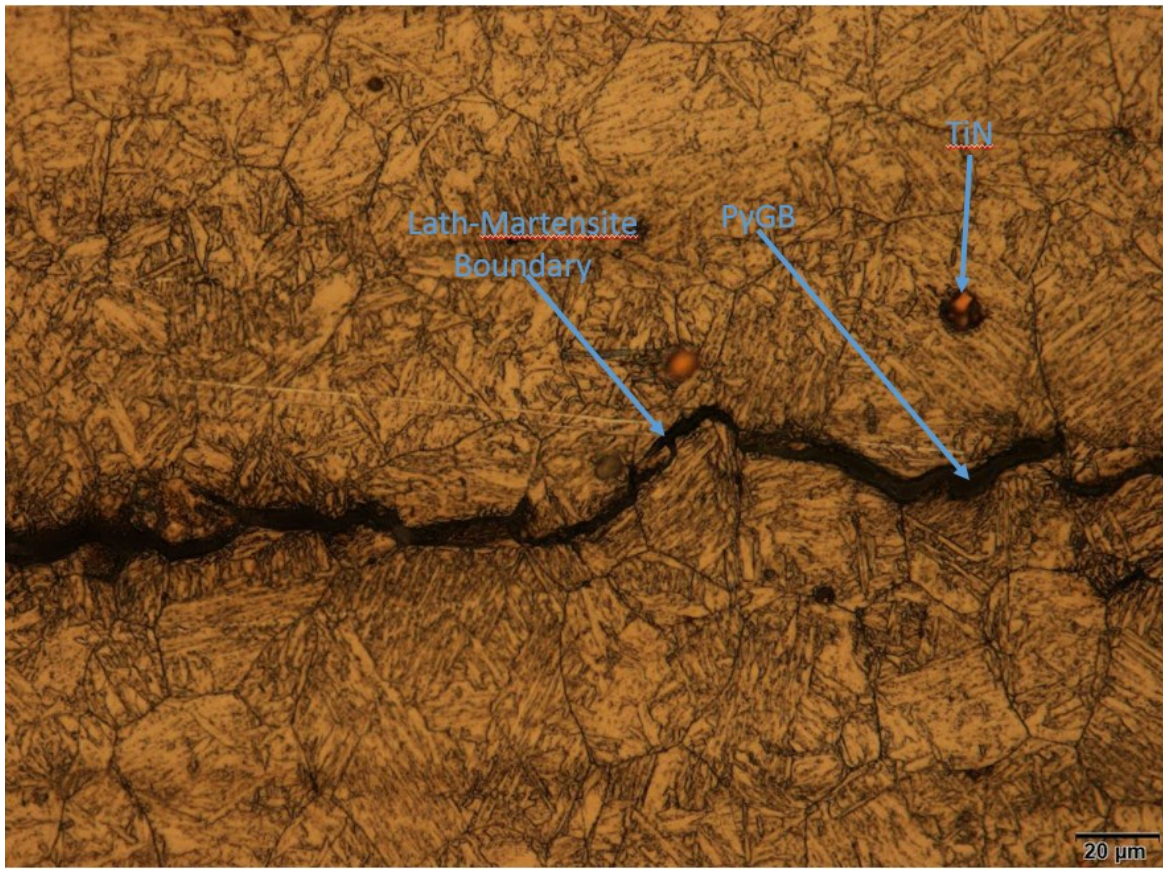


Figure 4.12: An optical micrograph of a TiB sample presenting a HIC crack at mid-thickness.

### 4.3.3. HIC initiation sites

HIC cracks were observed under both optical microscope and SEM equipped with EDX in order to identify the defects that were actually responsible for their initiation. Titanium nitride (TiN) inclusions were observed in some HIC cracks in TiB steel as shown in Figure 4.13.

However, in the other types of L80 steel, it was impossible to identify the initiation sites by microscopy due to the lack of contrast between the inclusions responsible for initiation of HIC cracks and the cracks where they are located.

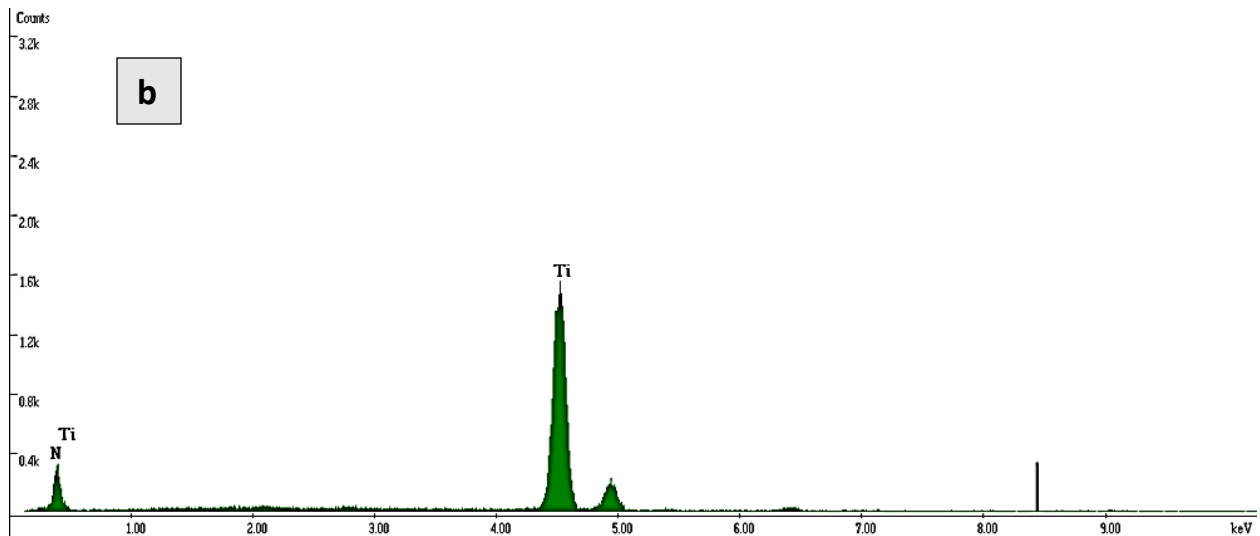
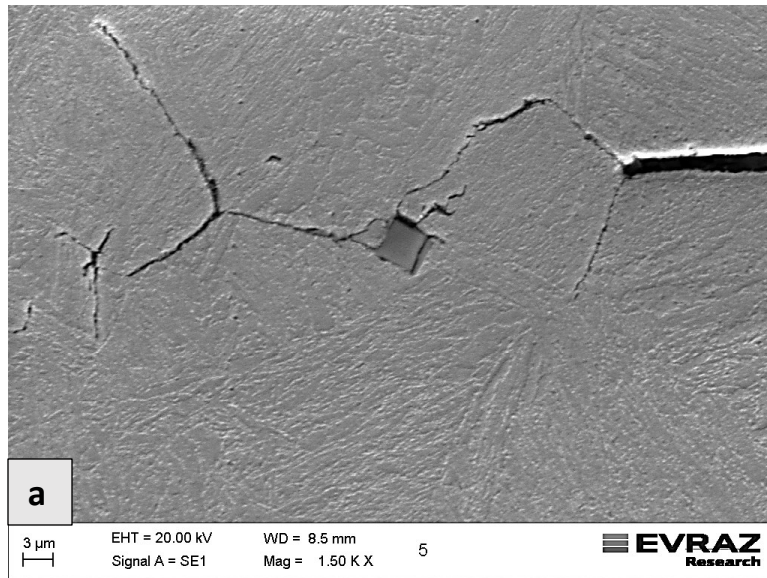


Figure 4.13: (a) SEM image of a TiN inclusion inside a HIC crack in TiB steel, (b) EDS X-ray spectrum of the TiN inclusion.

Thus, the HIC cracks in the most susceptible steels (i.e., High Mo and TiB) were opened and observed under SEM. Figure 4.14 is a fractograph of an opened HIC crack in High Mo steel. Figure 4.15 is a fractograph of an opened HIC crack in TiB steel. The two fractographs show the presence of long flat manganese sulfide (MnS) inclusions (marked with a blue rectangle), which suggests that MnS inclusions play a role in the initiation of HIC cracks. The length of MnS inclusions located in the two fracture surfaces is higher than 100  $\mu\text{m}$ . Figure 4.15 shows also an

intergranular fracture, which confirms that HIC cracks propagate mainly along prior austenite grain boundaries in TiB steel.

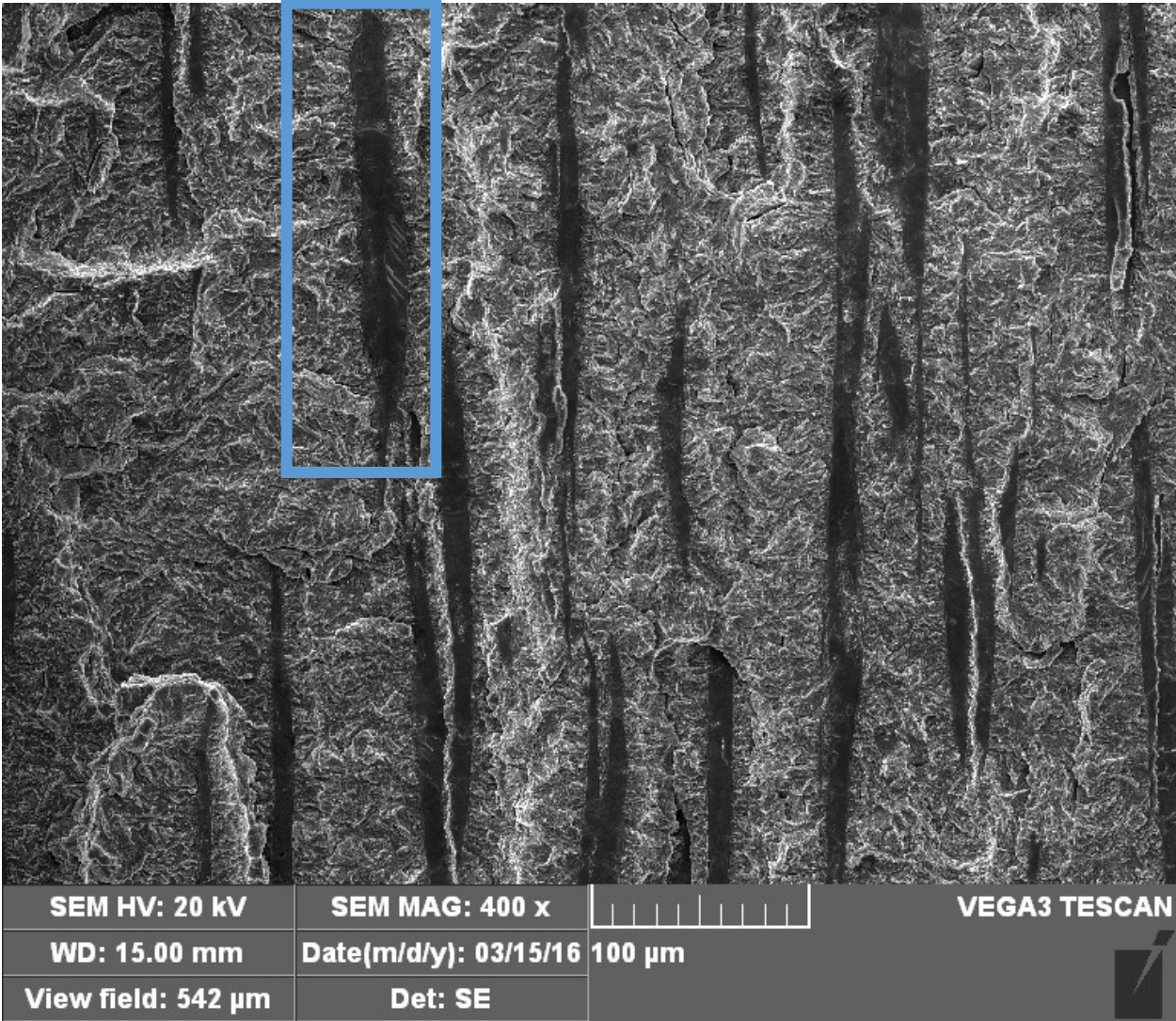


Figure 4.14: SEM image of an opened HIC crack in High Mo steel showing elongated flat MnS inclusions (blue rectangle).



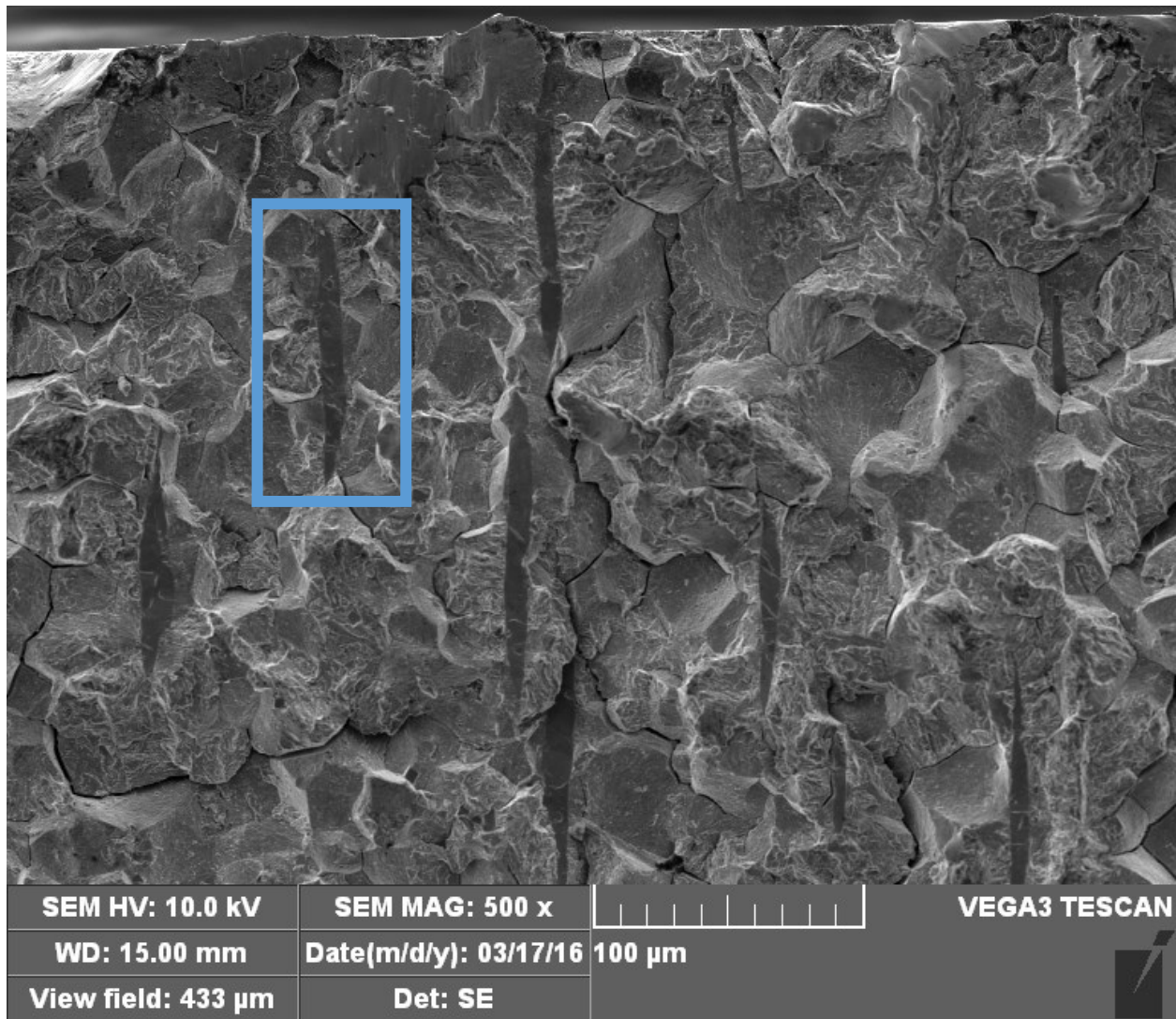


Figure 4.15: SEM image of an opened HIC crack in TiB steel showing elongated flat MnS inclusions (blue rectangle).

#### 4.4. Slow strain rate test results

SSRT tests were performed on smooth cylindrical specimens. Specimens were taken in the longitudinal direction. Tests were carried out in air and in an H<sub>2</sub>S saturated environment (NACE A test solution) at a constant crosshead speed of 0.05 μm/s and at room temperature. For each type of steel and each test environment, the SSRT test was repeated at least twice. The Reduction in Area Ratio (RAR) and the Plastic Strain to Failure Ratio (PSFR) (defined in Chapter 3.7.5) were calculated in order to evaluate the steels susceptibility to sulfide stress cracking (SSC). The fracture surfaces were also carefully observed using SEM.

#### 4.4.1. Stress-crosshead displacement curve

SSRT tests were performed on all 5 different compositions of L80 steel twice in air as well as twice in H<sub>2</sub>S saturated environment. The results of these tests were load versus crosshead displacement curves. The load was then converted to engineering stress (i.e., the load divided by the initial cross-sectional area).

Figure 4.16 shows the obtained stress versus crosshead displacement curves for High Mo steel. The two stress versus crosshead displacement curves in air are similar (i.e., YS, UTS, Elastic Modulus and Elongation values are close). Note that the initial portion of one test is not linear which is likely due to initializing conditions in the SSRT machine. Thus, the SSRT tests performed in air may be considered to yield similar tensile properties. The average values of reduction in area in air and the average values of plastic strain to failure in air were hence used respectively to calculate the reduction in area ratios and the plastic strain to failure ratios.

The two tensile tests carried out in H<sub>2</sub>S show both similarities and differences. In this case, one of the tests also dealt with initializing conditions of the SSRT machine. However, both tests indicate Elastic Moduli which are in agreement with each other and with the tests done in air. The shape of the yielding region of the two tests done in H<sub>2</sub>S show different behaviours. One demonstrating an upper and lower yield point while the other does not. In addition the former exhibits a higher UTS and percent elongation. This may be a result of the reduced number of inclusions present in that sample compared to the other. As seen in Figure H.1 (Appendix H), the inclusion content of two adjacent portions of a steel pipe can contain different amounts of inclusions. This makes the SSRT tests in H<sub>2</sub>S difficult to reproduce from sample to sample.

Based on Figure 4.16, the elongation of the specimens tested in an H<sub>2</sub>S saturated environment is significantly lower than the elongation of the specimens tested in air. The specimens tested in an H<sub>2</sub>S saturated environment failed in a brittle manner just after yielding without necking, which means that High Mo steel exhibits a high susceptibility to SSC.

Similar stress versus crosshead displacement curves were observed for all the other types of L80 steel (i.e., MnCr, TiB, High Mn and SMLS steels) and are presented in Appendix F.

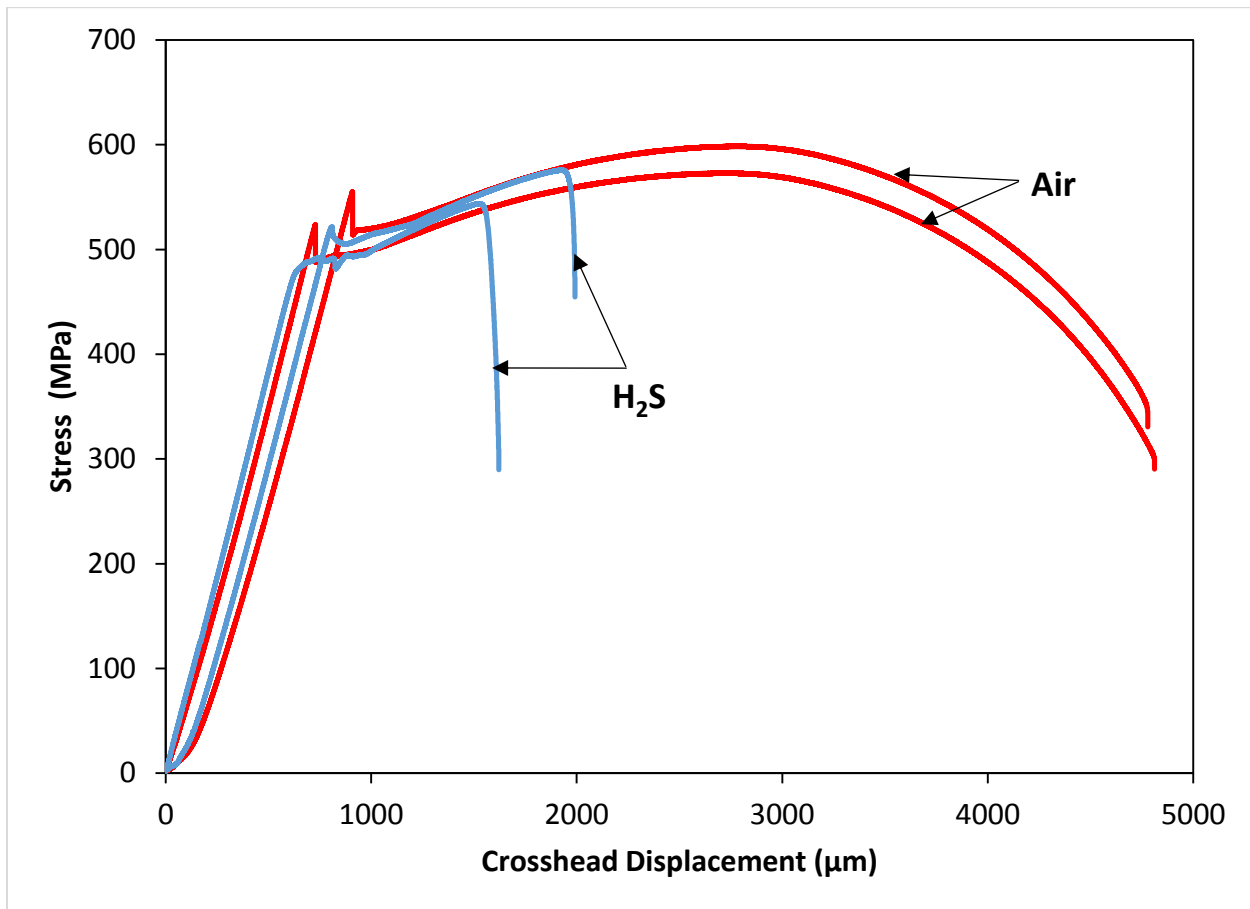


Figure 4.16: Stress-crosshead displacement curves for High Mo steel in air and in NACE A solution saturated with H<sub>2</sub>S.

#### 4.4.2. Reduction in area ratio (RAR)

The RAR is an indication of the loss of ductility in L80 steel due to SSC. A lower RAR means a higher susceptibility to SSC. Figure 4.17 shows the RAR values for all different tested L80 steels. Regardless of the type of the steel and of the number of the run, RAR is lower than 30%, which means that all tested L80 steels are highly susceptible to SSC. High Mo steel has the highest value of RAR (i.e., 27%) and hence the lowest susceptibility to SSC. SMLS exhibits the lowest value of RAR (i.e., 6.3%) and hence the highest susceptibility to SSC.

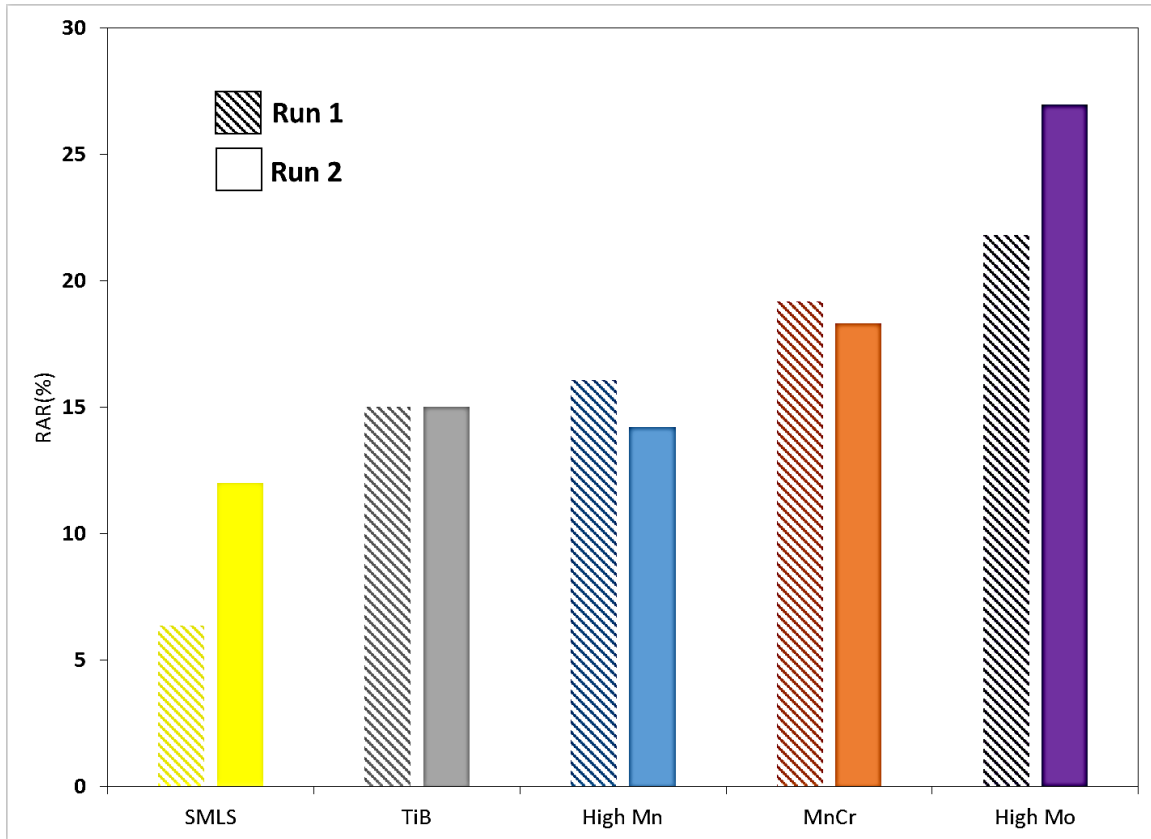


Figure 4.17: Reduction in Area Ratio (%) for different tested types of L80 steel.

#### 4.4.3. Plastic strain to failure ratio (PSFR)

The PSFR is also an indication of the loss of ductility in L80 steel due to SSC. A lower PSFR means a higher susceptibility to SSC.

Figure 4.18 shows the PSFR values for all different tested L80 steels. For TiB, High Mn and MnCr steels, PSFR is observed to vary significantly from Run 1 to Run 2, even though the tests were performed in the same conditions. For example, in MnCr steel, PSFR varies from 32.7% during Run 1 to 21.8% during Run 2. Additionally, the values of PSFR may be affected by necking. Thus, PSFR values were not used to assess the resistance of the different tested L80 steels to SSC.

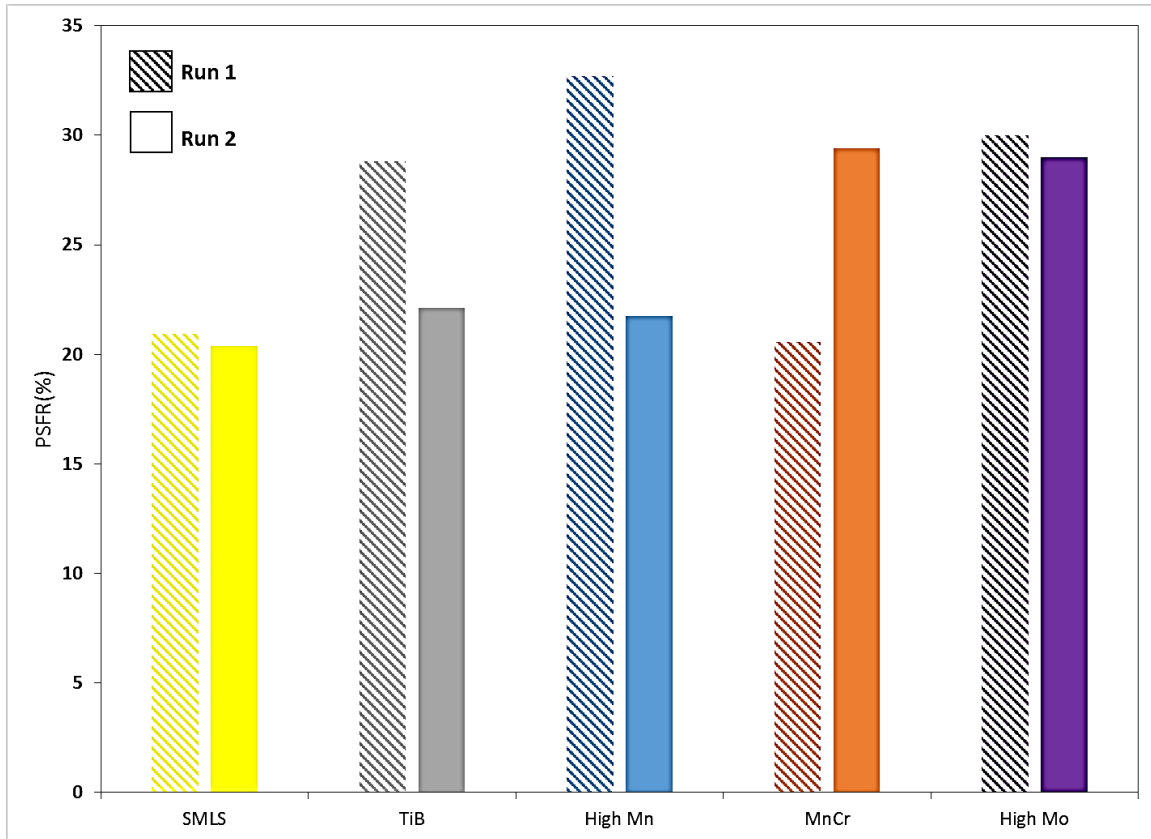


Figure 4.18: Plastic Strain to Failure Ratio (%) for different tested types of L80 steel.

## 4.6. Fractography

In this section, the fracture surfaces of the failed samples in air and in NACE A solution after SSRT testing are examined under SEM in order to determine the fracture mode.

### 4.6.1. Ductile fracture in air

Figure 4.19 is an example of a low-magnification SEM image showing the top and bottom fracture surfaces of a MnCr SSRT sample ruptured in air. The fracture surfaces of the other types of L80 steel tested in air are presented in Appendix G since they exhibit the same fracture mode in air.

A classical cup and cone fracture by micro-void coalescence in the center of the tensile specimen and final crack propagation by shear deformation is observed regardless of the chemical composition of the L80 steel.

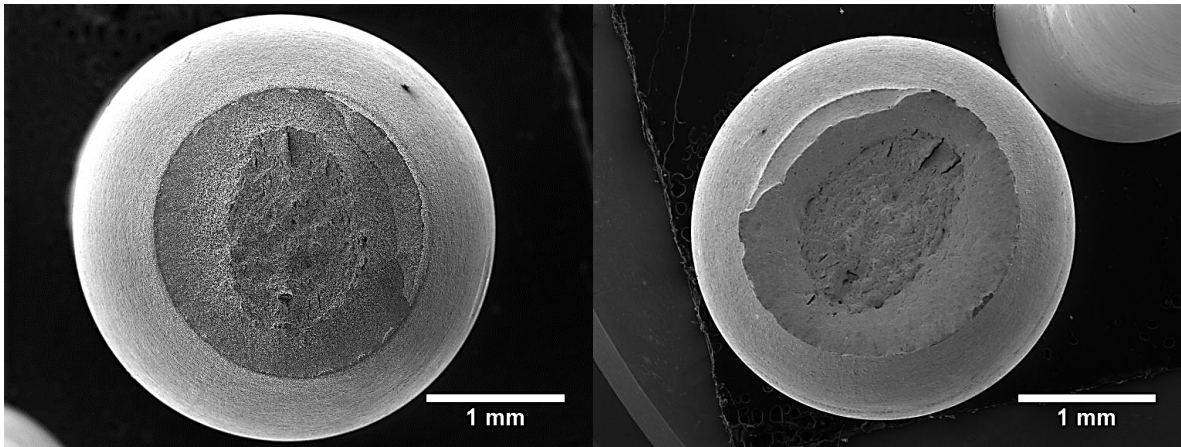


Figure 4.19: SEM image of the fracture surfaces of MnCr steel showing a typical cup and cone fracture after failure in air.

Figure 4.20 is a high-magnification SEM image of the center of one of the fracture surfaces shown in Figure 4.19. Many dimples with many different sizes are observed on the fracture surface. Void nucleation seems to occur by decohesion of the inclusion/matrix interface rather than by inclusion fracture.

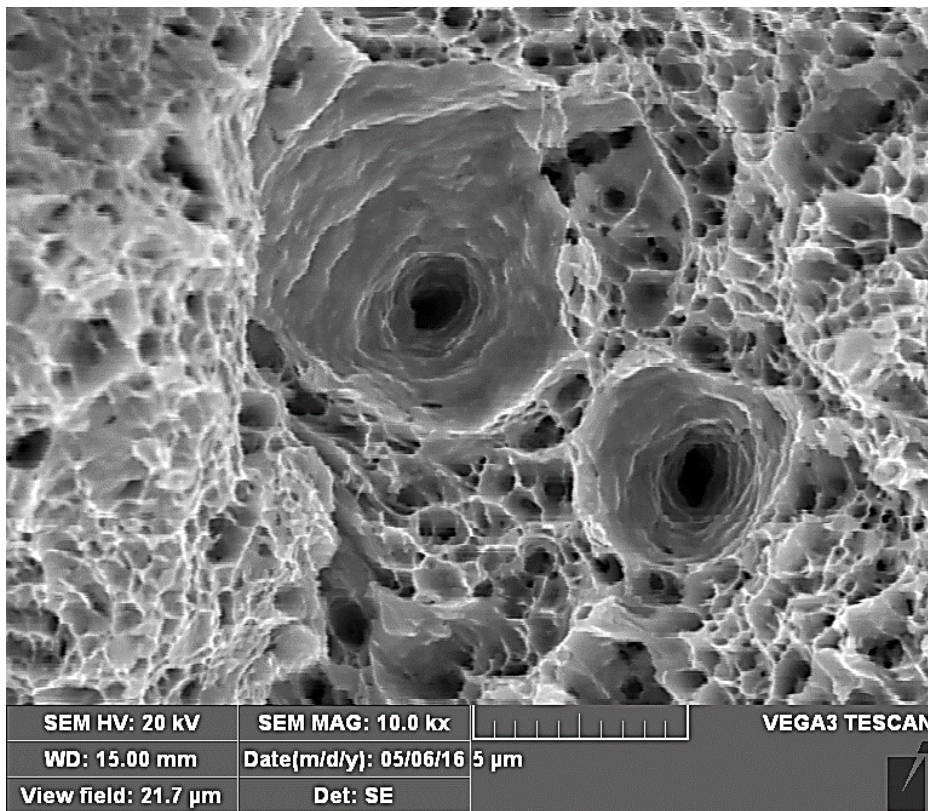


Figure 4.20: A high-magnification SEM image of a ductile fracture surface showing dimples.

#### 4.6.2. Brittle fracture in an H<sub>2</sub>S saturated environment

In this section, the fracture surfaces of SMLS steel are presented because SMLS exhibits the highest susceptibility to SSC. Figure 4.21 (a) shows a macroscopic SEM image of the fracture surface of a SMLS sample after SSRT testing in NACE A solution. Mainly two regions are observed on the fracture surface: a large brittle zone and a ductile zone. The large brittle zone was observed only in the SSRT sample tested in H<sub>2</sub>S saturated solution, which suggests that this large brittle zone is a manifestation of hydrogen embrittlement and that the main failure mechanism in this zone is SSC. The area of this brittle zone may be related to the susceptibility of the steel to SSC. The area of the brittle zone was then measured by selecting the area manually in ImageJ and divided by the total area of the fracture surface.

In Figure 4.21 (b), the percent area of the brittle fracture surface for all samples tested is plotted versus the percent RAR. With the exception of the MnCr and High Mo steels, the trend is clear that as the percent of brittle area decreases, the susceptibility to cracking increases (i.e., lower percent RAR). The images of sample fracture surfaces used to plot Figure 4.21 (b) are shown in Appendix G.

SSC crack initiates from the surface of the SSRT sample (solid arrow). The corrosion pits are the main cause for the surface crack formation (Figure 4.23). Then, SSC crack propagates in a brittle manner radially (dashed arrows) towards the center of the sample and perpendicularly to the applied stress until the remaining ligament cannot hold the applied load anymore. As a result, the remaining part of the specimen fractures into two parts by a ductile fracture. Some secondary microcracks are also observed on the fracture surface in Figure 4.21 (a). These secondary cracks are parallel to the applied stress, which means that these cracks are due to HIC.

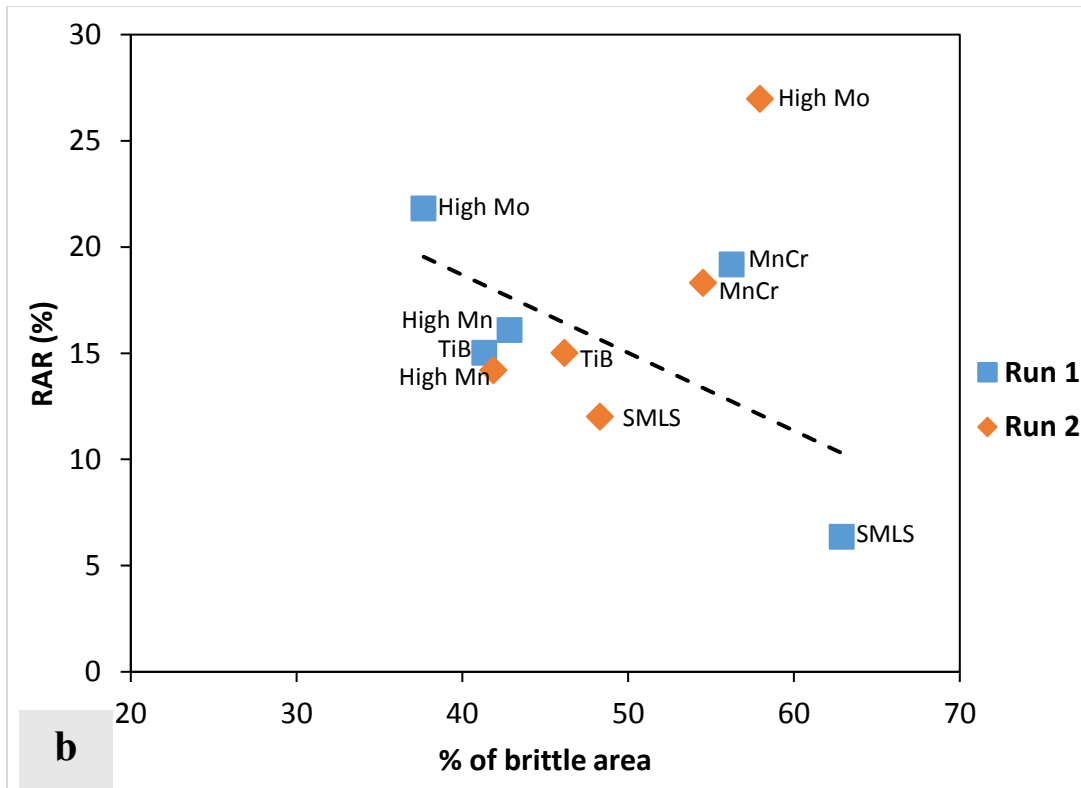
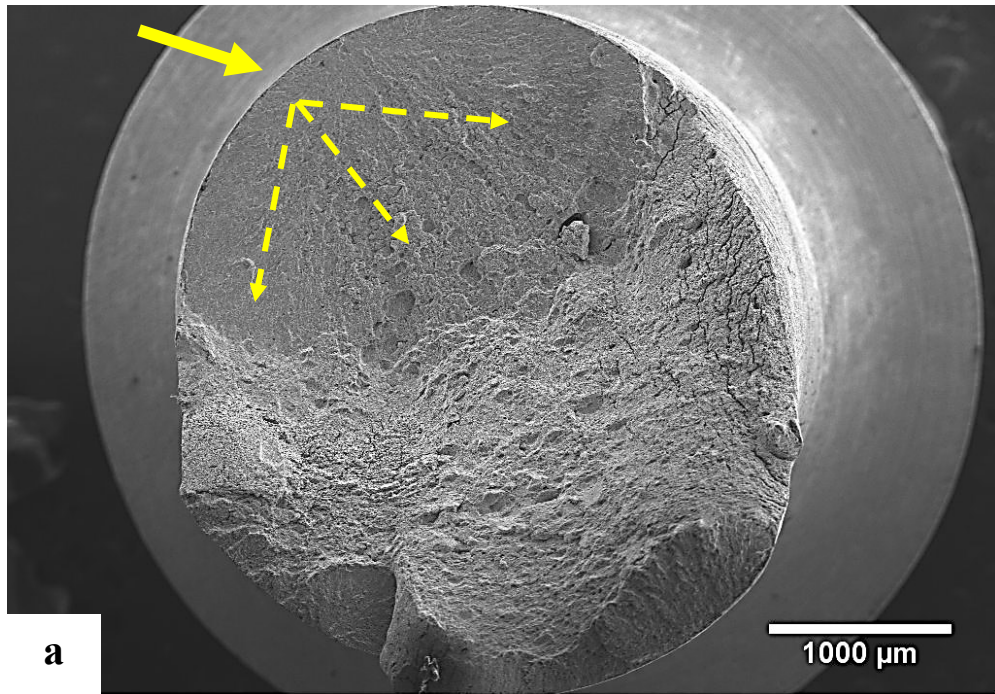


Figure 4.21: (a) A macroscopic SEM image of the fracture surface of SMLS sample after SSRT in an H<sub>2</sub>S saturated environment, (b) % RAR as a function of % area of the brittle fracture surface (the trend is shown by a dashed line connecting between the data points).



Figure 4.22 is a magnified SEM image of the initiation site of the large brittle zone (indicated by a solid arrow) in Figure 4.21. Unfortunately, it is hard to distinguish the initiation site on Figure 4.22.

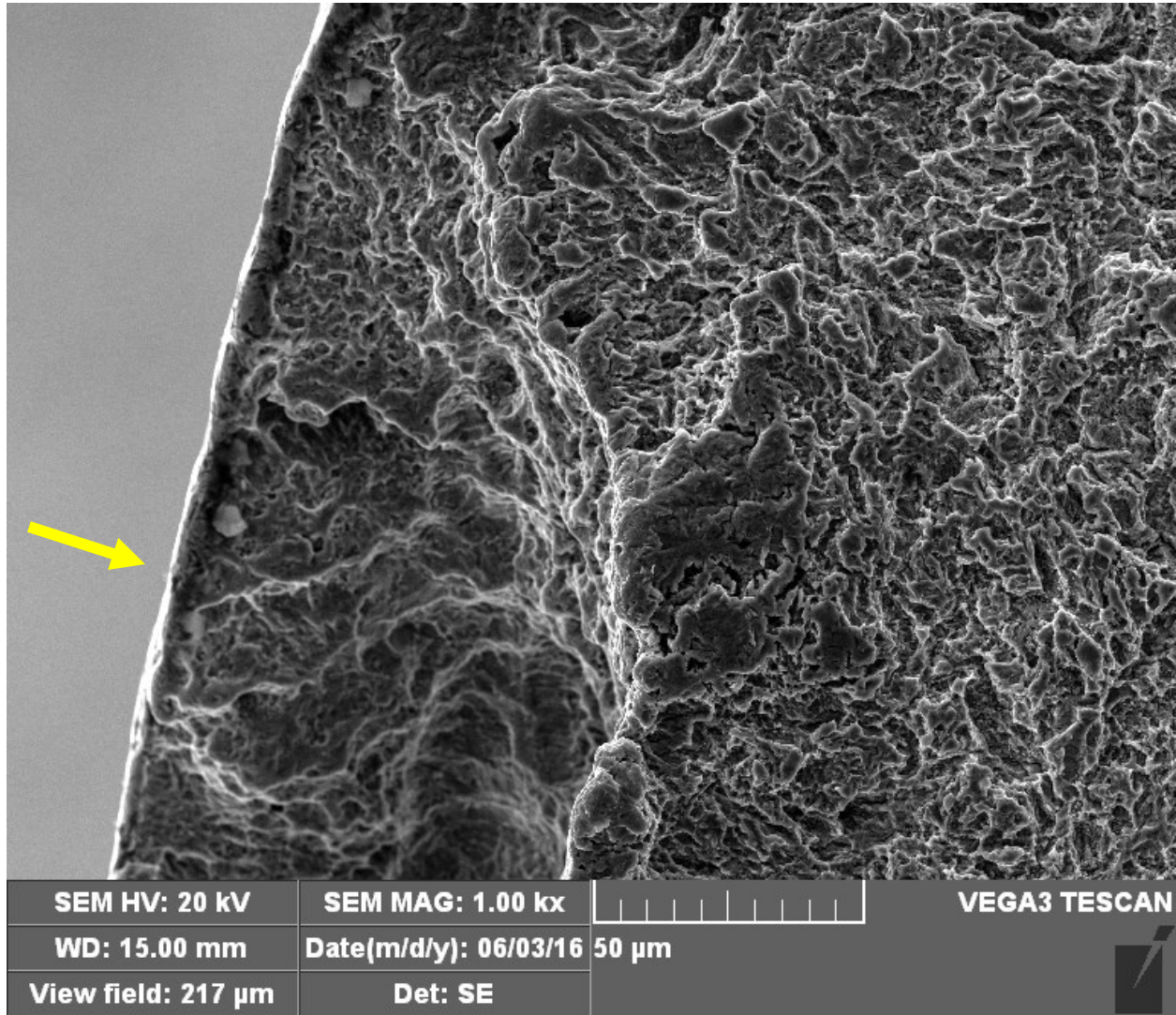


Figure 4.22: A magnified SEM image of the initiation site for SSC in Figure 4.21 (a).

For the other types of L80 steel (i.e., TiB, High Mn, MnCr and High Mo steels), similar fracture surfaces are observed and are presented in Appendix G. The initiation sites of the brittle zones in all the SSRT samples were not identified except for TiB steel. Figure 4.23 is a magnified SEM image of the initiation site of the brittle zone in TiB. Figure 4.23 shows that the corrosion pit area in TiB contains a clustering of globular inclusions, which suggests that inclusions are the main

initiation sites for the corrosion pits at the SSRT sample surface (will be discussed in detail in Section 5.3).

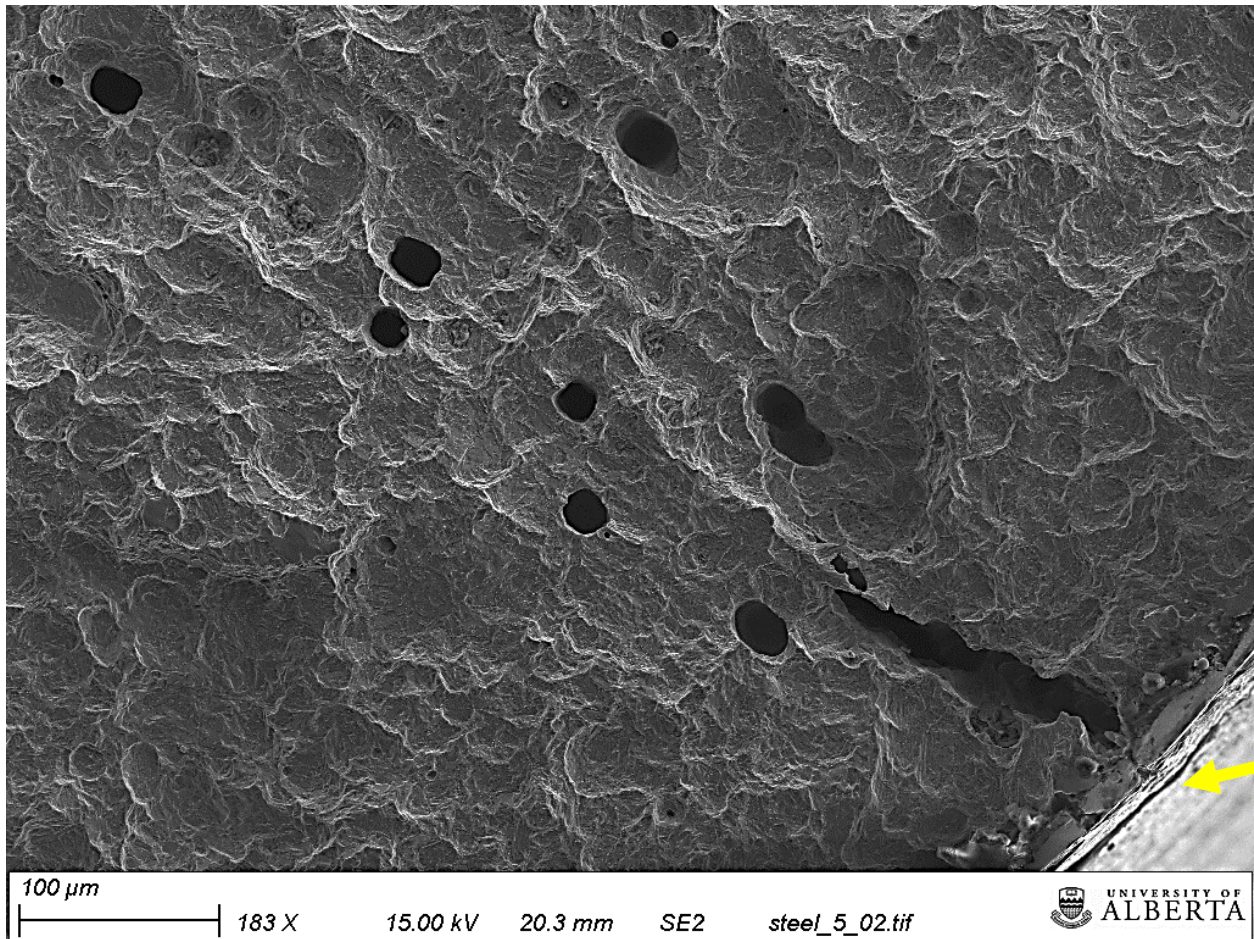


Figure 4.23: A magnified SEM image of the initiation site for SSC in TiB steel.

Figure 4.24 is a magnified SEM image of the brittle zone in SMLS steel. Regardless of the chemical composition of L80 steel, the fracture mode is a typical quasi-cleavage based on the surface appearance. No obvious features of plastic deformation (i.e., microvoid coalescence features) are observed in the brittle zone of the fracture surface as shown in Figure 4.24. This suggests that the hydrogen embrittlement mechanism is mainly hydrogen-induced decohesion.

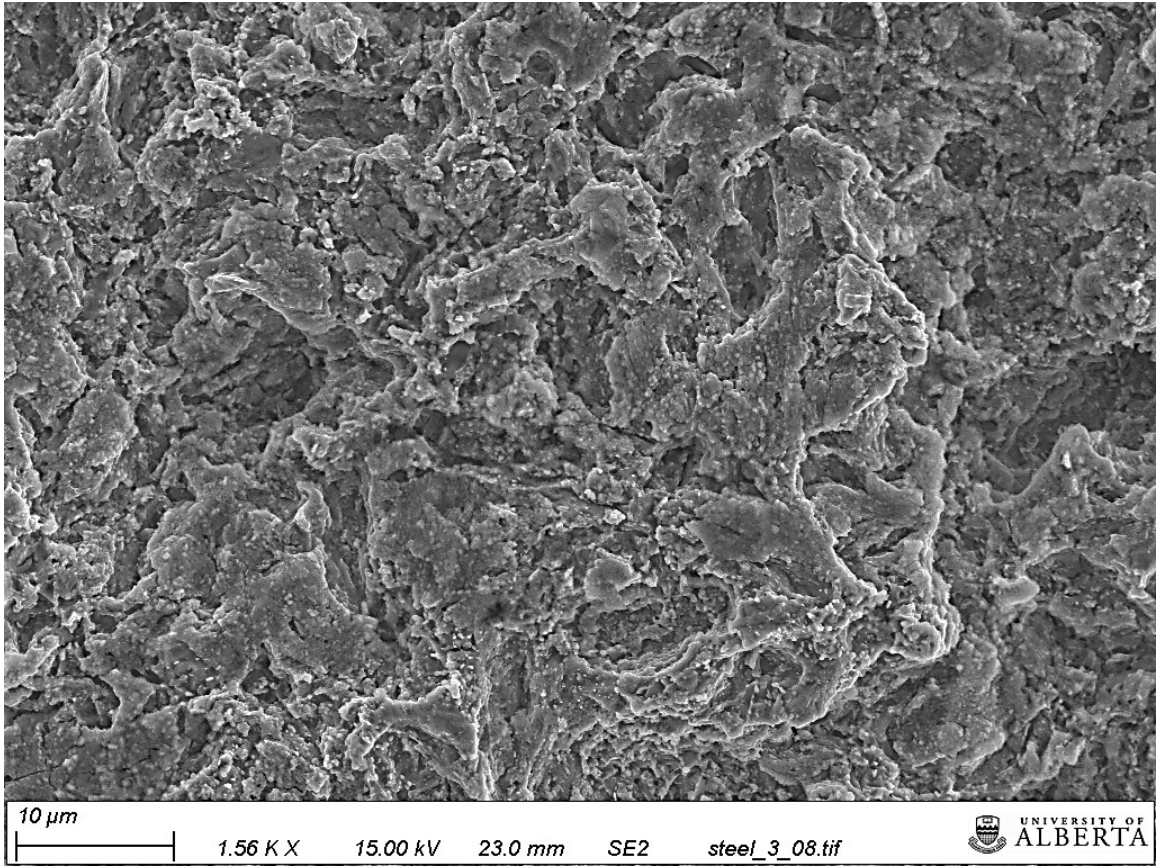


Figure 4.24: Fracture mode in SMLS steel.

## 4.7. Characterization of inclusions

This section will detail the both qualitative (chemical composition, morphology and distribution) and quantitative (size and fraction) analysis of the inclusions observed in all the L80 steels studied.

### 4.7.1. Qualitative analysis (Inclusions morphology, chemistry and distribution)

In all the tested L80 steels, two morphologies of inclusions were observed. These morphologies include globular and elongated inclusions as shown in Figure 4.25.

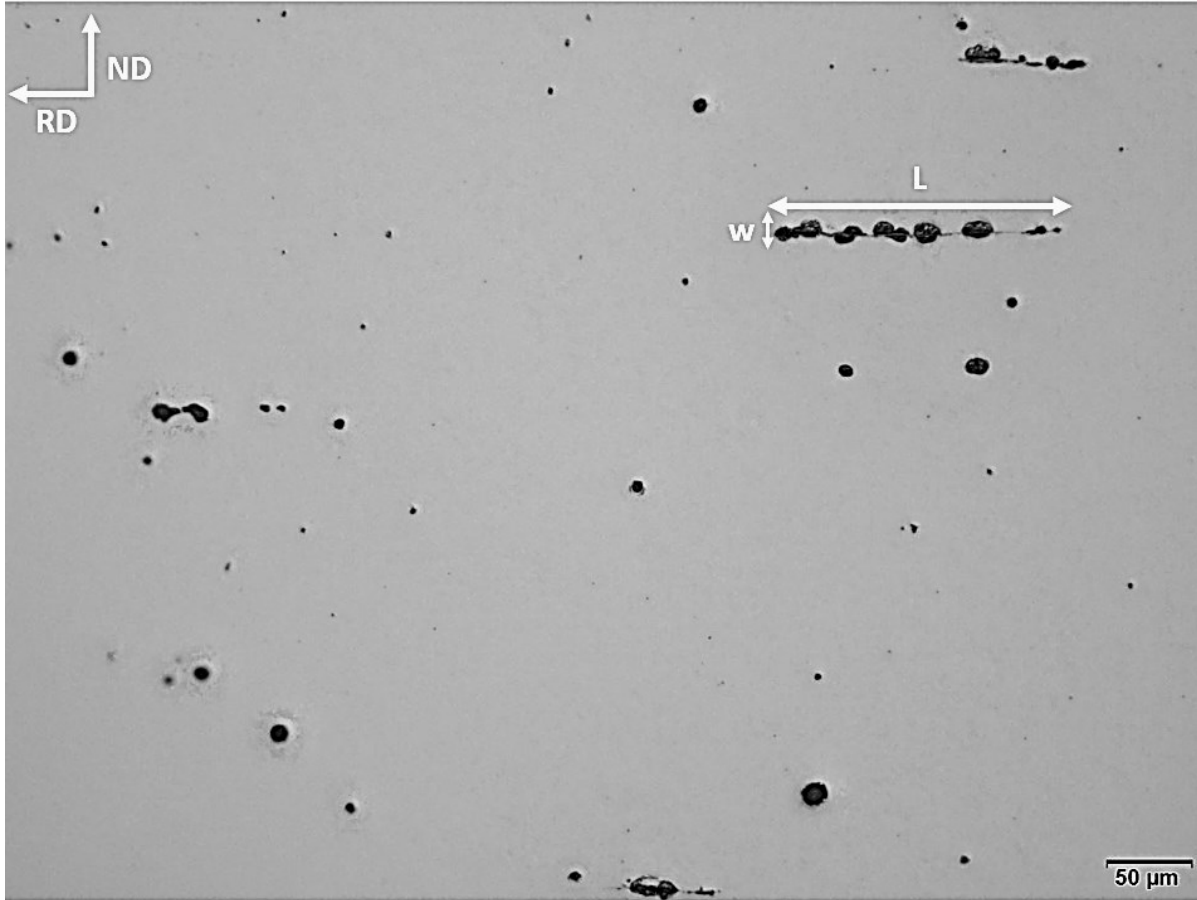
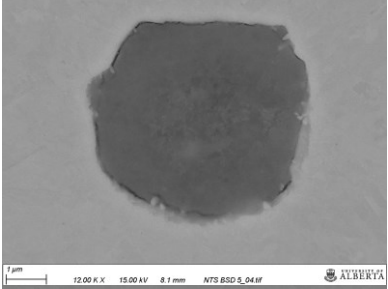
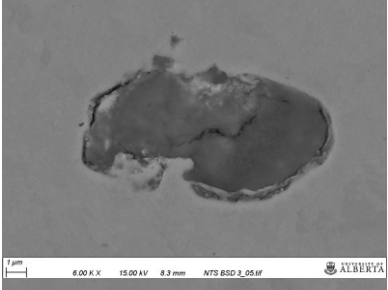
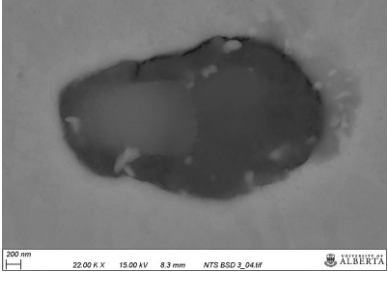

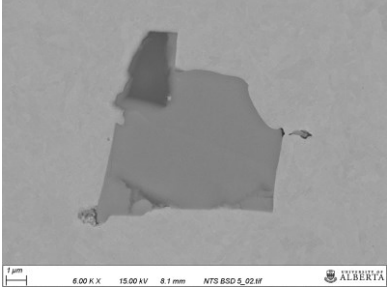


Figure 4.25: An optical micrograph taken at mid-thickness of High Mo steel and showing elongated and globular inclusions.

An analysis of the chemistry of these inclusions was performed using EDX. The globular inclusions are Al enriched inclusions (alumina or Al-rich oxides). The elongated inclusions are manganese sulfides (MnS).

In addition to these inclusions, cubic inclusions were observed in TiB steel due to its higher concentration of Ti compared to the other steels. These results are summarized in Table 4.1.

Table 4.1: Morphology and chemistry of the main inclusions found in all L80 steels studied.

Inclusion Morphology	SEM SE image	Chemistry (wt%)		Aspect Ratio $= \frac{\text{length}}{\text{width}}$
Globular		Al	50.55	< 2
		O	48.02	
		Mg	35.51	
		O	44.45	
		Al	6.96	
		C	13.08	
Elongated		Mn	63.71	≥ 2
		S	36.29	
Cubic		Ti	61.41	< 2
		N	26.32	
		C	12.27	

MnS inclusions are mainly located at mid thickness of ERW pipes as shown in Figure 4.26 and in Appendix H. Clustering of Al enriched inclusions is observed in all types of steels (ERW and SMLS pipes) as shown in Figure 4.26 and in Appendix H.

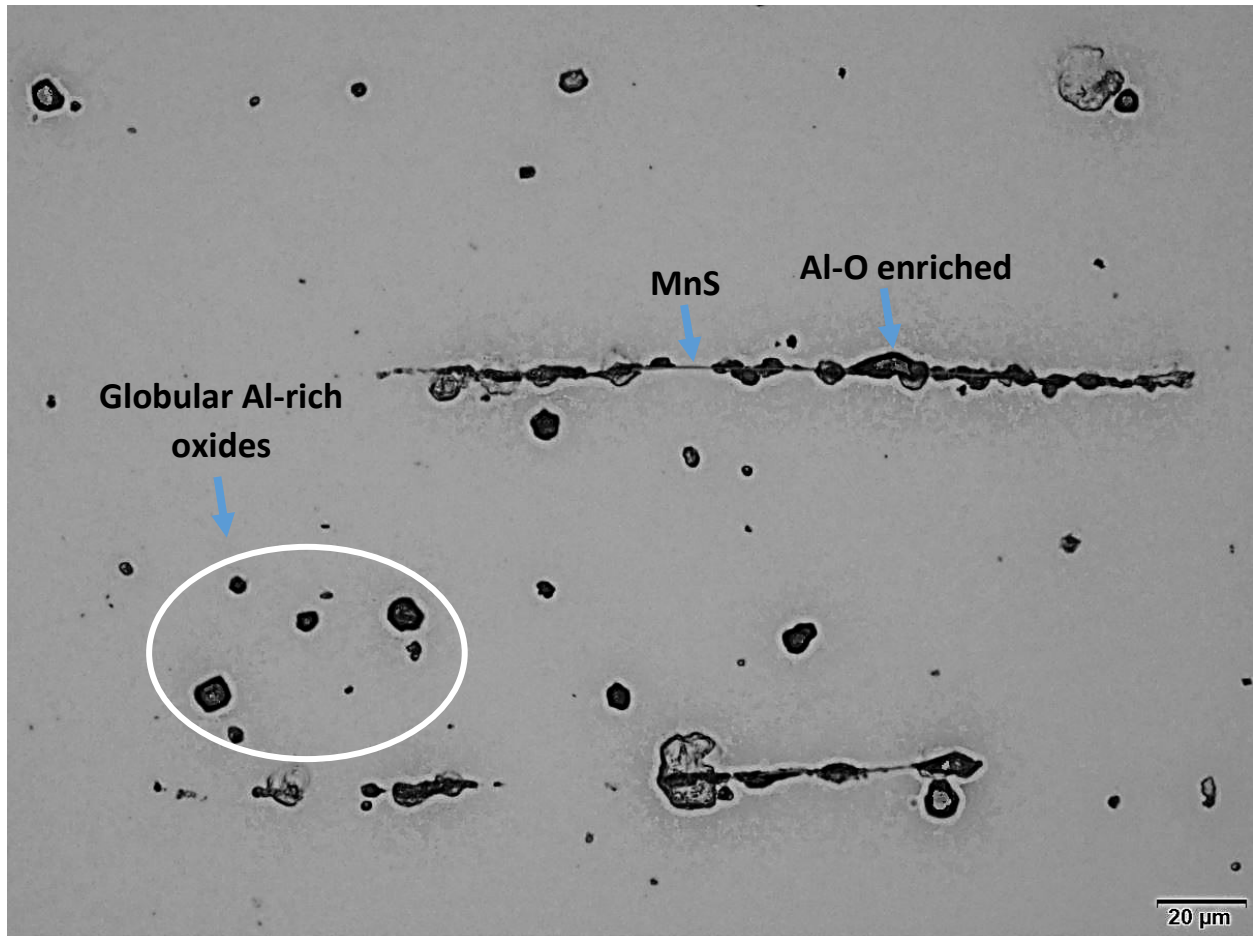


Figure 4.26: Optical micrograph taken at mid thickness of the pipe in High Mo steel.

#### 4.7.2. Size and fraction analysis of manganese sulfides (MnS)

The size and fraction of MnS in L80 steel were analyzed based on their aspect ratio ( $\geq 2$ ). The same area of each sample was analyzed. In total, 98 optical micrographs at a magnification of 240X were taken at the centerline of each sample and were processed using the software ImageJ. In order to generate the size distribution of MnS, only the inclusions of an aspect ratio  $\geq 2$  were taken into account in the calculations.

Figure 4.27 shows the size distribution of MnS in all L80 steels. It is clear that High Mo steel has a higher number of elongated manganese sulfides compared to the other tested steels, which may explain the highest susceptibility of High Mo steel to HIC.

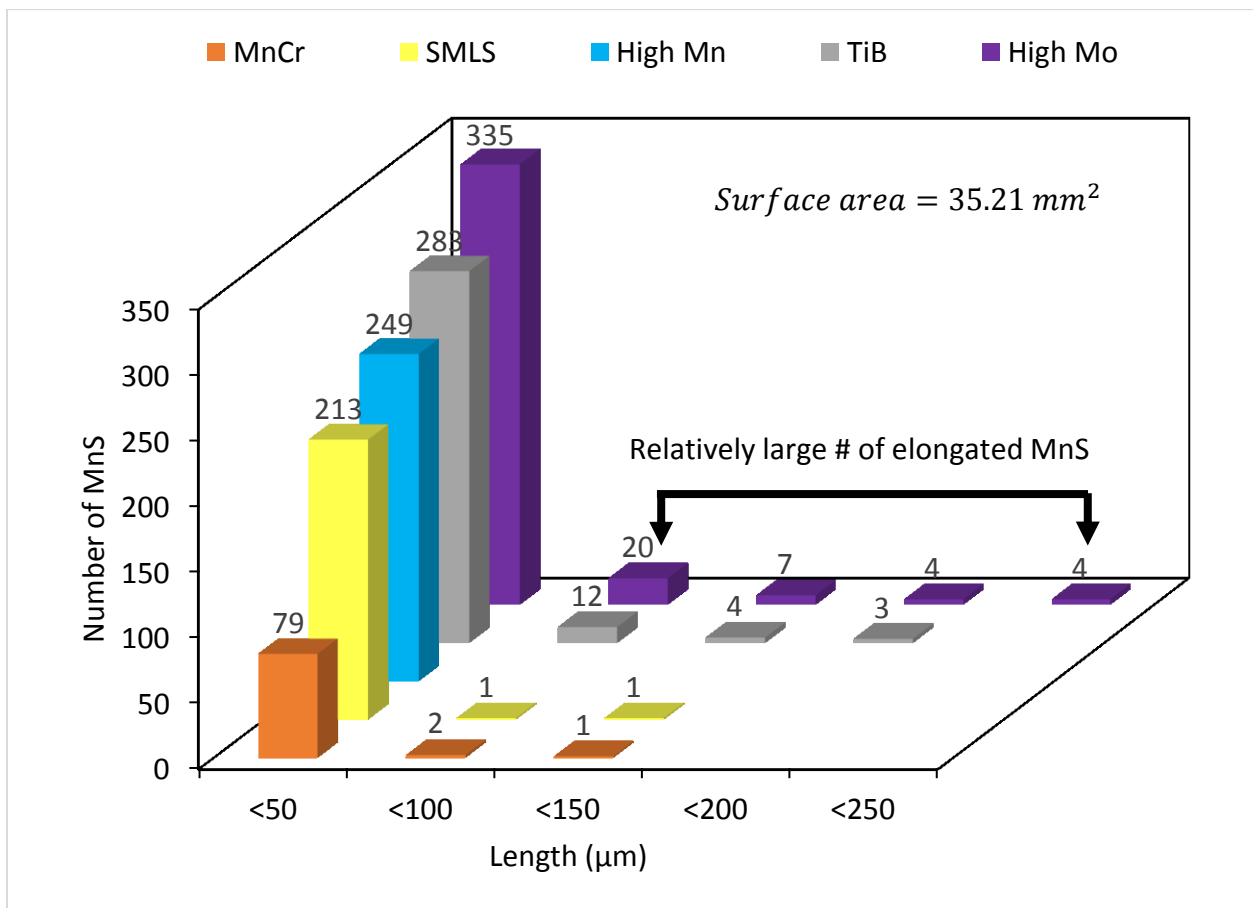


Figure 4.27: Size distribution of MnS inclusions in the different types of L80 steel.

Since the HIC cracks propagate along the rolling plane of the pipe sample as shown in Figure 4.11, the HIC cracks propagation is influenced by the MnS inclusion length (L) rather than by the MnS inclusion width (w) (mentioned in Figure 4.25). Thus, it is important to measure the

total length of MnS inclusions which is the sum of the lengths of MnS inclusions observed in the centerline. Figure 4.28 shows the total length of manganese sulfides for each tested steel. High Mo steel has the highest total length of manganese sulfides, which is consistent with Figure 4.27 and which suggests that High Mo steel has a higher hydrogen trapping efficiency (will be discussed in Chapter 5).

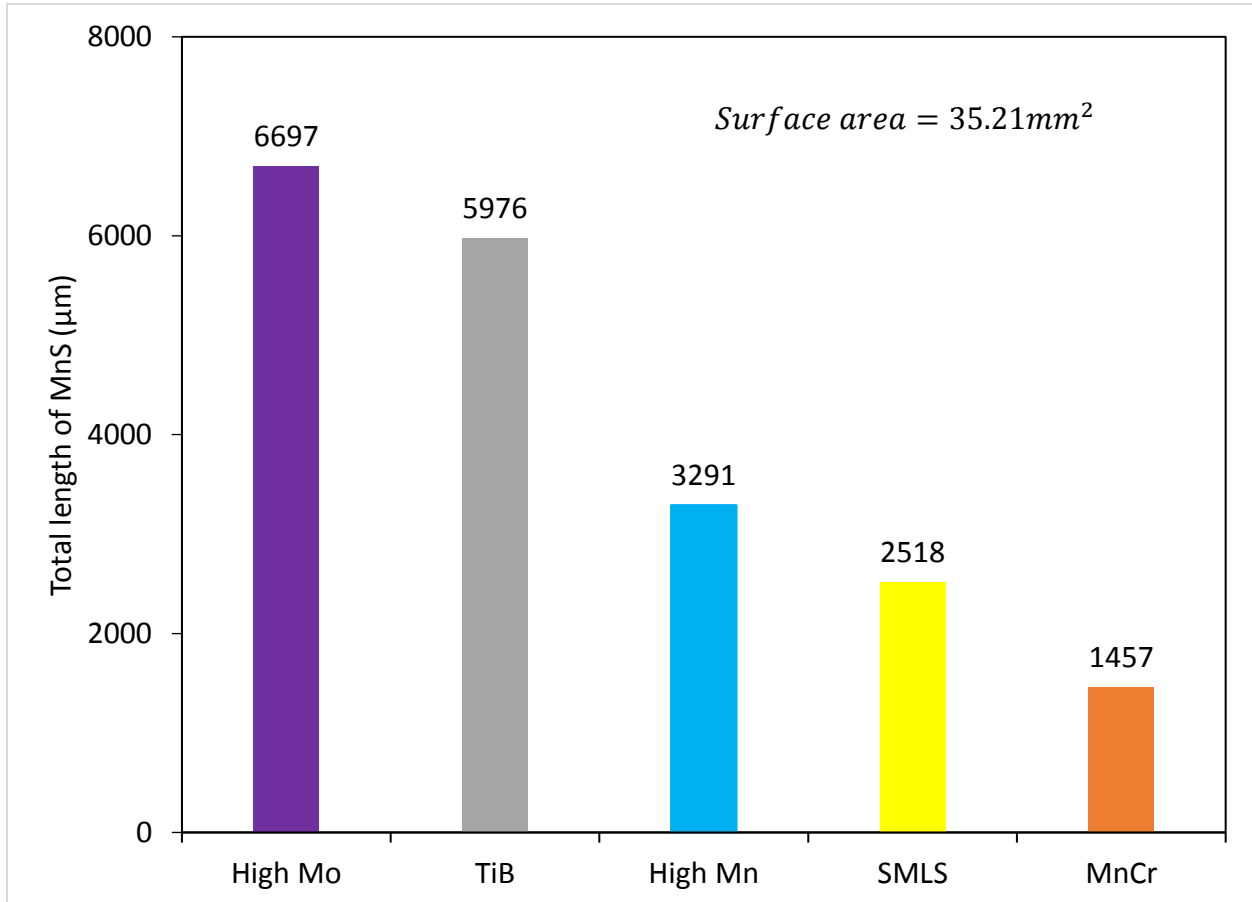


Figure 4.28: Total length of MnS inclusions for the different types of L80 steel.

#### 4.7.3. Size and fraction analysis of globular and cubic inclusions in L80 steel

The number and the size distribution of the globular and cubic inclusions were analyzed based on the aspect ratio ( $< 2$ ). The same procedure mentioned in Chapter 4.7.2 was followed in order to quantify these inclusions. Only the inclusions having an aspect ratio  $< 2$  were taken into account. The inclusions having an aspect ratio  $< 2$  in High Mo, SMLS, High Mn and MnCr steels are Al enriched inclusions. The inclusions having an aspect ratio  $< 2$  in TiB are Al



enriched and TiN inclusions. The average diameter of these inclusions was calculated from the surface area value by assuming that the inclusion is round.

Figure 4.29 shows the size distribution of Al enriched and TiN inclusions in all studied L80 steels. Regardless of the type of L80 steel, most of these inclusions had an average diameter lower than 35  $\mu\text{m}$  which is much lower than the length of MnS inclusions that can reach up to 250  $\mu\text{m}$ .

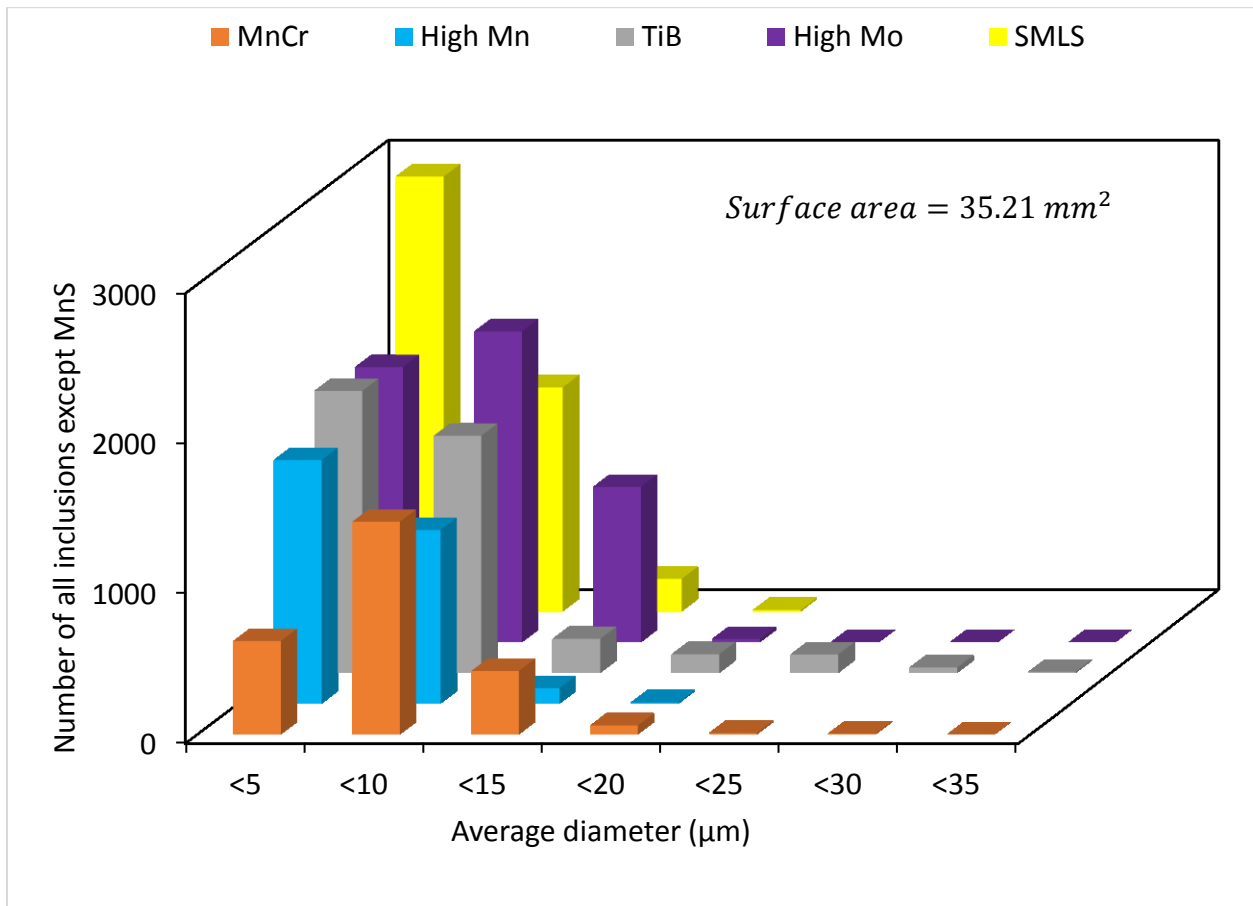


Figure 4.29: Size distribution of all inclusions except MnS in all studied L80 steels.

Figure 4.30 shows the number of all inclusions present in studied L80 steels except MnS inclusions. High Mo steel has the highest number of Al enriched inclusions whereas MnCr has the lowest number of Al enriched inclusions.

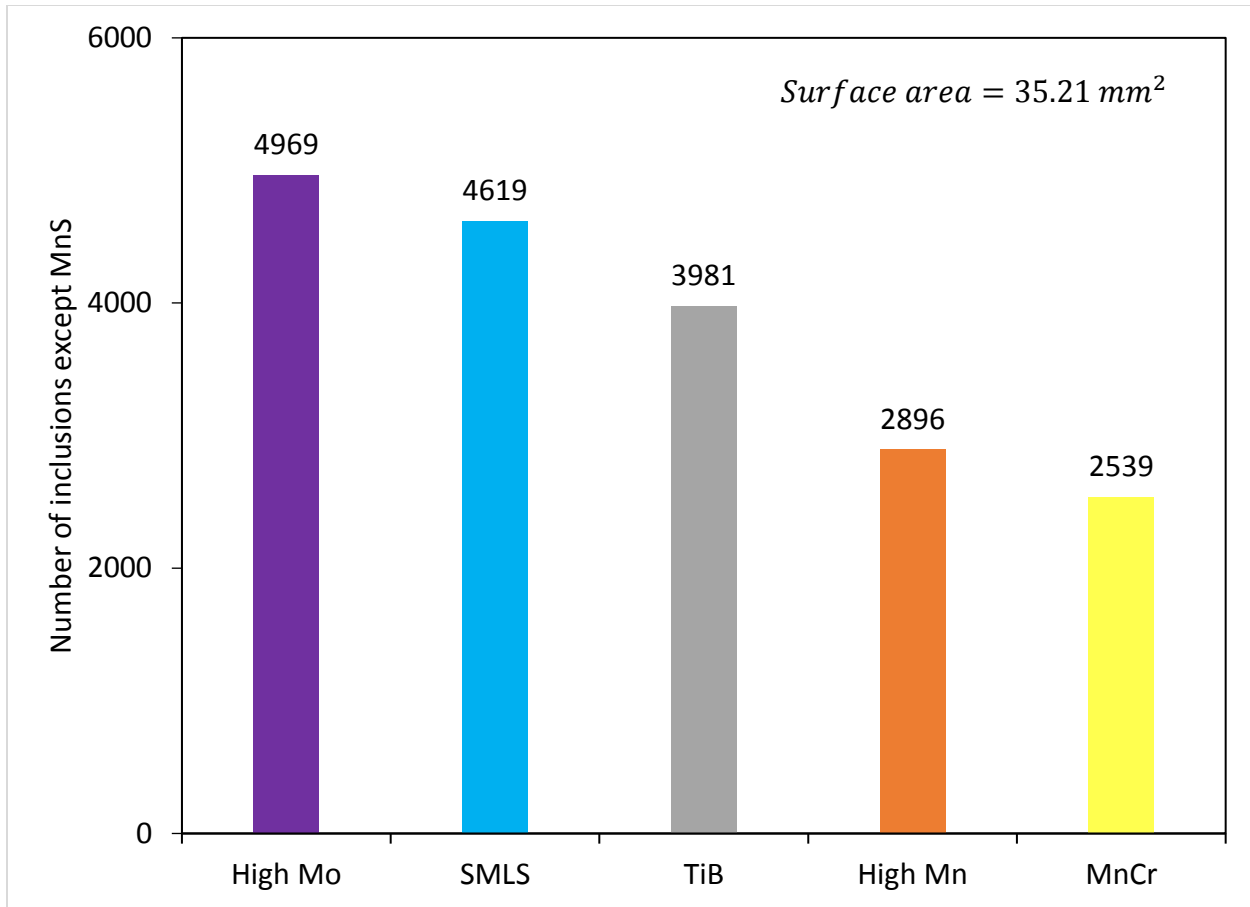


Figure 4.30: Total number of all inclusions present in all studied L80 steels except MnS inclusions.

#### 4.8. Study of centerline macro-segregation in L80 steel

An analysis of the centerline segregation of HIC tested L80 steel was undertaken using electron microprobe analysis (EMPA). A mapping technique was developed to qualitatively assess the magnitude of manganese (Mn), chromium (Cr), sulfur (S) and phosphorus (P) segregation. Following mapping, EMPA line scans were carried out in order to quantify the magnitude of segregation of Mn, Cr, P and silicon (Si). Both techniques were applied to a High Mo as received sample and to High Mo, TiB, High Mn and MnCr steels after HIC testing. This section will detail the results for High Mo steel (both as received and HIC tested samples) because it was the most susceptible steel to HIC. The EMPA results for the other steels (i.e., TiB, High Mn and MnCr steels) are presented in Appendix I.1, Appendix I.2 and Appendix I.3. The centerline

segregation in SMLS steel was not studied since SMLS steel showed the lowest susceptibility to HIC (i.e., CLR  $\approx$  0.3 %).

#### 4.8.1. EMPA X-ray mapping

This section shows the Mn X-ray map obtained by EMPA and performed on an as received sample of High Mo steel across the pipe wall thickness. This is followed by X-ray maps generated for Mn, S, Cr and P by EMPA and performed on a HIC tested sample of High Mo steel.

##### 4.8.1.1. As received sample

Figure 4.31 shows an EMPA X-ray map generated for Mn across the pipe wall thickness in an as received sample from High Mo pipe. Thus, the EMPA X-ray map shows the spatial distribution of Mn across the pipe wall thickness. The bright zones indicate a higher concentration of Mn whereas the dark zone indicate a lower concentration of Mn. It is clear that Mn concentration distribution is less homogeneous at the center of the pipe, where positive and negative segregations of Mn are observed together. This zone (marked by a dashed rectangle on Figure 4.31) represent the centerline macro-segregation band.

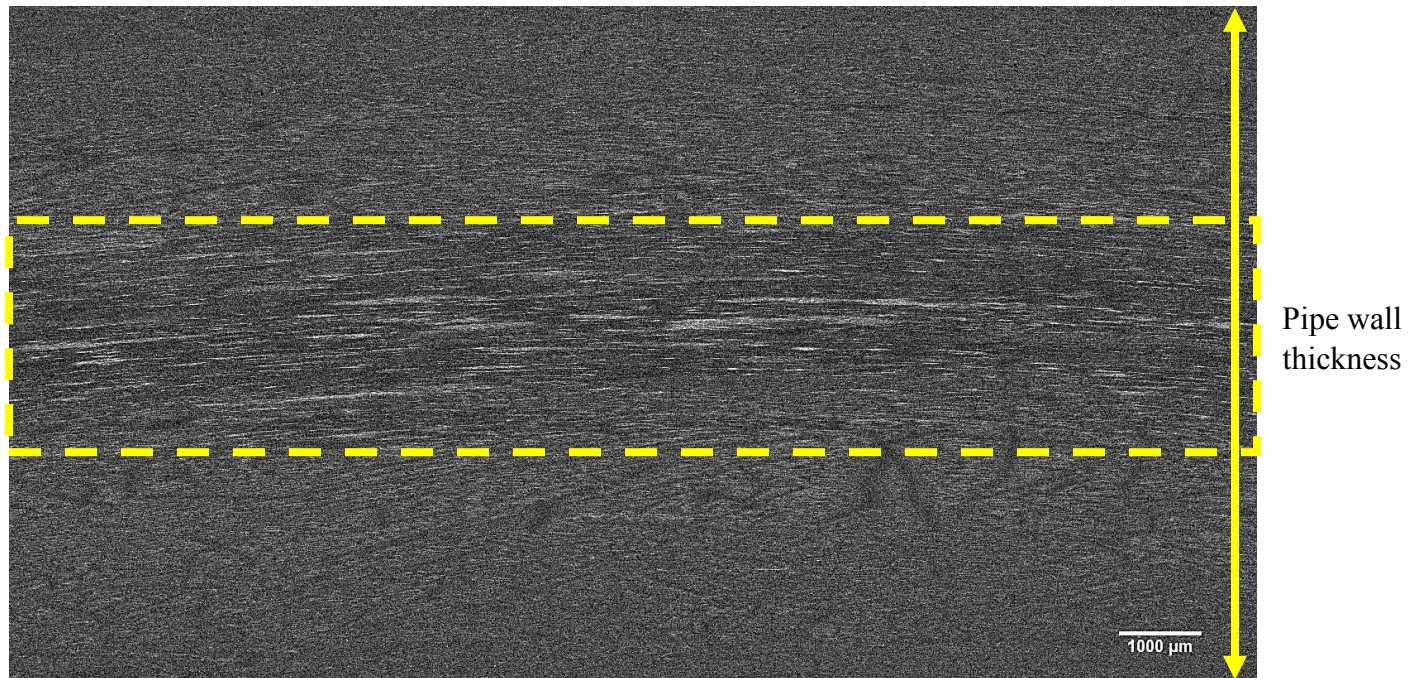


Figure 4.31: EMPA X-ray map generated for Mn across the pipe wall thickness in an as received sample taken at 90° from the weld in High Mo steel (the dashed rectangle indicates the centerline macro-segregation band and the double headed arrow shows the pipe wall thickness).

#### 4.8.1.2. HIC tested samples

The EMPA mapping conditions used for all samples were: a 200 nA current, a 20 kV voltage, a fully focused beam, a 10 μm × 10 μm pixel size and a peak counting time of 20 msec/pixel. Figure 4.32 (a) shows an EMPA SE image of a HIC crack in High Mo steel. Figure 4.32 (b) is the EMPA map generated for Mn. The bright zones in Figure 4.32 (b) indicate higher levels of Mn. The HIC crack is located in the centerline segregation band. However, unexpectedly, the HIC crack does not propagate entirely along the band that contains the highest concentration of Mn (i.e., highest intensity).

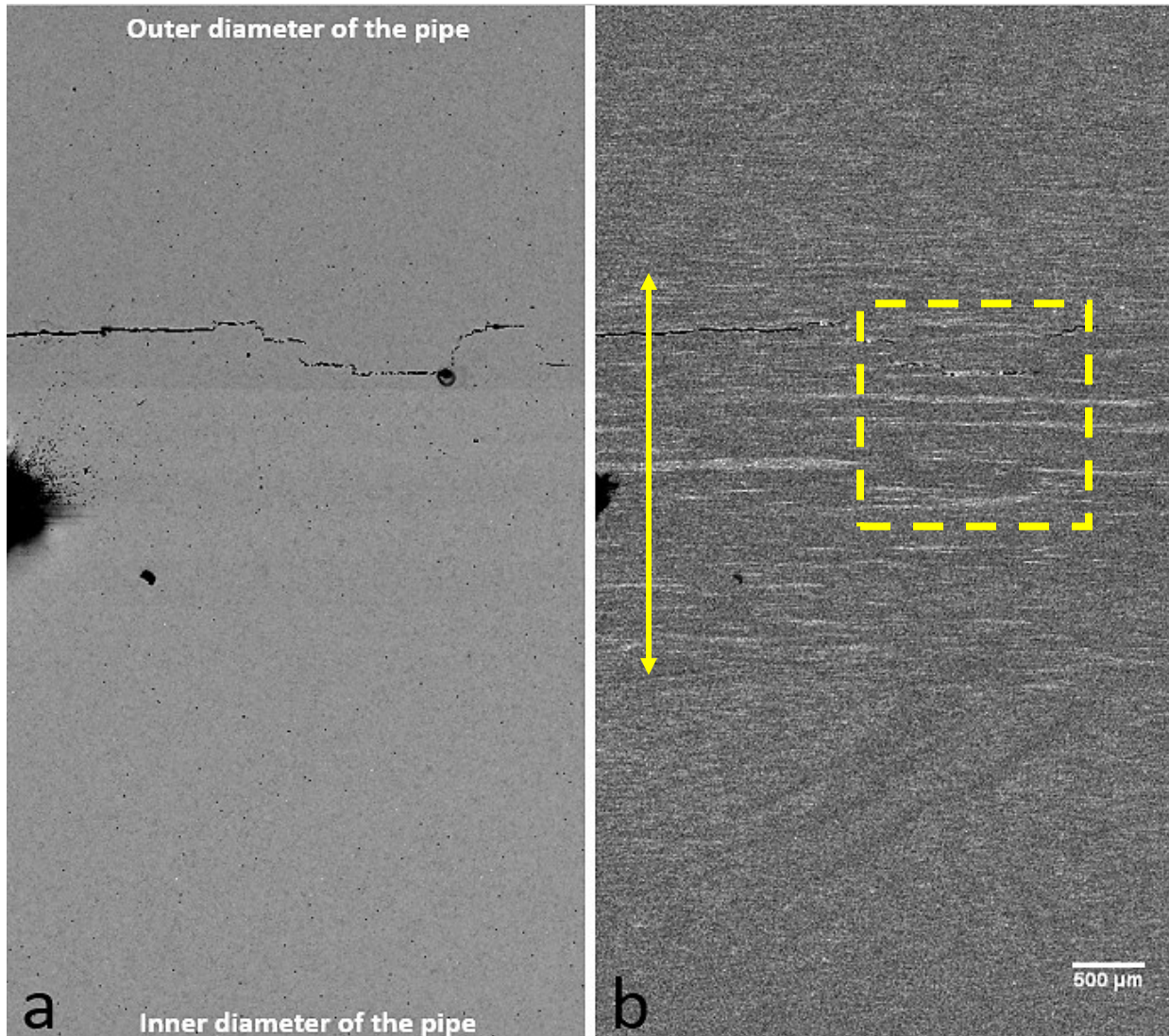


Figure 4.32: (a) EMPA SE image showing High Mo sample after HIC test, (b) Mn EMPA X-ray map of the surface shown in (a) (the double headed arrow shows the centerline segregation band).

A further investigation of the influence of the segregation of Mn and other alloying elements (Cr, P and S) on the HIC propagation was carried out. The area indicated by a dashed square in Figure 4.32 (b) was finely mapped using this time a smaller pixel size ( $1\ \mu\text{m} \times 1\ \mu\text{m}$  pixel size). Mn X-ray map is presented in this section. Figure 4.33 (a) is an optical micrograph of the finely mapped area that was etched with Nital 2%. Figure 4.33 (b) shows the EMPA map generated for Mn of the same area shown in Figure 4.33 (a). By comparing between Figure 4.33 (a) and (b), it is clear that Nital 2% is able to reveal the zones enriched with Mn since the dark brown bands

revealed in Figure 4.33 (a) match with the bright zones revealed in Figure 4.33 (b). Small white spots are also observed on Figure 4.33 (b) which indicates the presence of inclusions highly enriched with Mn.

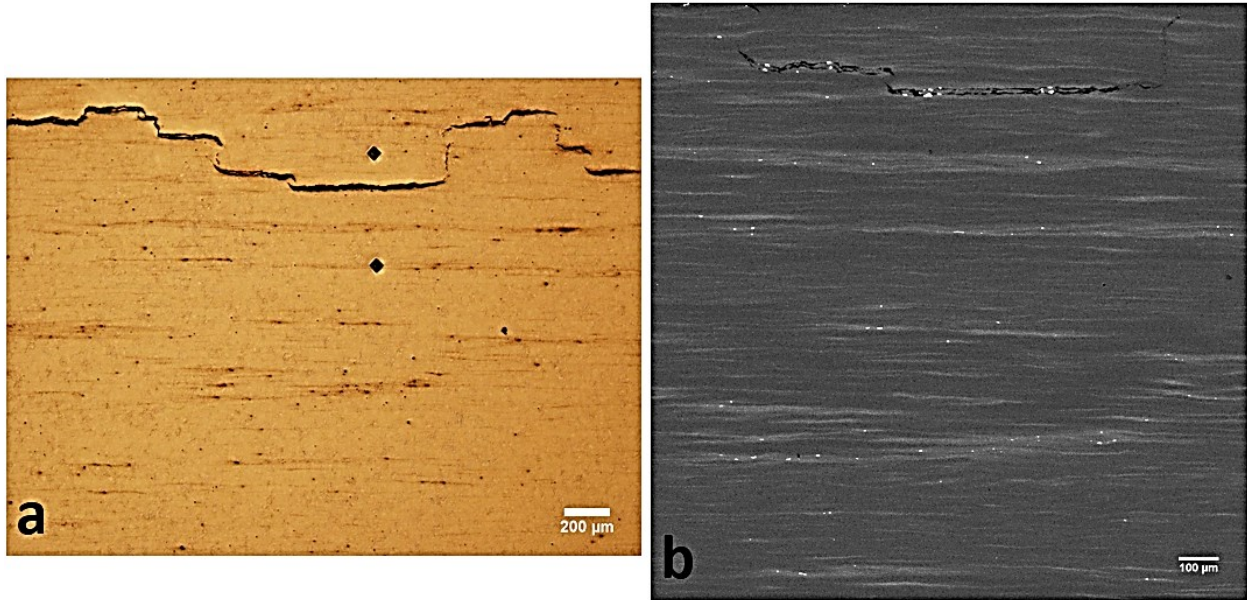


Figure 4.33: (a) Optical micrograph of High Mo sample lightly etched with Nital 2%, (b) Mn EMPA X-ray map of the region shown in (a).

Figure 4.34 shows an EMPA map generated for S of the same area shown in Figure 4.33 (b). Figure 4.34 reveals that S segregates mostly as inclusions and that these inclusions match the Mn enriched inclusions revealed in Figure 4.33 (b), which suggests that S segregates mostly as MnS inclusions. In Figure 4.33 (b) and Figure 4.34 (b), MnS inclusions are observed inside the HIC cracks as well as outside the cracks. However, the inclusions located inside the cracks are larger in size, which can be the cause for the initiation of the HIC at this location.

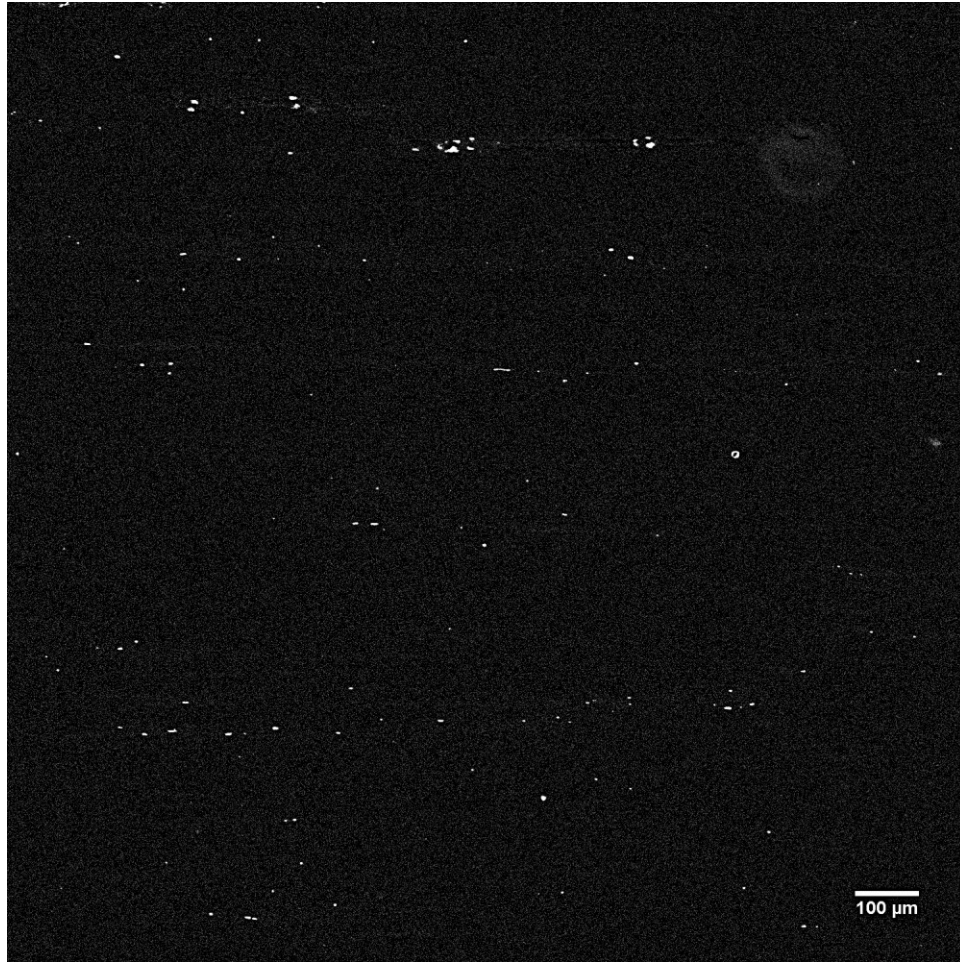


Figure 4.34: S EMPA X-ray map of the same area shown in Figure 4.33 (b).

Figure 4.35 shows an EMPA X-ray map of the same area shown in Figure 4.33 (b) generated for Cr. The Cr X-ray map is similar to the Mn X-ray map. Several segregation bands are observed across the sample (around and outside the HIC crack).

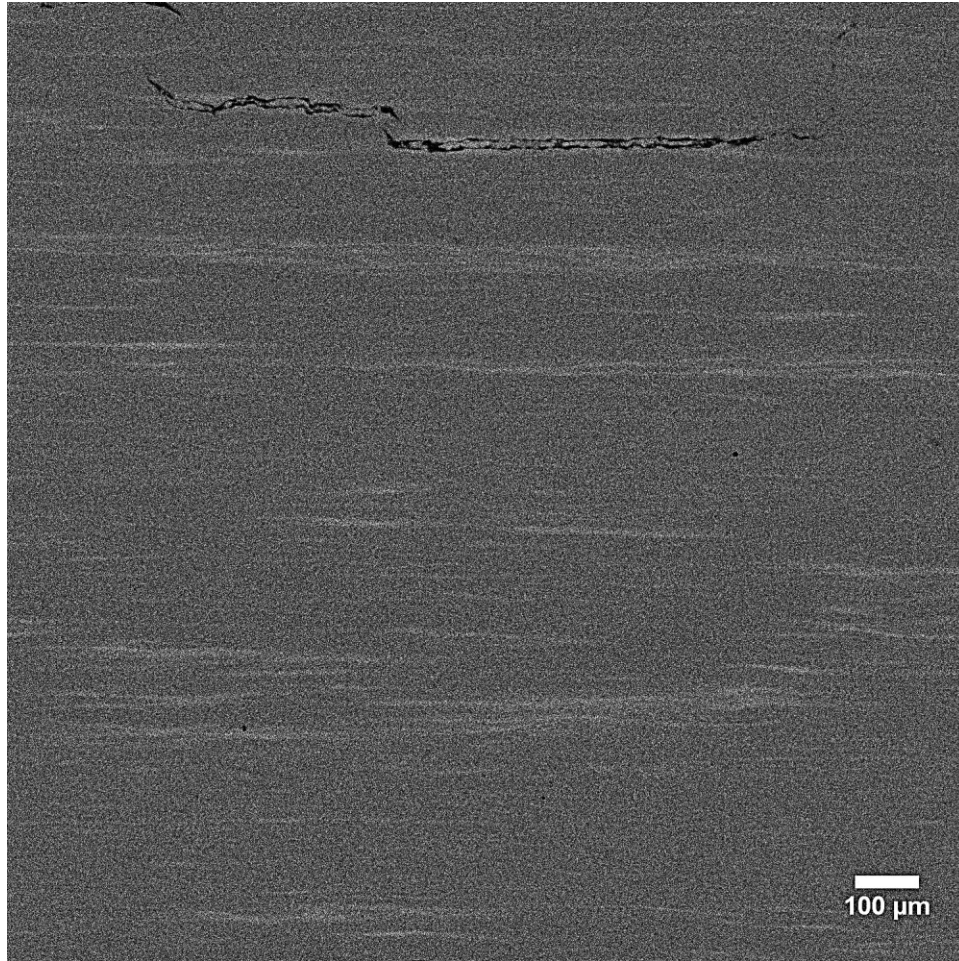


Figure 4.35: Cr EMPA X-ray map of the same area shown in Figure 4.33 (b).

Figure 4.36 is a P X-ray map of the same area shown in Figure 4.33 (b). The bright zones indicate a higher concentration of P.

Figure 4.36 shows that P segregates mostly around the HIC crack unlike the other investigated alloying elements (Mn, Cr and S), which may explain the appearance of the HIC crack at this specific location of the pipe and which is confirmed later by the concentration profile obtained from the line scans through the crack and the segregation bands.

A P line scan across the centerline band on the as received sample mentioned in Section 4.8.1.1 was also performed to make sure that the high concentration of P around the HIC crack (observed on Figure 4.36) is not due to contamination of HIC cracks during the preparation of the HIC tested samples.



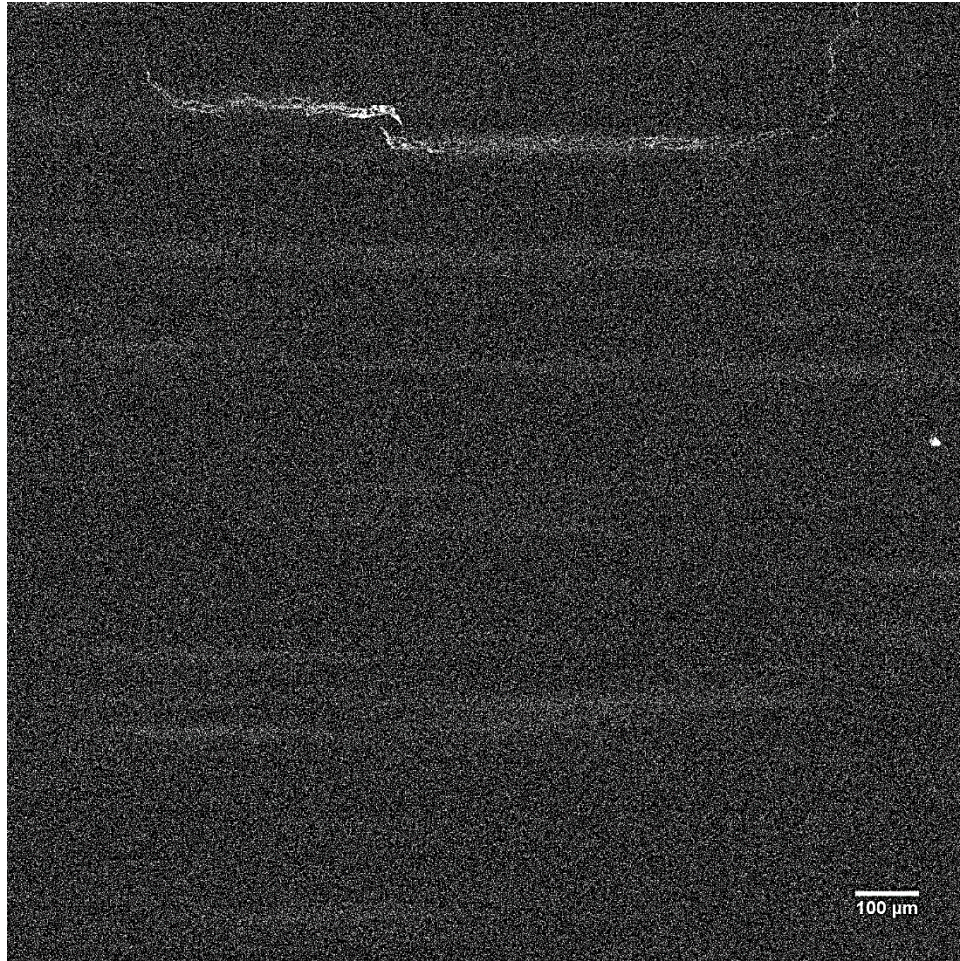


Figure 4.36: P EMPA X-ray map of the same area shown in Figure 4.33 (b).

## 4.8.2. EMPA Line scans

This section shows EMPA line scans generated for Mn and P and performed on an as received sample of High Mo steel across the centerline macro-segregation band. This is followed by EMPA line scans generated for Mn, Si, Cr and P and performed on a HIC tested sample of High Mo steel across the HIC crack.

### 4.8.2.1. As received sample

An EMPA line scan was performed across the centerline segregation band revealed in Figure 4.31 in order to measure the concentration profiles of Mn and P across this segregation band. The location of this line scan is shown in Figure 4.37 (dashed arrow).

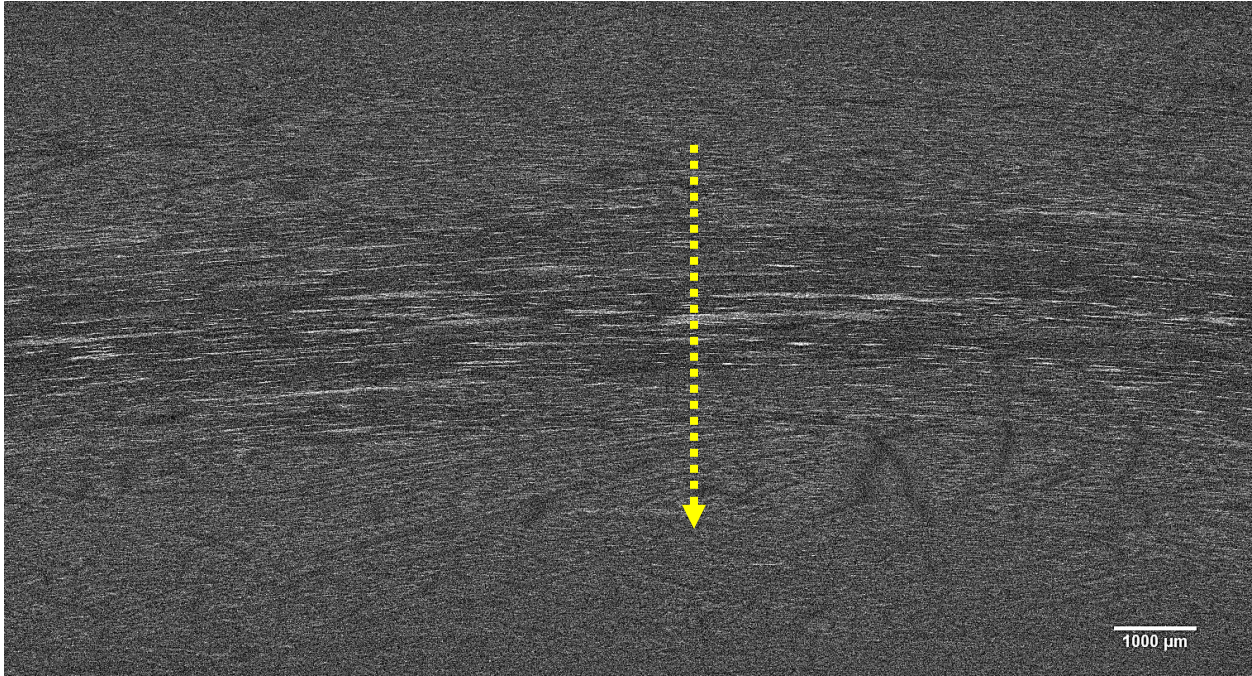


Figure 4.37: Location of the line scan on the Mn EMPA X-ray map of a High Mo as received sample.

Figure 4.38 shows the Mn concentration profile obtained along the line scan shown in Figure 4.37. There are various closely spaced concentration peaks of Mn (between 8 and 9 wt%) observed across the Mn concentration profile, which makes the Mn concentration profile look flat.

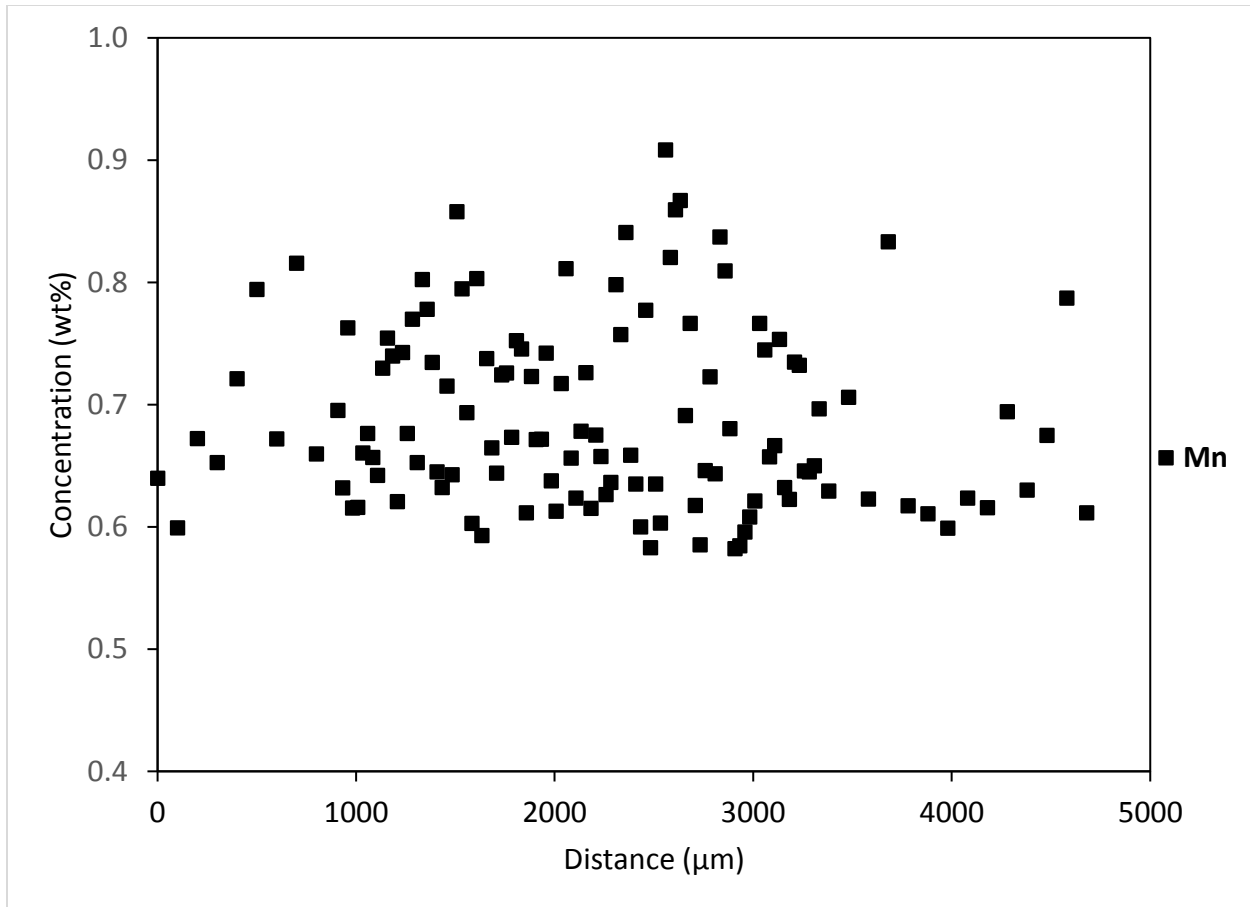


Figure 4.38: Mn concentration profile along the line scan shown in Figure 4.37.

Figure 4.39 shows the P concentration profile obtained along the line scan shown in Figure 4.37. Unlike the Mn concentration profile, the P concentration profile shows clearly one P concentration peak (i.e., 0.059 wt%) at the center of the line scan. This suggests that P segregates at a specific location in the centerline segregation band of the pipe while Mn segregates all over this band. This confirms that the detected high concentration of P around the HIC crack in Figure 4.36 does not come from contamination but from the segregation of P during continuous casting.

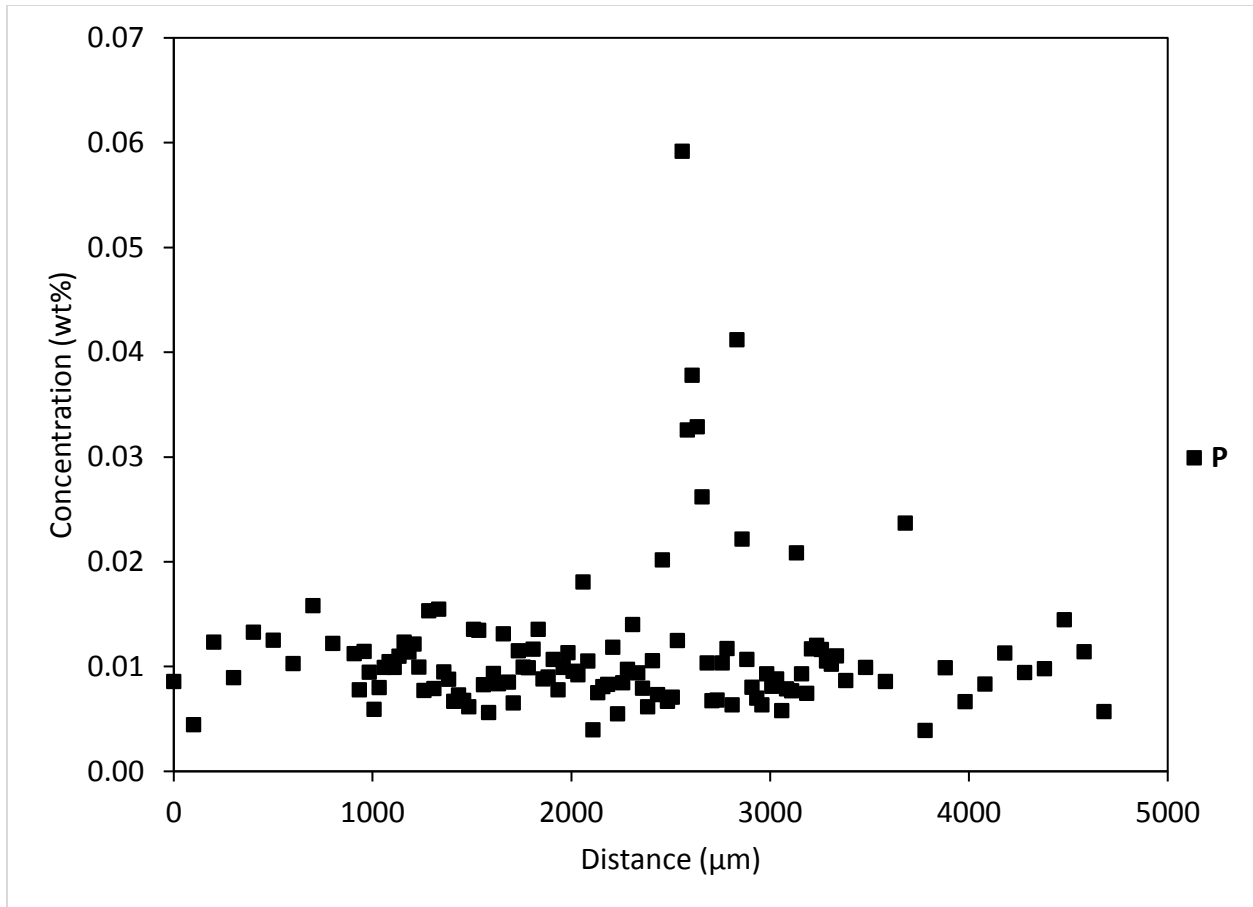


Figure 4.39: P concentration profile along the line scan shown in Figure 4.37.

#### 4.8.2.2. HIC tested samples

Mn, Cr, Si and P line scans were performed on a High Mo sample showing a long HIC crack at the center in order to quantify the extent of segregation of these elements across the HIC crack. Two identical line scans were performed as shown in Figure 4.40 (line 1 and line 2). The inclusions and large precipitates were avoided during setting up the line scans in order to measure the concentration of the above mentioned elements in solid solution.

For sake of simplicity, the HIC crack shown in Figure 4.40 will be designated by the letter C. The segregation band located below the HIC crack will be designated by the letter B.

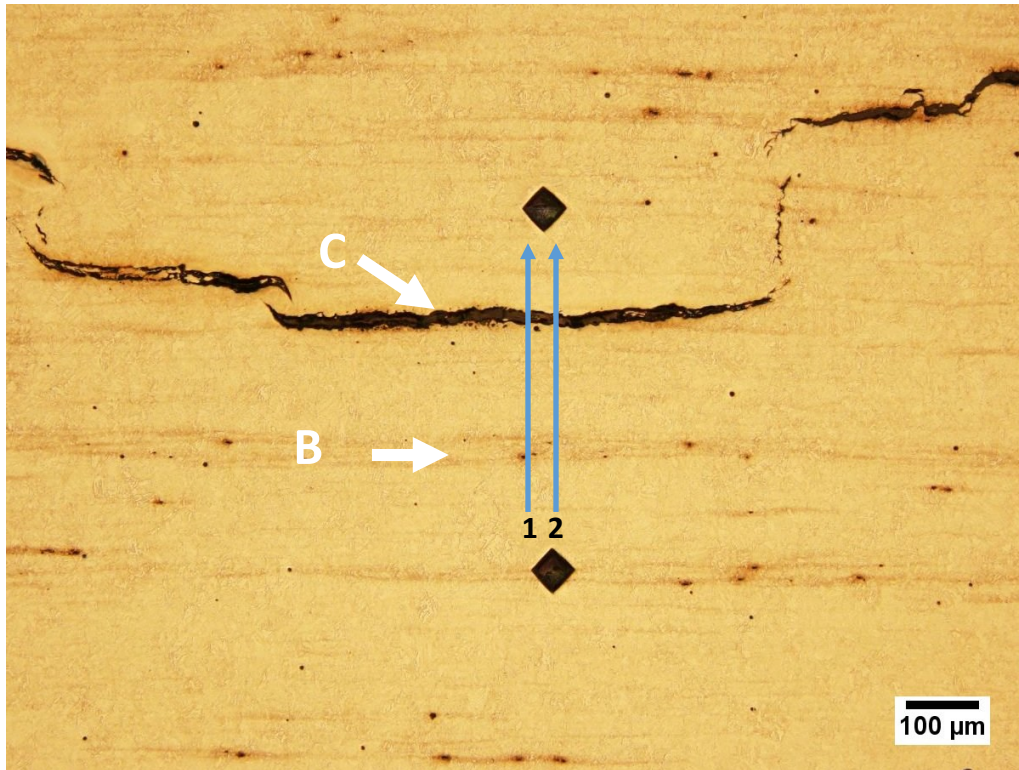


Figure 4.40: Location of the line scans on the optical micrograph of High Mo sample.

Figure 4.41 shows the Mn concentration profile obtained along the line scans 1 and 2 shown in Figure 4.40. The concentration peak of Mn at the segregation band B (i.e., 1.06 wt%) is higher than the concentration peak of Mn around the HIC crack (i.e., 0.84 wt%), which is expected. Figure 4.33 (b) shows that the HIC crack C contains larger MnS inclusions than the segregation band B. The amount of Mn in solid solution around the HIC crack C is then expected to be lower than the amount of Mn in solid solution in the segregation band B.

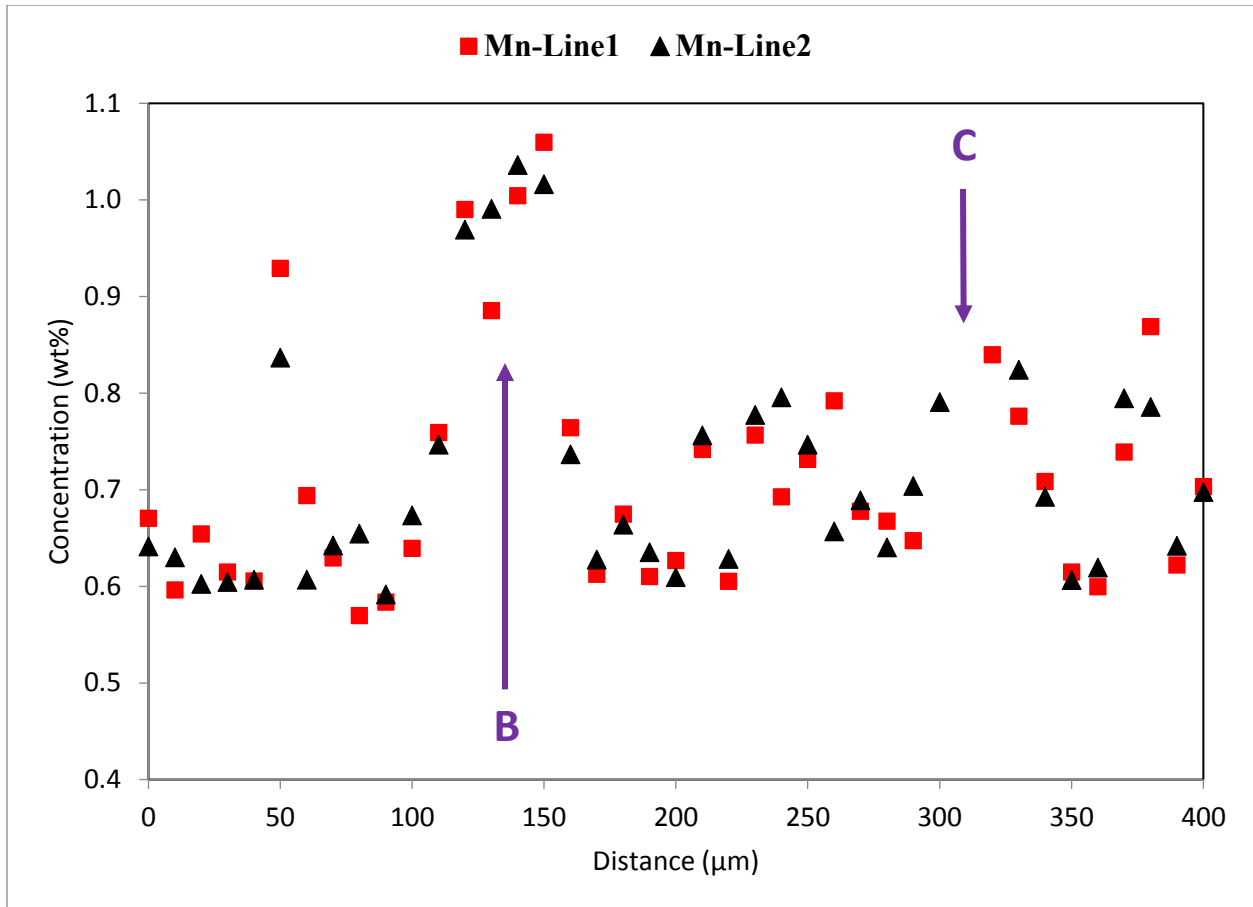


Figure 4.41: Mn concentration profile along the line scans 1 and 2 shown in Figure 4.40.

In order to compare between the degrees of segregation of the different alloying elements (Mn, Cr, Si and P) and due to the differences between the concentrations of these elements, the segregation ratio was calculated as the maximum concentration (wt%) of an element at a given position divided by the baseline concentration (wt%) of the same element.

Figure 4.42 shows the variation of the segregation ratios of Mn, Cr and Si along the line scans 1 and 2 (shown in Figure 4.40). The segregation ratios of Mn, Cr and Si at a given position are similar. Two concentration peaks are found: a 1<sup>st</sup> peak between 120 and 150 μm at the segregation band B and a 2<sup>nd</sup> peak at 310 μm around the HIC crack C. The peak around the crack C is obviously lower than the peak at the segregation band B, which suggests that the segregation of Mn, Cr and Si does not play a significant role in the propagation of HIC cracks.

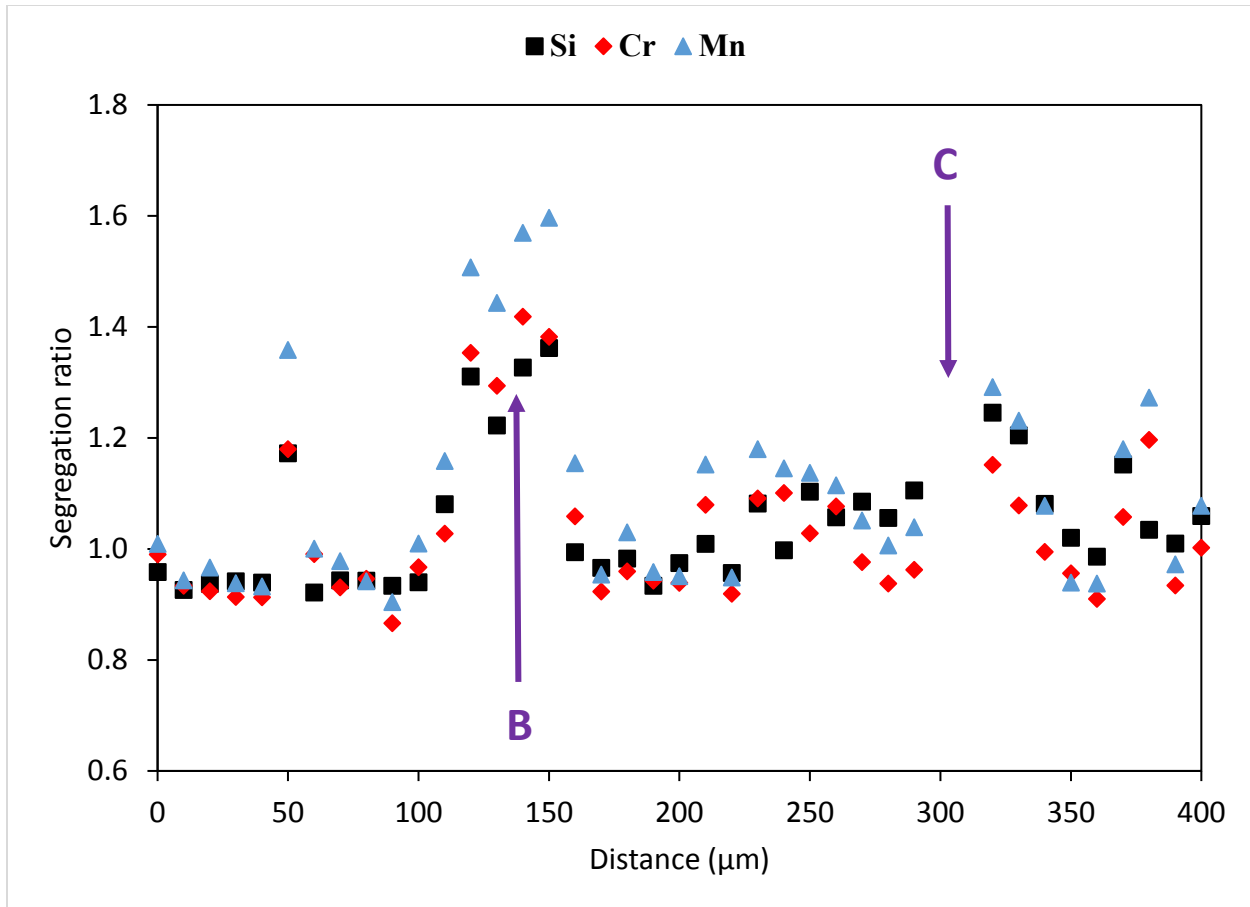


Figure 4.42: Variation of segregation ratios of Mn, Cr and Si along the line scans 1 and 2 shown on Figure 4.40.

Figure 4.43 shows the variation of the segregation ratio of P along the line scans 1 and 2 shown in Figure 4.40. Unlike Mn, Cr and Si, the concentration peak of P around the HIC crack C is higher than its concentration peak at the segregation band B. In fact, the EMPA measured concentration of P around the HIC crack C (i.e., 0.047 wt%) is about 6 times higher than the EMPA measured baseline concentration of P (i.e., 0.008 wt%). This increase in P concentration around the HIC crack does not come from contamination because a similar increase in the P concentration was measured in the center of an as received sample as seen in Figure 4.39.

The appearance of the HIC crack at the location where there is a significant increase in the P concentration suggests the role of P in the HIC crack propagation, which will be discussed in detail in Section 5.4.

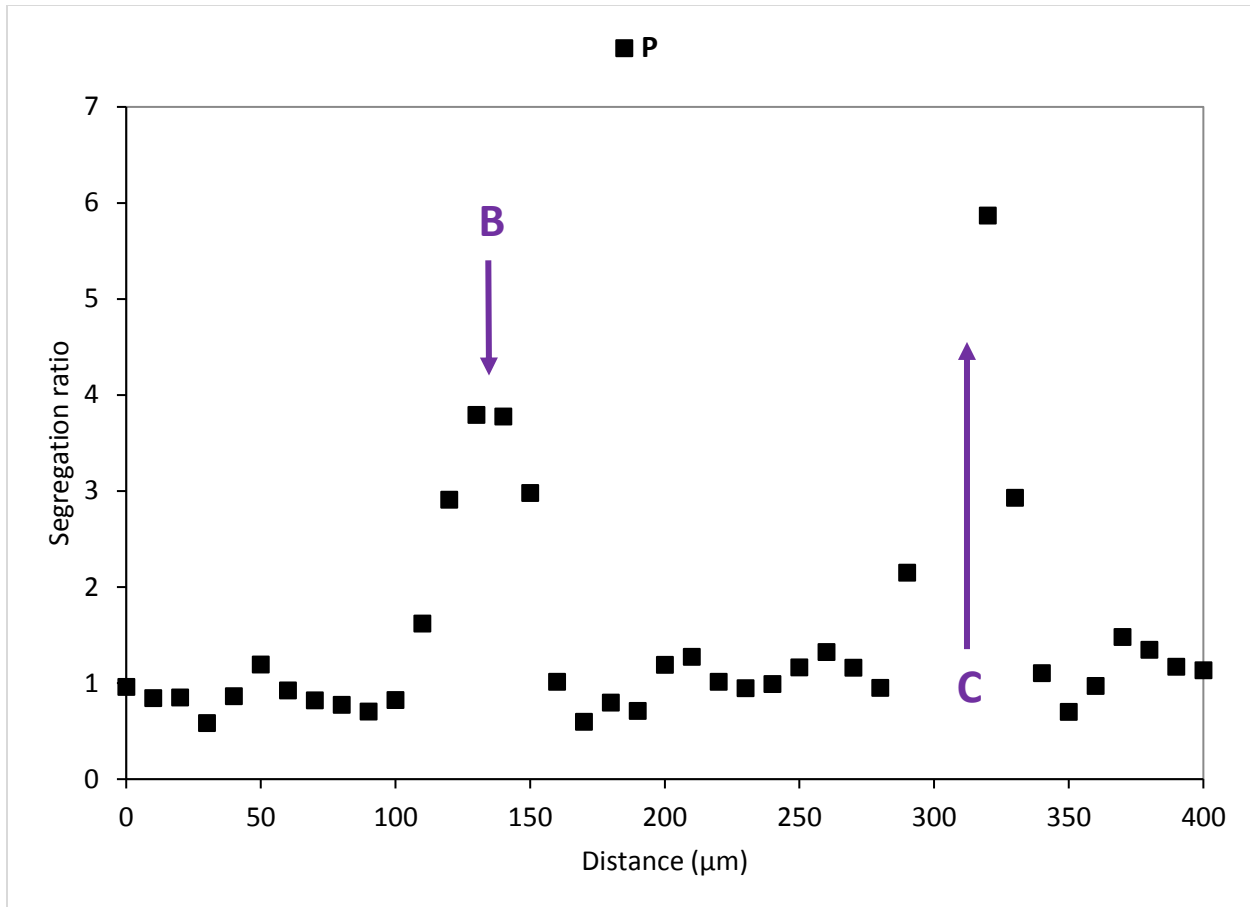


Figure 4.43: Variation of the segregation ratio of P along the line scans 1 and 2 shown on Figure 4.40.

## 4.9. Summary

The main findings of this chapter are:

1. High Mo and TiB steels are the most susceptible steels to HIC whereas SMLS steel is the most resistant to HIC. The HIC susceptibility decreases in the following order: High Mo, TiB, High Mn, MnCr and SMLS steels.
2. The HIC cracks are located mainly in the center of the HIC tested samples.
3. Long manganese sulfide inclusions (>100 μm) are found in the opened HIC cracks fracture surfaces.
4. All L80 steels are highly susceptible to SSC. In terms of RAR, SMLS steel is the most susceptible to SSC while High Mo steel is the least susceptible to SSC. The SSC susceptibility increases in the following order: High Mo, MnCr, High Mn, TiB and SMLS steels.



5. During SSRT tests performed in H<sub>2</sub>S saturated environment, SSC cracks initiate from corrosion pits located at the surface of the SSRT sample and propagate in a brittle manner to the center of the sample. A cluster of globular inclusions is found near to the origin of the SSC crack in TiB steel.
6. High Mo steel contains the highest number of elongated MnS inclusions. The length of MnS goes up to 250 μm.
7. EMPA mapping and line scanning showed an enrichment of the area around the HIC in alloying elements Mn, Si, Cr and P. For High Mo steel, the concentration of P around the HIC crack is about 6 times higher than the baseline concentration while the concentrations of Mn, Si and Cr are about 1.2 times higher than their baseline concentrations.

## Chapter 5 Discussion

The previous chapter has presented the HIC results, the SSRT results, qualitative and quantitative analysis of inclusions in all L80 steels studied and centerline macro-segregation study results.

This chapter will begin with a discussion of the precipitation of MnS inclusions in L80 steels. This is followed by a study of the role of inclusions especially MnS inclusions, Al enriched inclusions and Ti nitrides in the initiation and the propagation of HIC and SSC cracks. Finally, the role of centerline macro-segregation of Mn, Si, Cr and P in the propagation of HIC cracks will be discussed.

### 5.1. Precipitation of Manganese sulfide (MnS) inclusions in L80 steel

This section begins with a study of the effect of Mn and S contents on the formation of MnS inclusions in L80 steel. Thermodynamic calculations are performed to predict the formation of MnS inclusions in the different L80 steels studied and compared with the experimental results.

#### 5.1.1. Effect of Mn and S contents on MnS number and length

MnS inclusions are known to precipitate preferentially in interdendritic liquid during solidification, due to the segregation of Mn and S. MnS inclusion is thermodynamically stable when the concentration product (K) is larger than the solubility product (K<sub>eq</sub>) [118].

$$\log K_{eq} = \frac{-8750}{T} + 4.68 \quad (5.1)$$

$$K = [S][Mn] \quad (5.2)$$

where T is the temperature in K, [S] is the concentration of S in liquid in wt% and [Mn] is the concentration of Mn in liquid in wt% [118].

Hence, in addition to the cooling rate, the concentration of Mn and S are important factors for MnS formation.

Figure 5.1 plots the number and total length of MnS inclusions in L80 steels as a function of the nominal concentration product [Mn][S]. Both the number and the length of MnS increase with an increasing nominal concentration product [Mn][S].

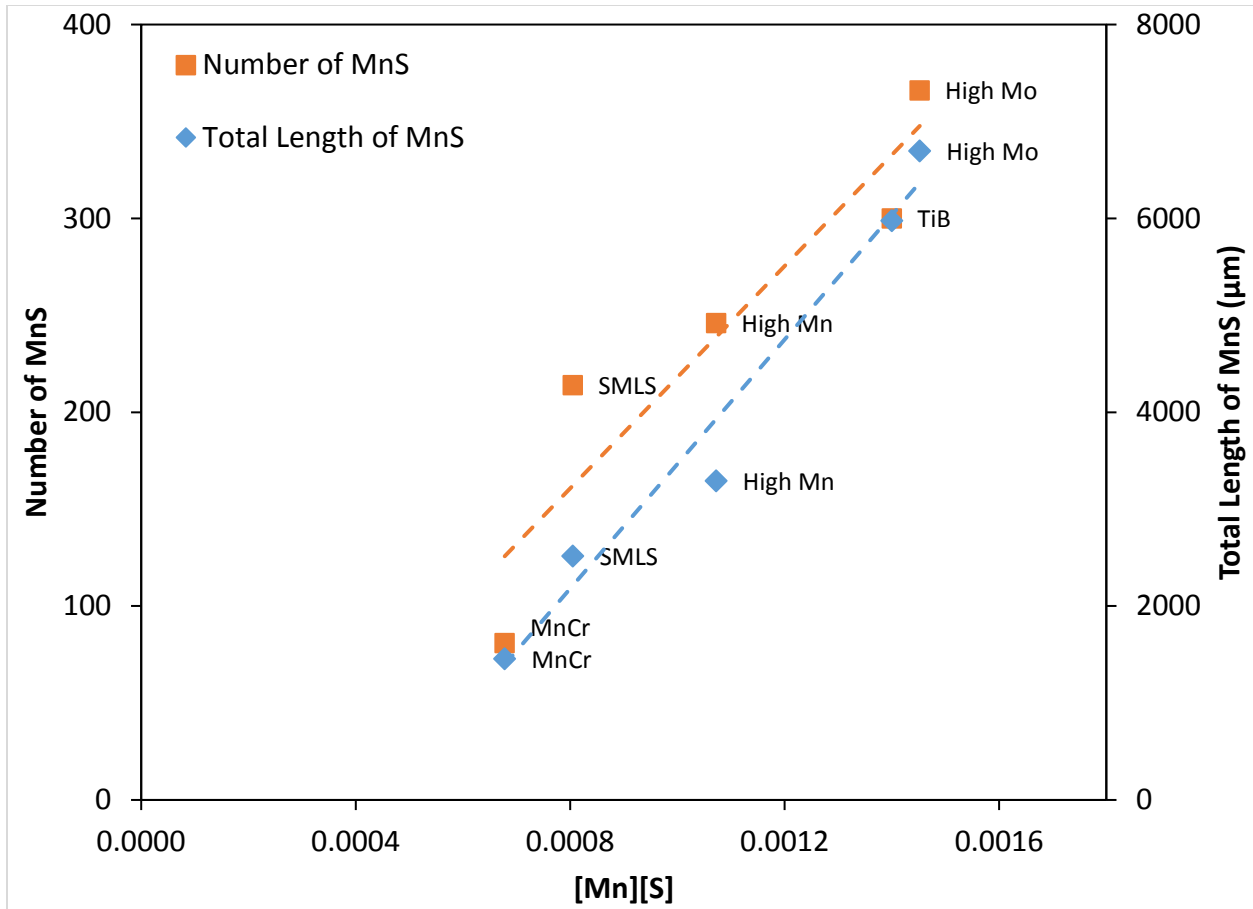


Figure 5.1: Effect of  $[Mn][S]$  on number and total length of MnS inclusions (the trends are shown by the dashed lines connecting the data points).

### 5.1.2. Thermodynamic calculations

In order to explain the trend shown in Figure 5.1, the level of segregation of Mn and S in residual liquid during solidification in different L80 steels studied was assessed by computational thermodynamics using the Scheil-Gulliver model.

Scheil-Gulliver calculations are qualitative since the Scheil equation considers no diffusion in the solid, infinite diffusion in the liquid and thermodynamic equilibrium at the moving interface described by the equilibrium partition coefficient  $k$ . Although these assumptions are a simplification of actual conditions in continuous casting, the calculation provides trends for different steel chemistries [119].

Thermo-Calc software and TCFE8 database were used in these calculations. The nominal concentrations of the main alloying elements (Mn, S, C, Cr, P and C) were the input values. The

output values were the segregated concentrations of Mn and S in the liquid during solidification. The product of the concentrations of Mn and S in liquid was calculated and plotted against the temperature as shown in Figure 5.2.

Figure 5.2 shows that High Mo steel is the first steel to reach the solubility curve (i.e., 1428°C), which promotes nucleation and growth of MnS precipitates. This prediction matches well with the experimental result shown in Figure 5.1.

For High Mo and TiB steels, MnS inclusions start to precipitate in the liquid during the last stages of the solidification (i.e.,  $L + \delta \rightarrow L + \gamma$ ), which is consistent with the experimental observation of large MnS inclusions mainly at the centerline region of the pipe sample (Appendix H).

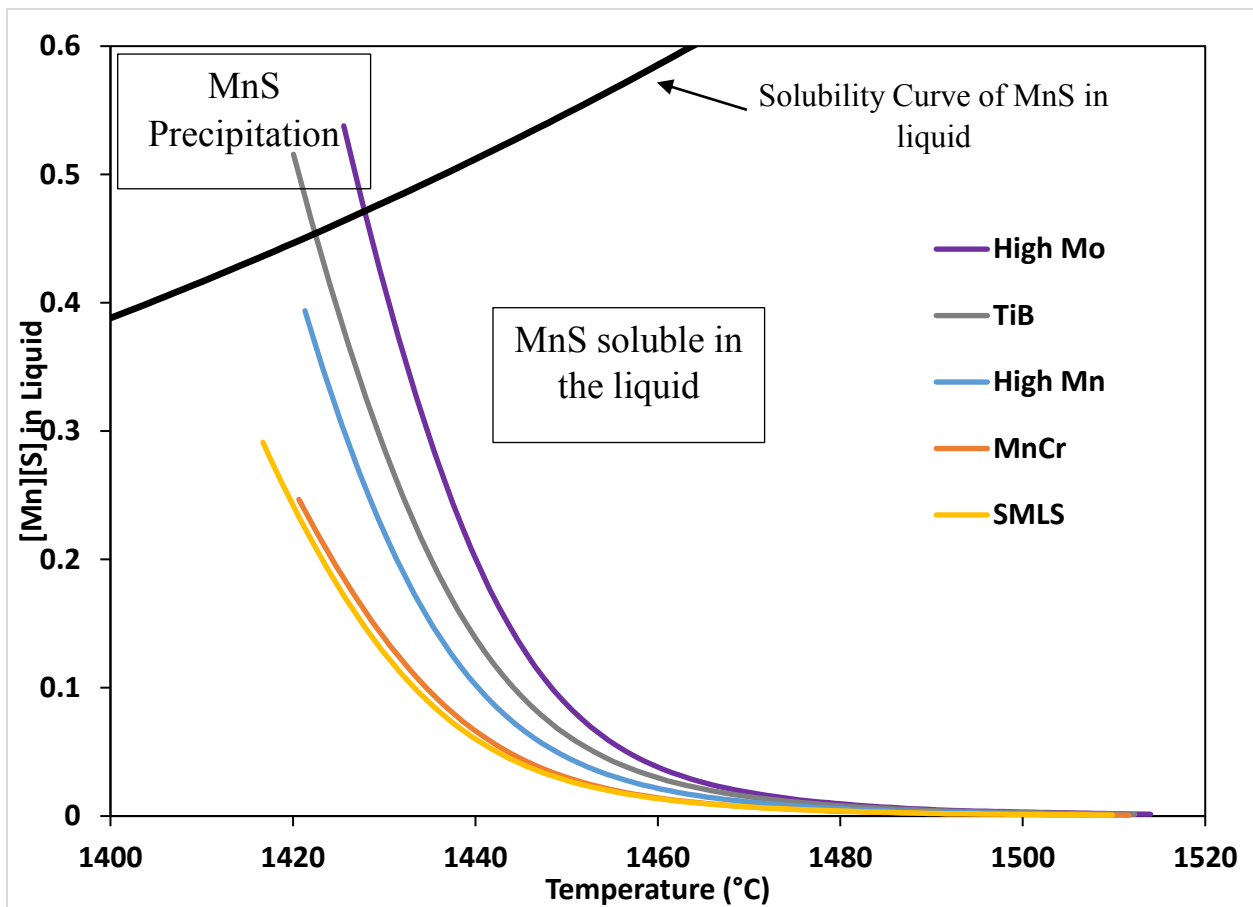


Figure 5.2: Prediction of MnS inclusions precipitation using the Scheil-Gulliver model (Thermo-Calc).

## 5.2. Role of inclusions in HIC

Previous investigations have shown that HIC nucleates from nonmetallic inclusions [42,59,60,62,120–124]. Clusters of alumina [59,60,94,122] as well as coarse TiN precipitates ( $>1\ \mu\text{m}$ ) [123,124] are reported to be associated with HIC cracks. The elongated MnS are reported as the most susceptible sites due to their sharp ends [42,120,121].

The effect of these inclusions (i.e., MnS, Al enriched and TiN inclusions) on the resistance of L80 steel to HIC is investigated in this section. Firstly, the role of MnS inclusions in initiation of HIC cracks will be discussed. Secondly, the role of Al enriched inclusions and Ti nitrides in initiation of HIC cracks will be discussed. Finally, the susceptibility of these different types of inclusions to HIC cracks will be compared.

### 5.2.1. Role of MnS inclusions

Fractographs of opened HIC cracks in the most susceptible steels High Mo and TiB presented in Section 4.3.3 show clearly that very elongated MnS inclusions ( $> 100\ \mu\text{m}$ ) are located inside the HIC cracks. In addition, all the HIC cracks observed in L80 ERW steels (i.e., High Mo, TiB, High Mn, MnCr steels) are located approximately at mid thickness of the pipe samples, where MnS inclusions are mainly formed.

These two observations suggest that elongated MnS inclusions are the main nucleation sites for HIC cracks in L80 steel, which is consistent with the literature [42,120,121]. This is mainly due to two properties of MnS inclusions that are related to the Fe-MnS interface and their shape. The effect of these two properties on HIC initiation will be discussed in detail below.

MnS has a larger coefficient of thermal expansion than the steel matrix as shown in Table 5.1. Thus, MnS inclusions will tend to contract in volume much more on cooling than the surrounding steel matrix. Such shrinkage will lead to the formation of voids at the MnS-steel matrix interface, which results in the accumulation of hydrogen at this interface.

MnS inclusions are significantly more deformable than other inclusion types, so they elongate to larger sizes in the rolling direction (e.g., the length of MnS inclusions in High Mo steel goes up to  $250\ \mu\text{m}$  while the diameter of other inclusions goes up to  $35\ \mu\text{m}$ ). Therefore, if a crack nucleates around these elongated inclusions, the resulting stress concentration will be more severe than for smaller globular inclusions such as Al enriched oxides [125].

Therefore, under these conditions, a high concentration of hydrogen can accumulate at the voids between MnS inclusions and the steel matrix. Subsequently the hydrogen recombines to form hydrogen gas. When the hydrogen gas pressure in these voids is sufficiently high, the stress imposed by the hydrogen on the steel matrix will be high due to the stress concentration at the tip of the MnS inclusion. Thus, cracks can develop around the MnS inclusions [90,126,127].

Table 5.1: Mean coefficients of linear expansion of steel matrix and different inclusions [127].

<b>Material</b>	<b>Mean coefficient of thermal expansion <math>\alpha</math> (<math>\times 10^{-6}</math>) per <math>^{\circ}\text{C}</math></b>
Steel matrix	12.5
MnS	18.1
TiN	9.4
Al <sub>2</sub> O <sub>3</sub>	8
MnO.Al <sub>2</sub> O <sub>3</sub>	8
MgO.Al <sub>2</sub> O <sub>3</sub>	8.4

Variables including the amount, the length and the distribution of MnS inclusions are reported to play a significant role in HIC initiation and propagation [120]. Therefore, the effect of the amount and the length of MnS on the susceptibility of L80 steel to HIC are investigated in the two following sections 5.2.1.1 and 5.2.1.2.

### 5.2.1.1. Effect of the number of MnS

Figure 5.3 shows CLR and CSR as a function of the number of MnS counted on the same surface area per sample (i.e., 35.2 mm<sup>2</sup>). The dashed line is drawn to emphasize the trend in the data. As the number of MnS inclusions increases, CLR and CSR increase and hence the susceptibility of L80 steel to HIC increases which is consistent with literature [42,120,121,128]. Huang et al. found that an increase in the amount of inclusions results in an increase in the hydrogen trapping efficiency and hence makes the steel more susceptible to HIC [121].

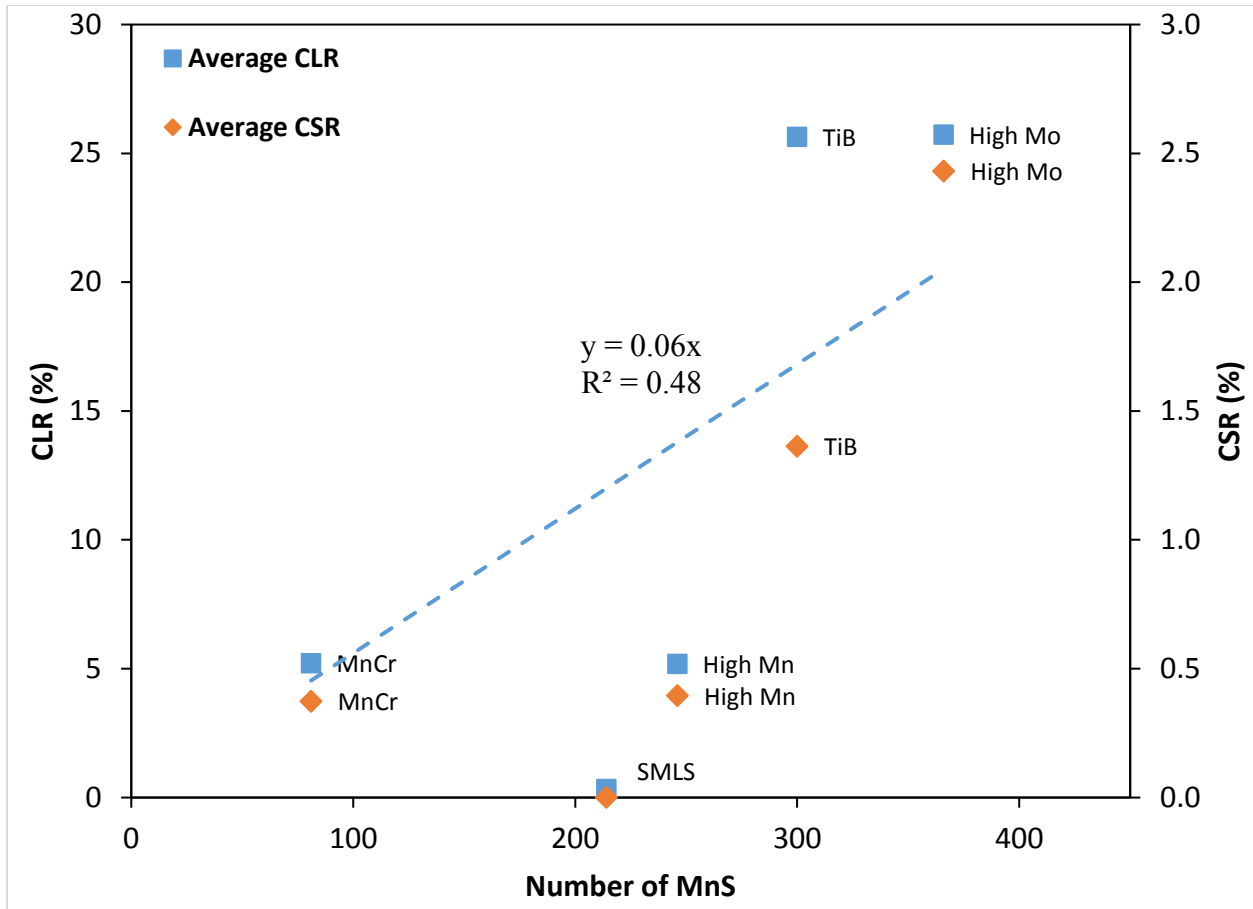


Figure 5.3: Effect of number of MnS inclusions on HIC resistance.

### 5.2.1.2. Effect of the length of MnS

Fractographs of the opened HIC cracks in the most susceptible steels (i.e., High Mo and TiB steels) presented in Chapter 4 shows that the minimum length of the inclusions present in these cracks is about 100  $\mu\text{m}$ , which suggests that the longest MnS inclusions are more harmful than the shortest ones.

Figure 5.4 plots CLR and CSR as a function of the maximum length of MnS inclusions in the studied L80 steels. It is clear that High Mo and TiB steels that have the longest MnS inclusions exhibit the highest values of CLR and CSR, which is in good agreement with literature [2, 3].

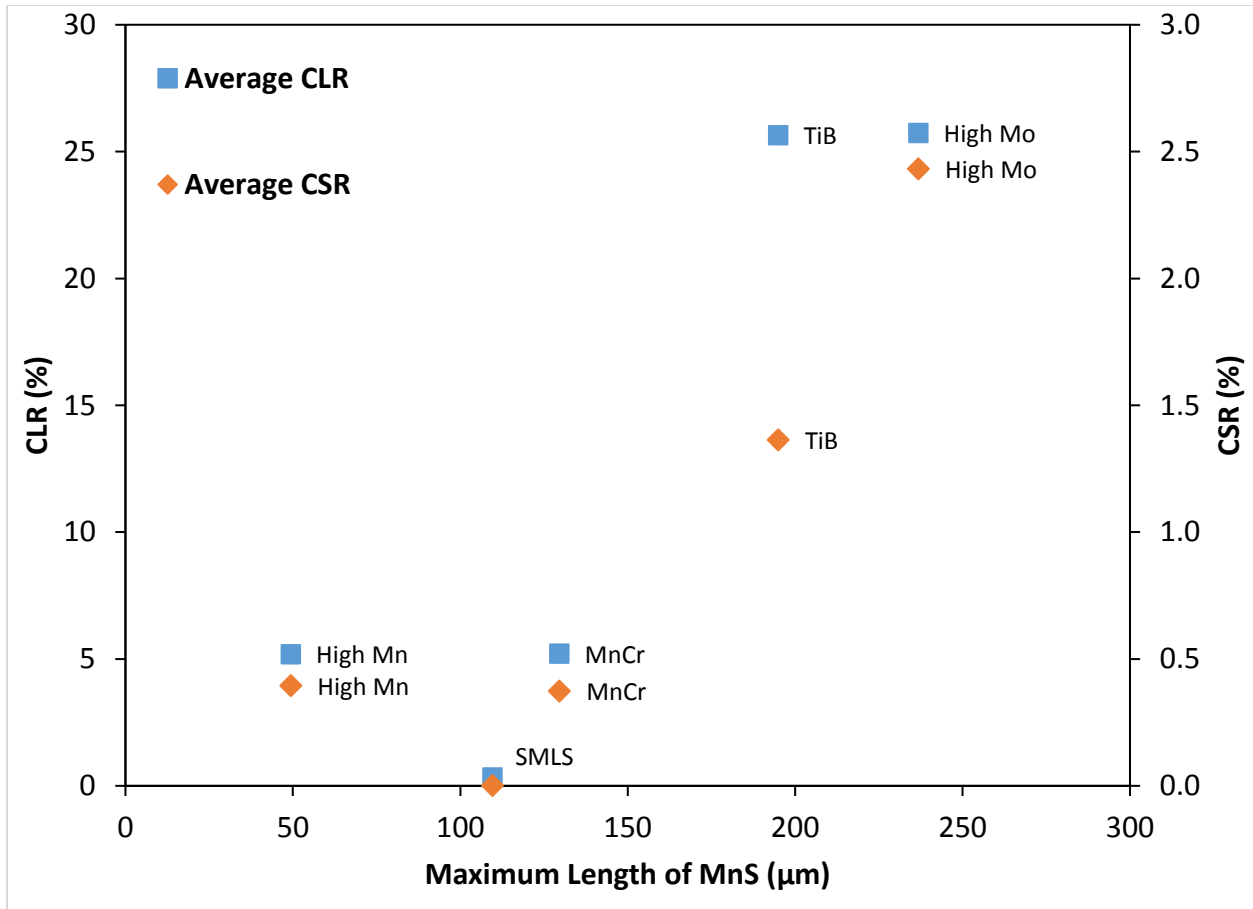


Figure 5.4: Effect of maximum length of MnS on HIC resistance.

### 5.2.2. Role of Al enriched and TiN inclusions

Figure 5.5 plots CLR and CSR as a function of the number of all inclusions present in L80 steel except the MnS inclusions (i.e., Al enriched inclusions in High Mo, High Mn, MnCr and SMLS steels and Al enriched and TiN inclusions in TiB steel). A correlation can be seen between CLR or CSR and the number of these inclusions for all L80 ERW steels, which suggest that Al enriched inclusions and Ti nitrides play a role in HIC (consistent with literature [59,60,94,122]). However, the HIC crack does not seem to initiate initially from Al enriched inclusions. SMLS has a low CLR ( $\approx 0.3\%$ ) although it contains Al enriched inclusions. Therefore, HIC cracks can initiate from Al enriched inclusions. But HIC cracks initiate mainly from MnS inclusions. Then clusters of alumina inclusions located around the MnS inclusions will help the HIC crack to propagate.



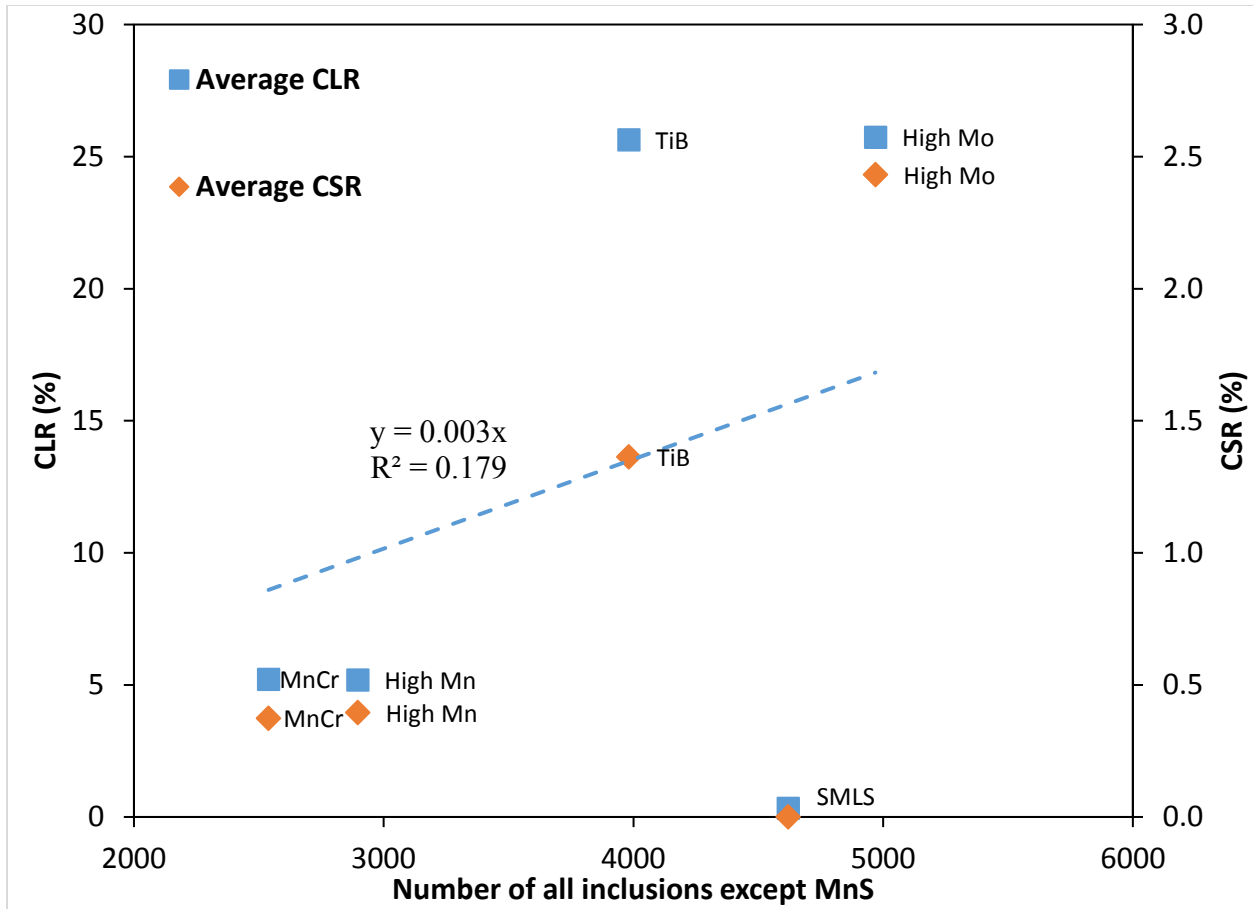


Figure 5.5: Effect of Al enriched and TiN inclusions on HIC resistance.

### 5.2.3. Susceptibility of different inclusions to HIC

The susceptibility of different types of inclusions (i.e., MnS, Al enriched and TiN inclusions) to HIC can be evaluated based on the slope of the linear relationship between CLR and number of inclusions in Figure 5.3 and Figure 5.5.

The slope of the linear relationship between CLR and number of MnS (Figure 5.3) is higher than the slope of the linear relationship between CLR and number of other types of inclusions (Figure 5.5). It can be concluded that MnS inclusions are therefore more susceptible to HIC than Al enriched and TiN inclusions.

Thus, MnS inclusions located at the centerline of the L80 pipe samples are the main nucleation sites of HIC cracks. The HIC resistance is further affected by the presence of clusters of Al enriched inclusions at the centerline.

### 5.3. Role of inclusions in SSC

The SSC susceptibility of L80 steel was evaluated using the SSRT test. In chapter 4, it was found that the SSC cracks initiate from corrosion pits that form at the surface of the SSRT sample and that these cracks propagate afterwards normal to the applied tensile stress until fracture of the sample. In this section, the effect of various types of inclusions present in L80 steel on SSC propagation will be discussed. The effect of the different inclusions on initiation of SSC cracks will be also discussed.

#### 5.3.1. Effect of toughness anisotropy on SSC propagation

Regarding SSC crack initiation, all inclusions play a detrimental role regardless of their chemical type because all of them offer surface discontinuities for corrosion pits to develop [129–133]. These issues will be discussed further in Section 5.3.2 and 5.3.3.

However, during SSC cracks propagation, inclusions may have different effects depending on their orientation as described below [63]. For example, due to their slender shape in the rolling direction, MnS inclusions have different influences on the fracture toughness depending on whether the loading is applied in the longitudinal direction, or in the transverse direction [63,134]. Furthermore, due to their high deformability, MnS inclusions improve the fracture toughness when the crack propagation direction is perpendicular to the elongated direction of the MnS inclusions as shown in Figure 5.6 [63,134]. However, due to their sharp edges, MnS inclusions are detrimental when the crack propagation direction is parallel to the elongated direction of the MnS inclusions [63,134].

During this work, SSRT tests were performed in the longitudinal direction as presented in Figure 5.6. Thus, when the SSC crack is initiated from an inclusion of any type located at the surface of the SSRT sample (as observed in Section 4.6.2), MnS inclusions located at the centerline inside the SSRT sample can arrest the SSC crack propagation. Therefore, MnS inclusions may in some instances impede the propagation of SSC cracks during SSRT tests, which will be discussed in Section 5.3.2. The HIC microcracks that were observed on the fracture surface of an SSRT sample (Figure 4.21(a)) and that may have initiated from MnS inclusions are also responsible for the fracture toughening. To summarize, the MnS inclusions when they are oriented parallel the

applied load and the HIC cracks that initiate from these inclusions may impede the propagation of the SSC crack.

Due to their shape isotropy, alumina or nitrides inclusions have the same effect on toughness regardless of the orientation of the sample. Unlike MnS inclusions which are soft inclusions, alumina and nitrides inclusions are reported as hard inclusions with low deformability, which lowers the fracture toughness of the steel and which enhances SSC propagation [135,136]. This detrimental effect will be discussed in Section 5.3.3.

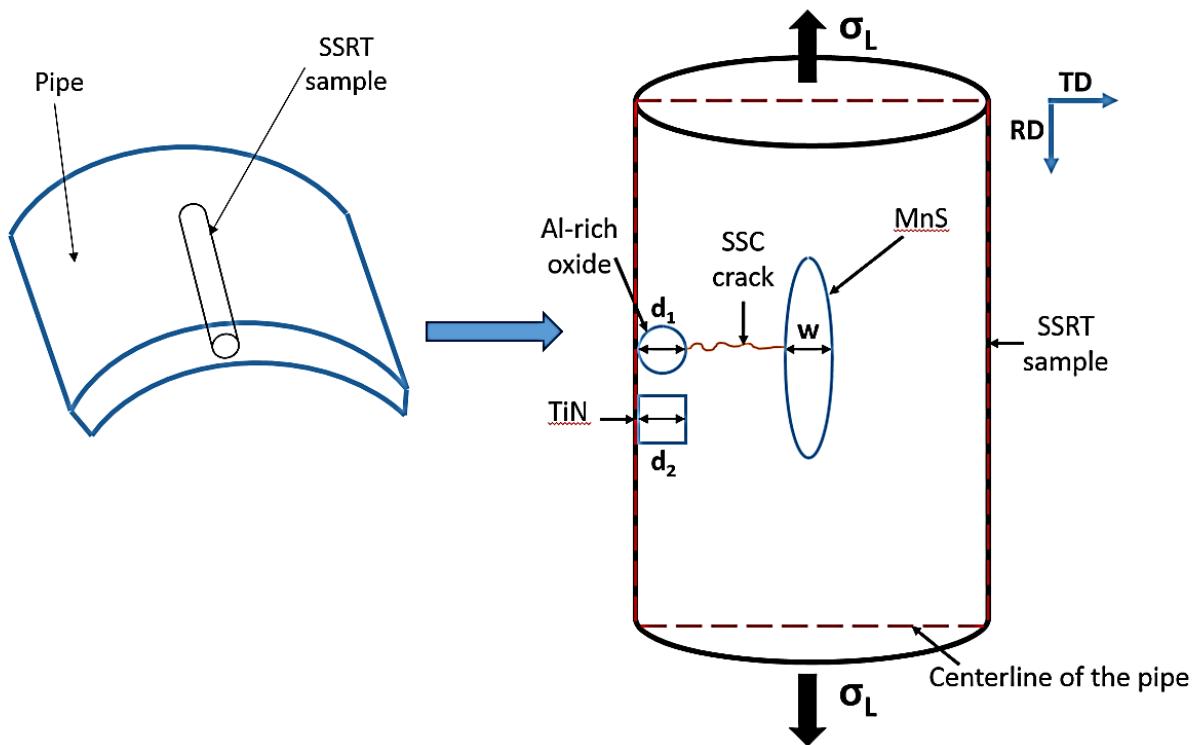


Figure 5.6: Schema of orientation of different types of inclusions during SSRT performed in the longitudinal direction for a sample taken from an ERW pipe.

### 5.3.2. Role of MnS inclusions

In section 5.1, Figure 5.1 shows a linear relationship between  $[Mn][S]$  and the total length of MnS. The same figure shows also a linear relationship between  $[Mn][S]$  and the number of MnS inclusions. Therefore, in order to study the effect of MnS inclusions on SSRT tests, one can plot RAR versus  $[Mn][S]$  as shown in Figure 5.7.

A best fit line is generated for the data in Figure 5.7. No clear relationship is found between RAR and MnS inclusions, as evident by the low value of  $R^2$ . This suggests that the role of MnS inclusions in impeding the SSC propagation as described in Section 5.3.1 is less dominant.

In addition, the high susceptibility of SMLS steel to SSC shows that MnS inclusions are not the sole cause of pit initiation and that Al enriched inclusions (see Figure H.6) which are the main inclusions present in SMLS steel may play a significant role in pit initiation (will be discussed in Section 5.3.3). This is in good agreement with literature [63,131,136].

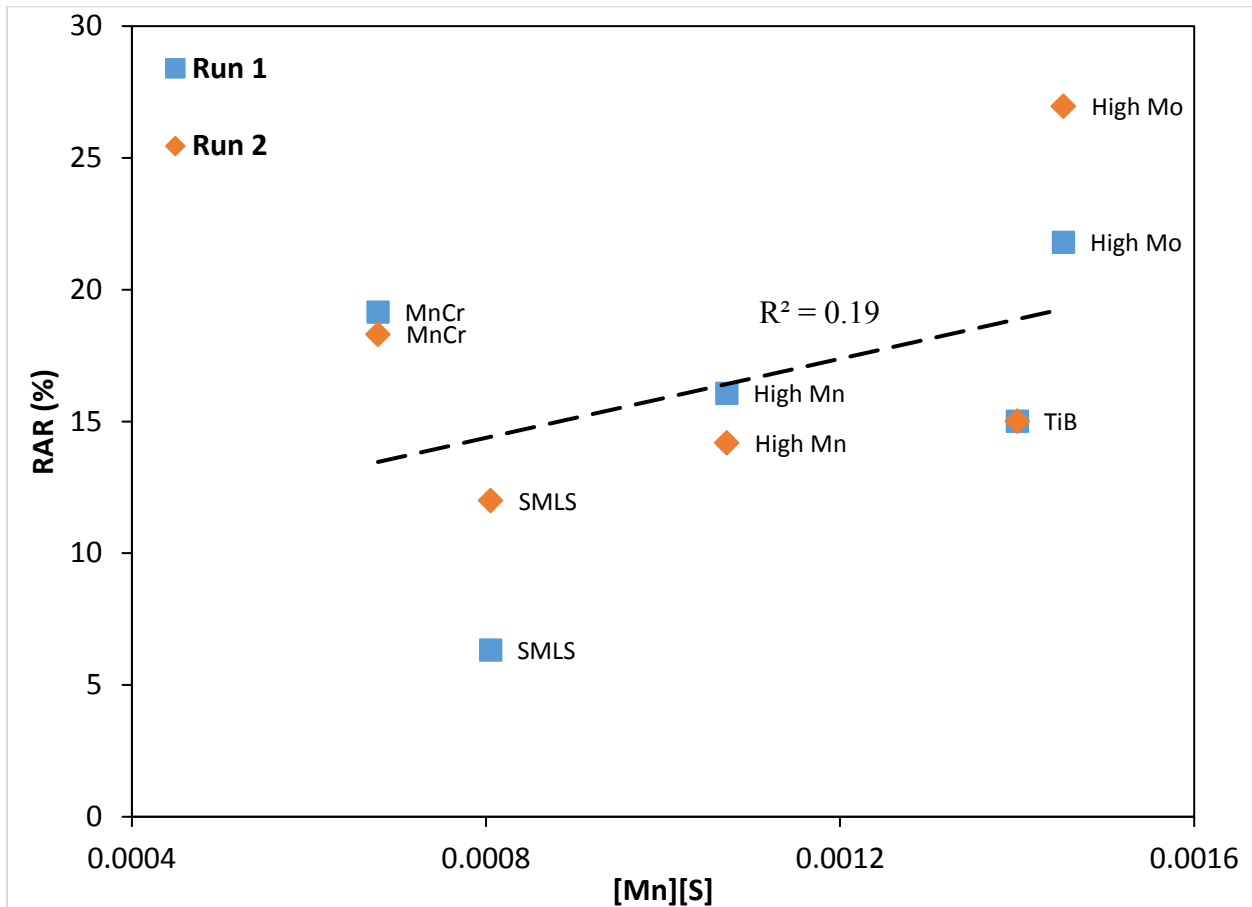


Figure 5.7: Effect of MnS inclusions on RAR.

### 5.3.3. Role of Al enriched and TiN inclusions

Figure 5.8 shows the relationship between RAR and the number of Al enriched and TiN inclusions. An obvious relationship is observed between RAR and the number of these inclusions when High Mo steel is not considered.

Despite having the highest number of Al enriched inclusions, High Mo steel shows the highest values of RAR and hence the lowest susceptibility to SSC. This is mainly due to the beneficial role played by MnS inclusions and by the HIC microcracks generated from these inclusions (described in Section 5.3.1).

For the other steels (i.e., TiB, High Mn, MnCr and SMLS steels), RAR decreases as the number of Al enriched and TiN inclusions increases, which suggests that Al enriched and TiN inclusions are detrimental to SSC initiation and propagation and that this detrimental role is more dominant than the role of MnS inclusions. The detrimental role of Al enriched and TiN inclusions in SSC propagation was described in Section 5.3.1. However, their detrimental role in initiation of SSC cracks will be discussed in detail below.

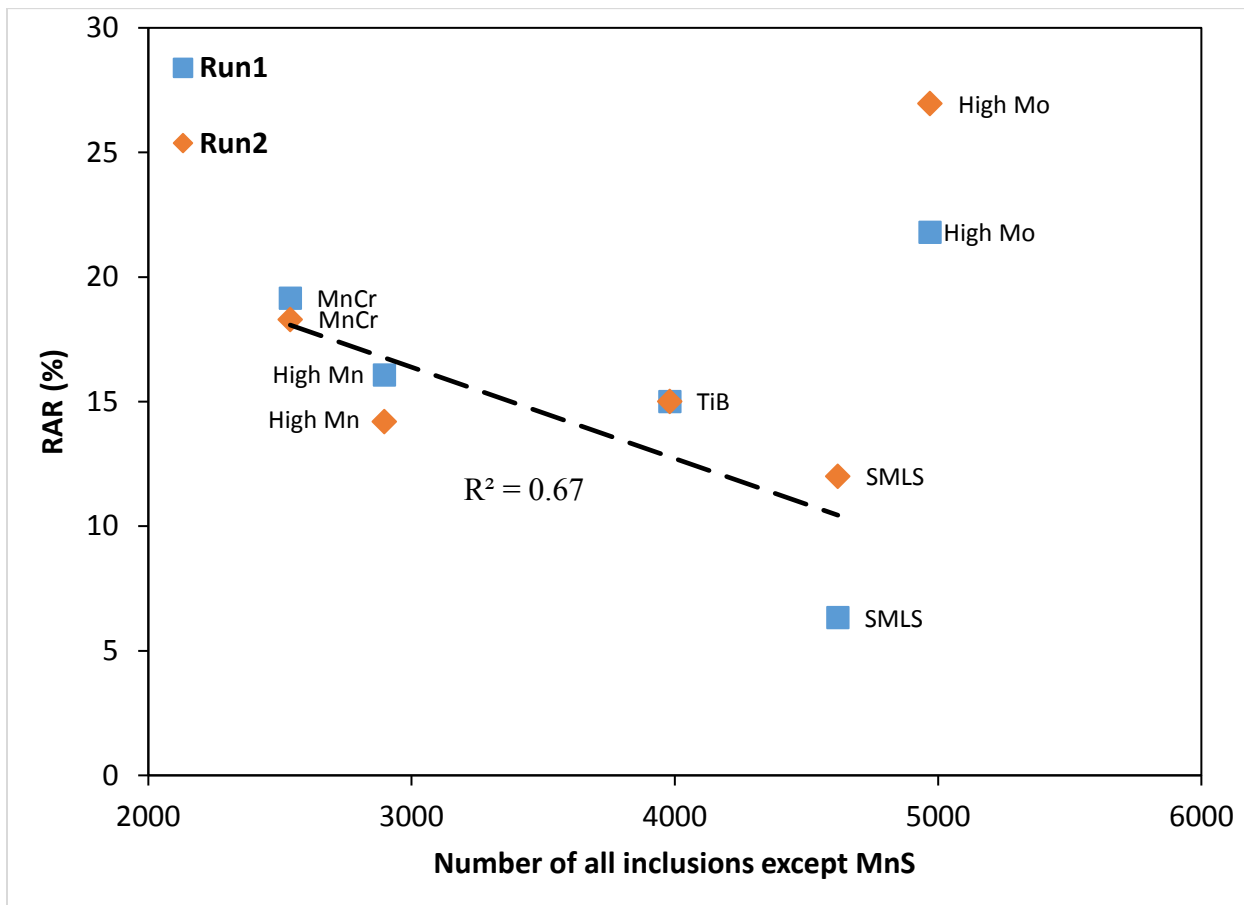


Figure 5.8: Effect of Al enriched and TiN inclusions on RAR.

Corrosion pits at the surface of the SSRT sample are found to be the initiation sites of the SSRT cracks. Pits form usually at inclusions located at the surface of the sample. Corrosion pits are associated with various inclusions including MnS inclusions, alumina, oxy-sulfides and Ti nitrides [131]. For example, pits initiating at a MnS inclusion or at an oxide inclusion such as  $\text{Al}_2\text{O}_3$ , are due to a preferential dissolution of the adjacent steel at the steel/inclusion interface [131]. Therefore, the chemistry does not explain why Al enriched oxides are the preferential sites of initiation of SSC cracks.

However, the number, the distribution and the geometric characteristics of Al enriched oxides can explain this detrimental effect. The following explanation will focus on Al enriched oxides rather than Ti nitrides because Al enriched oxides are the dominant inclusions in all L80 steels.

### **Number**

Figure 5.9 shows the number of MnS inclusions as well as the number of the other inclusions which consist mainly of globular Al enriched oxides in all different types of steels. It is clear that the number of Al enriched oxides is much higher than the number of MnS inclusions, which means that there is more chance that corrosion pits will initiate from Al enriched oxides than from MnS inclusions.

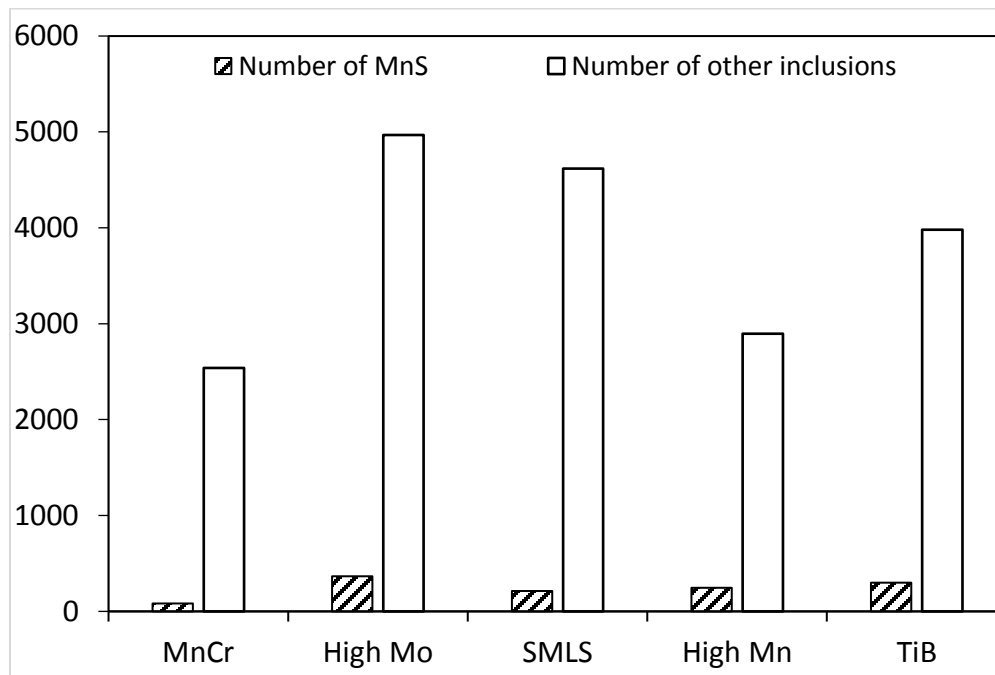


Figure 5.9: Number of MnS inclusions versus number of other inclusions in different L80 steels.

### **Distribution**

In addition, Al enriched oxides are present all over the thickness of the pipe while MnS inclusions are located only at the centerline of the pipe. Therefore, Al enriched oxides are present on the outer surface of the SSRT sample while MnS inclusions are present only at the intersection between the centerline of the pipe and the outer surface of the SSRT sample as shown schematically in Figure 5.6. In addition, clustering of globular Al enriched inclusions was observed in all types of steels as shown in Appendix H. These appear to be the site of crack initiation (see Figure 4.23). Therefore, closely spaced pits that form around Al enriched oxides can merge to become a large crack [130].

### **Geometric characteristics**

Finally, during an SSRT test performed in the longitudinal direction as shown in Figure 5.6, the stress concentration which leads to crack initiation depends on the geometric characteristics of the inclusions that are perpendicular to the applied stress. Thus, based on Figure 5.6, the decisive dimensions are the width of MnS inclusions ( $w$ ), the diameter of Al enriched oxides ( $d_1$ ) and the length of Ti nitrides ( $d_2$ ). The length of MnS inclusions is then no longer important because it is parallel to the applied stress  $\sigma_L$  [63,136].

Figure 5.10 compares the dimensions of MnS inclusions to the dimensions of other inclusions (mainly globular Al enriched oxides) projected onto the plane perpendicular to the applied stress. The width of MnS is similar to the diameter of Al enriched oxides or the length of Ti nitrides. Hence, the stress concentration at the interface between the corrosion pit and the steel matrix is quite similar, which means that the crack can initiate from all types of inclusions and that the dominant factors are the number of the inclusions and how close these inclusions are rather than their type.

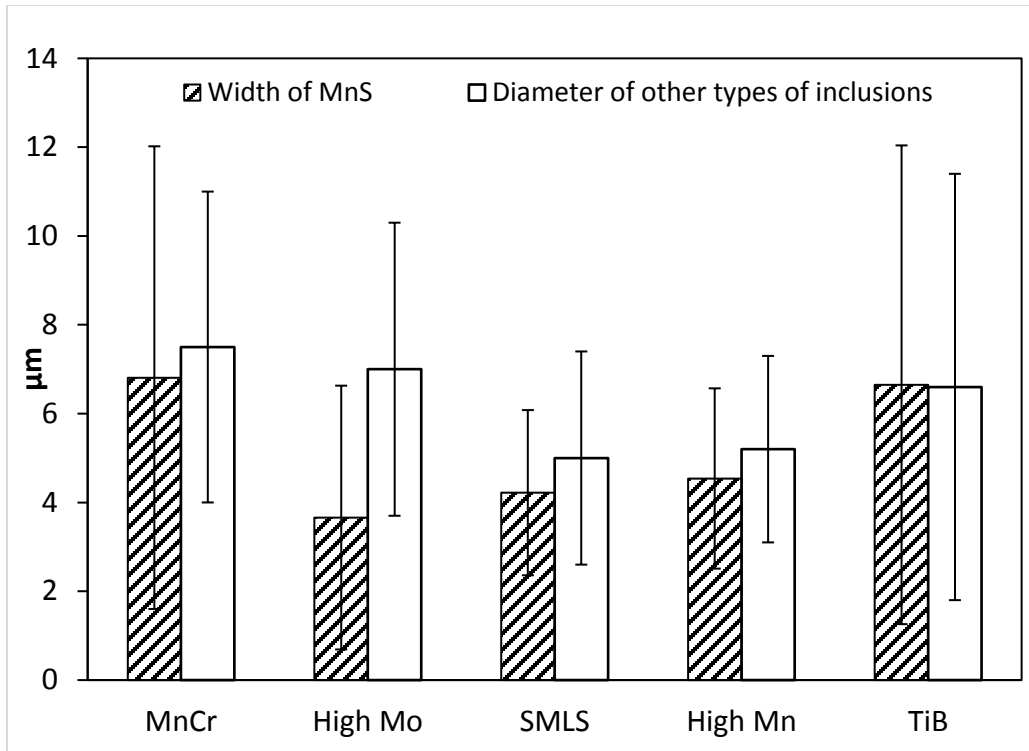


Figure 5.10: Comparison between dimensions of MnS inclusions and dimensions of other inclusions (mainly Al enriched oxides) in the plane perpendicular to the applied stress.

#### 5.4. Centerline macro-segregation

Centerline macro-segregation was studied in Chapter 4. EMPA technique was used in order to assess qualitatively and quantitatively the segregation degrees of the some alloying elements (Mn, P, Si and Cr). Mn X-ray maps through the whole thickness of the tested pipe samples showed clearly that HIC cracks occur at the centerline segregation band. The segregation ratio of P around the HIC crack is higher than the segregation ratios of Mn, Si, and Cr which are similar. The concentration peaks of Mn, Si and Cr associated with the HIC crack are not always the highest ones, whereas the highest P level is generally associated with the HIC crack.

In this section, the differences in the segregation behaviors of these analyzed elements (Mn, Si, Cr and P) will be discussed. The effect of these elements on the HIC resistance of the studied steels will also be examined.



### 5.4.1. Centerline macro-segregation behavior of Mn, Cr, Si and P

Figure 5.11 summarizes the segregation ratios of Mn, Cr, Si and P measured across the HIC crack by EMPA in 4 sections of L80 steel. The analyzed sections are taken from L80 ERW steels (i.e., High Mo, High Mn, TiB and MnCr steels) and all these sections show HIC cracks at the centerline.

It is clear that P has the highest segregation ratio. The concentration of P around the HIC crack is between about 6 and 10 times higher than the baseline concentration depending on the L80 steel. This significant increase in P concentration is not due to P contamination during preparing the HIC tested samples because a High Mo as received sample that was not HIC tested showed a high concentration of P (i.e., 0.059 wt%) at the centerline compared to a baseline concentration of about 0.01 wt% as seen in Figure 4.39.

Mn, Cr and Si have the lowest segregation ratios ( $< 2$ ), which is expected due to their higher partition coefficients between austenite and liquid, which will be discussed in detail below [137].

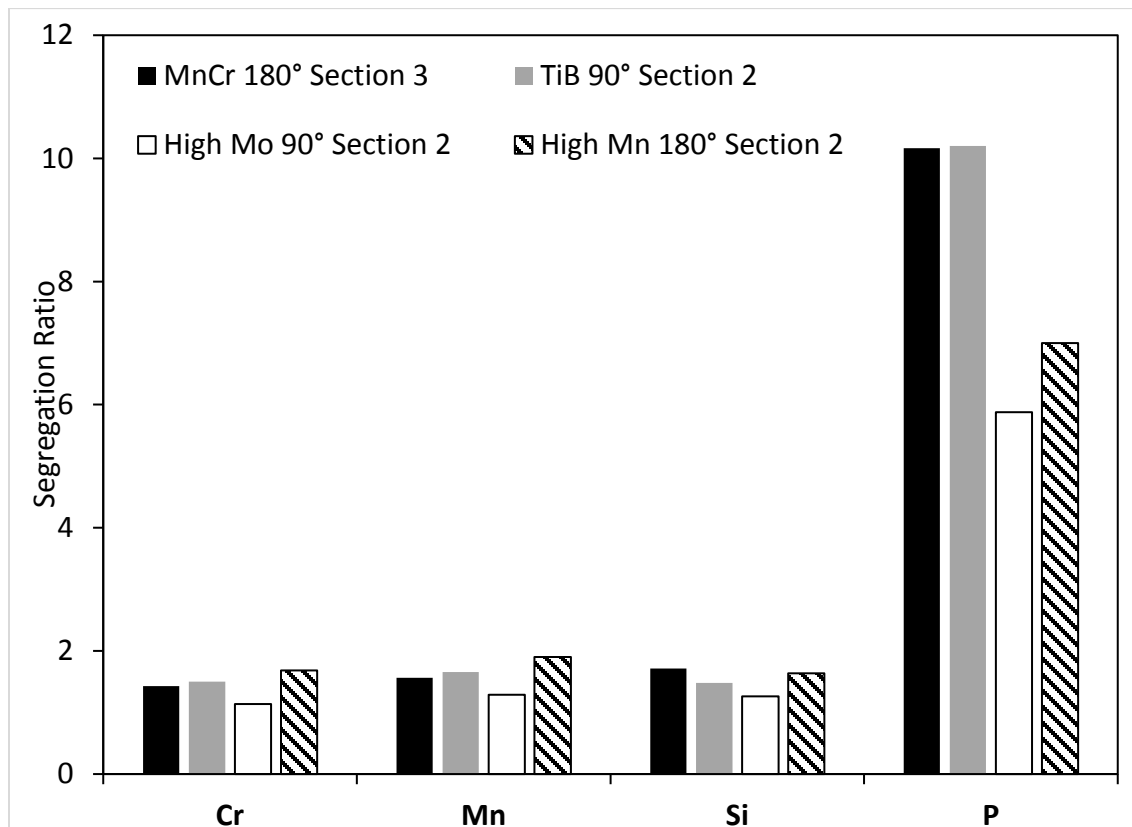


Figure 5.11: EMPA measured segregation ratios (SR) of Mn, Si, Cr and P across the HIC cracks in 4 HIC tested L80 samples.

The partition coefficient  $k$  of an element is the ratio between the concentration of this element in solid to its concentration in the liquid. A lower partition coefficient ( $k < 1$ ) results in a higher degree of segregation to the liquid phase. Then, the segregation behavior of an alloying element can be characterized by the partition coefficient.

Table 5.2 shows the equilibrium partition coefficients of Mn, Si, Cr and P between  $\delta$  ferrite and austenite with liquid. These values are assumed to be independent of temperature and are determined from binary phase diagrams [137].

The values of  $k^{\gamma/L}$  shown in Table 5.2 are in good agreement with the measured segregation ratios from EMPA line scans and shown in Figure 5.11. For example, P has the lowest partition coefficient  $k^{\gamma/L}$ , which means that it has a higher tendency than other elements to segregate into liquid and which is confirmed by the high segregation ratios of P determined by EMPA.

Table 5.2: Equilibrium partition coefficients of solute elements in  $\delta$ -ferrite and in austenite [137].

<b>Element</b>	<b><math>k^{\delta/L}</math></b>	<b><math>k^{\gamma/L}</math></b>
Mn	0.76	0.78
Si	0.77	0.52
Cr	0.95	0.86
P	0.23	0.13

#### 5.4.2. Effect of centerline macro-segregation on HIC propagation

In Chapter 4, it was observed that all HIC cracks propagate along the centerline macro-segregation band, which confirms the role of centerline segregation on HIC. This observation is consistent with the literature [114,138,139].

Due to the segregation of Mn and S at the last stages of the solidification, MnS inclusions tend to form at the centerline. Thus, HIC cracks initiate at MnS inclusions located at the centerline. Segregation of alloying elements at the centerline also promotes the formation of hard phases, which enhances HIC propagation and which explains the presence of long cracks at mid thickness of the HIC sample.

The HIC cracks in all the tested L80 steels were located mainly at the band where the concentration of P was the highest through the full thickness of the pipe (see Figure 4.36, Figure

4.43, Figure I.6, Figure I.12 and Figure I.18). This suggests that P plays a more significant role in the propagation of HIC cracks compared to the other analyzed alloying elements (i.e., Mn, Cr and Si).

In addition, the effect of centerline macro-segregation on HIC propagation will be investigated quantitatively by plotting CLR as a function of the segregation ratios determined by EMPA.

Mn, Si and Cr have similar segregation ratios as shown in Figure 5.11. Thus, in this section, only the effect of the segregation ratios of Mn and P on the propagation of HIC cracks will be discussed.

Figure 5.12 plots the EMPA measured segregation ratios of Mn next to the HIC crack versus the length ratio of the same HIC cracks. High Mo steel shows the lowest segregation ratio of Mn compared to the other steels, which makes sense. In fact, High Mo steel has the highest number of MnS inclusions and hence the lowest amount of Mn in solid solution.

Figure 5.13 plots the EMPA measured segregation ratios of P next to the HIC crack versus the length ratio of the same HIC cracks. The sample (TiB 90° Section 2) with the highest CLR (i.e., the longest crack length among these 4 sections) exhibits the highest segregation ratio of P ( $\approx 9$ ). SEM image of an opened HIC crack in TiB presented in Section 4.3.3 (see Figure 4.15) shows an intergranular propagation of the HIC crack, which is consistent with the high segregation ratio of P determined by EMPA in this steel. P tends to segregate mostly at the centerline of the pipe more specifically at the grain boundaries that provide an easy propagation path for HIC cracks. Therefore, most of the HIC cracks in TiB steel propagate intergranularly at the centerline of the pipe.

However, no clear relationship is found between CLR and the segregation ratios of Mn as well as between CLR and the segregation ratios of P, which means that the length of HIC cracks does not depend only on the segregation ratios of Mn and P and that there are other factors that may play a role in the propagation of HIC cracks with segregation (e.g., spacing between MnS inclusions, microstructure, size and orientation of the prior austenite grain boundaries).

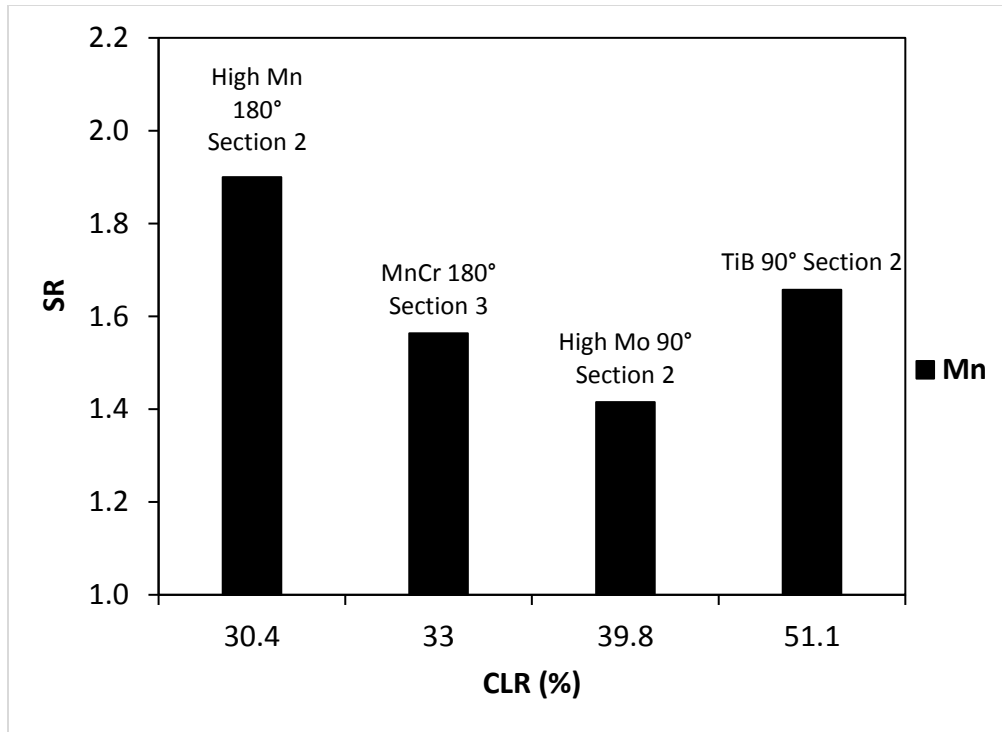


Figure 5.12: Relationship between the segregation ratio of Mn determined by EMPA across the HIC crack and the crack length ratios measured on each section.

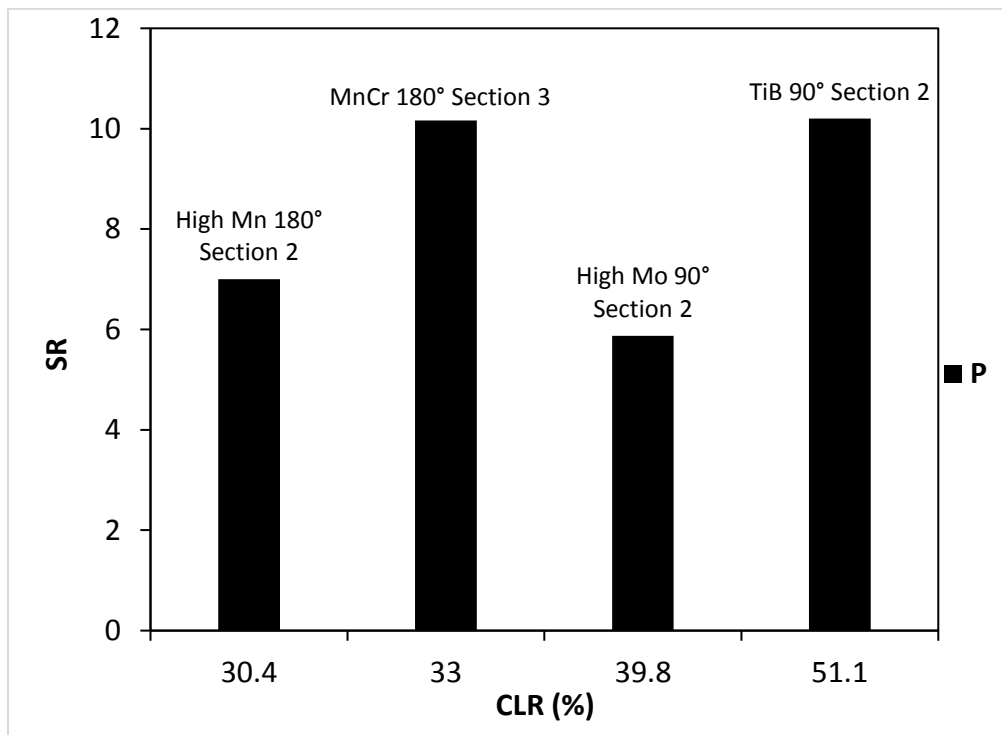


Figure 5.13: Relationship between the segregation ratio of P determined by EMPA across the HIC crack and the crack length ratios measured on each section.

## 5.5. Summary

1. A linear relationship was found between the number of MnS inclusions and the nominal concentration product  $[\text{Mn}][\text{S}]$  ( $[\text{Mn}]$  and  $[\text{S}]$  are in wt%). Another linear relationship was also found between the total length of MnS inclusions and  $[\text{Mn}][\text{S}]$ . Thermodynamic calculations with Thermo-Calc showed that MnS inclusions form at the last stages of solidification and that they start to form earlier during the solidification process in High Mo steel which explains the increased number and length of MnS inclusions observed in this steel.
2. HIC cracks initiate mainly from MnS inclusions. Due to the presence of MnS inclusions in the centerline and to the enrichment of the centerline band in alloying elements (e.g., Mn, Cr, Si and P), HIC cracks appear mainly at the centerline segregation band. Clusters of Al enriched and TiN inclusions in the centerline are found to enhance the propagation of HIC cracks.
3. SSC cracks were found to initiate mainly from corrosion pits formed at the surface of the SSRT sample. The corrosion pits are associated with clusters of globular Al enriched inclusions, which is confirmed by SEM observations and by the correlation found between RAR and the number of these inclusions.
4. EMPA X ray mapping confirmed the propagation of HIC cracks along the centerline segregation band. HIC cracks appear specifically where there is a significant increase in the concentration of P in the centerline. The segregation ratio of P around the HIC cracks is much higher than the segregation ratios of Mn, Cr and Si around these cracks. Thus P plays a more important role in the propagation of HIC cracks than the above mentioned elements (i.e., Mn, Cr and Si).
5. However, no clear correlation was found between CLR and the segregation ratios of Mn, Si, Cr and P determined by EMPA which shows that HIC cracks do not depend only on the degree of segregation of alloying elements. HIC cracks depend also on other factors such as grain size, spacing between MnS inclusions and microstructures that need to be studied in the future to complete this study.

## Chapter 6 Conclusions and Recommendations

This chapter begins with a summary of the findings in this study followed by recommendations.

### 6.1. Conclusions

The resistance of L80 ERW and Seamless steel pipe, with five different chemical compositions, to (i) hydrogen induced cracking (HIC) and to (ii) sulfide stress cracking (SSC) was evaluated. Analysis of the centerline macro-segregation was studied using electron microprobe analysis (EMPA). Characterization of the inclusions present in each steel was undertaken. The size, composition, morphology and number of the inclusions in each steel were correlated with the HIC and SSC cracking parameters.

The main findings of this work are:

- 1] HIC cracks propagate along the centerline segregation band of HIC samples.
- 2] EMPA analysis of the region around the HIC cracks shows the presence of MnS inclusions and an increased Mn content in the solid solution.
- 3] EMPA line scans of Mn, Cr, Si and P across the HIC cracks show that there is an increase in the concentration of these alloying elements around the HIC cracks. The segregation ratio of P (between 6 and 10) around the HIC crack is much higher than the segregation ratios of Mn, Si and Cr (between 1.2 and 2.0), which suggests that segregation of P plays a more important role in HIC propagation than the other alloying elements.
- 4] The crack length ratio (CLR) increased both with the number and with the maximum length of MnS inclusions. These results suggest the role of MnS inclusions in initiation of HIC cracks.
- 5] The CLR also increased with the number of other inclusions (i.e., mainly globular Al enriched oxides in all types of steels + few counts of cubic Ti nitrides in TiB) present in the steel if the HIC crack has already initiated at MnS inclusions.
- 6] No clear correlation was found between CLR and the segregation ratios of Mn, Si, Cr and P. This suggests that, in addition to segregation, there are other factors (e.g., spacing between MnS

inclusions, grain size, and microstructure) that play a role in HIC propagation and that need to be studied in the future to complete this study.

7] These differences in the number and length of MnS inclusions in the L80 steels studied is related to the Mn and S contents. A higher nominal concentration of Mn and S (i.e., [Mn][S] with [Mn] and [S] in wt%) leads to a greater number of elongated MnS inclusions. This is confirmed by thermodynamic calculations performed by Thermo-Calc.

8] SSC cracks are found to nucleate from corrosion pits located at the SSRT sample surface. Corrosion pits are found to initiate mainly from clusters of globular Al enriched oxides.

## 6.2. Recommendations

1] A lower [Mn][S] leads to a higher CLR and hence to a higher susceptibility to HIC. Therefore, it is recommended to lower [Mn][S] in order to increase the resistance of L80 steel to HIC. This may be accomplished by reducing S content in the steels. For example, High Mo exhibits the lowest nominal composition of Mn (0.66 wt%). However, it has the highest nominal composition of S (0.0022wt%). High Mo has then the highest value of [Mn][S]. It is expected by lowering the S content in High Mo steel to 0.0006 wt% (i.e., S content in MnCr steel) to increase the HIC resistance of High Mo steel.

2] HIC cracks in TiB steel are mostly intergranular. Thus the grain boundaries seem to play an important role in the propagation of HIC cracks. Finer grain size was found to increase the HIC resistance due to the increasing grain boundary area per unit volume [98]. Hence grain refinement by thermomechanical treatment may enhance the resistance of L80 steel to HIC.

In addition, there is still some confusion regarding the role of crystallographic texture on HIC propagation. Venegas et al. [102] found that a  $\{111\}$ //ND dominant texture increases the HIC resistance. However, Mohtadi-bonab et al. [105] found that there is no preferred direction for HIC propagation. Therefore, the role of crystallographic texture on HIC propagation can be explored.

3] The morphology of MnS inclusions was found to play a significant role in the initiation of HIC cracks. Increased number and length of MnS inclusions lower the resistance of L80 steel to HIC. Hence it is important to modify the morphology of MnS inclusions. This may be

accomplished by calcium treatment. Inclusions in calcium treated steels are spherical with a low melting point calcium aluminate core covered by calcium and manganese sulfides [140]. This would be expected to improve the resistance of L80 steel to HIC.



## References

- [1] M. Iannuzzi, Environmentally assisted cracking (EAC) in oil and gas production, in: *Stress Corros. Crack.*, Norway, 2011: pp. 570–607.
- [2] M. Elboujdaini, Hydrogen-Induced Cracking and Sulfide Stress Cracking, in: *Uhlig's Corros. Handb.*, John Wiley & Sons, Inc., Hoboken, NJ, USA, 2011: pp. 183–194.
- [3] T. Zhao, Z. Liu, C. Du, J. Hu, X. Li, A Modelling Study for Predicting Life of Downhole Tubes Considering Service Environmental Parameters and Stress, *Materials (Basel)*. 9 (2016) 741.
- [4] M.A. Al-Anezi, G.S. Frankel, A.K. Agrawal, Susceptibility Of Conventional Pressure Vessel Steel To HIC And SOHIC In H<sub>2</sub>S Diglycolamine Solutions, *Corrosion*. 55 (1999) 1101–1109.
- [5] A. Barnoush, H. Vehoff, Recent developments in the study of hydrogen embrittlement: Hydrogen effect on dislocation nucleation, *Acta Mater*. 58 (2010) 5274–5285.
- [6] S. Papavinasam, Mechanisms, in: *Corros. Control Oil Gas Ind.*, 2014: pp. 249–300.
- [7] R.D. Kane, M.S. Cayard, Roles of H<sub>2</sub>S in the behavior of engineering alloys: a review of literature and experience, *Corrosion*. (1998) 28.
- [8] P.F. Timmins, Failure Control in Process Operations, Fatigue and Fracture, in: *ASM Handb.*, 1996: pp. 468–482.
- [9] T.G. Oakwood, Corrosion of Wrought Low-Alloy Steels, *Corrosion: Materials*, in: *ASM Handb.*, 2005: pp. 11–27.
- [10] M.C. Tiegel, M.L. Martin, A.K. Lehmberg, M. Deutges, C. Borchers, R. Kirchheim, Crack and blister initiation and growth in purified iron due to hydrogen loading, *Acta Mater*. 115 (2016) 24–34.
- [11] M.C. Zhao, M. Liu, A. Atrens, Y.Y. Shan, K. Yang, Effect of applied stress and microstructure on sulfide stress cracking resistance of pipeline steels subject to hydrogen sulfide, *Mater. Sci. Eng. A*. 478 (2008) 43–47.
- [12] *A Comparative Analysis of Pipeline Performance 2000–2009*, 2011.
- [13] ERCB, Directive 010 : Minimum Casing Design Requirements, 2009.
- [14] NACE MR0175/ ISO 15156-1, Petroleum and natural gas industries. Materials for use in H<sub>2</sub>S-containing Environments in oil and gas production., 2009.

- [15] T.E. Perez, Corrosion in the Oil and Gas Industry : An Increasing Challenge for Materials, *JOM*. 65 (2013) 1033–1042.
- [16] G. Waid, R. Stiglitz, The development of a new high strength casing steel with improved hydrogen sulfide cracking resistance for sour oil and gas well applications, in: *NACE Corros. Conf.*, Houston, Tex, 1979: pp. 1317–1324.
- [17] B.E. Urband, SPE 52843 High Strength Sour Service C110 Casing, *SPE/IADC Drill. Conf.* (1999).
- [18] API Specification 5CT, Specification for Casing and Tubing, 2012.
- [19] W. Huang, Sulfide Stress Cracking Susceptibility of Low Alloy Steels for Casing-Application in Sour Environments, University of Alberta, 2012.
- [20] B. Urband, F. Bernard, S. Morey, B. Bradley, F. Legay, H. Marchebois, C. Linne, G. Lynn, Latest Enhancements in High Strength Sour Service Tubulars, in: *SPE/IADC Drill. Conf. Exhib.*, 2009: pp. 1–19.
- [21] W. Renpu, Production Casing and Cementing, in: *Adv. Well Complet. Eng.* (Third Ed., 2011: pp. 221–294.
- [22] G. Krauss, Quench and Tempered Martensitic Steels: Microstructures and Performance, in: *Compr. Mater. Process.*, Elsevier, 2014: pp. 363–378.
- [23] B.L. Bramfitt and S.J. Lawrence, Metallography and Microstructures of Carbon and Low-Alloy Steels, *Metallography and Microstructures*, Vol 9, in: *ASM Handb.*, 2004: pp. 608–626.
- [24] H.K. Birnbaum, P. Sofronis, Hydrogen-enhanced localized plasticity-a mechanism for hydrogen-related fracture, *Mater. Sci. Eng. A*. 176 (1994) 191–202.
- [25] I.M. Robertson, The effect of hydrogen on dislocation dynamics, *Eng. Fract. Mech.* 68 (2001) 671–692.
- [26] B.M. Dadfarnia, P. Novak, D.C. Ahn, J.B. Liu, P. Sofronis, D.D. Johnson, I.M. Robertson, Recent Advances in the Study of Structural Materials Compatibility with Hydrogen, *Adv. Mater.* 22 (2010) 1128–1135.
- [27] H.K. Birnbaum, *Mechanisms of Hydrogen Related Fracture of Metals*, 1989.
- [28] S.M. Teus, V.N. Shivanyuk, B.D. Shanina, V.G. Gavriljuk, Effect of hydrogen on electronic structure of fee iron in relation to hydrogen embrittlement of austenitic steels, *Phys. Status Solidi Appl. Mater. Sci.* 204 (2007) 4249–4258.

- [29] A.R. Troiano, The Role of Hydrogen and Other Interstitials in the Mechanical Behavior of Metals: (1959 Edward De Mille Campbell Memorial Lecture), *Metallogr. Microstruct. Anal.* 5 (2016) 557–569.
- [30] V.G. Gavriljuk, V.N. Shivanyuk, B.D. Shanina, Change in the electron structure caused by C, N and H atoms in iron and its effect on their interaction with dislocations, *Acta Mater.* 53 (2005) 5017–5024.
- [31] D. Eliezer, E. Tal-Gutelmacher, T. Boellinghaus, Hydrogen embrittlement in hydride- and non hydride- forming systems - microstructural / phase changes and cracking mechanisms, in: *Proc. 11th Int. Conf. Fract. Turin, Italy, 2016*.
- [32] P. Sofronis, Hydrogen Transport and Interaction with Material Deformation: Implications for Fracture, in: *Handb. Mater. Behav. Model.*, 2001: pp. 864–874.
- [33] J. Lee, T. Lee, Y.J. Kwon, D.J. Mun, J.Y. Yoo, C.S. Lee, Effects of vanadium carbides on hydrogen embrittlement of tempered martensitic steel, *Met. Mater. Int.* 22 (2016) 364–372.
- [34] W. Brocks, R. Falkenberg, I. Scheider, Coupling aspects in the simulation of hydrogen-induced stresscorrosion cracking, *Procedia IUTAM.* 3 (2012) 11–24.
- [35] M.B. Djukic, V. Sijacki Zeravcic, G.M. Bakic, A. Sedmak, B. Rajcic, Hydrogen damage of steels: A case study and hydrogen embrittlement model, *Eng. Fail. Anal.* 58 (2015) 485–498.
- [36] X. Xu, Sulphide formation in low-carbon low-manganese steel, University of Wollongong, 2014.
- [37] B.L. Bramfitt, Carbon And Alloy Steels, in: Myer Kutz (Ed.), *Handb. Mater. Sel.*, Bethlehem, Pennsylvania, 2002: pp. 27–64.
- [38] J.D. Verhoeven, The Low-Alloy AISI Steels, in: *Steel Metall. Non-Metallurgist*, ASM International, 2007: pp. 55–61.
- [39] W.K. Kim, S.U. Koh, B.Y. Yang, K.Y. Kim, Effect of environmental and metallurgical factors on hydrogen induced cracking of HSLA steels, *Corros. Sci.* 50 (2008) 3336–3342.
- [40] D. Hejazi, A.J. Haq, N. Yazdipour, D.P. Dunne, A. Calka, F. Barbaro, E. V. Pereloma, Effect of manganese content and microstructure on the susceptibility of X70 pipeline steel to hydrogen cracking, *Mater. Sci. Eng. A.* 551 (2012) 40–49.
- [41] Y. Qi, H. Luo, S. Zheng, C. Chen, Z. Lv, M. Xiong, Comparison of tensile and impact

- behavior of carbon steel in H<sub>2</sub>S environments, *J. Mater.* 58 (2014) 234–241.
- [42] G. Domizzi, G. Anteri, J. Ovejero-García, Influence of sulphur content and inclusion distribution on the hydrogen induced blister cracking in pressure vessel and pipeline steels, *Corros. Sci.* 43 (2001) 325–339.
- [43] N. Ishikawa, Oil and Gas Pipelines, in: R.W. Revie (Ed.), *Oil Gas Pipelines Integr. Saf. Handb.*, John Wiley & Sons, Inc., Hoboken, New Jersey, 2015.
- [44] J.G. Williams, Advances in steels for high strength ERW linepipe application in Australia, *Mater. Forum.* 31 (2007) 1–10.
- [45] H. Asahi, Y. Sogo, M. Ueno, H. Higashiyama, Effects of Mn, P, and Mo on sulfide stress cracking resistance of high strength low alloy steels, *Metall. Trans. A.* 19 (1988) 2171–2177.
- [46] S.Y. Han, S.Y. Shin, C.H. Seo, H. Lee, J.H. Bae, K. Kim, S. Lee, N.J. Kim, Effects of Mo, Cr, and V additions on tensile and Charpy impact properties of API X80 pipeline steels, *Metall. Mater. Trans. A Phys. Metall. Mater. Sci.* 40 (2009) 1851–1862.
- [47] C.M. Liao, J.L. Lee, Effect of molybdenum on sulfide stress cracking resistance of low-alloy steels, *Corrosion.* 50 (1994) 695–704.
- [48] B.D. Craig, The Role of Mo in the Enhanced Resistance to Hydrogen Stress Cracking of AISI4100 Steels, *Metall. Trans. A.* 13 (1982) 1099–1101.
- [49] C. García De Andrés, C. Capdevila, I. Madariaga, I. Gutiérrez, Role of molybdenum in acicular ferrite formation under continuous cooling in a medium carbon microalloyed forging steel, *Scr. Mater.* 45 (2001) 709–716.
- [50] S.U. Koh, J.M. Lee, B.Y. Yang, K.Y. Kim, Effect of Molybdenum and Chromium Addition on the Susceptibility to Sulfide Stress Cracking of High-Strength, Low-Alloy Steels, (2007) 220–230.
- [51] J.R. Davis, Carbon and Alloy Steels, in: *Alloy Underst. Basics*, 2001: pp. 123–253.
- [52] S. Aminorroaya-Yamini, Effect of titanium additions to low carbon, low manganese steels on sulphide precipitation, 2008.
- [53] H.S. El-faramawy, S.N. Ghali, M.M. Eissa, Effect of Titanium Addition on Behavior of Medium Carbon Steel, *J. Miner. Mater. Charact.* 2012 (2012) 1108–1112.
- [54] B. Beidokhti, A. Dolati, A.H. Koukabi, Effects of alloying elements and microstructure on the susceptibility of the welded HSLA steel to hydrogen-induced cracking and sulfide

- stress cracking, *Mater. Sci. Eng. A.* 507 (2009) 167–173.
- [55] R. Valentini, A. Solina, S. Matera, P. Gregorio, Influence of titanium and carbon contents on the hydrogen trapping of microalloyed steels, *Metall. Mater. Trans. A.* 27 (1996) 3773–3780.
- [56] Y. Palizdar, Understanding the effect of aluminium on the microstructure on low level nitrogen steel, (2011).
- [57] X.S. Du, W.B. Cao, C.D. Wang, S.J. Li, J.Y. Zhao, Y.F. Sun, Effect of microstructures and inclusions on hydrogen-induced cracking and blistering of A537 steel, *Mater. Sci. Eng. A.* 642 (2015) 181–186.
- [58] W.K. Kim, S.U. Koh, B.Y. Yang, K.Y. Kim, Effect of environmental and metallurgical factors on hydrogen induced cracking of HSLA steels, *Corros. Sci.* 50 (2008) 3336–3342.
- [59] H.B. Xue, Y.F. Cheng, Characterization of inclusions of X80 pipeline steel and its correlation with hydrogen-induced cracking, *Corros. Sci.* 53 (2011) 1201–1208.
- [60] T.Y. Jin, Z.Y. Liu, Y.F. Cheng, Effect of non-metallic inclusions on hydrogen-induced cracking of API5L X100 steel, *Int. J. Hydrogen Energy.* 35 (2010) 8014–8021.
- [61] Z.Y. Liu, X.G. Li, C.W. Du, L. Lu, Y.R. Zhang, Y.F. Cheng, Effect of inclusions on initiation of stress corrosion cracks in X70 pipeline steel in an acidic soil environment, *Corros. Sci.* 51 (2009) 895–900.
- [62] C.F. Dong, Z.Y. Liu, X.G. Li, Y.F. Cheng, Effects of hydrogen-charging on the susceptibility of X100 pipeline steel to hydrogen-induced cracking, *Int. J. Hydrogen Energy.* 34 (2009) 9879–9884.
- [63] J. Sojka, M. Jérôme, M. Sozańska, P. Váňová, L. Rytířová, P. Jonšta, Role of microstructure and testing conditions in sulphide stress cracking of X52 and X60 API steels, *Mater. Sci. Eng. A.* 480 (2008) 237–243.
- [64] B.E. Wilde, D.C. KIM, H. E. PHELPS, Some Observation on the Role of Inclusions in the hydrogen iduced Blister Vrackng og Linepipe Steel in Sulfide Environments, *NACE Coorosion.* 36 (1980) 625–632.
- [65] J.H. Ryu, S.K. Kim, C.S. Lee, D.-W. Suh, H.K.D.H. Bhadeshia, Effect of aluminium on hydrogen-induced fracture behaviour in austenitic Fe-Mn-C steel, *Proc. R. Soc. A Math. Phys. Eng. Sci.* 469 (2012) 14.
- [66] T. Dieudonné, L. Marchetti, M. Wery, J. Chêne, C. Allely, P. Cugy, C.P. Scott, Role of

- copper and aluminum additions on the hydrogen embrittlement susceptibility of austenitic Fe-Mn-C TWIP steels, *Corros. Sci.* 82 (2014) 218–226.
- [67] T. Lis, Modification of Oxygen and Sulphur Inclusions in Steel by Calcium Treatment, *Metalurgija.* 48 (2009) 95–98.
- [68] Z. Han, Mechanism and Kinetics of Transformation of Alumina Inclusions By Calcium Treatment, Helsinki University of Technology Publications in Materials Science and Engineering, 2006.
- [69] A. V. Nikolaeva, Y.A. Nikolaev, Y.R. Kevorkyan, Grain-boundary segregation of phosphorus in low-alloy steel, *At. Energy.* 91 (2001) 534–542.
- [70] S. Song, Z. Yuan, D. Shen, L. Weng, Effects of phosphorus grain boundary segregation and hardness on the ductile-to-brittle transition for a 2.25Cr1Mo steel, *J. Wuhan Univ. Technol. Mater. Sci. Ed.* 22 (2007) 1–6.
- [71] M. Guttman, Interfacial Segregation and Temper Embrittlement, *Encycl. Mater. Sci. Technol.* (2001) 1–8.
- [72] B.S. Bokshtein, A.N. Khodan, O.O. Zabusov, D.A. Mal'tsev, B.A. Gurovich, Kinetics of phosphorus segregation at grain boundaries of low-alloy low-carbon steel, *Phys. Met. Metallogr.* 115 (2014) 146–156.
- [73] S.H. Song, J. Wu, L.Q. Weng, Z.X. Yuan, Fractographic changes caused by phosphorus grain boundary segregation for a low alloy structural steel, *Mater. Sci. Eng. A.* 497 (2008) 524–527.
- [74] J. Kameda, Equilibrium and growth characteristics of hydrogen-induced intergranular cracking in phosphorus-doped and high purity steels, *Acta Metall.* 34 (1986) 1721–1735.
- [75] K. Yoshino, C.J. McMahon, The cooperative relation between temper embrittlement and hydrogen embrittlement in a high strength steel, *Metall. Trans.* 5 (1974) 363–370.
- [76] H. Shimazu, S. Konosu, Y. Tanaka, M. Yuga, H. Yamamoto, N. Ohtsuka, Combined Effect of Temper and Hydrogen Embrittlement on Threshold for Hydrogen-Induced Fracture in Cr-Mo Steels, Vol. 6 *Mater. Fabr. Parts A B.* 135 (2012) 825.
- [77] B.L. Bramfitt, A.O. Benschoter, Introduction to Steels and Cast Irons, in: *Metallogr. Guid.*, 2002: pp. 2–8.
- [78] R.O. Ritchie, M.H.C. Cedenio, V.F. Zackay, E.R. Parker, Effect of silicon additions and retained austenite on stress corrosion cracking in ultrahigh strength steel, *Metall. Trans. A.*

- 9 (1978) 35–40.
- [79] R. Song, N. Fonstein, N. Pottore, H.J. Jun, D. Bhattacharya, S. Jansto, Effect of Nb on Delayed Fracture Resistance of Ultrahigh Strength Martensitic Steels, HSLA Steels 2015, Microalloying 2015 Offshore Eng. Steels 2015 Conf. Proc. (2015) 541–547.
- [80] K.H. Kim, S.H. Lee, N.D. Nam, J.G. Kim, Effect of cobalt on the corrosion resistance of low alloy steel in sulfuric acid solution, *Corros. Sci.* 53 (2011) 3576–3587.
- [81] S.A. Park, D.P. Le, J.G. Kim, Alloying Effect of Chromium on the Corrosion Behavior of Low-Alloy Steels, *Mater. Trans.* 54 (2013) 1770–1778.
- [82] J. Capus, ASTM STP407, The Mechanism of Temper Brittleness, 1968.
- [83] J. Albarran, L. Martinez, H. Lopez, Effect of heat treatment on the stress corrosion resistance of a microalloyed pipeline steel, *Corros. Sci.* 41 (1999) 1037–1049.
- [84] R.A. Carneiro, R.C. Ratnapuli, V. de Freitas Cunha Lins, The influence of chemical composition and microstructure of API linepipe steels on hydrogen induced cracking and sulfide stress corrosion cracking, *Mater. Sci. Eng. A.* 357 (2003) 104–110.
- [85] M.A. Mohtadi-Bonab, J.A. Szpunar, L. Collins, R. Stankievich, Evaluation of hydrogen induced cracking behavior of API X70 pipeline steel at different heat treatments, *Int. J. Hydrogen Energy.* 39 (2014) 6076–6088.
- [86] M. Zhao, B. Tang, Y.-Y. Shan, K. Yang, Role of microstructure on sulfide stress cracking of oil and gas pipeline steels, *Metall. Mater. Trans. A.* 34 (2003) 1089–1096.
- [87] C.F. Dong, Z.Y. Liu, X.G. Li, Y.F. Cheng, Effects of hydrogen-charging on the susceptibility of X100 pipeline steel to hydrogen-induced cracking, *Int. J. Hydrogen Energy.* 34 (2009) 9879–9884.
- [88] G.T. Park, S.U. Koh, H.G. Jung, K.Y. Kim, Effect of microstructure on the hydrogen trapping efficiency and hydrogen induced cracking of linepipe steel, *Corros. Sci.* 50 (2008) 1865–1871.
- [89] M. Van ende, Formation and Morphology of non-Metallic Inclusions in Aluminium Killed Steels, Universite Catholique de Louvain, Ecole Polytechnique de Louvain, 2010.
- [90] Z. Szklarska-Smialowska, E. Lunarska, The effect of sulfide inclusions on the susceptibility of steels to pitting, stress corrosion cracking and hydrogen embrittlement, *Werkstoffe Und Korrosion.* 32 (1981) 478–485.
- [91] T. Ohki, M. Tanimura, K. Kinoshita, R. Ohki, Effect of Inclusions on Sulfide Stress

- Cracking, (2016).
- [92] H.Y. Liou, R.I. Shieh, F.I. Wei, S.C. Wang, Roles of microalloying elements in hydrogen induced cracking resistant property HSLA steel, *Corrosion*. 49 (1993) 389–398.
  - [93] O.M.I. Todoshchenko, Y. Yagodzinsky, T. Saukkonen, H. Hänninen, Role of nonmetallic inclusions in hydrogen embrittlement of high-strength carbon steels with different microalloying, *Metall. Mater. Trans. A Phys. Metall. Mater. Sci.* 45 (2014) 4742–4747.
  - [94] C.F. Dong, X.G. Li, Z.Y. Liu, Y.R. Zhang, Hydrogen-induced cracking and healing behaviour of X70 steel, *J. Alloys Compd.* 484 (2009) 966–972.
  - [95] S.U. Koh, H.G. Jung, K.B. Kang, G.T. Park, K.Y. Kim, Effect of microstructure on hydrogen-induced cracking of linepipe steels, *Corrosion*. 64 (2008) 574–585.
  - [96] K. Knarbakk, Hydrogen Induced Stress Cracking of Inconel 718 under Cathodic Polarization. Effect of Hydrogen on the Initiation and Propagation of Cracks, (2015) 1–142.
  - [97] I.M. Bernstein, A.W. Thompson, Resisting Hydrogen Embrittlement, ACADEMIC PRESS, INC., 1976.
  - [98] H. Fuchigami, H. Minami, M. Nagumo, Effect of grain size on the susceptibility of martensitic steel to hydrogen-related failure, *Philos. Mag. Lett.* 86 (2006) 21–29.
  - [99] K. Takasawa, Y. Wada, R. Ishigaki, R. Kayano, Effects of grain size on hydrogen environment embrittlement of high strength low alloy steel in 45 MPa gaseous hydrogen, *Strength, Fract. Complex.* 7 (2011) 87–98.
  - [100] M. Ichimura, Y. Sasajima, M. Imabayashi, Grain Boundary effect on diffusion of hydrogen in pure aluminum, *Mater. Trans.* 32 (1991) 1109–1114.
  - [101] N. Yazdipour, A.J. Haq, K. Muzaka, E. V. Pereloma, 2D modelling of the effect of grain size on hydrogen diffusion in X70 steel, *Comput. Mater. Sci.* 56 (2012) 49–57.
  - [102] V. Venegas, F. Caleyó, T. Baudin, J.H. Espina-Hernández, J.M. Hallen, On the role of crystallographic texture in mitigating hydrogen-induced cracking in pipeline steels, *Corros. Sci.* 53 (2011) 4204–4212.
  - [103] A. Ghosh, S. Kundu, D. Chakrabarti, Effect of crystallographic texture on the cleavage fracture mechanism and effective grain size of ferritic steel, *Scr. Mater.* 81 (2014) 8–11.
  - [104] M. Masoumi, C.C. Silva, H.F.G. de Abreu, Effect of crystallographic orientations on the



- hydrogen-induced cracking resistance improvement of API 5L X70 pipeline steel under various thermomechanical processing, *Corros. Sci.* 111 (2016) 121–131.
- [105] M.A. Mohtadi-bonab, Mechanism of Failure By Hydrogen-Induced Cracking in Pipeline Steels, University of Saskatchewan, 2015.
- [106] B.G. Thomas, Continuous Casting, *Encycl. Mater. Sci. Technol.* (Second Ed. (2001) 1595–1598.
- [107] S. Louhenkilpi, Continuous Casting of Steel, in: *Treatise Process Metall.*, Elsevier Ltd., 2014: pp. 373–434.
- [108] A.S. Ghosh, Segregation in cast products, in: *Acad. Proc. Eng. Sci.*, 2001: pp. 5–24.
- [109] A. Ludwig, M. Wu, A. Kharicha, On Macrosegregation, *Met. Mater. Trans. A.* 46 (2015) 4854–4867.
- [110] S.K. Choudhary, S. Ganguly, Morphology and Segregation in Continuously Cast High Carbon Steel Billets, *ISIJ Int.* 47 (2007) 1759–1766.
- [111] T. Kajitani, J.-M. Drezet, M. Rappaz, Numerical Simulation of Deformation-Induced Segregation in Continuous Casting of Steel, *Met. Mater. Trans. A.* 32 (2001) 1479–1491.
- [112] T. Murao, T. Kajitani, H. Yamamura, K. Anzai, K. Oikawa, T. Sawada, Simulation of the Center-Line Segregation Generated by the Formation of Bridging, *ISIJ Int.* 54 (2014) 359–365.
- [113] M. Miyazaki, K. Isobe, T. Murao, Formation mechanism and modeling of centerline segregation, *Nippon Steel Tech. Rep.* (2013) 48–53.
- [114] A. Brown, C.L. Jones, Hydrogen Induced Cracking in Pipeline Steels., *Corrosion.* 40 (1984) 330–336.
- [115] K. Matsumoto, Y. Kobayashi, K. Ume, K. Murakami, K. Taira, K. Arikata, Hydrogen Induced Cracking Susceptibility of High-Strength Line Pipe Steels., *Corrosion.* 42 (1986) 337–345.
- [116] T.L. Anderson, Fracture Mechanisms in Metals, in: *Fract. Mech. Fundam. Appl.*, 2005: pp. 219–254.
- [117] J. Pokluda, P. Andera, Brittle and Ductile Fracture, in: *Micromechanisms Fract. Fatigue*, 2010: pp. 69–123.
- [118] D. You, S.K. Michelic, G. Wieser, C. Bernhard, Modeling of manganese sulfide formation during the solidification of steel, *J. Mater. Sci.* (n.d.).

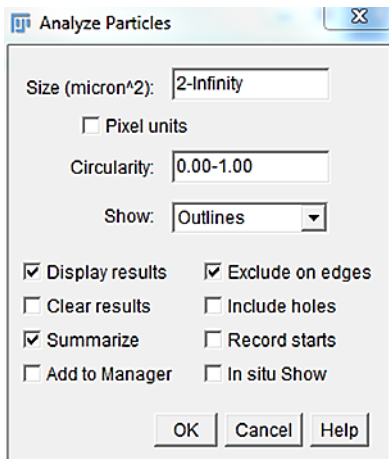
- [119] M.G. Lage, A. Luiz, V. Da Costa E Silva, Evaluating segregation in HSLA steels using computational thermodynamics, *Integr. Med. Res.* 4 (2015) 353–358.
- [120] M. Elboudjaini, W. Revie, Effect of Non-Metallic Inclusions on Hydrogen Induced Cracking, (n.d.).
- [121] F. Huang, J. Liu, Z.J. Deng, J.H. Cheng, Z.H. Lu, X.G. Li, Effect of microstructure and inclusions on hydrogen induced cracking susceptibility and hydrogen trapping efficiency of X120 pipeline steel, *Mater. Sci. Eng. A.* 527 (2010) 6997–7001.
- [122] F. Huang, X.G. Li, J. Liu, Y.M. Qu, C.W. Du, Effects of alloying elements, microstructure, and inclusions on hydrogen induced cracking of X120 pipeline steel in wet H<sub>2</sub>S sour environment, *Mater. Corros.* 63 (2012) 59–66.
- [123] D. Hejazi, A.J. Haq, N. Yazdipour, D.P. Dunne, A. Calka, F. Barbaro, E. V. Pereloma, Effect of manganese content and microstructure on the susceptibility of X70 pipeline steel to hydrogen cracking, *Mater. Sci. Eng. A.* 551 (2012) 40–49.
- [124] J. Moon, C. Park, S.J. Kim, Influence of Ti addition on the hydrogen induced cracking of API 5L X70 hot-rolled pipeline steel in acid sour media, *Met. Mater. Int.* 18 (2012) 613–617.
- [125] K.O. Findley, M.K. O'Brien, H. Nako, Critical Assessment 17: Mechanisms of hydrogen induced cracking in pipeline steels, *Mater. Sci. Technol.* 31 (2015) 1673–1680.
- [126] W. Li, X. Zhu, J. Yao, X. Jin, X. Ding, Hydrogen Traps and Hydrogen Induced Cracking in 20CrMo Steel, *ISIJ Int.* 57 (2017) 170–175.
- [127] K.W. Brooksbank, D. Abd Andrew, Thermal expansion of some inclusions found in steels and relation to tessellated stresses, *J. Iron Steel Inst.* 206 (1968) 595–599.
- [128] M. Elboudjaini, Susceptibility of Steels containing Cr, Ni, and Mo in H<sub>2</sub>S Environments, *Icf12.* (2009) 1–7.
- [129] R.H. Jones, R.E. Ricker, Mechanisms of stress-corrosion cracking, in: *Stress. Crack. Mater. Perform. Eval.*, 1992: pp. 1–10.
- [130] M. Elboudjaini, Y.Z. Wang, R.W. Revie, Initiation of stress corrosion cracking on X-65 linepipe steels in near-neutral pH environment, in: *Int. Pipeline Conf.*, 2000.
- [131] X.Y. Peng, G.C. Liang, T.Y. Jin, Y.F. Cheng, Correlation of initiation of corrosion pits and metallurgical features of X100 pipeline steel, *Can. Metall. Q.* 52 (2013) 484–487.
- [132] F. Meng, J. Wang, E.H. Han, W. Ke, The role of TiN inclusions in stress corrosion crack

- initiation for Alloy 690TT in high-temperature and high-pressure water, *Corros. Sci.* 52 (2010) 927–932.
- [133] S.M.R. Ziaei, A.H. Kokabi, J. Mostowfi, Failure analysis: Sulfide stress corrosion cracking and hydrogen-induced cracking of A216-WCC wellhead flow control valve body, *J. Fail. Anal. Prev.* 14 (2014) 376–383.
- [134] H.T. N. Tsunekage, Effects of Sulfur Content and Sulfide-forming Elements Addition on Impact Properties of Ferrite–Pearlitic Microalloyed Steels, *ISIJ Int.* 41 (2001) 498–505.
- [135] H. Bhadeshia, R. Honeycombe, The Embrittlement and Fracture of Steels, in: *Steels Microstruct. Prop.*, 4th ed., Elsevier Ltd, 2017: pp. 303–341.
- [136] Y. Murakami, T. Kanazaki, P. Sofronis, Hydrogen embrittlement of high strength steels: Determination of the threshold stress intensity for small cracks nucleating at nonmetallic inclusions, *Eng. Fract. Mech.* 97 (2013) 227–243.
- [137] D. Zhang, Characterisation and modelling of segregation in continuously cast steel slab, Ph.D. thesis, School of Metallurgy and Materials, University of Birmingham, (2015).
- [138] M.A. Mohtadi-Bonab, J.A. Szpunar, S.S. Razavi-Tousi, A comparative study of hydrogen induced cracking behavior in API 5L X60 and X70 pipeline steels, *Eng. Fail. Anal.* 33 (2013) 163–175.
- [139] M.A. Mohtadi-Bonab, J.A. Szpunar, S.S. Razavi-Tousi, Hydrogen induced cracking susceptibility in different layers of a hot rolled X70 pipeline steel, *Int. J. Hydrogen Energy.* 38 (2013) 13831–13841.
- [140] R.E. Lino, Â.M.F. Marins, L.A. Marchi, J.A. Mendes, L.V. Penna, J.G.C. Neto, J.H.P. Caldeira, A.L.V. da Costa e Silva, Influence of the chemical composition on steel casting performance, *J. Mater. Res. Technol.* 6 (2016) 1–7.

## Appendix A ImageJ processing procedure

In this Appendix, the procedure for analyzing inclusions using Image J is described. The version of Image J used in this work is ImageJ 1.51h. The followed steps in this procedure are:

- Open a micrograph with ImageJ
- Set measurement scale (Analyze → Set scale)
- Convert image to 8-bit type image
- Adjust threshold
- Process → Binary → Fill Holes
- Remove noise (Noise → Despeckle)
- Analyze → Set measurements → Check Area, Area fraction, Fit ellipse and Shape descriptors
- Analyze → Analyze particles →



The result is the following table where the 1<sup>st</sup> column indicates the number of the particle, the 2<sup>nd</sup> column indicates the area of the corresponding particle, the 3<sup>rd</sup> column indicates the value of the major axis of the particle (i.e., the length of the particle), the 4<sup>th</sup> column indicates the value of the minor axis of the particle (i.e., the width of the particle) and the 8<sup>th</sup> column indicates the aspect ratio of the particle.

Results										
File	Edit	Font	Results							
	Area	Major	Minor	Angle	Circ.	%Area	AR	Round	Solidity	
1	8.662	3.613	3.053	90.000	1.000	100	1.184	0.845	0.929	
2	8.995	3.883	2.950	140.404	1.000	100	1.316	0.760	0.885	
3	4.664	2.740	2.168	24.358	1.000	100	1.264	0.791	0.848	
4	9.662	4.622	2.661	27.821	0.877	100	1.737	0.576	0.829	
5	8.329	3.973	2.669	24.264	0.954	100	1.488	0.672	0.862	
6	3.998	2.256	2.256	0.000	1.000	100	1.000	1.000	0.857	
7	2.665	2.014	1.685	90.000	0.914	100	1.195	0.837	0.800	
8	7.663	3.396	2.873	59.957	1.000	100	1.182	0.846	0.885	
9	21.654	6.874	4.884	6.888	0.578	100	4.884	0.378	0.748	

## Appendix B Safety precautions in handling H<sub>2</sub>S

### Hazard identification of the test

Hydrogen sulfide H<sub>2</sub>S was used for both the SSRT and HIC experiments. It is a toxic, flammable liquid and gas under pressure. It is responsible for more industrial poisoning accidents than is any other single chemical. It could be fatal if inhaled. It can form explosive mixtures with air and may cause respiratory tract and central nervous system damage. The OSHA maximum allowable concentration of H<sub>2</sub>S in air for an eight-hour work day is 20 ppm, well above the level detectable by smell. However, the olfactory nerves can become deadened to the odor after exposure of 2 to 15 minutes. Thus the odor is not completely reliable alarm system. Table B.1 summarizes the health effects from short-term exposure to hydrogen sulfide.

Table B.1: Health effects from short-term exposure to hydrogen sulfide.

<b>Concentration in ppm</b>	<b>Health effect</b>
<b>0.01-0.3</b>	Odor threshold
<b>1-20</b>	Offensive odor; possible nausea; tearing of eyes; headaches
<b>20-50</b>	Nose, throat and lung irritation; loss of appetite; acute conjunctivitis
<b>100-200</b>	Severe nose, throat and lung irritation; loss of sense of smell
<b>250-500</b>	Pulmonary edema
<b>500</b>	Severe lung irritation; dizziness; unconsciousness within 15 minutes and death within 30 minutes
<b>500-1000</b>	Respiratory paralysis, irregular heartbeat, collapse and death
<b>&gt;1000</b>	Instantaneous unconsciousness, complete respiratory failure, cardiac arrest and death

Additional information on the toxicity of H<sub>2</sub>S can be obtained from the Chemical Safety Data Sheet SD-36. The MSDS information on glacial acetic acid and sodium hydroxide must be read.

Corrosive, flammable and toxic chemicals should be handled with precaution and in a well-ventilated fume hood. Personal protective equipment (PPE) should be worn: safety glasses, rubber gloves, respirator etc.

### **Training required**

All the personnel performing the test should be familiar with NACE TM0177, ASTM G129 and NACE TM0198 standards and the MSDS sheets of the chemicals used in the test. They should be WHMIS trained, know how to use the PPE and how to act in emergency situations.

### **Safety procedures during testing**

- The test shall be performed in a fume hood with adequate ventilation to exhaust all of the H<sub>2</sub>S. The fume hood should be usually checked. This can be done by holding a kimwipe at the face of the hood and observing the draw into the hood. The test will be performed in the fume hood in CME213.
- Before starting the test, warning signs 'Hazardous Gas Test is in Progress. Do not enter and call Saoussen immediately if the alarm goes off!' will be posted on both doors of the lab to restrict access. Make sure that all the persons in the lab CME 213 are aware of the H<sub>2</sub>S test and review emergency response procedure with them before starting the test. Remind them to evacuate the lab as soon as they hear the alarm. Keep a written record of the training.
- Ensure the area around the fume hood is clear to allow enough space to perform the experiment.
- The H<sub>2</sub>S gas cylinder and the SSRT machine should be inside the fume hood.
- There must be three 'Altair' H<sub>2</sub>S detectors in the test area. The first one is inside the fume hood near the SSRT machine. The second one is located on the floor near to the fume hood. The third one should be carried by the person performing the test. If H<sub>2</sub>S level reaches 10 ppm, the detectors will produce a loud sound and flashing light signal. If any one of those detectors is on alarm, the valve of the H<sub>2</sub>S bottle should be turned off immediately and all personnel should evacuate the test area. Keep a record of when the detectors have been checked and recalibrated by our instrument shop.
- The sash on the fume hood should be maintained as low as possible at all times.

- 2L of 25% NaOH solution should be used as a scrubber.
- Ensure the scrubber solution is clear and replace it when it turns milky.
- Because H<sub>2</sub>S is in liquid form in the cylinders, the high pressure gauge on the cylinder must be checked frequently. The cylinder shall be replaced by the time it reaches 0.5 to 0.7 MPa (75 to 100 psi) because the regulator may become erratic.
- Ensure the flow of H<sub>2</sub>S in the solution is very slow for the duration of the test (1 or 2 bubbles per second).
- Ensure the stop valves and the safety valves are connected properly.
- The fire extinguisher must be at the test area, no open flames should be used in the lab and all the electrical equipment must be in spark-proof performance.
- PPE must be worn when performing the test: lab coat, safety glasses, rubber gloves and a suitable cartridge respirator.
- Turn off the gas flow of the cylinder when the test finishes.
- Dispose the test solution and the scrubber as hazardous waste when the test finishes.

### **Emergency procedure**

When one of the three H<sub>2</sub>S detectors is on alarm, close the valve at the H<sub>2</sub>S bottle and evacuate all personnel from the lab. The University of Alberta Environment, Health and Safety Office should be reported at [780-492-7790](tel:780-492-7790). The leak of H<sub>2</sub>S must be documented and a copy should be given to Mrs. Andree Koenig.

### **Hazardous waste disposal**

All hazardous waste should be disposed through the University Hazardous Waste Management System. All the chemical waste should be packed properly and labelled with the name of the hazardous product. Hazardous waste pick-up are made through CHEMATIX. The name of the waste must be filled out in full.



## Appendix C Vickers micro-hardness results

Appendix C.1, C.2, C.3 and C.4 show respectively Vickers micro-hardness profile of TiB, High Mn, MnCr and SMLS steels. For ERW pipes (i.e., TiB, High Mn, MnCr), the Vickers micro-hardness profiles were taken vertically across the centerline segregation band. For SMLS pipe, the Vickers micro-hardness profile was taken from the inner surface to the center of the pipe.

### Appendix C.1

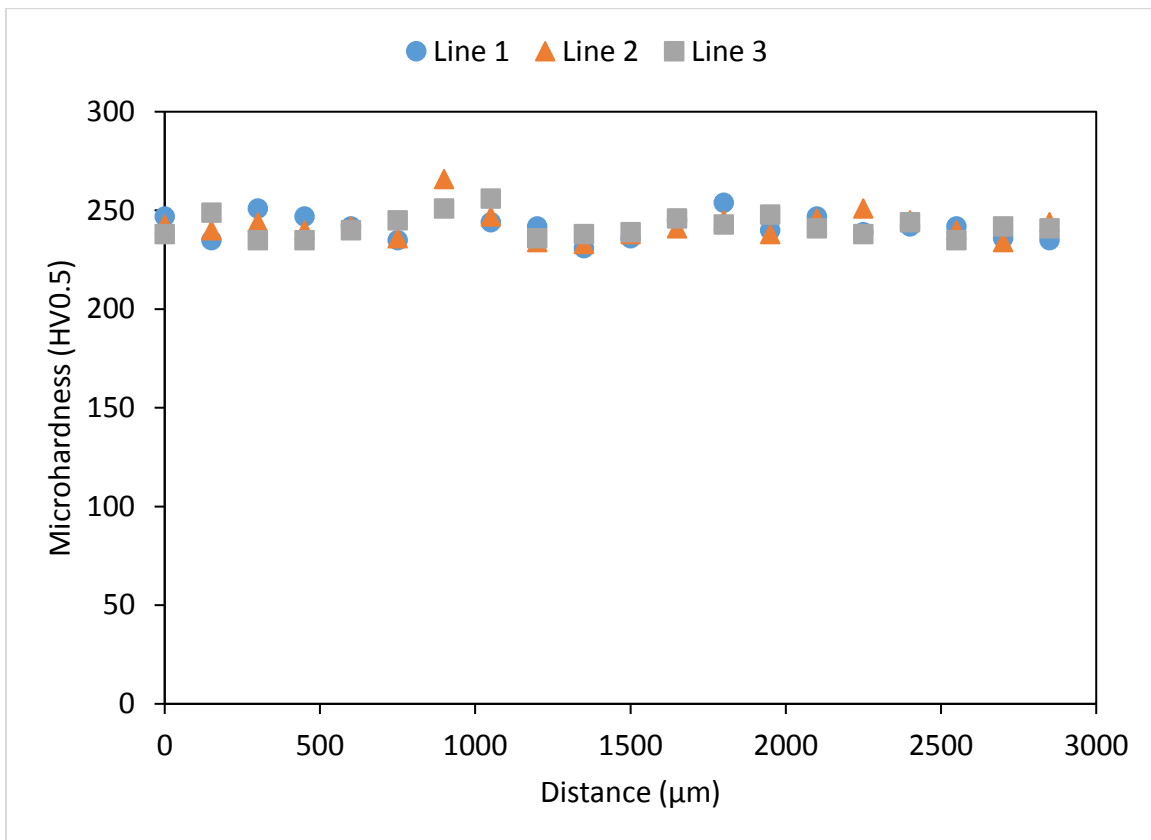


Figure C.1: Vickers Micro-hardness profile across the centerline band in TiB steel.

## Appendix C.2

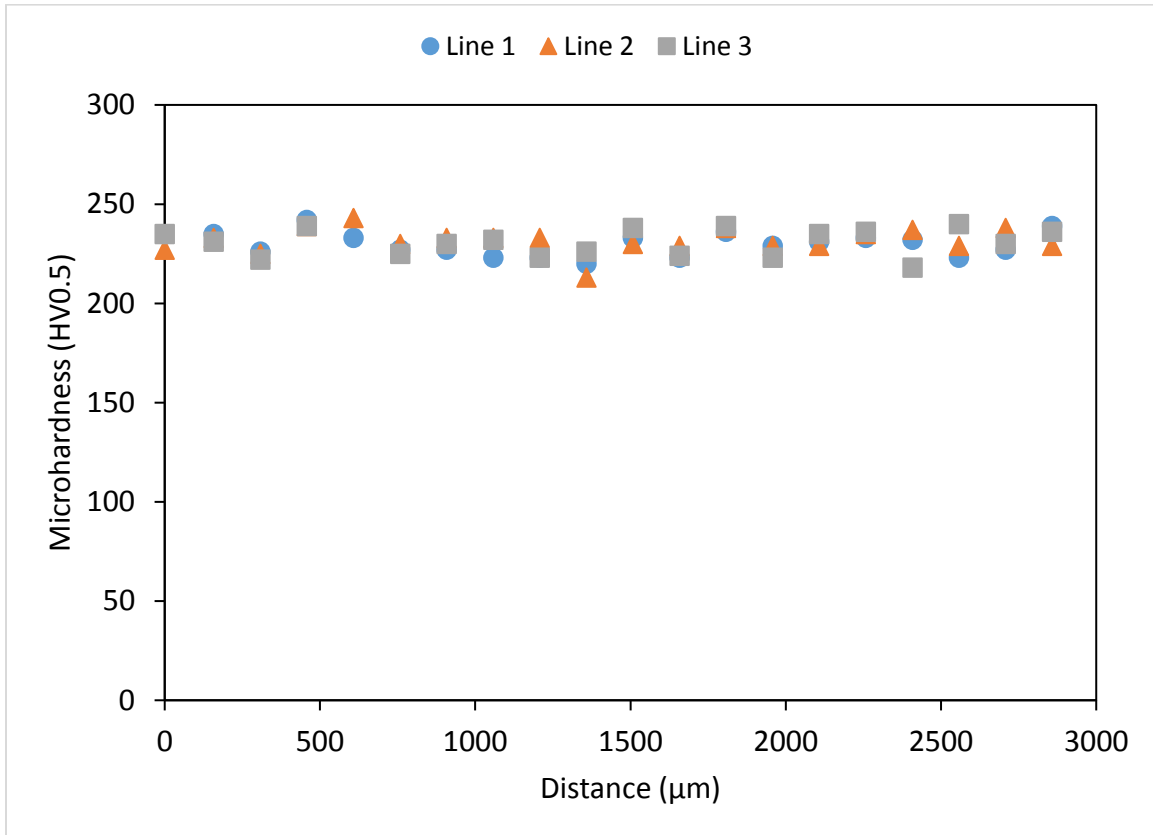


Figure C.2: Vickers micro-hardness profile across the centerline band in High Mn steel.

Appendix C.3

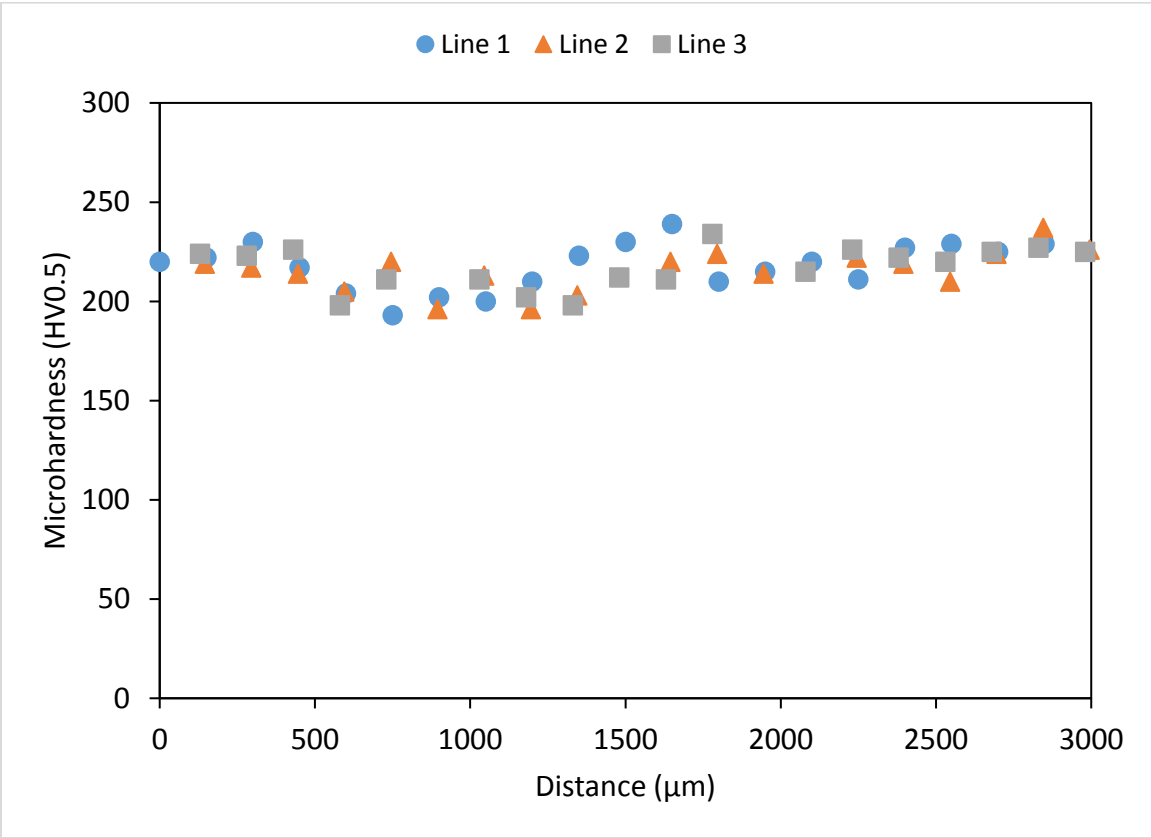


Figure C.3: Vickers micro-hardness profile across the centerline band in MnCr steel.

### Appendix C.4

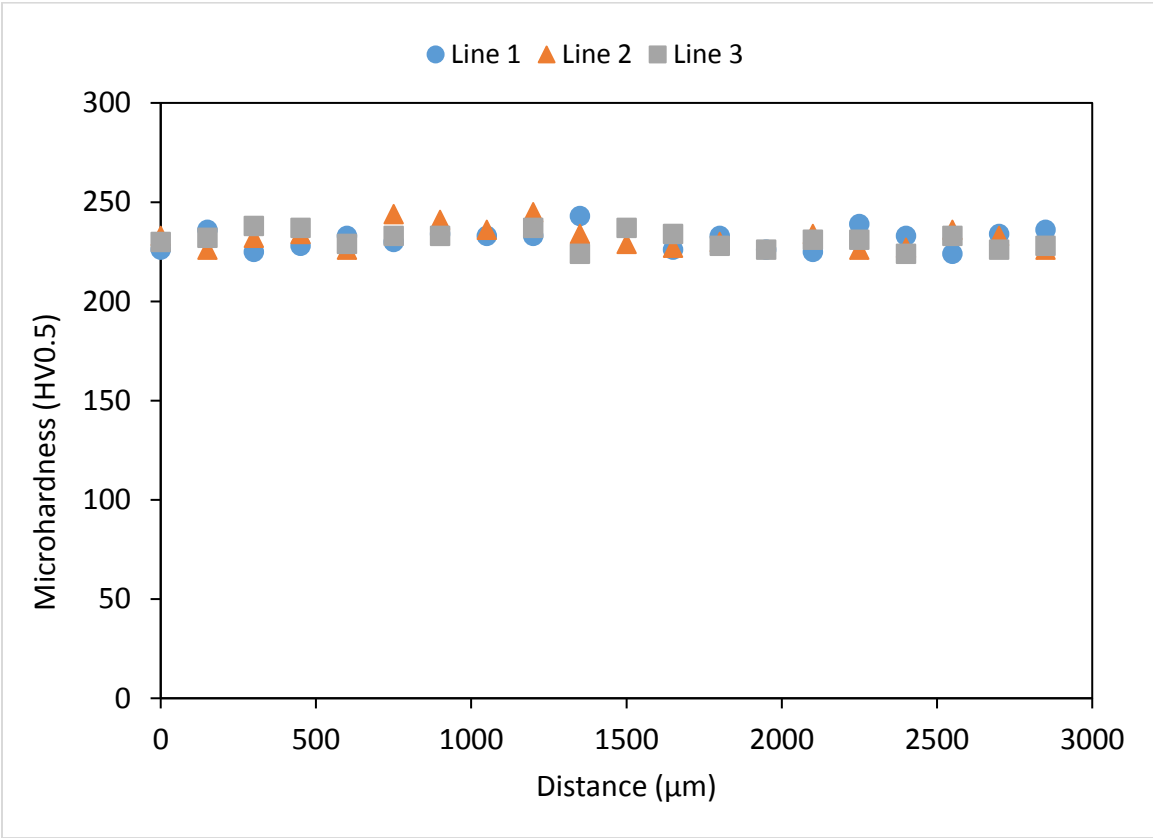


Figure C.4: Vickers micro-hardness profile from the inner surface to the center of the pipe in SMLS steel.

## Appendix D HIC parameters (CLR, CTR, CSR) results

The values of CLR, CTR and CSR at different locations (i.e., weld, 90° and 180° for ERW pipes and 0°, 120° and 240° for SMLS pipe) are included in this appendix.

### Appendix D.1

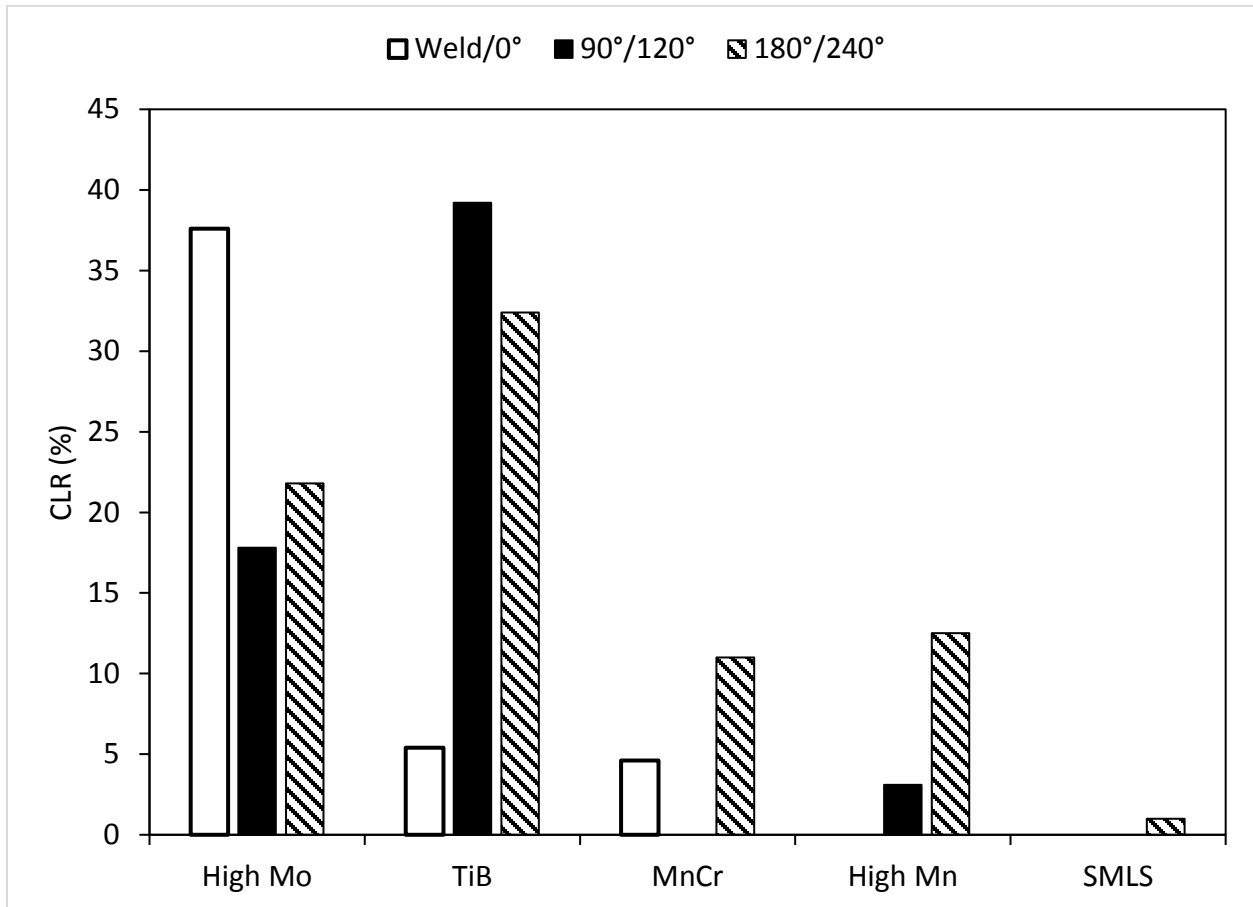


Figure D.1: CLR (%) values measured at different locations in the pipe for the HIC tested L80 steels.

Appendix D.2

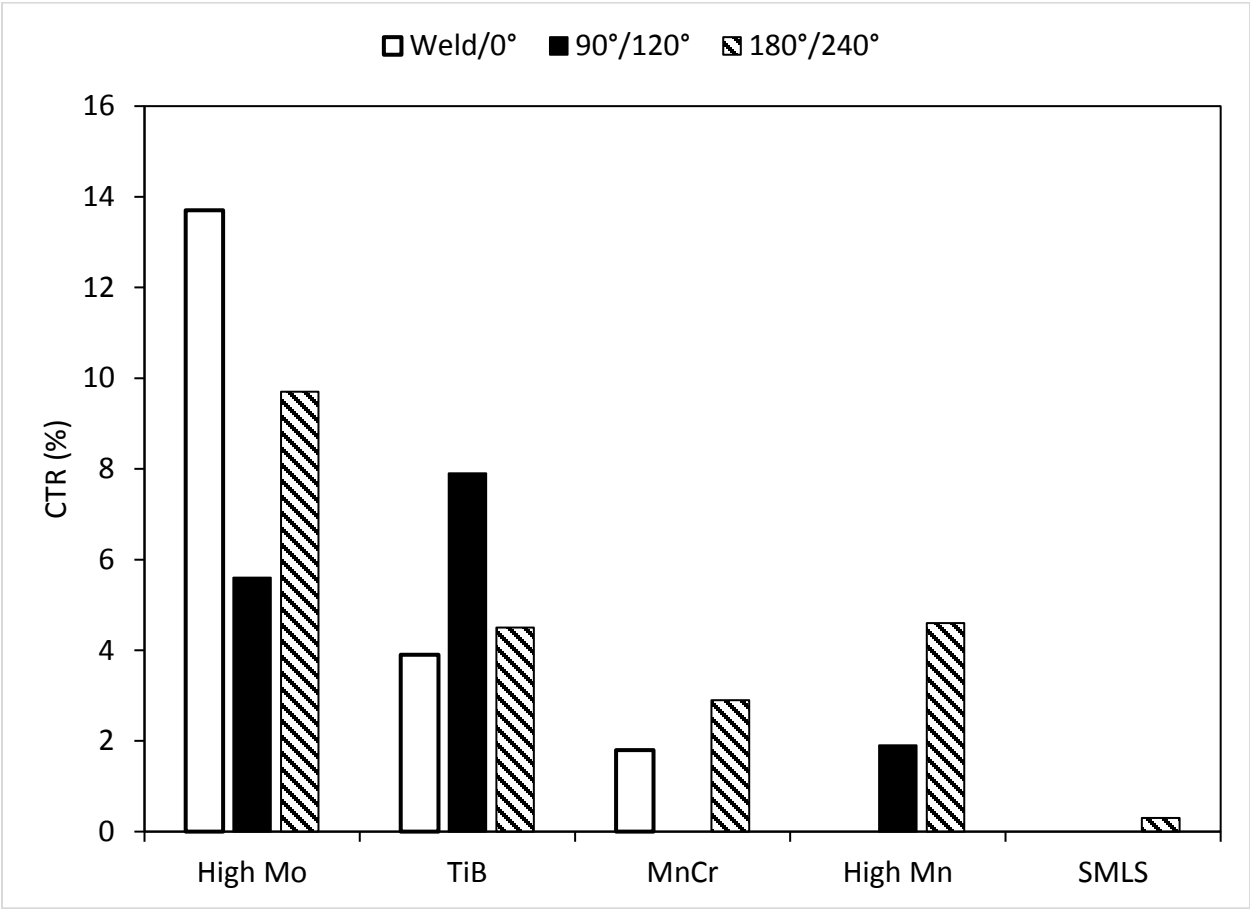


Figure D.2: CTR (%) values measured at different locations in the pipe for the HIC tested L80 steels.

Appendix D.3

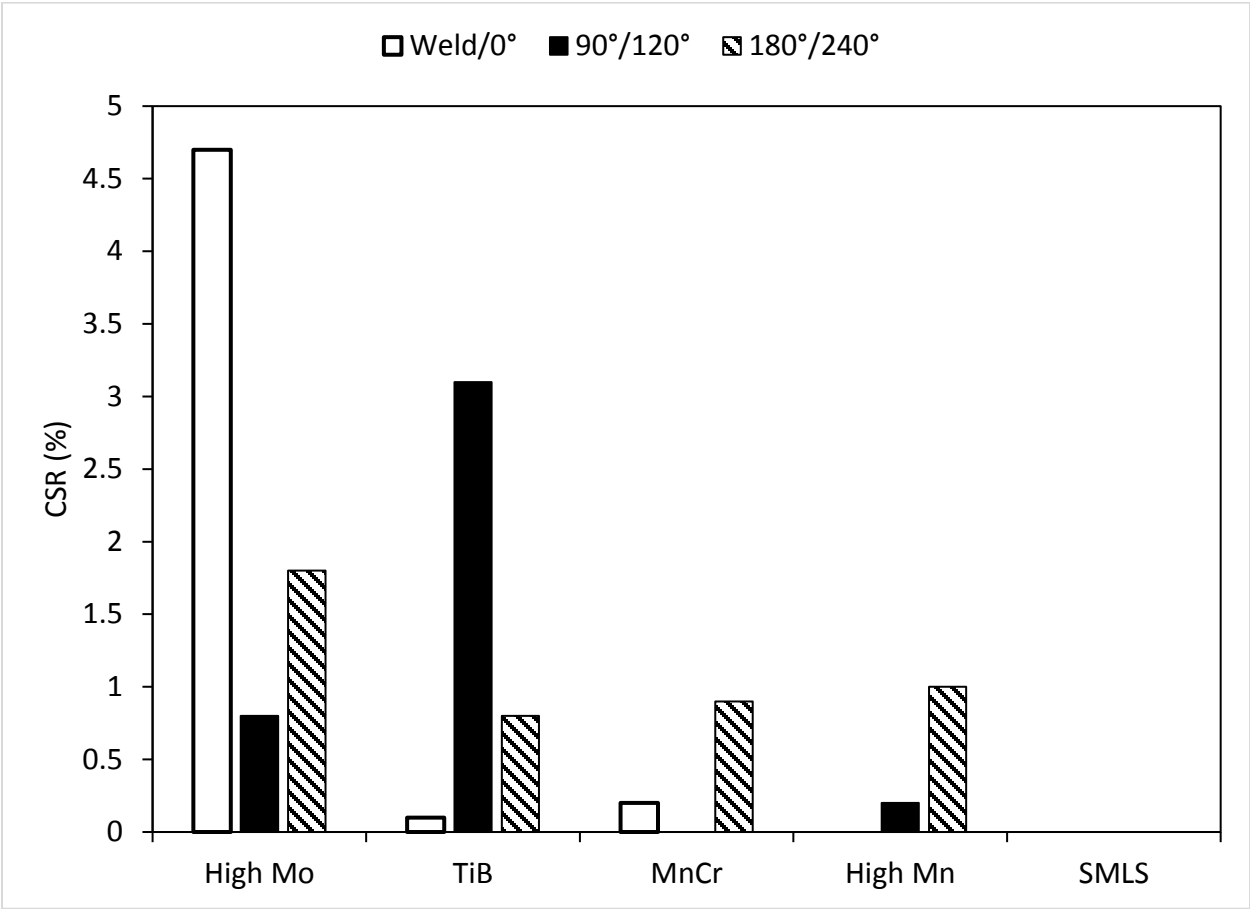


Figure D.3: CSR (%) values measured at different locations in the pipe for the HIC tested L80 steels.

## Appendix E Morphologies of HIC cracks

Examples of observed HIC cracks in L80 steels are presented in this appendix. The HIC cracks are mainly located at the center of the samples and have a stepwise appearance.



Figure E.1: Optical micrograph of a HIC crack observed in a section cut at 90° from High Mo steel.

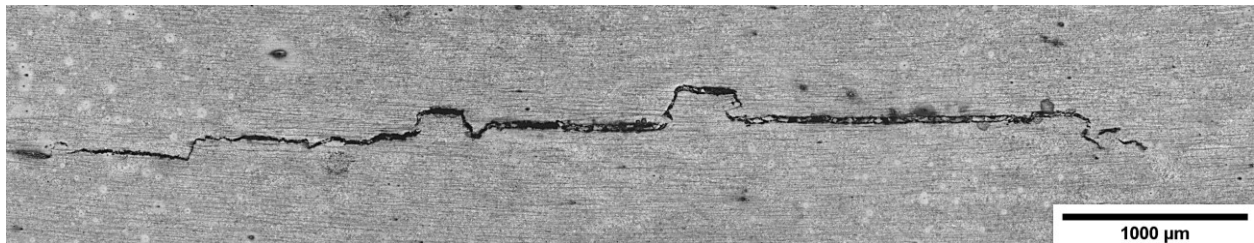


Figure E.2: Optical micrograph of a HIC crack observed in a section cut at 180° from High Mn steel.

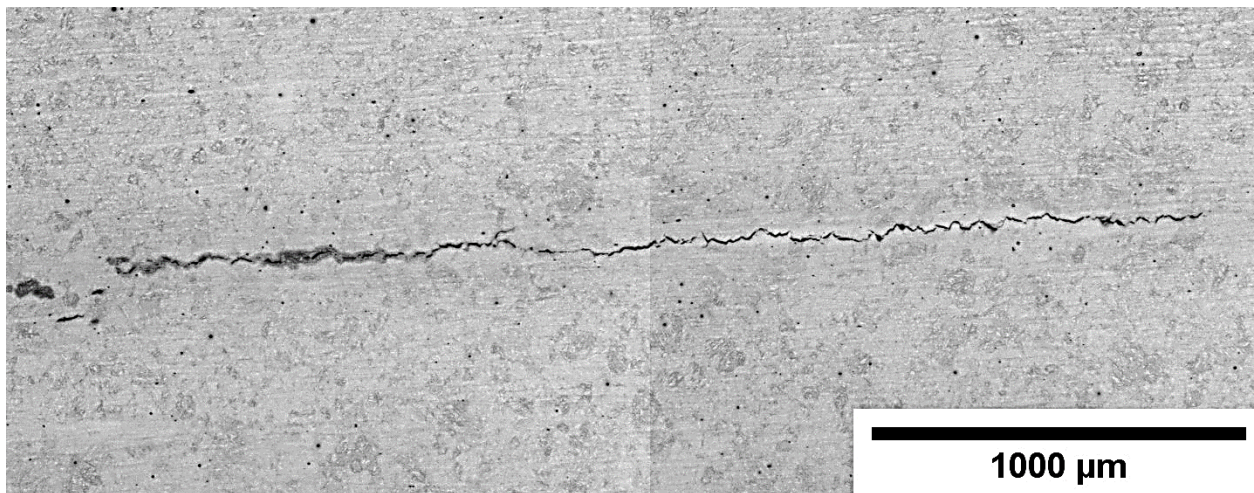


Figure E.3: Optical micrograph of a HIC crack observed in a section cut at 180° from TiB steel.



## Appendix F SSRT results of samples tested in air and H<sub>2</sub>S solution

Stress versus crosshead displacement curves of L80 steels are presented in this appendix. For each type of steel, two SSRT tests were performed in air and two SSRT tests were performed in NACE A solution saturated with H<sub>2</sub>S.

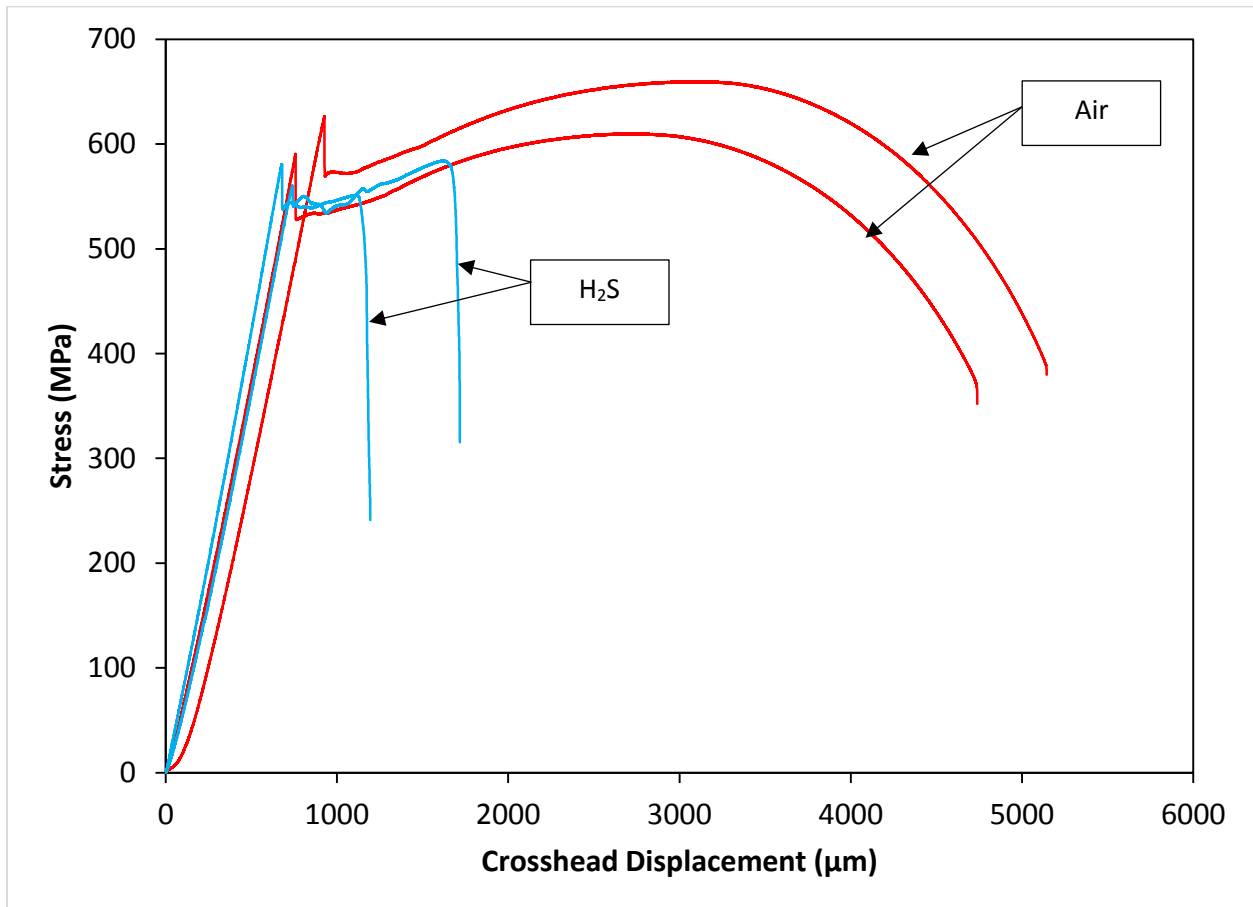


Figure F.1: Stress versus crosshead curves for MnCr steel.

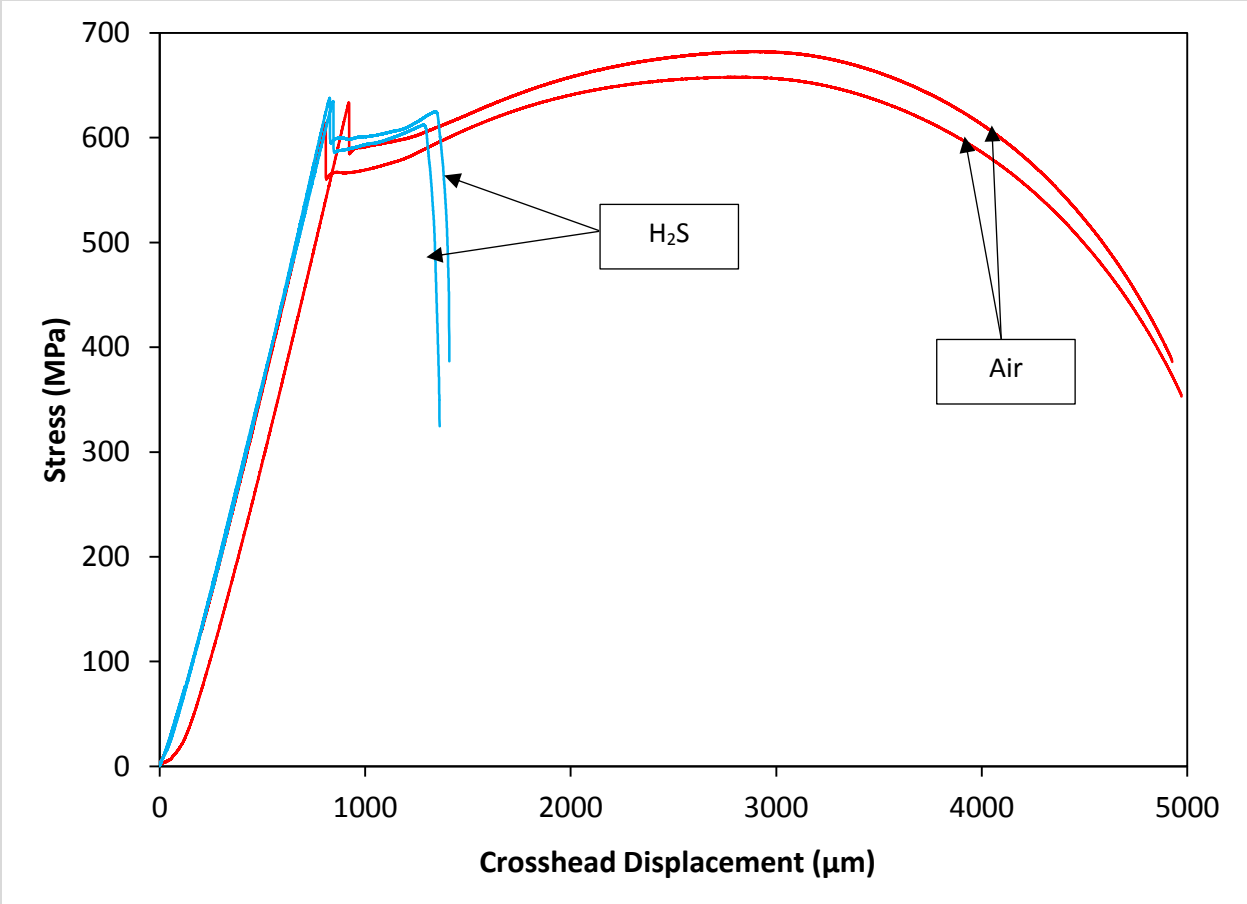


Figure F.2: Stress versus crosshead displacement curves for SMLS steel.

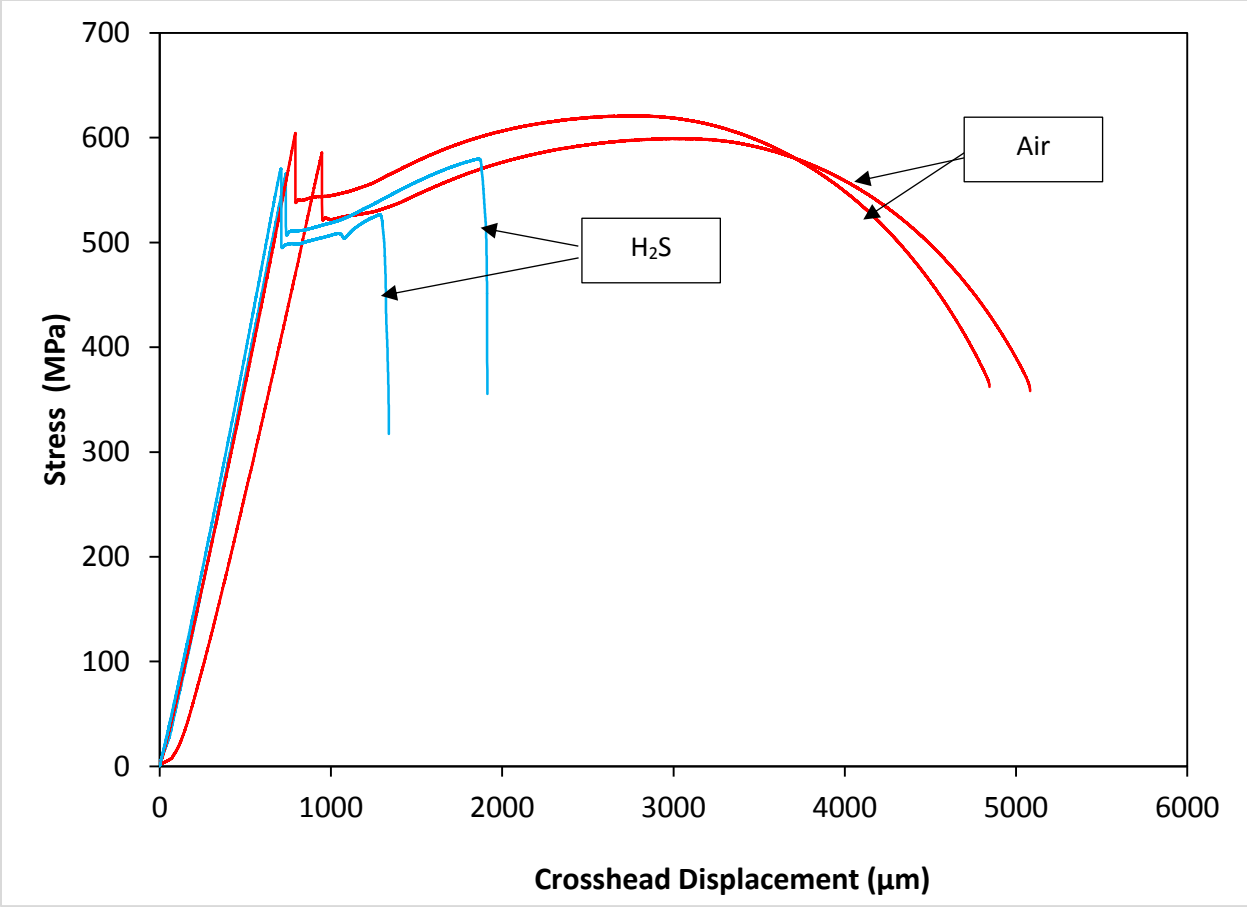


Figure F.3: Stress versus crosshead displacement curves for High Mn steel.

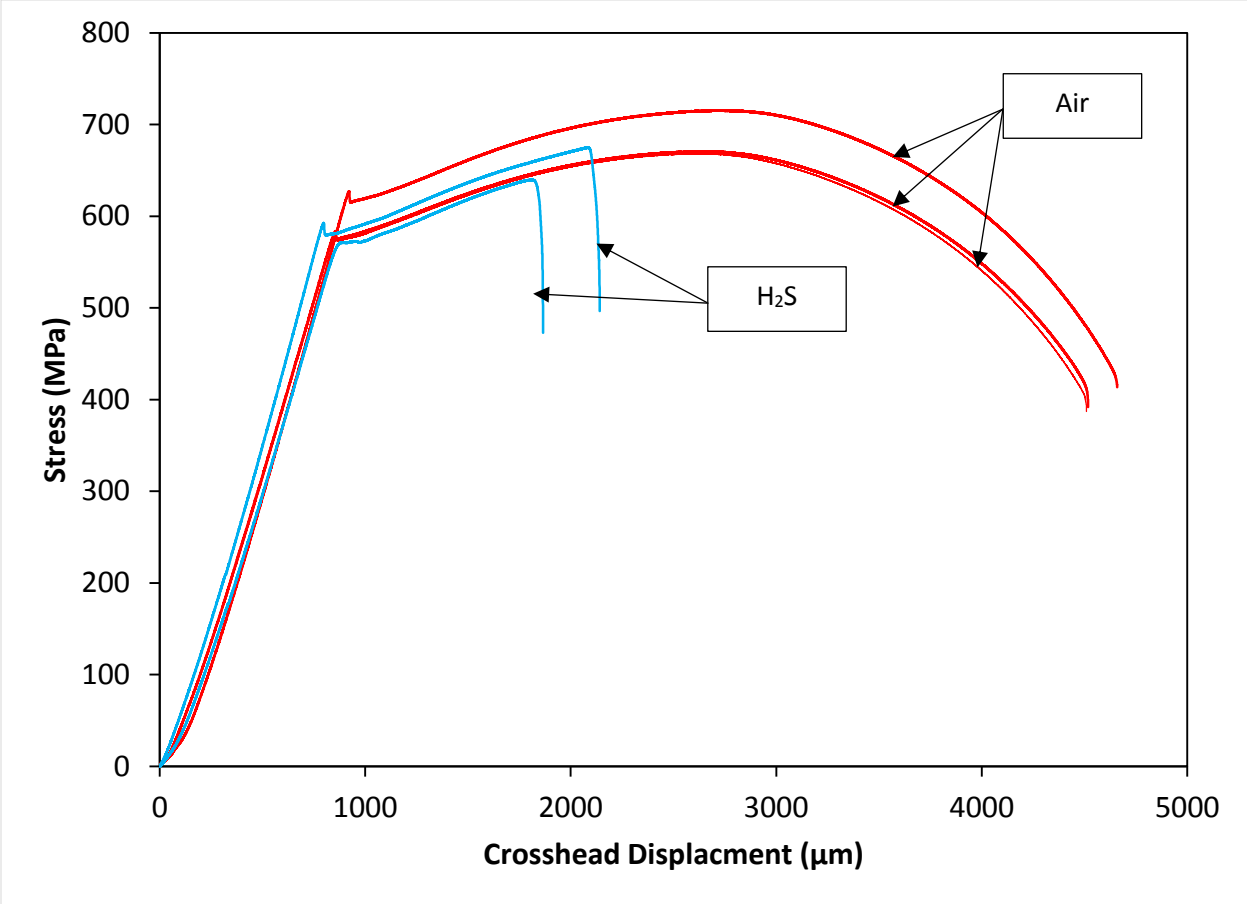


Figure F.4: Stress versus crosshead displacement curves for TiB steel.

## Appendix G Representative fractographs of SSRT samples

The fracture surfaces of the SSRT samples tested in air and in NACE A solution saturated with H<sub>2</sub>S are presented in this appendix.

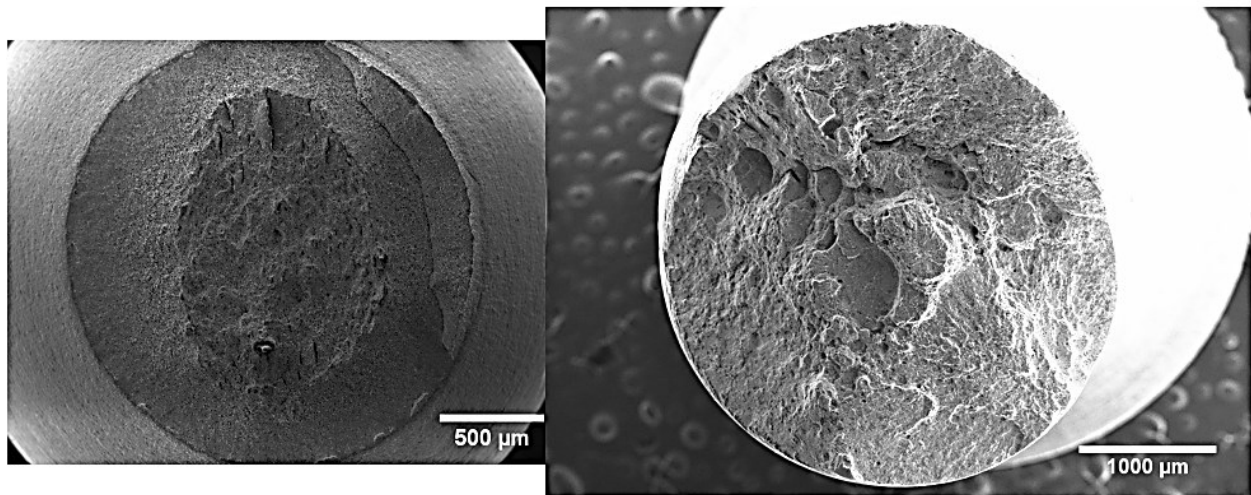


Figure G.1: SEM images of the fracture surface of MnCr steel in air (left) and in H<sub>2</sub>S (right).

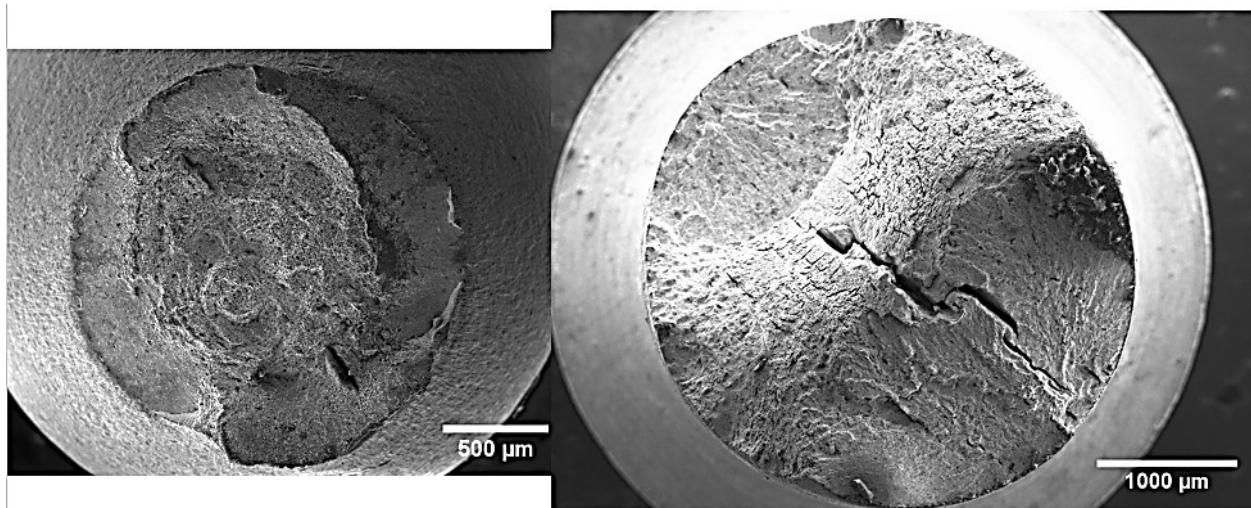


Figure G.2: SEM images of the fracture surface of High Mo steel in air (left) and in H<sub>2</sub>S (right).

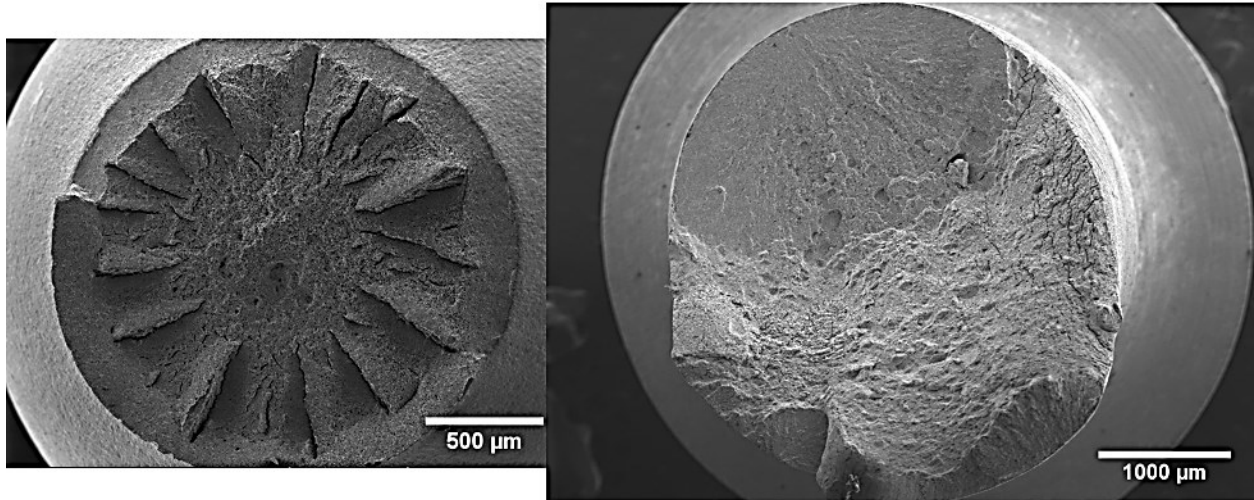


Figure G.3: SEM images of the fracture surface of SMLS steel in air (left) and in H<sub>2</sub>S (right).

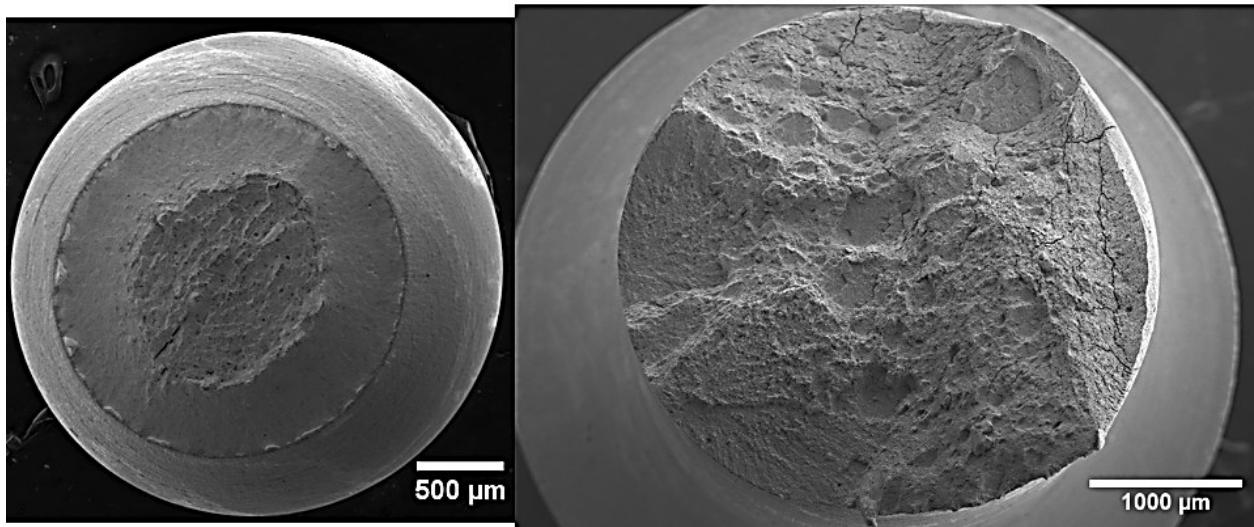


Figure G.4: SEM images of the fracture surface of High Mn steel in air (left) and in H<sub>2</sub>S (right).

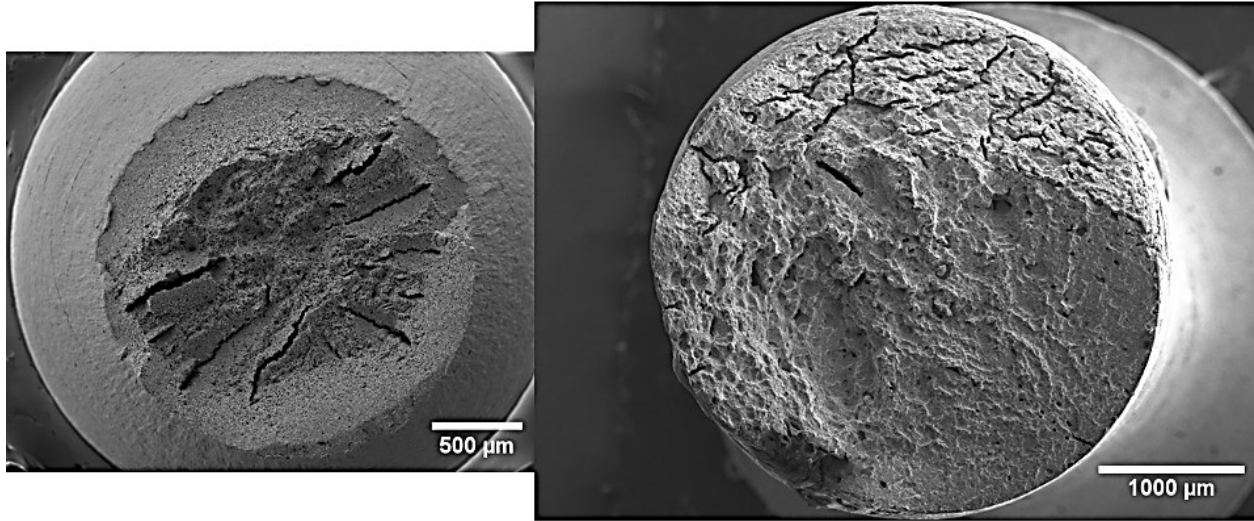


Figure G.5: SEM images of the fracture surface of TiB steel in air (left) and in H<sub>2</sub>S (right).

Appendix H Dispersion of inclusions

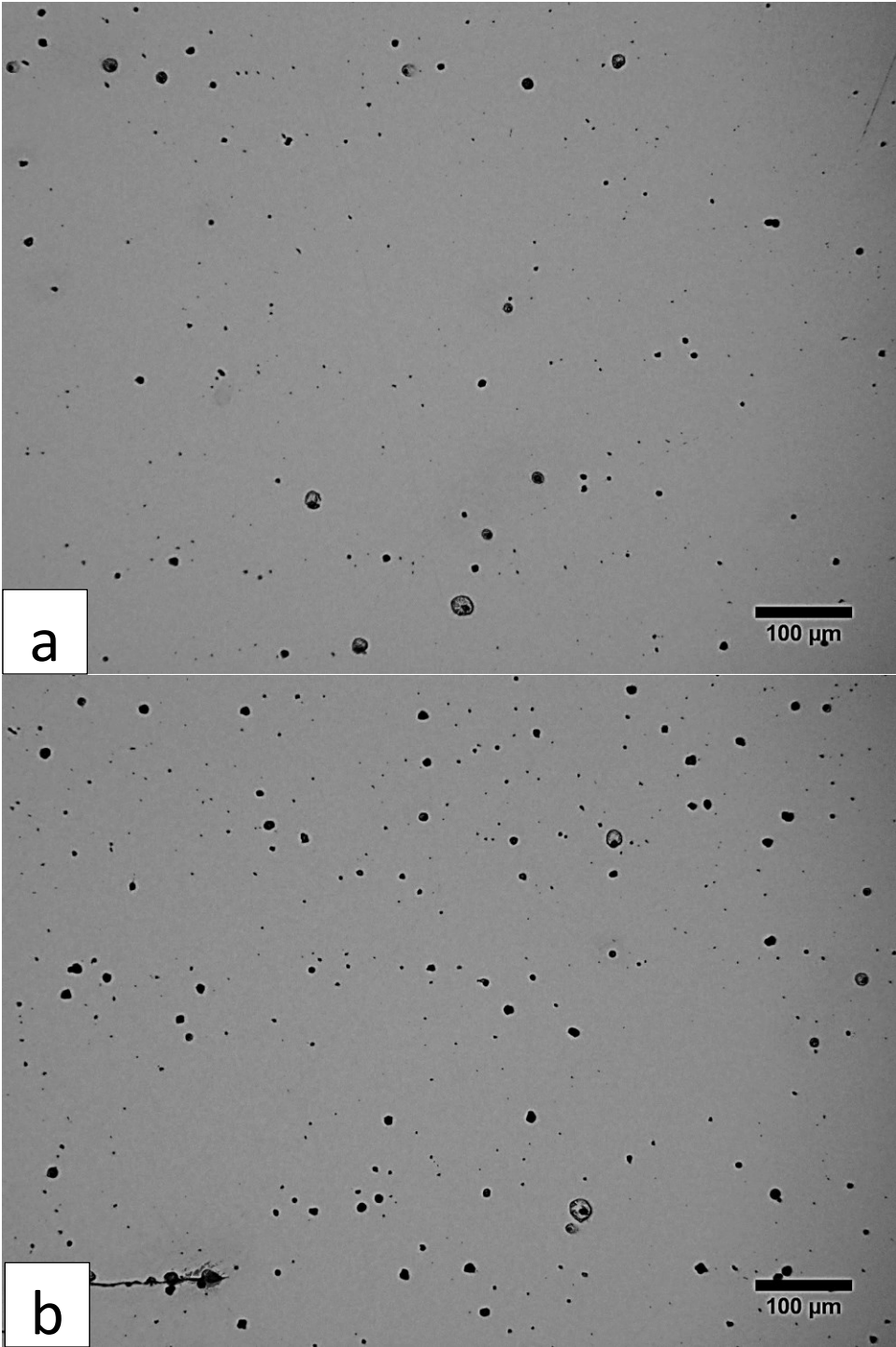


Figure H.1: Two optical micrographs taken in High Mo pipe at 90° from the weld and at the center of the pipe and adjacent to each other showing different distributions of inclusions, (a) shows a lower number of inclusions, (b) shows a higher number of inclusions.



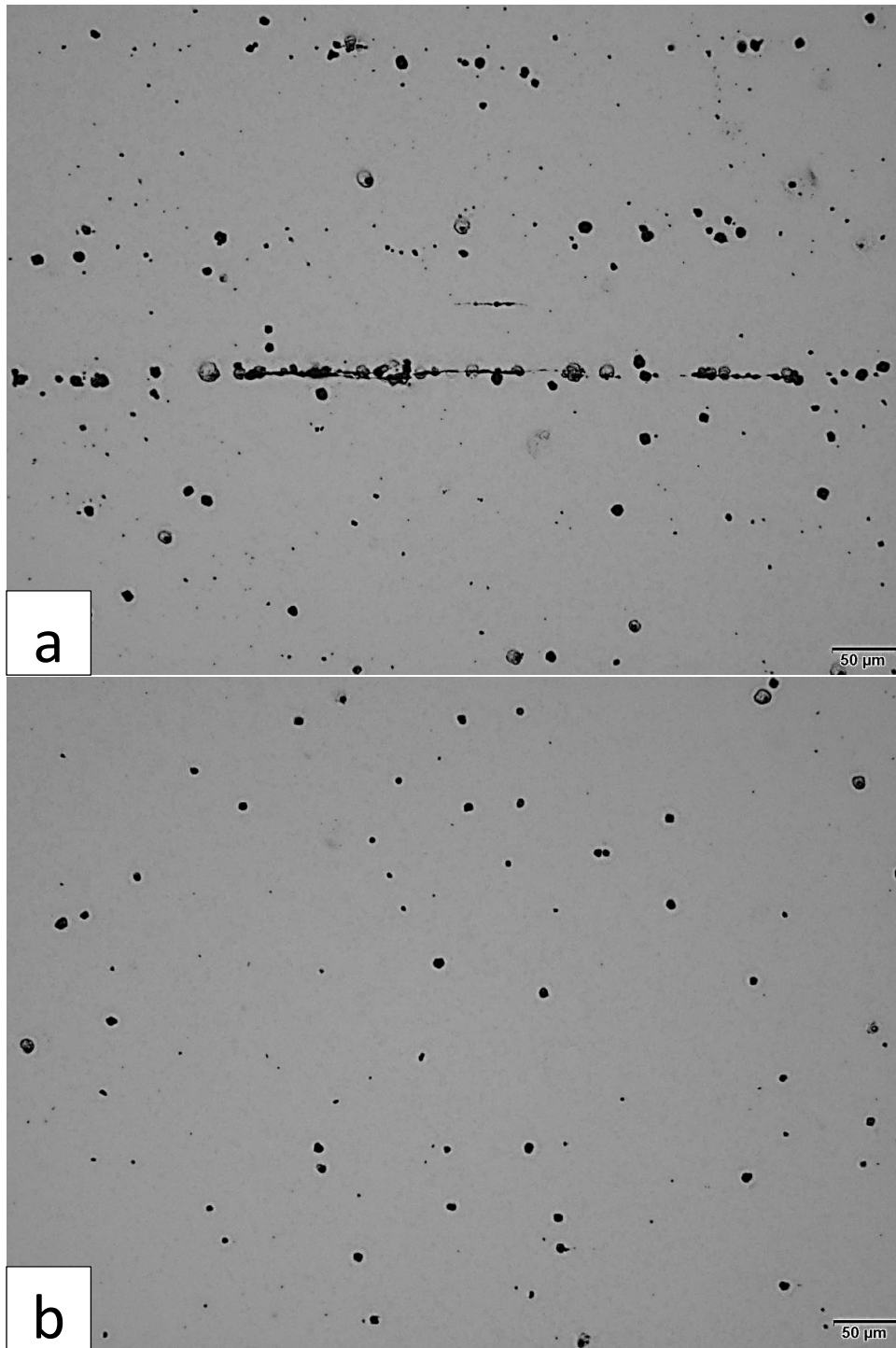


Figure H.2: Optical micrograph taken at (a) centerline and (b) close to the pipe wall in High Mo steel.

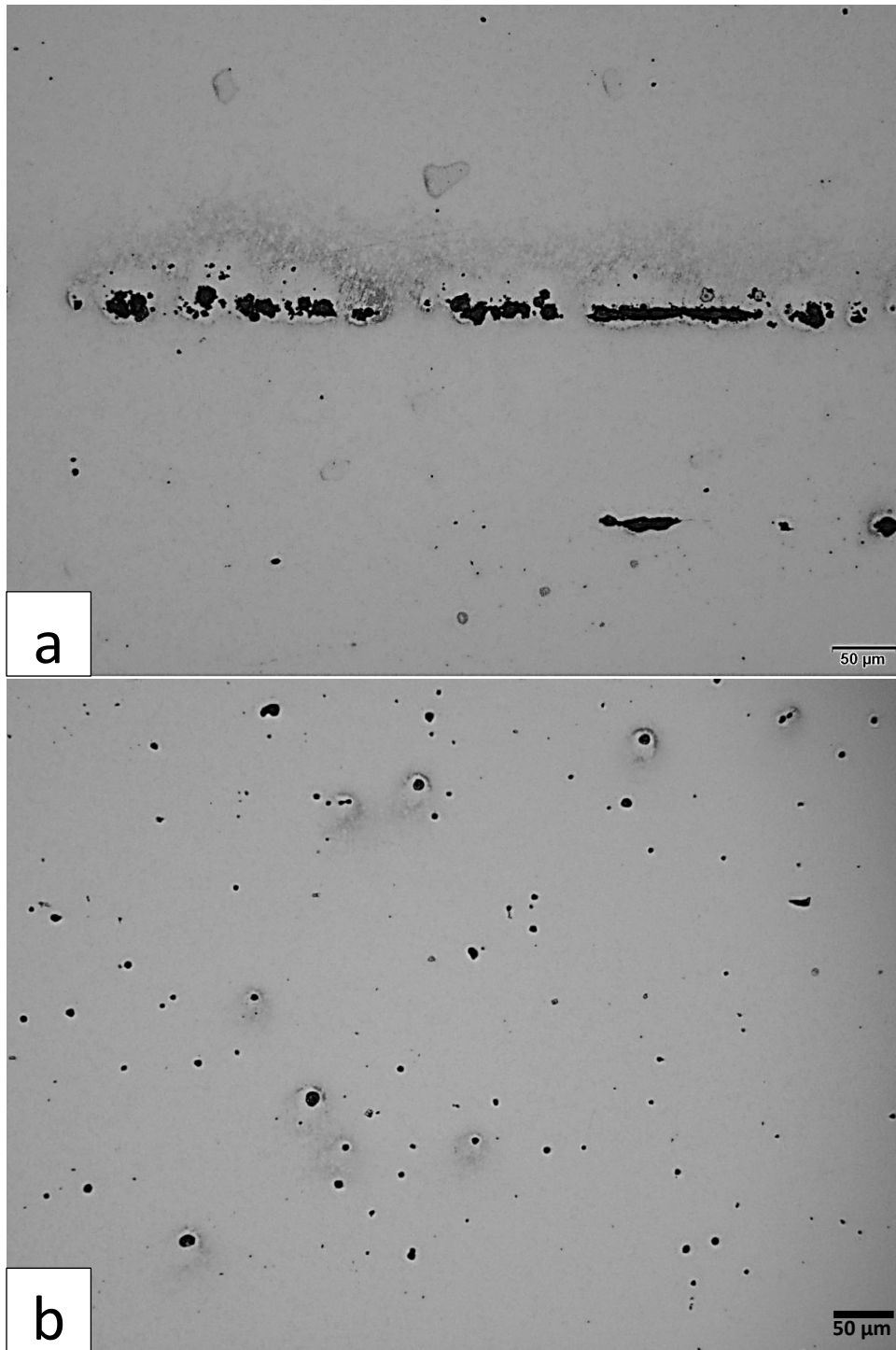


Figure H.3: Optical micrograph taken at (a) centerline and (b) close to the pipe wall in TiB steel.

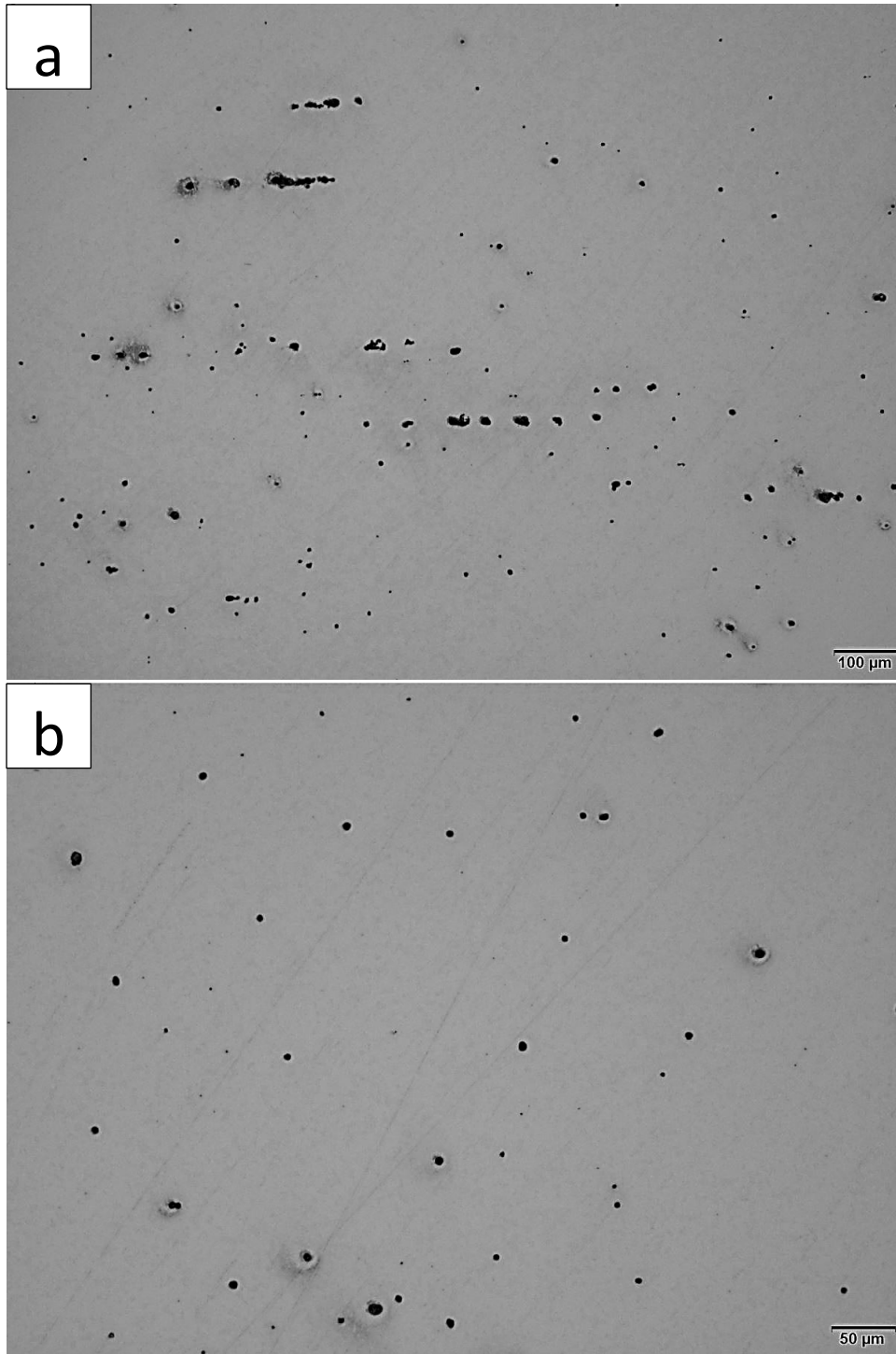


Figure H.4: Optical micrograph taken at (a) centerline and (b) close to the pipe wall in MnCr steel.

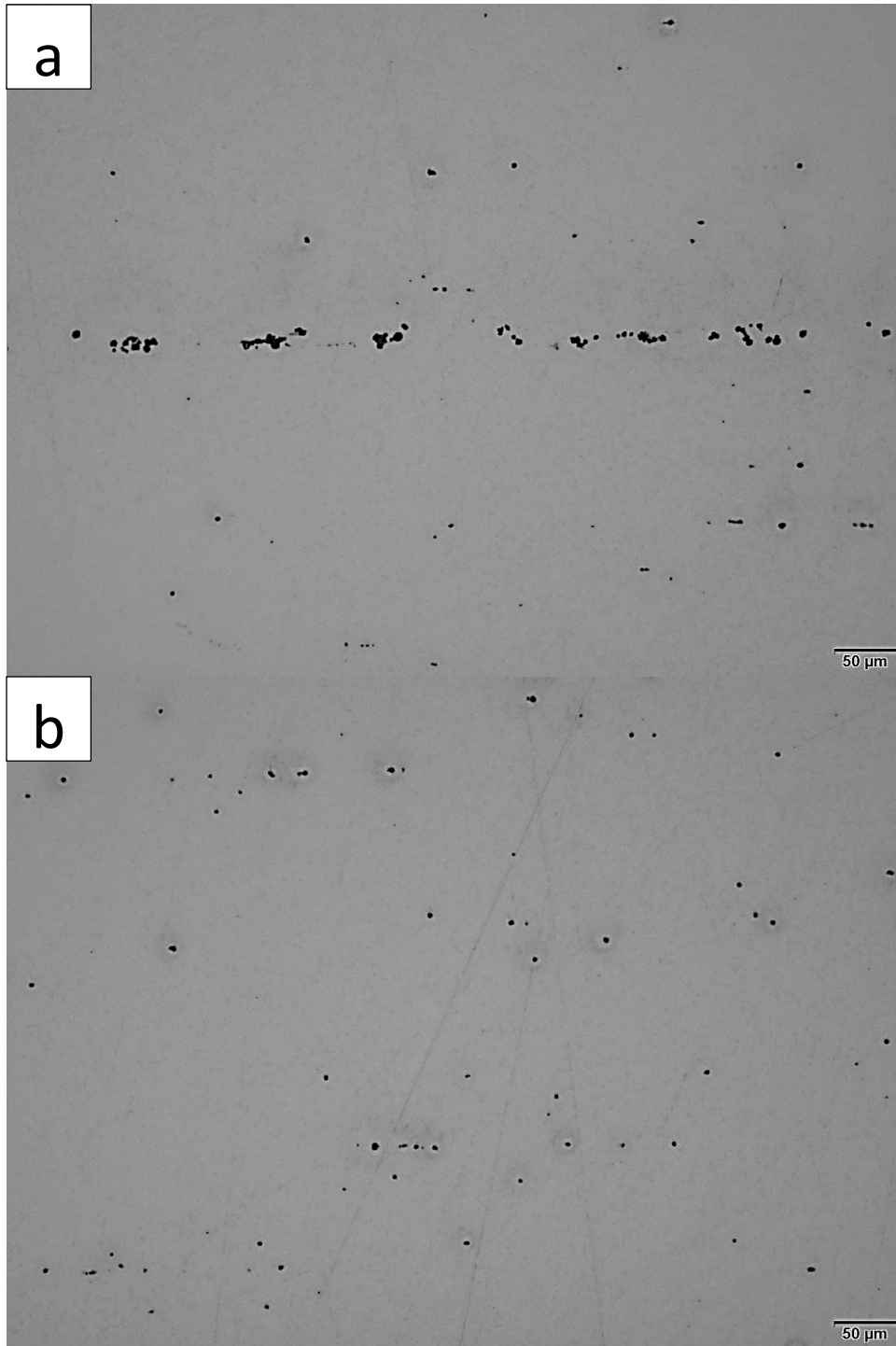


Figure H.5: Optical micrograph taken at (a) centerline and (b) close to the pipe wall in High Mn steel.

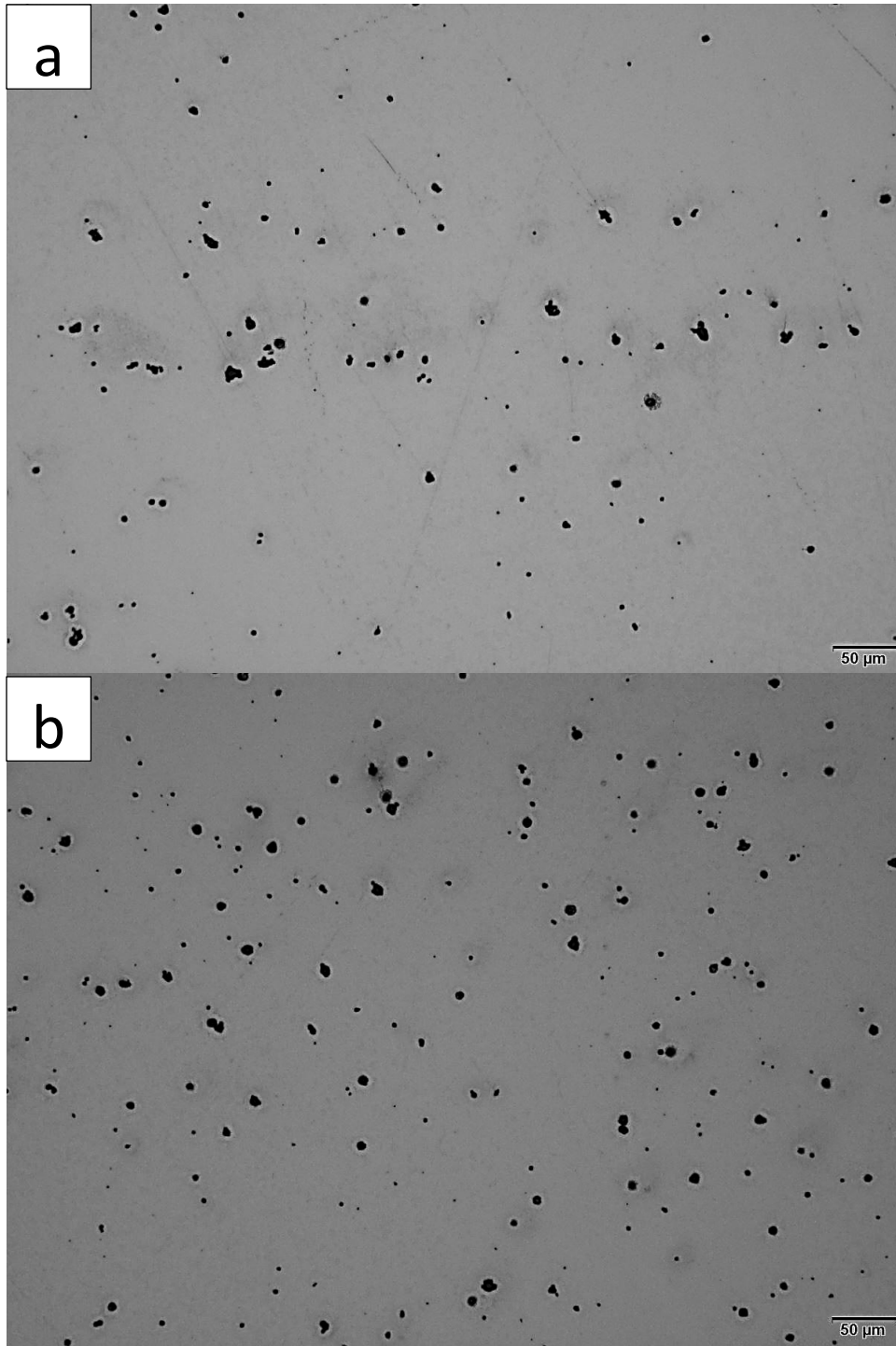


Figure H.6: Optical micrograph taken at (a) centerline and (b) close to the pipe wall in SMLS steel.

## Appendix I EMPA results

EMPA results including Mn X-ray maps and Mn, Cr, Si and P line scans for MnCr 180° Section 3, High Mn 180° Section 2 and TiB 90° Section 2 are presented in this appendix.

### Appendix I.1

This appendix shows EMPA results for MnCr 180° Section 3. MnCr 180° Section 3 means that the analyzed section was the third section taken from a HIC sample cut at 180° from MnCr pipe. Figure I.1 shows Mn EMPA X-ray map performed across the total thickness of MnCr 180° Section 3. It is clear that the HIC crack is located at the centerline segregation band. The lighter zones indicate a higher concentration of Mn.

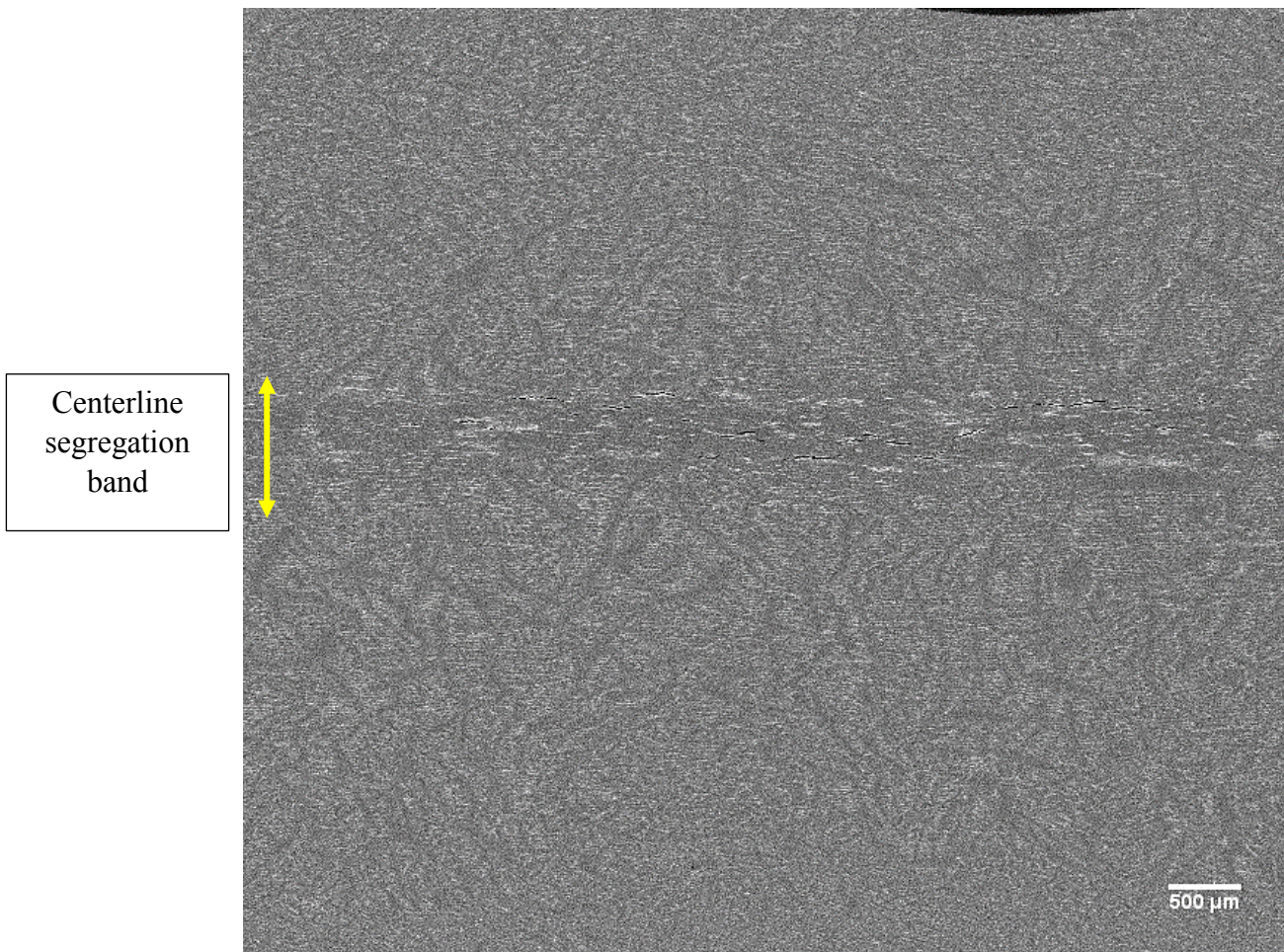


Figure I.1: Mn EMPA X-ray map across the total thickness of MnCr 180° Section 3.

Mn EMPA X-ray map of a small area around a portion of the HIC crack in Figure I.1 is shown in Figure I.2.

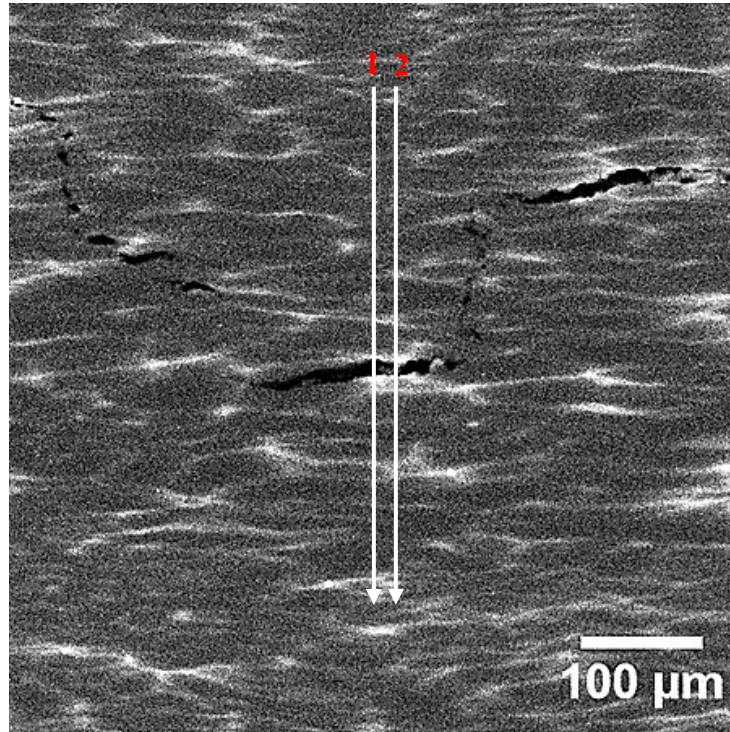


Figure I.2: Mn EMPA X-ray map of a small area around a HIC crack in MnCr 180° Section 3.

Two EMPA line scans indicated by the arrows in Figure I.2 were performed and the detected elements were Mn, Cr, Si and P. The concentrations profiles of these elements across the HIC crack obtained from these two line scans are shown in the following figures in Appendix I.1.

Figure I.3 shows the Mn concentration profile along the line scans 1 and 2. A concentration peak of Mn ( $\approx 1.8$  wt%) is found around the HIC crack. The HIC crack is represented by the dashed arrow.

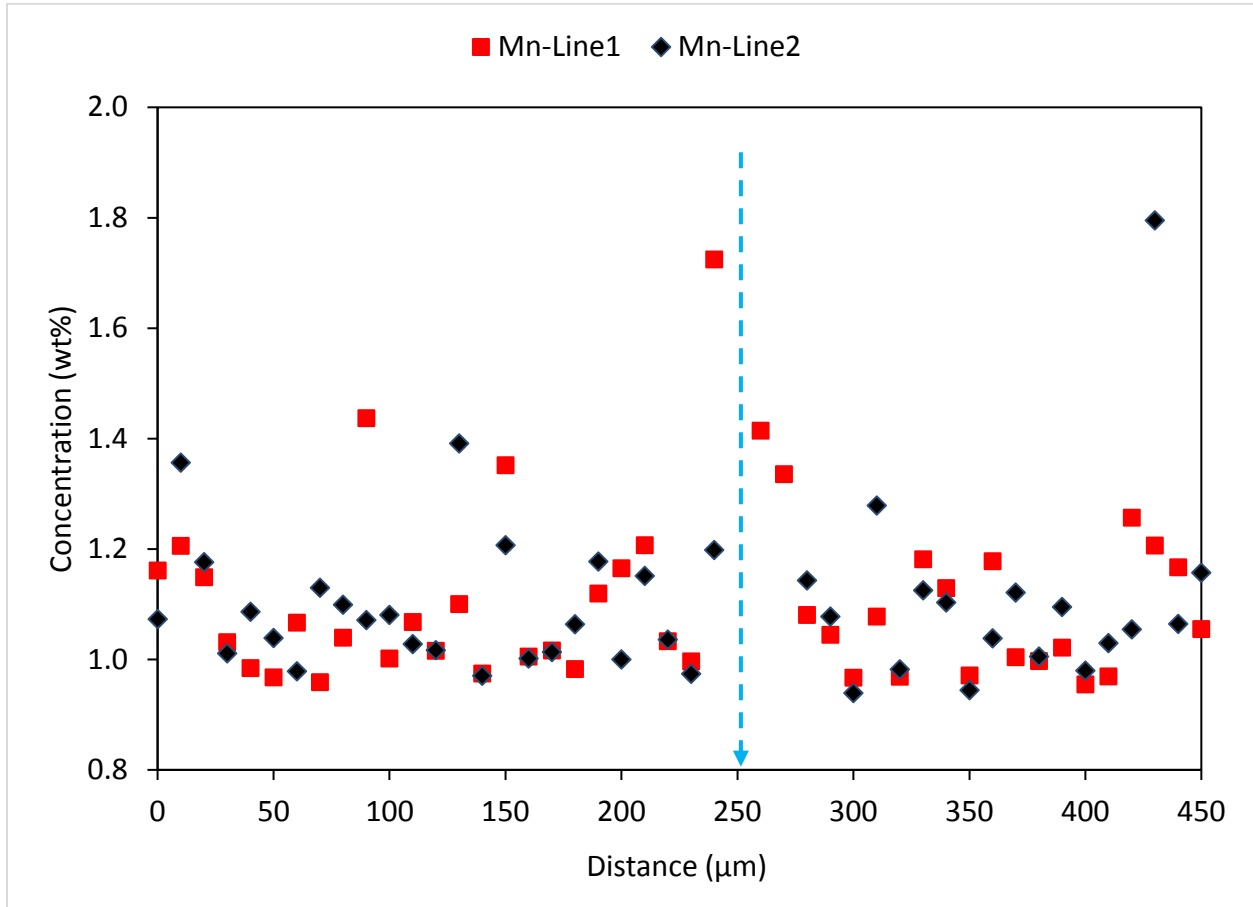


Figure I.3: Mn concentration profile along the line scans 1 and 2 shown in Figure I.2.



Figure I.4 shows Cr concentration profile along the line scans 1 and 2. A higher concentration of Cr ( $\approx 0.4$  wt%) is observed around the HIC crack. The HIC crack is represented by the dashed arrow.

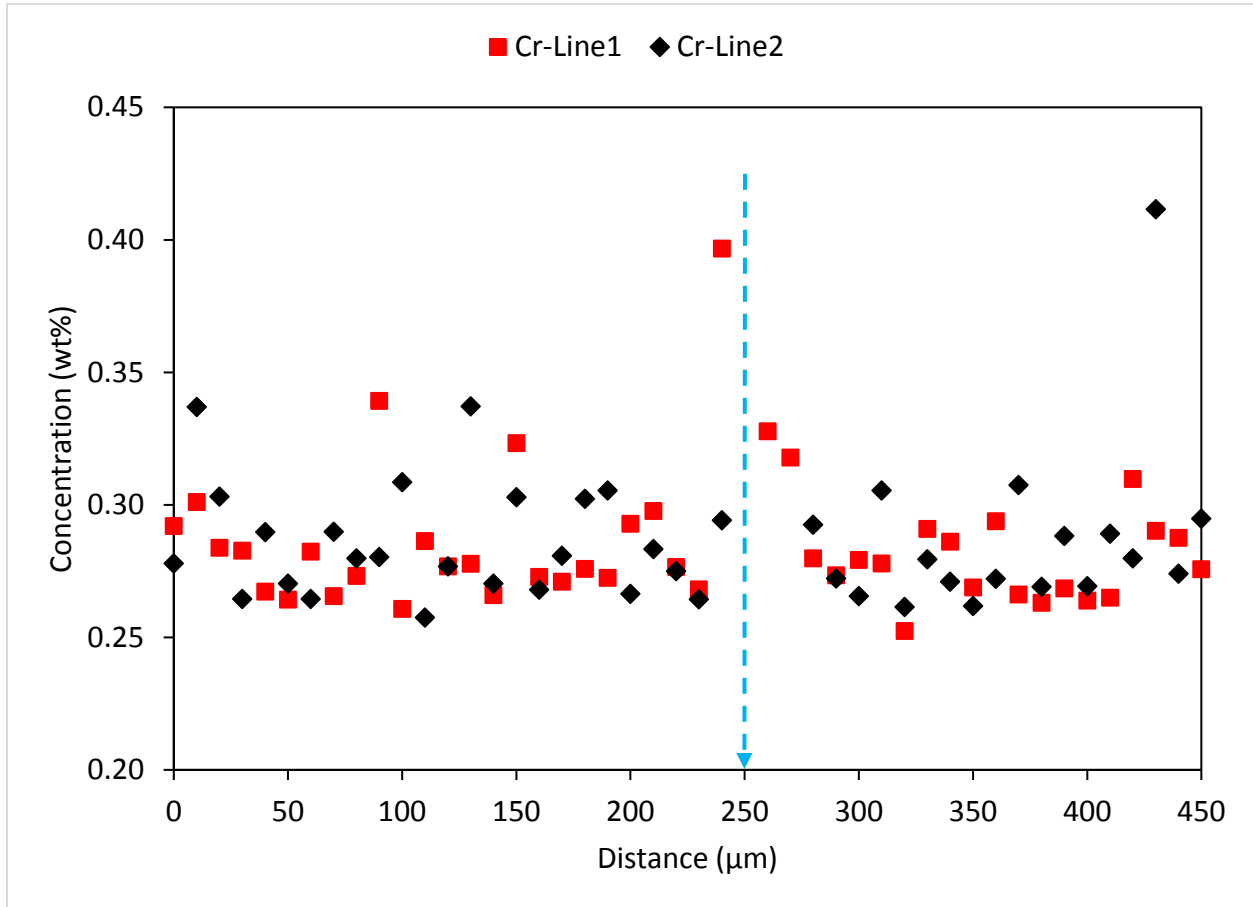


Figure I.4: Cr concentration profile along line scans 1 and 2 shown in Figure I.2.

Figure I.5 shows Si concentration profile along the line scans 1 and 2. A higher concentration of Si ( $\approx 0.35$  wt%) is observed around the HIC crack. The HIC crack is represented by the dashed arrow.

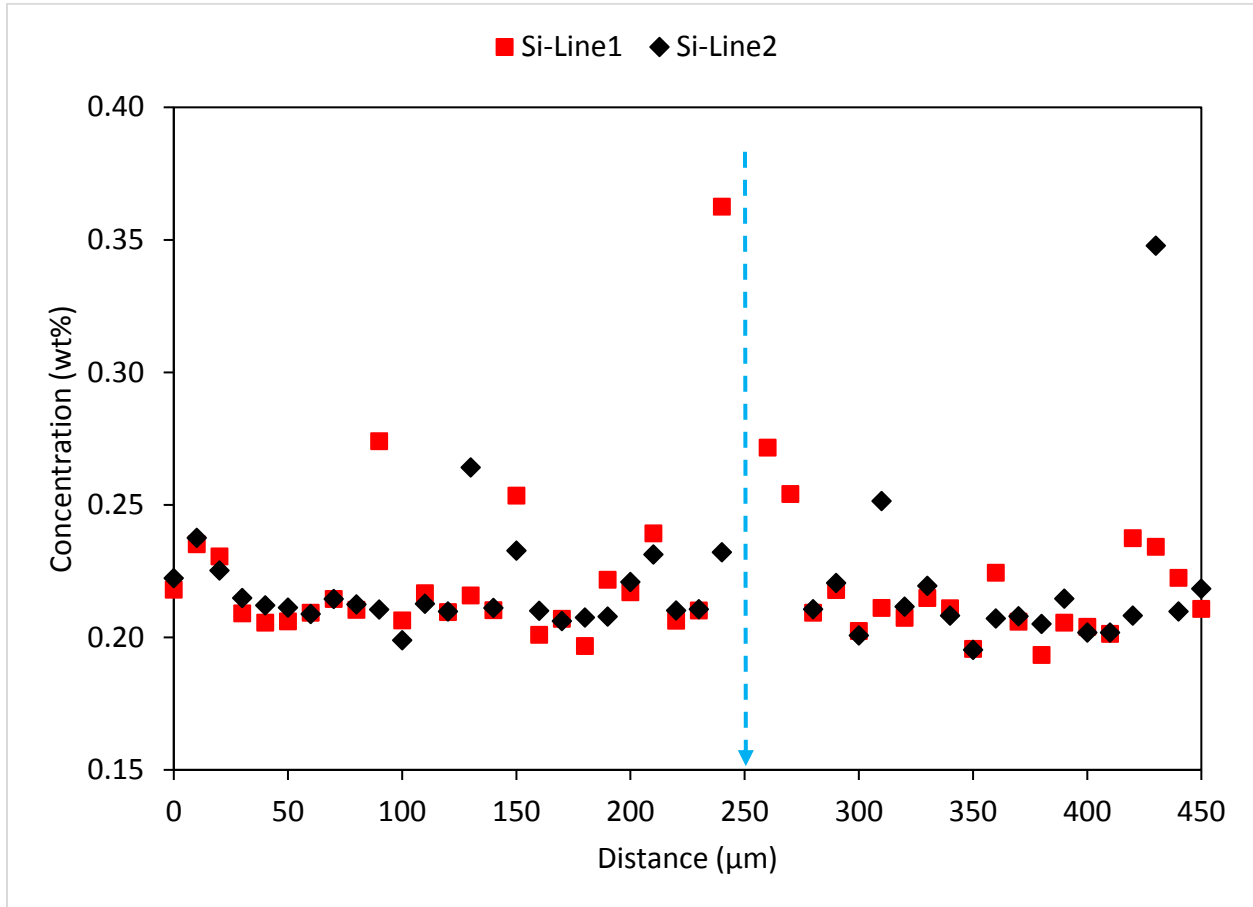


Figure I.5: Si concentration profile along line scans 1 and 2 shown in Figure I.2.

Figure I.6 shows P concentration profile along the line scans 1 and 2. A higher concentration of P ( $\approx 0.06$  wt%) is observed around the HIC crack. The HIC crack is represented by the dashed arrow.

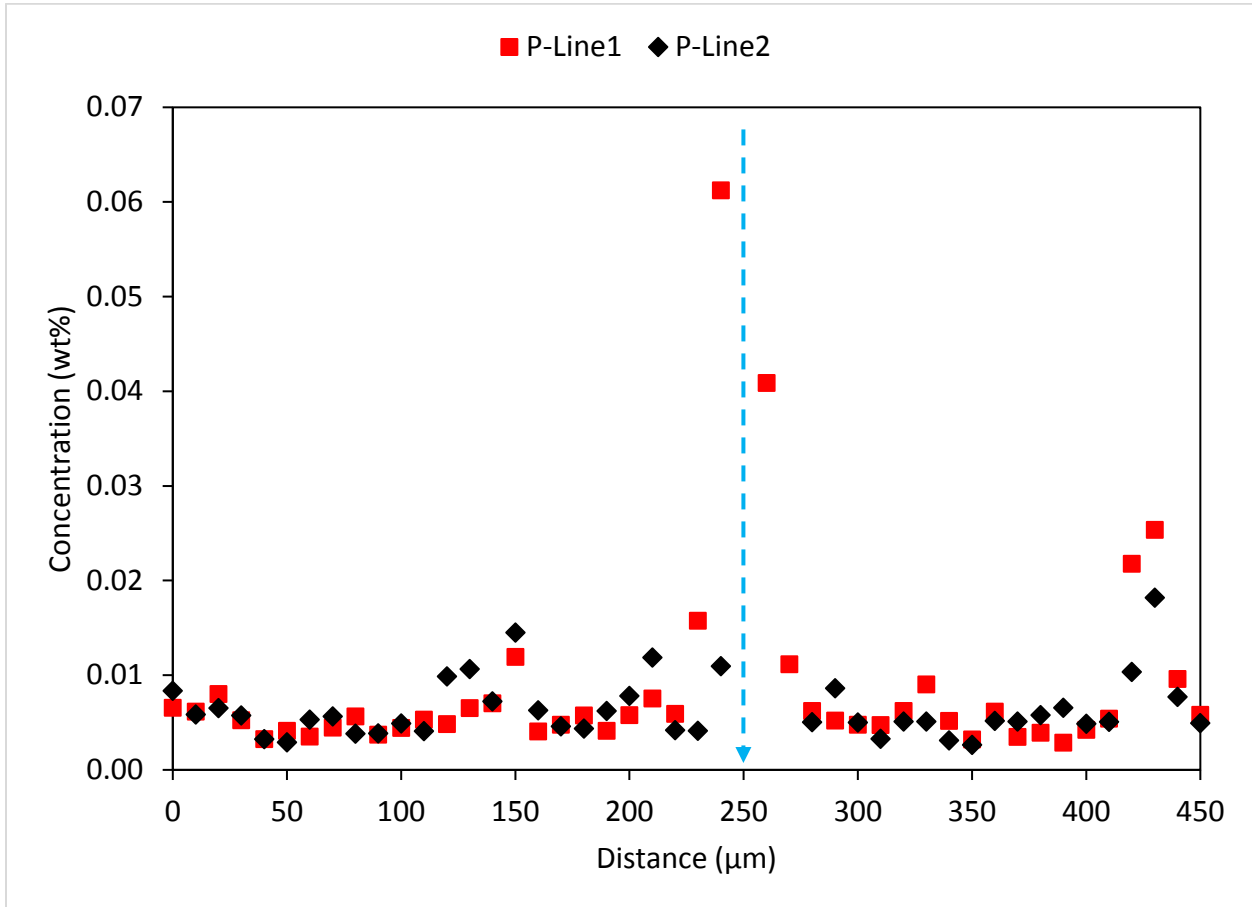


Figure I.6: P concentration profile along line scans 1 and 2 shown in Figure I.2.

## Appendix I.2

This appendix shows EMPA results for High Mn 180° Section 2. High Mn 180° Section 2 means that the analyzed section was the second section taken from a HIC sample cut at 180° from High Mn pipe.

Figure I.7 shows Mn EMPA X-ray map performed across the total thickness of High Mn 180° Section 2. It is clear that the HIC crack is located at the centerline segregation band. The lighter zones indicate a higher concentration of Mn.

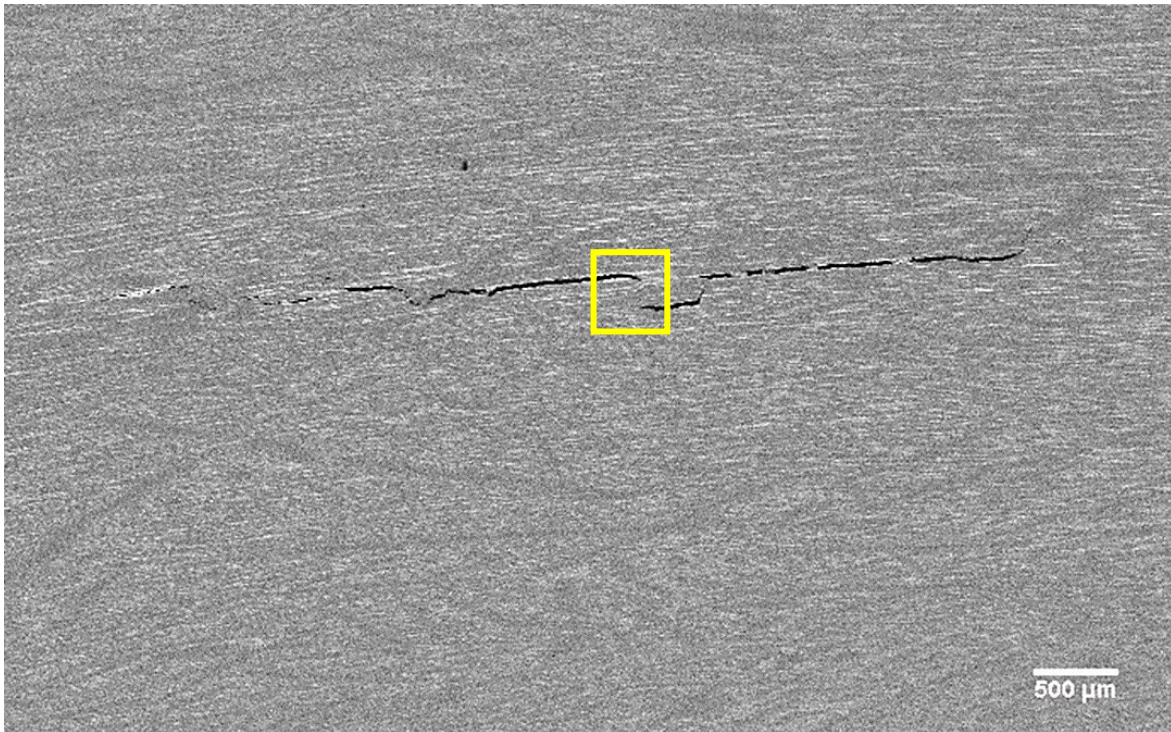


Figure I.7: Mn EMPA X-ray map across the total thickness of High Mn 180° Section 2.

Mn EMPA X-ray map was generated for the area indicated by a square on Figure I.7 and the result is shown in Figure I.8. The white lines indicate a higher concentration of Mn. The segregation lines located at the zone marked by the yellow double headed arrow on Figure I.8 are deformed due to shear.

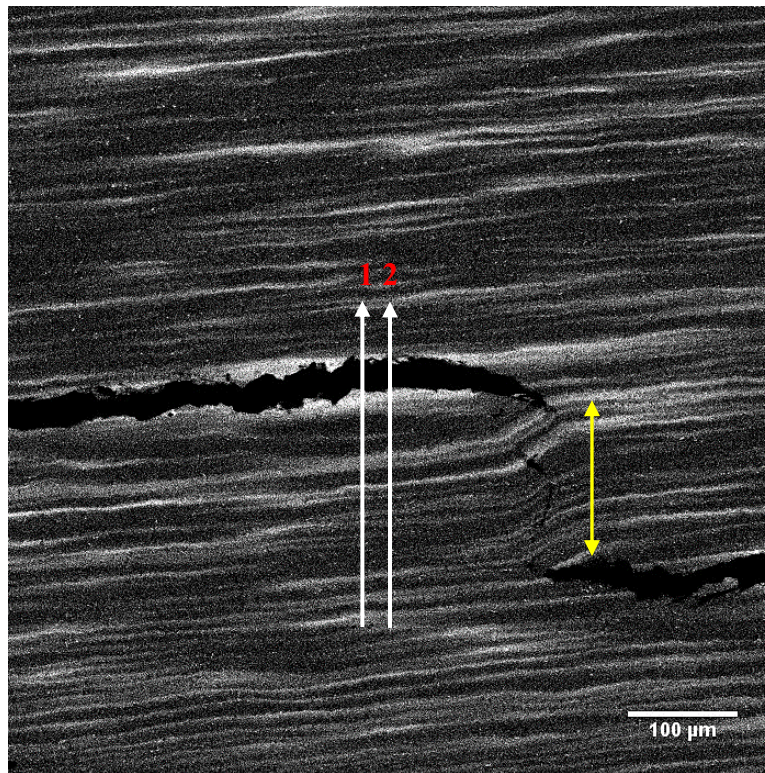


Figure I.8: Mn EMPA X-ray map of the area indicated by a square in Figure I.7.

Two EMPA line scans indicated by the arrows in Figure I.8 were performed and the detected elements were Mn, Cr, Si and P. The concentrations profiles of these elements across the HIC crack obtained from these two line scans are shown in the following figures in Appendix I.2.

Figure I.9 shows the Mn concentration profile along the line scans 1 and 2. A concentration peak of Mn ( $\approx 2.5$  wt%) is found around the HIC crack. The HIC crack is represented by the dashed arrow.

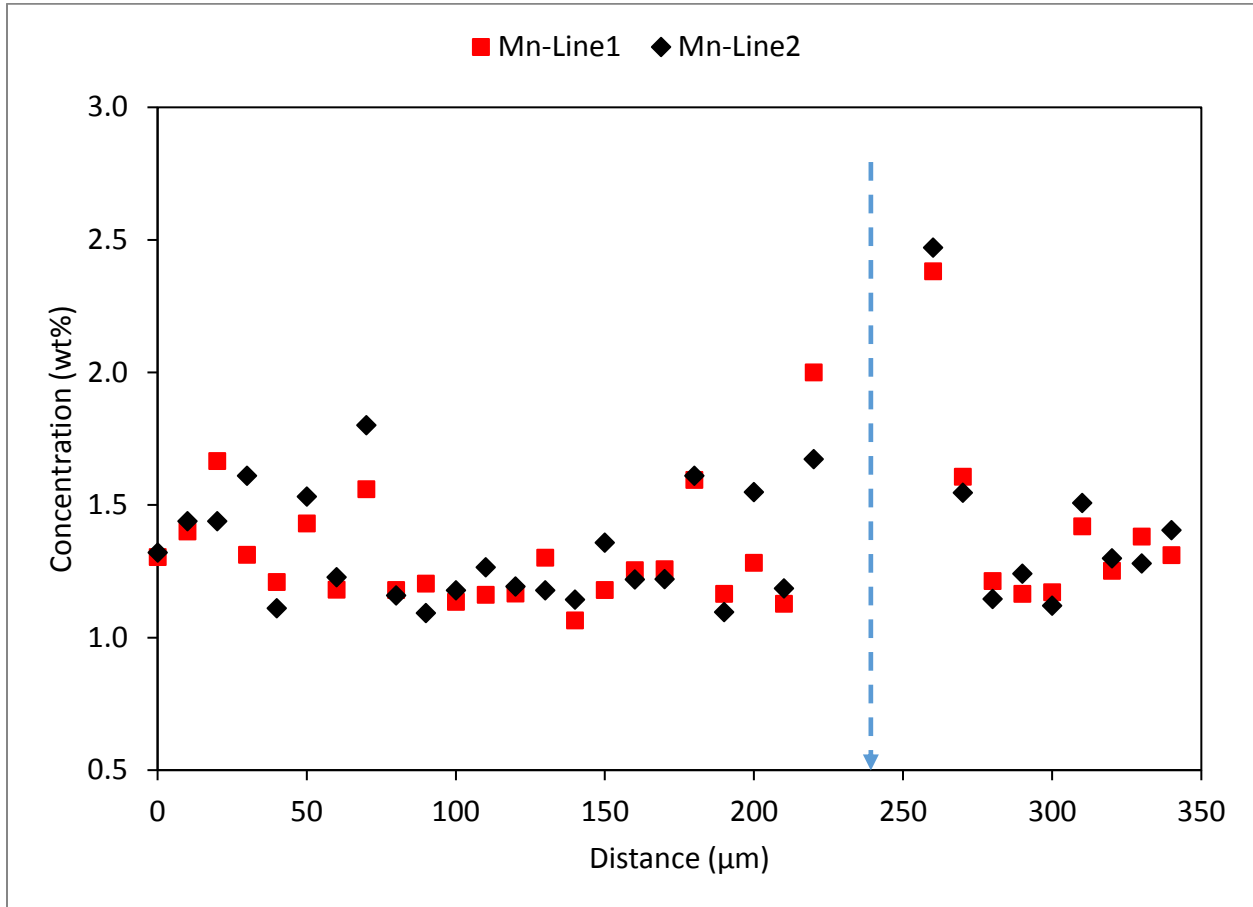


Figure I.9: Mn concentration profile along the line scans 1 and 2 shown in Figure I.8.

Figure I.10 shows the Cr concentration profile along the line scans 1 and 2. A concentration peak of Cr ( $\approx 0.35$  wt%) is found around the HIC crack. The HIC crack is represented by the dashed arrow.

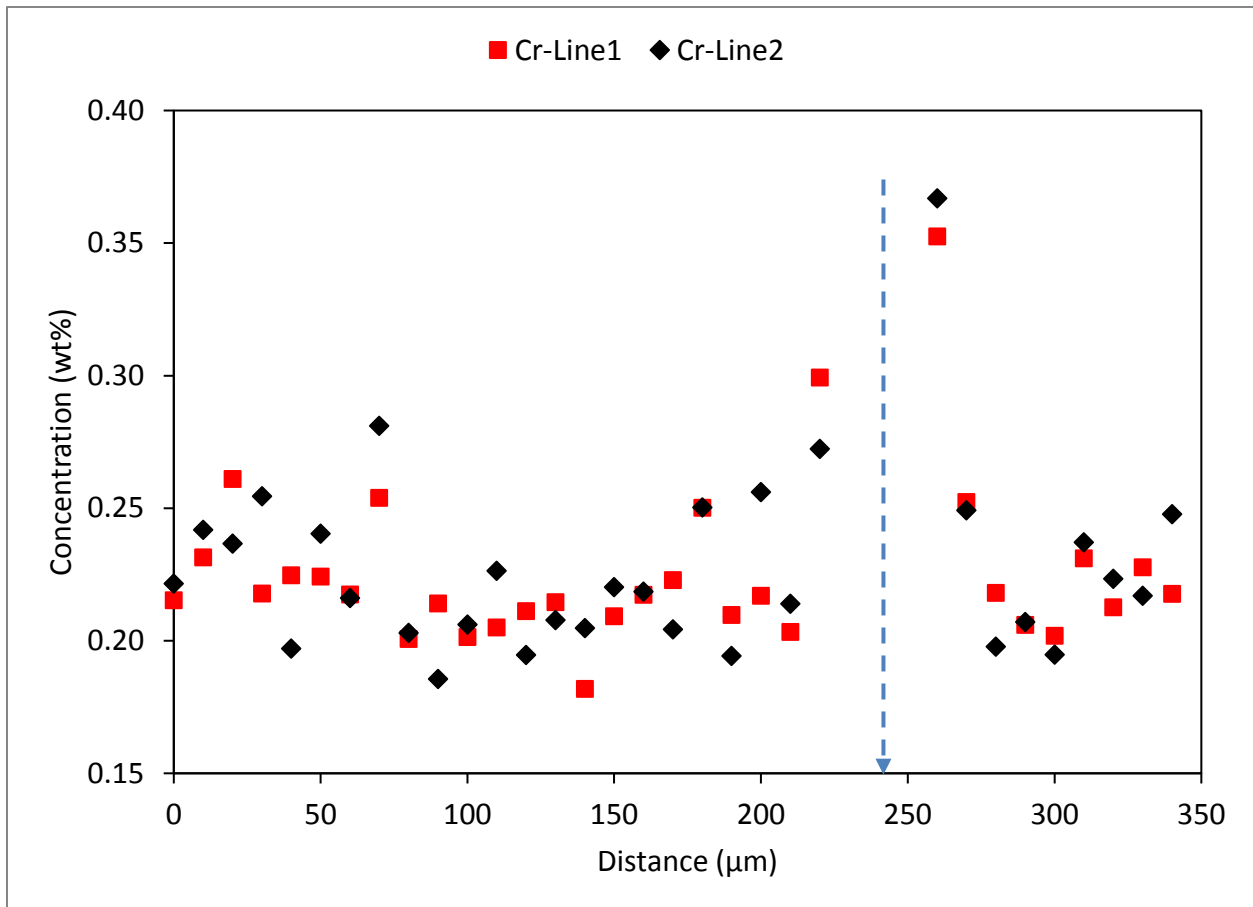


Figure I.10: Cr concentration profile along line scans 1 and 2 shown in Figure I.8.

Figure I.11 shows the Si concentration profile along the line scans 1 and 2. A concentration peak of Si ( $\approx 0.36$  wt%) is found around the HIC crack. The HIC crack is represented by the dashed arrow.

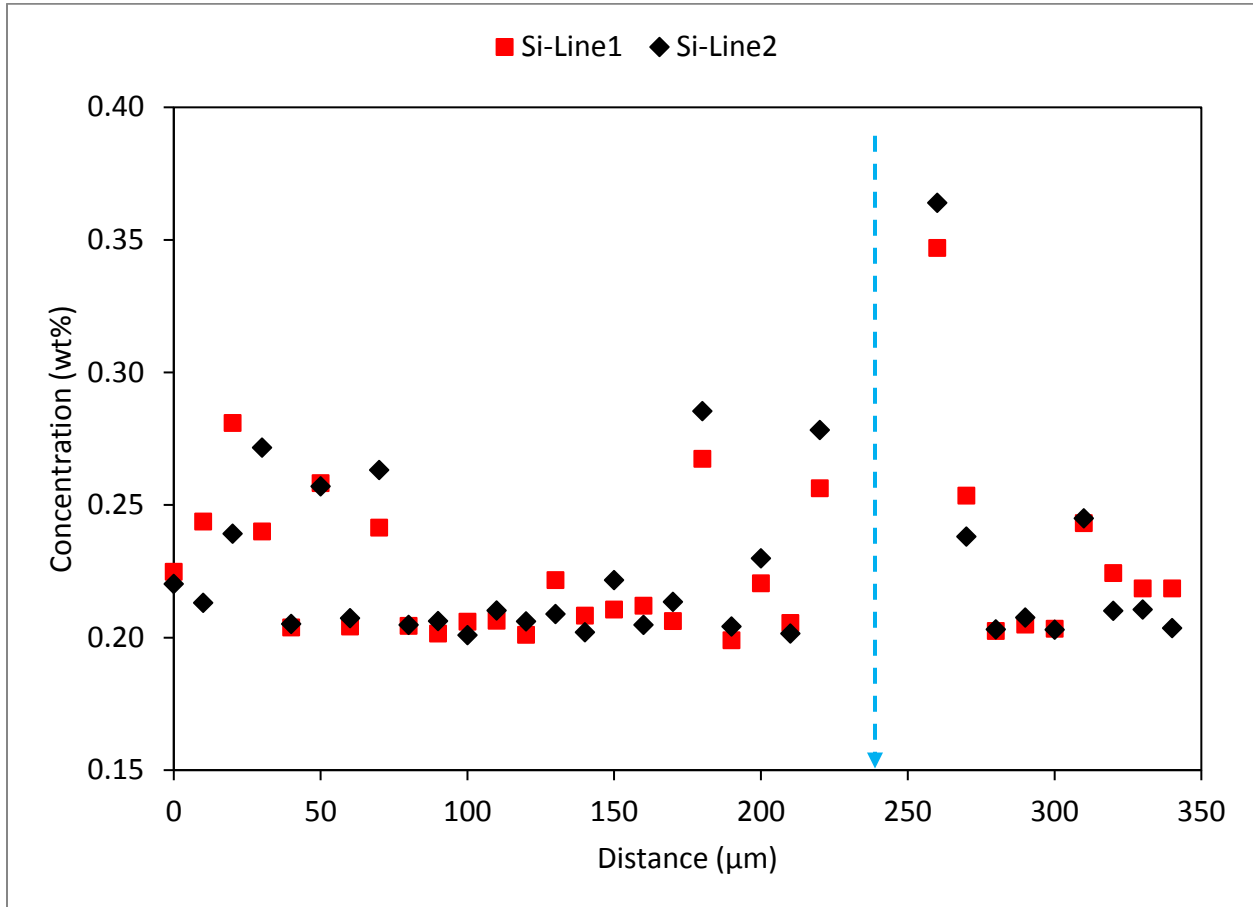


Figure I.11: Si concentration profile along line scans 1 and 2 shown in Figure I.8.



Figure I.12 shows the P concentration profile along the line scans 1 and 2. A concentration peak of P ( $\approx 0.06$  wt%) is found around the HIC crack. The HIC crack is represented by the dashed arrow.

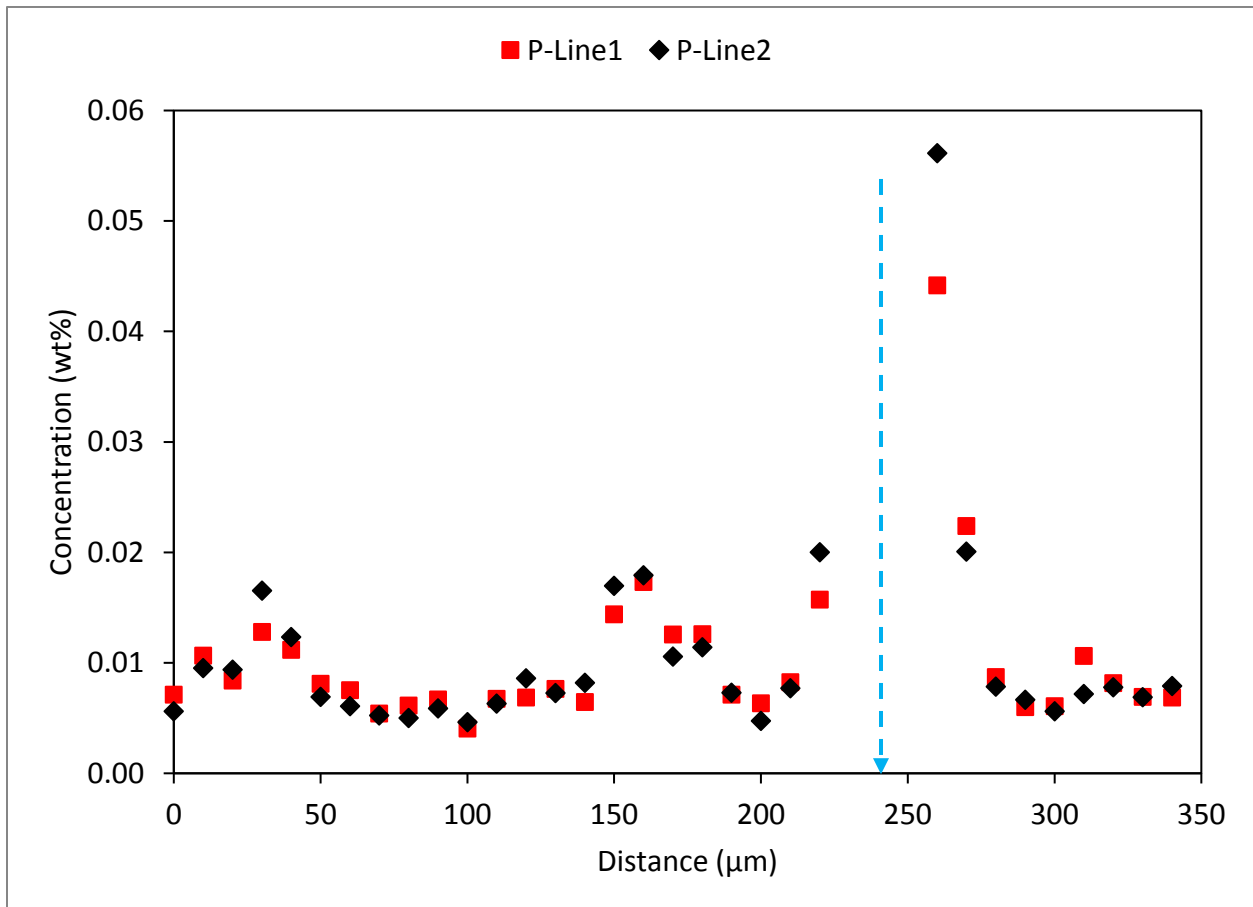


Figure I.12: P concentration profile along line scans 1 and 2 shown in Figure I.8.

## Appendix I.3

This appendix shows EMPA results for TiB 90° Section 2. TiB 90° Section 2 means that the analyzed section was the second section taken from a HIC sample cut at 90° from TiB pipe.

Figure I.13 shows Mn EMPA X-ray map performed across the total thickness of TiB 90° Section 2. It is clear that the HIC crack is located at the centerline segregation band. The lighter zones indicate a higher concentration of Mn.

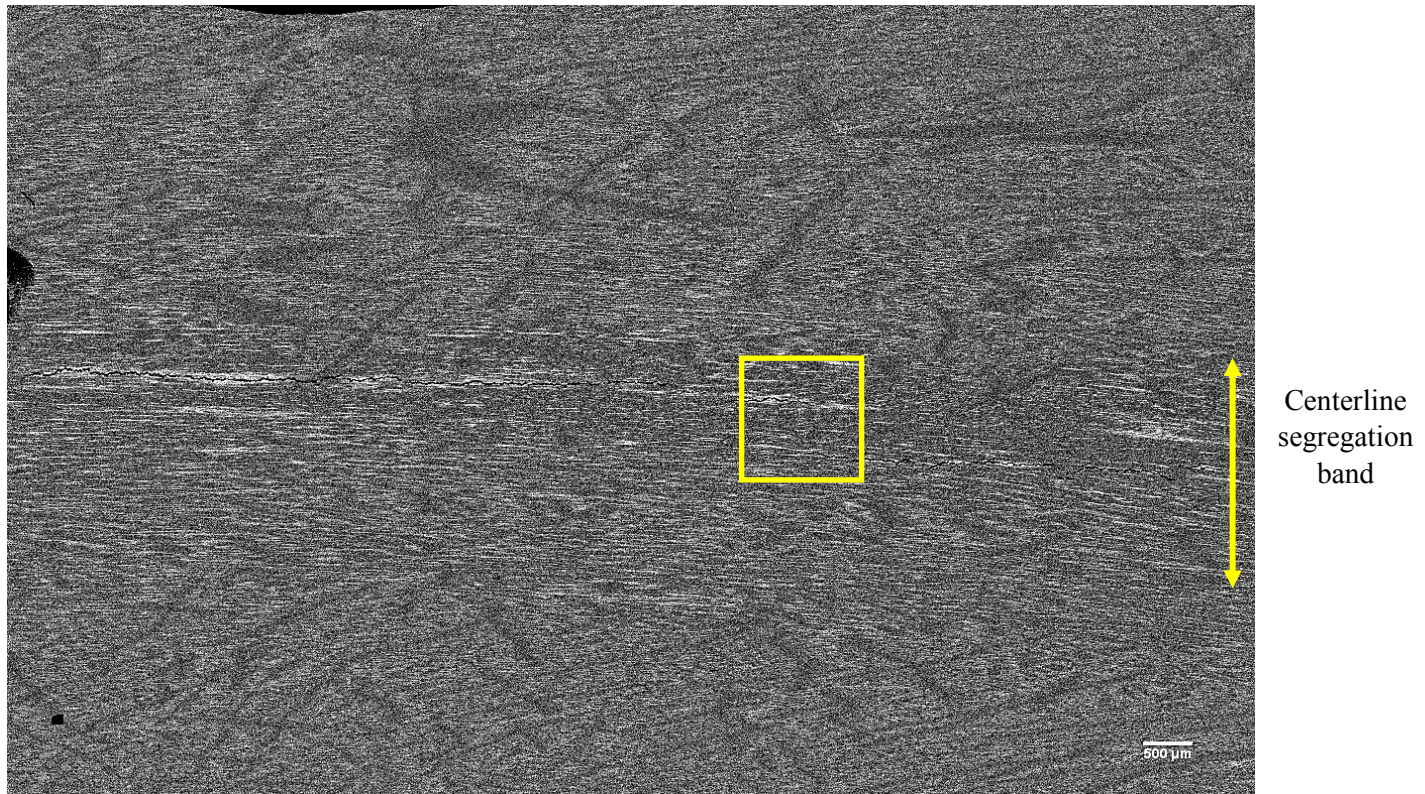


Figure I.13: Mn EMPA X-ray map across the total thickness of TiB 90° Section 2.

Mn EMPA X-ray map was generated for the area indicated by a square on Figure I.13 and the result is shown in Figure I.14.

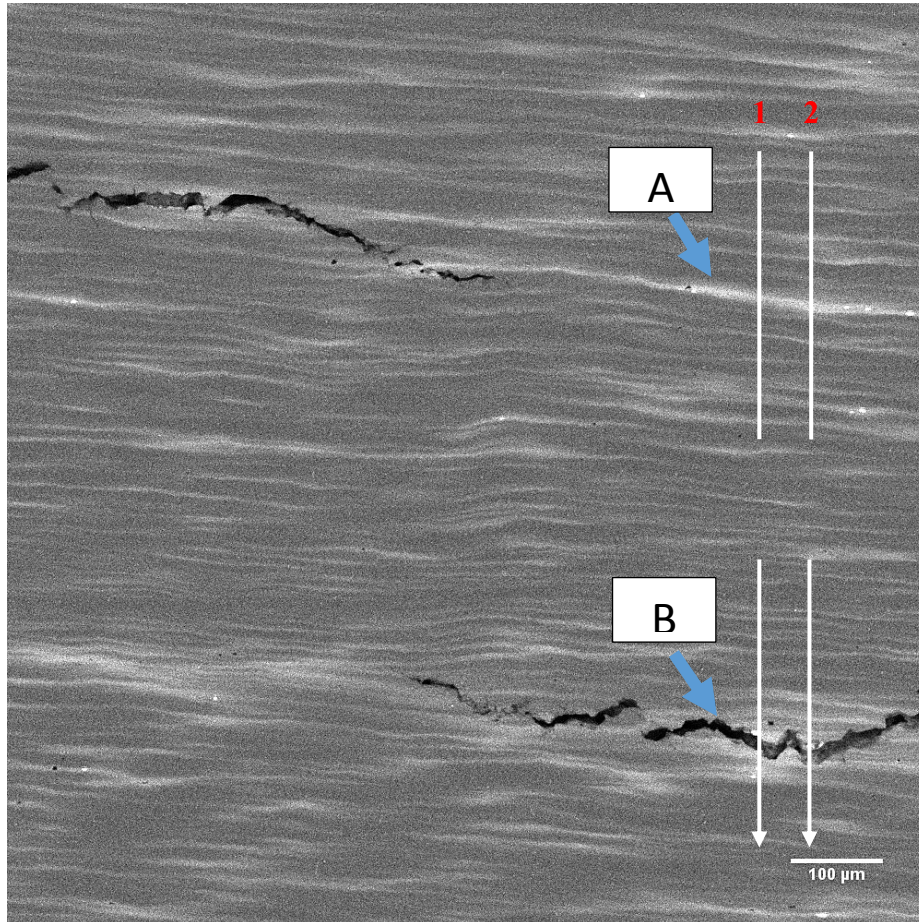


Figure I.14: Mn EMPA X-ray map of the area indicated by a square in Figure I.13.

Two EMPA line scans were performed across the segregation band A and the HIC crack B as shown in Figure I.14 and the detected elements were Mn, Cr, Si and P.

Figure I.15 shows the Mn concentration profile along the line scans 1 and 2. A concentration peak of Mn ( $\approx 1.68$  wt%) is found around the HIC crack B.

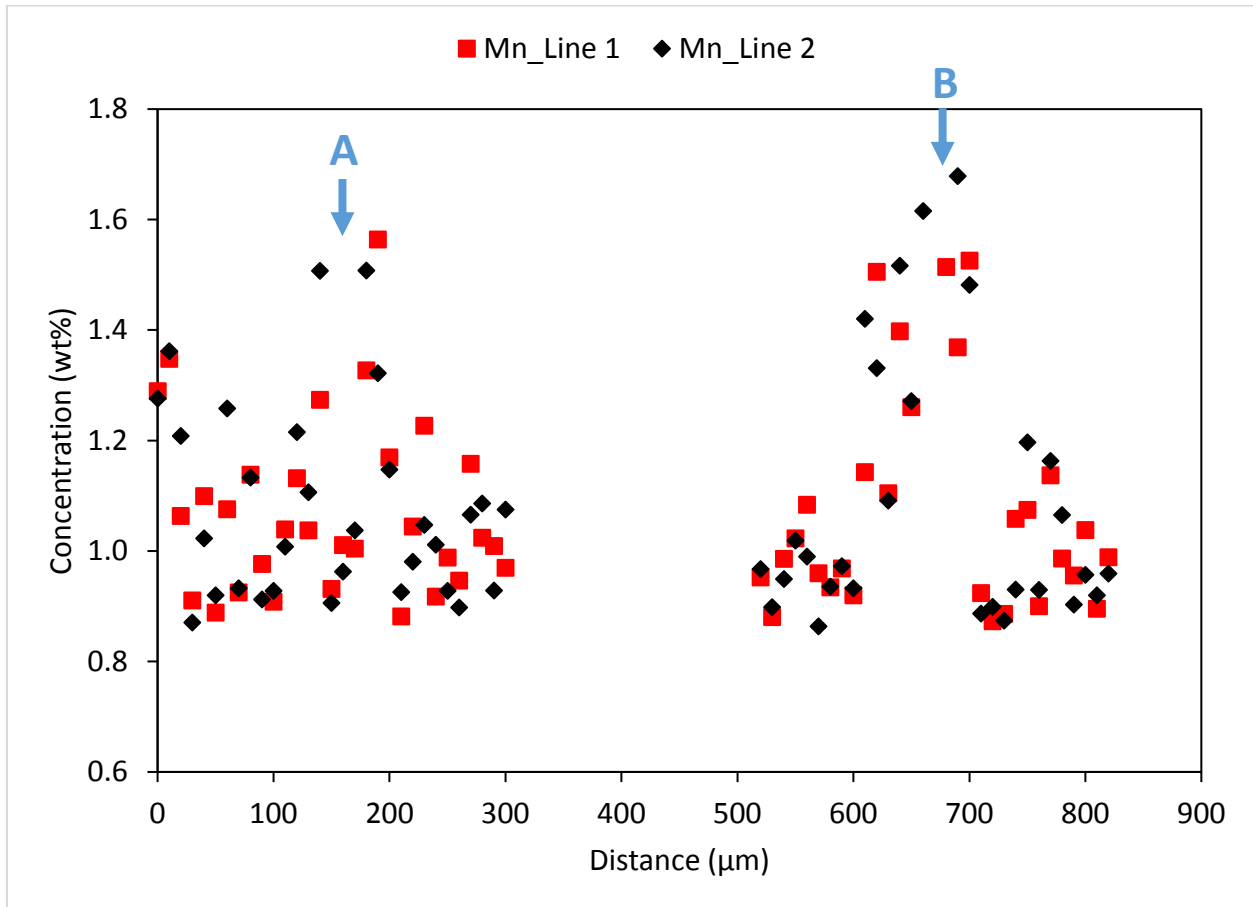


Figure I.15: Mn concentration profile along the line scans 1 and 2 shown in Figure I.14.

Figure I.16 shows the Cr concentration profile along the line scans 1 and 2. A concentration peak of Cr ( $\approx 0.21$  wt%) is found around the HIC crack B.

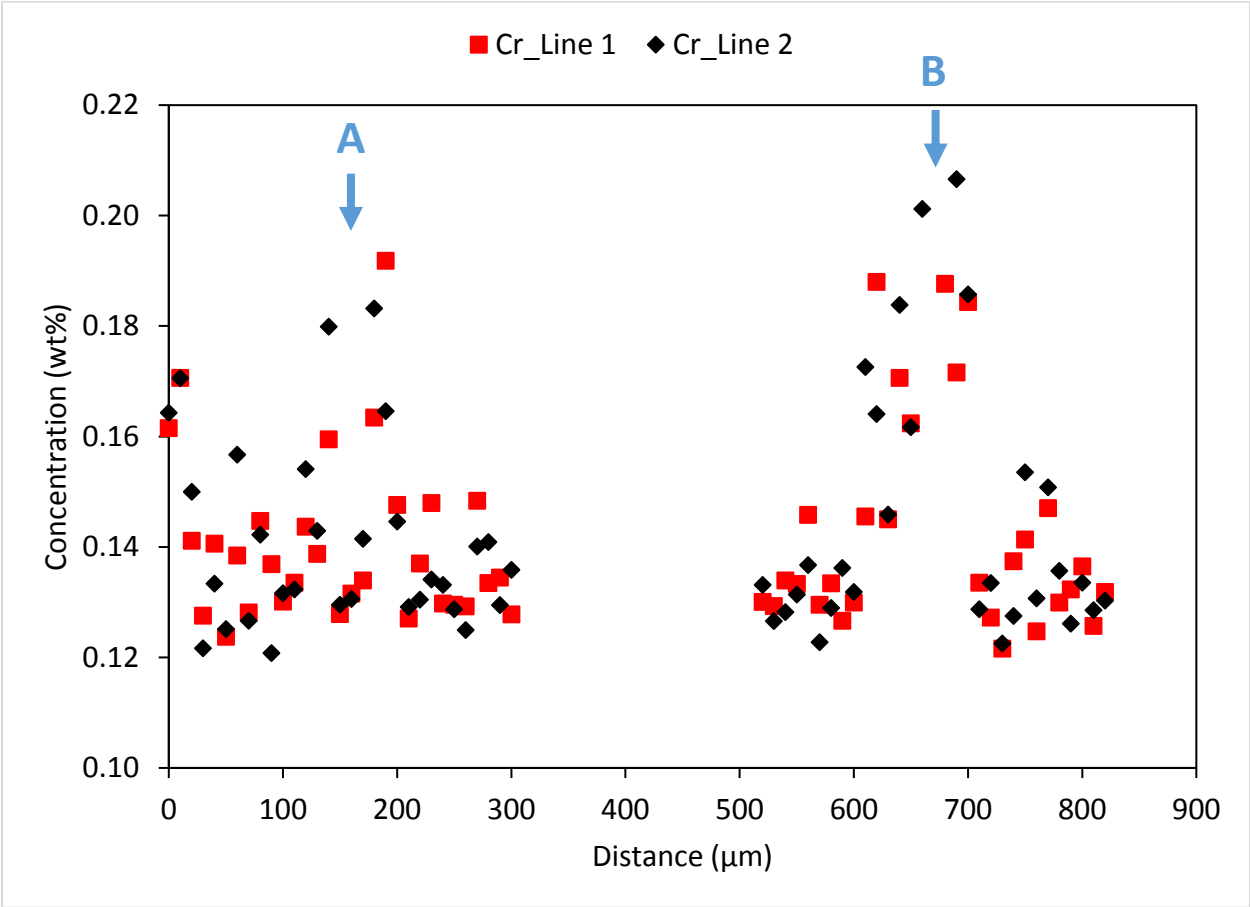


Figure I.16: Cr concentration profile along the line scans 1 and 2 shown in Figure I.14.

Figure I.17 shows the Si concentration profile along the line scans 1 and 2. A concentration peak of Si ( $\approx 0.35$  wt%) is found around the HIC crack B.

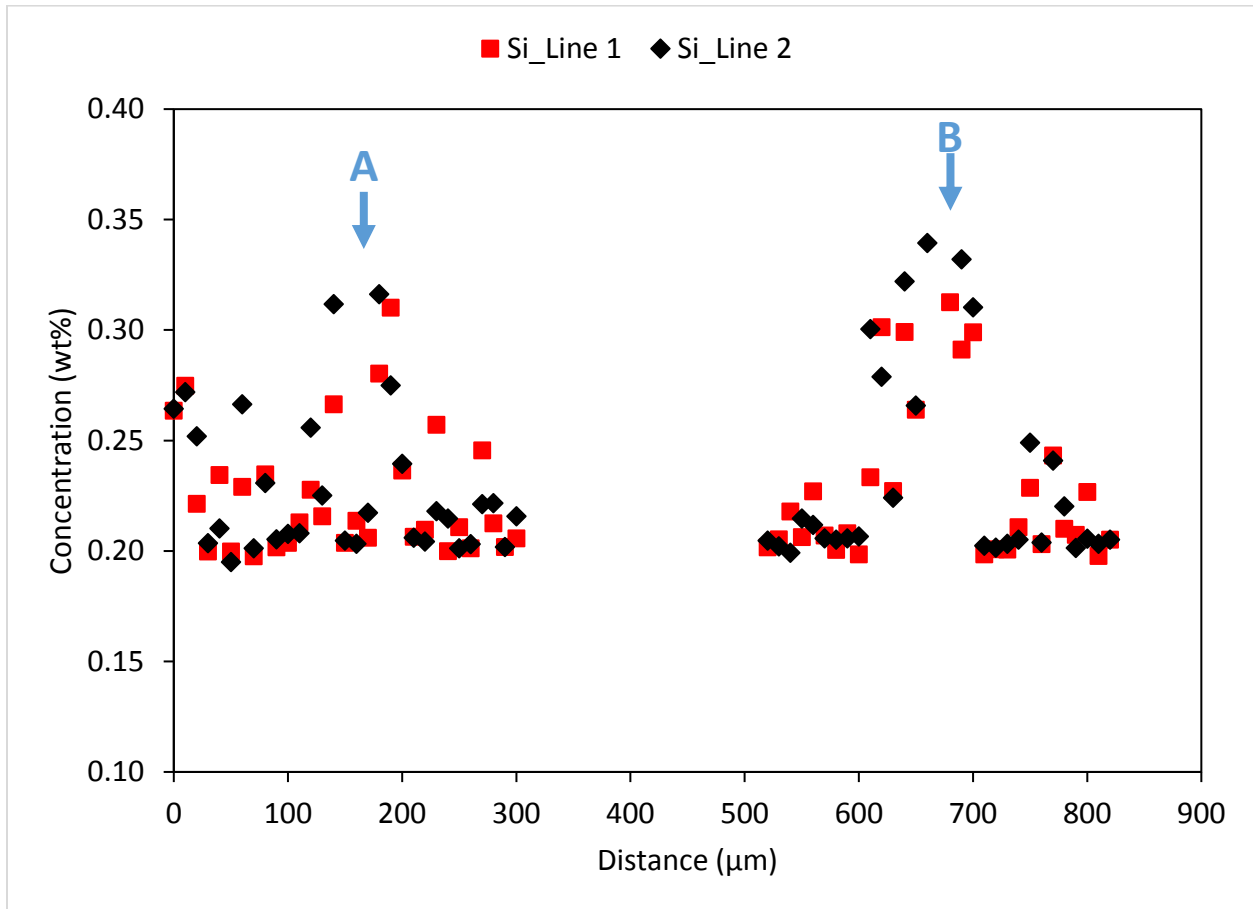


Figure I.17: Si concentration profile along the line scans 1 and 2 shown in Figure I.14.

Figure I.18 shows the P concentration profile along the line scans 1 and 2. A concentration peak of P ( $\approx 0.1$  wt%) is found around the HIC crack B. The concentration peak of P at the HIC crack B is higher than the concentration peak of P at the segregation band A, which confirms that P plays a role in the propagation of the HIC crack.

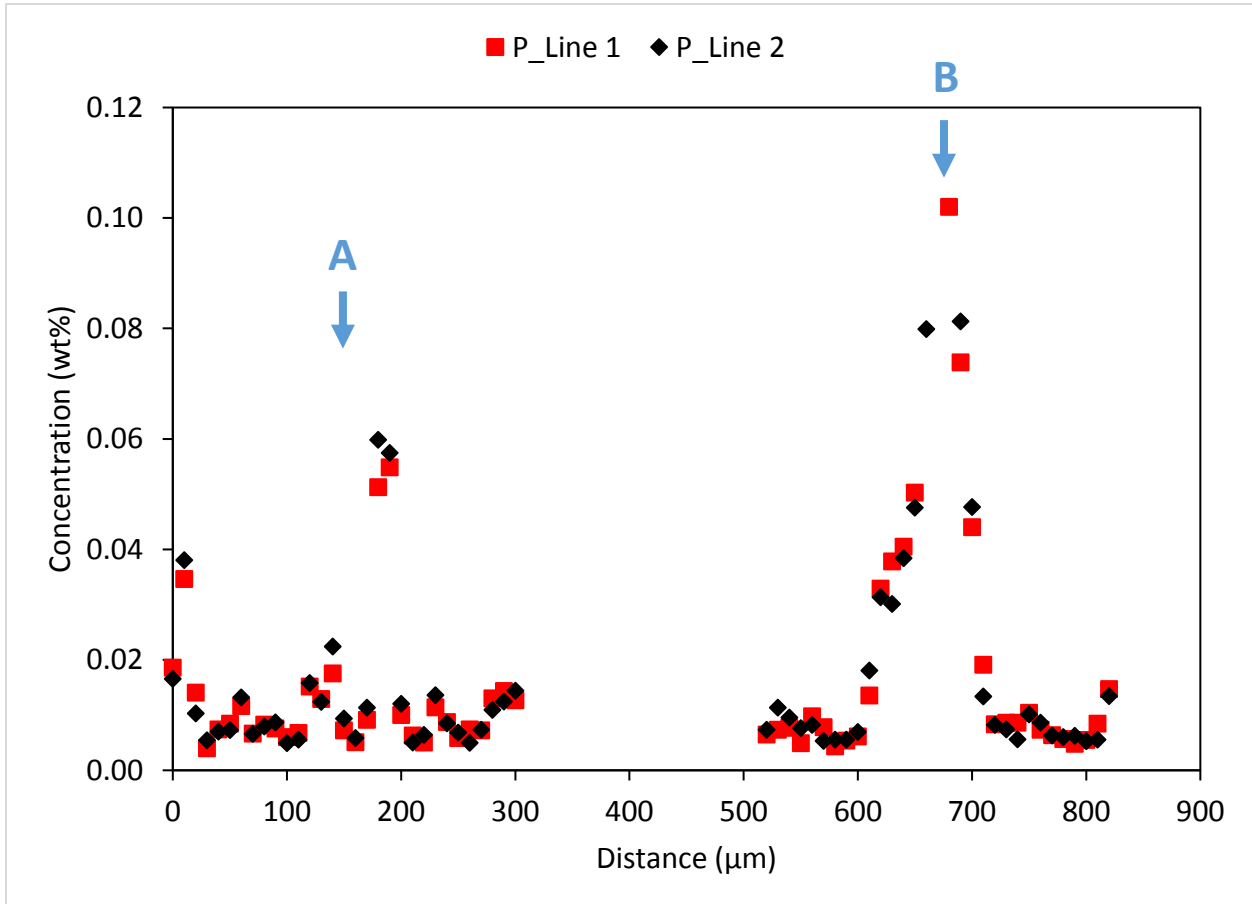


Figure I.18: P concentration profile along the line scans 1 and 2 shown in Figure I.14.